DIODE-LASER PUMPED, HIGH-REPETITION-RATE, ND:YLF LASER AND ITS FREQUENCY CONVERSION.

Christian Rahlff

A Thesis Submitted for the Degree of PhD
at the
University of St Andrews

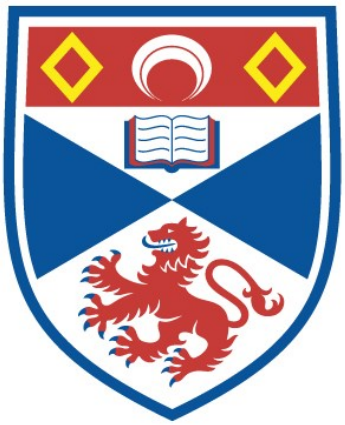

1996

Diode-Laser Pumped, High-Repetition-Rate, Nd:YLF Laser and Its Frequency Conversion

A thesis presented by

Christian Rahlff, Dipl. Phys.

to the

University of St. Andrews

in application for the degree of

Doctor of Philosophy

April 1996

'You need a busload of faith to get by'

Lou Reed

('Busload of Faith', New York (1989))

Für meine Eltern

&

Sara

Declarations

I, Christian Rahlff, hereby certificate that this thesis has been composed by myself, that it is a record of my own work, and that it has not been accepted in partial or complete fulfilment of any other degree of professional qualification. I was admitted to the Faculty of Science of the University of St. Andrews under Ordinance General No.12 on 6th January 1992 and as a candidate for the degree of Ph.D. on 1st October 1992.

Christian Rahlff April 1996

I hereby certify that the candidate has fulfilled the conditions of the Resolution and Regulations appropriate to the Degree of. Ph.D.

Prof. Malcolm H. Dunn April 1996

In submitting this thesis to the University of St. Andrews I understand that I am giving permission for it to be made available for use in accordance with the regulations of the University Library for the time being in force, subject to any copyright vested in the work not being affected thereby. I also understand that the title and abstract may be made and supplied to any *bona fide* library or research worker.

Acknowledgements

I wish to gratefully thank my supervisor, Prof. Malcolm Dunn, for his guidance, suggestions and patience displayed during the course of this work. His dedication, physical insight and enthusiasm has always been a motivation in trying to come to a better understanding of the contents of this thesis.
I would also like to thank my co-supervisor, Prof. Wilson Sibbett, for the discussions and his constant interest and encouragement. To both of them I owe a large debt of gratitude in providing the funding and facilities, which makes research like this possible, as well as providing my personal funding over the last four years, making it possible for me to come to Scotland.

In a work based on the development of a laser system, technical support is very important. Many thanks are due to the mechanical and electronical workshops at St. Andrews. In particular to Jimmy Lindsay, for building the first pump module and realising new standards in translation stage density per cubic inch, Miles Whyte, for the second pump module and the most excellent slab cooler, as well as George Radley and Jim Clark and Fritz Akerboom for providing 'vital' mounts on short notice.

Angus Henderson, Callum Norrie, Andy Harvey, Dom Withers and Sara Shepherd were very helpful in making the change from Berlin to St. Andrews easier during the first months in Scotland. Callum Norrie's advice during the first few months at St. Andrews was very important and gave my Ph.D. a good start.
In particular Sara, Angus and Dom made life in St. Andrews very pleasant. It is a pity that Angus's abilities as a golfer could not be matched by his abilities to teach ('Keep ya heed dun..') the game. However, the 'Himalayas' are fine with me and Dom Withers was always a worthwhile opponent in these somewhat competitive putting events.

I thank all the group members of the physics department for their help, good humour and willingness to lend equipment. Special thanks are due to:
Gordon Robertson, Angus Henderson Finlay Colville, Jonny Terry, Neil MacKinnon, Nigel Gallagher, Cameron Rae, Garry Morisson, Yan Tang, Dom Withers, the whole EIT crew (Sara, Richard, David, James and Litsa), Steven French and the W squad, especially Gordon Kennedy, Dave Burns, Karen Oppo, Derek Reed and Bill Sleat. Many thanks to John Jardine to provide (the often needed) realignment with reality.

Finally I have to thank my father for having taught me a lot, besides supporting me over all these years, as well as Sara for keeping it all together.

Abstract

This thesis describes the development of a continuous-wave (cw), diode pumped, repetitively Q-switched Nd:YLF laser, and its application as a pump source for non-linear optical frequency converters and optical parametric oscillators (OPO's), with typical pulse widths of several tens of nanoseconds and repetition rates in the kHz region.

At the core of this thesis is the proposal and realisation of a novel rhombic Nd:YLF slab geometry, which is pumped by two 20W cw AlGaAs diode arrays, each focused by means of 3 lenses into a folded resonator path. The novelty of this adaptation is that it uses Yttrium Lithium Fluoride (YLF), known for its comparatively low tensile strength, as the Neodymium host crystal, by addressing and solving the thermal stress fracture problem in YLF for pump powers up to 20W per surface in an end-pumped configuration. With the excellent beam quality, high average output power and short pulses achieved, Nd:YLF has been established as an excellent material for high density, diode pumped, Q-switched lasers at 1047nm.

With identical slabs coated for 1321nm operation also available, the performance and laser parameters such as crossection, linewidth and thermal lensing for these two transitions were compared. The pronounced change in the thermal lensing of the 1321nm transition led to an investigation of excited state upconversion (ESA) in Nd:YLF at 1047 and 1321nm under cw and Q-switched operation. The excellent access to the pumped volume made not only a time dependent spectral analysis of the visible and near UV fluorescence bands possible, but also permitted a spatial analysis of the different up-conversion areas. This pump density and laser transition dependent loss mechanism has implications on the end-effect governed lensing, upper state lifetime and Q-switched pulse form.

The low threshold, high repetition rate conversion schemes realised during this thesis expanded the spectral cover of the 1μm pump laser from the near UV (349nm) at one end of the spectrum over the green (523.5nm) and 1.5μm region up to the near infrared at 3.445μm. The progress in this area lies not in the well known phase match configuration of the materials used such as KTP, KTA and LBO, but in the adaptation of these non-linear converters and non-critically phase matched (NCPM) OPO's to achieve high conversion efficiencies at low pulse energies (typically less than 1mJ, 40kW). With average output powers in the green of 3W (~60% conversion from the IR at 6kHz repetition rate), 750mW in the UV, 1W at 1.54μm and 280mW at 3.44μm it has been demonstrated that the high average output power of the repetitively Q-switched system can be preserved in the up- and down-converted radiation.

Contents

Outline of the rhombic Nd:YLF slab (~7 x 7mm²) developed during this work. The pumped areas are clearly recognisable, as is the folded resonator path, emerging under Brewster's angle from the slab through the unpumped windows. A display of the whole cavity path is possible through an up-conversion process involving the 1.321μm laser radiation

The good mode quality, high average power and short pulse durations made frequency conversion schemes with high efficiencies (up to 65% for frequency doubling) possible. The picture shows the green (523.5nm) and near UV (349nm) laser output during frequency mixing experiments in LBO.

Characteristic pulse forms for the high repetition rate Nd:YLF laser for an average power of 4.8W at 6kHz repetition rate, operating on the 1.047μm line in Nd:YLF. The short pulse duration and high temporal stability (124 pulses are samples over ~10s) made the 1μm laser an ideal pump source for non-linear optics experiments.

Conversion / back-conversion cycles for the green radiation within a KTP crystal (10mm) during single path, external doubling experiments. The reduction in the coherence length is introduced by a rotation in the ϕ-plane of the doubler, thus introducing phase-mismatch.

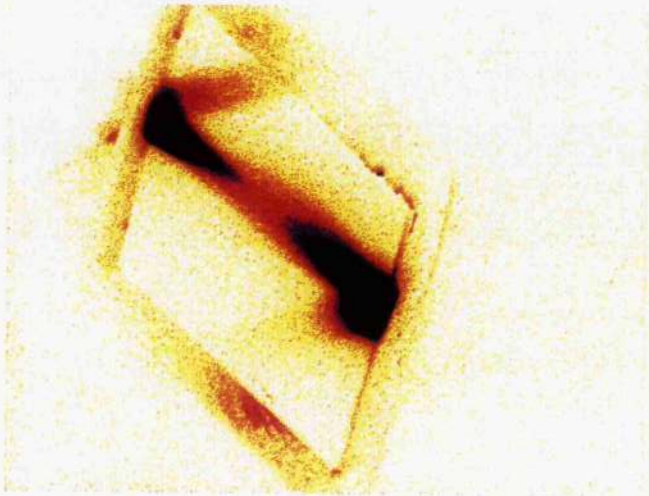

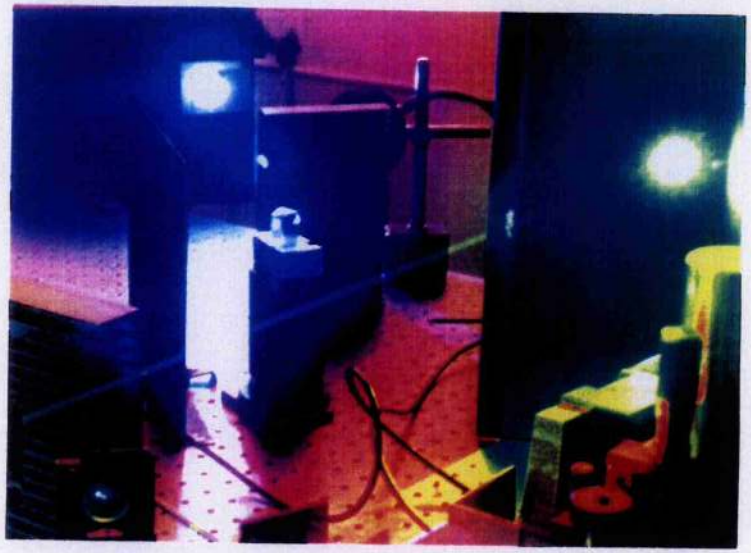

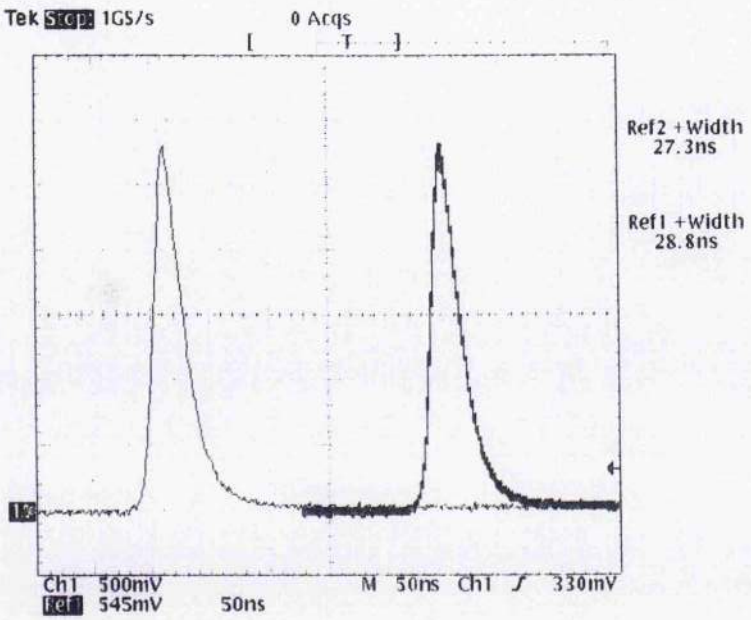
Tek Stop: 1GS/s
0 Acqs
Ref2 +Width
27.3ns
Ref1 +Width
28.8ns
Ch1 500mV
Ref1 545mV
50ns
M 50ns Ch1 ƒ 330mV

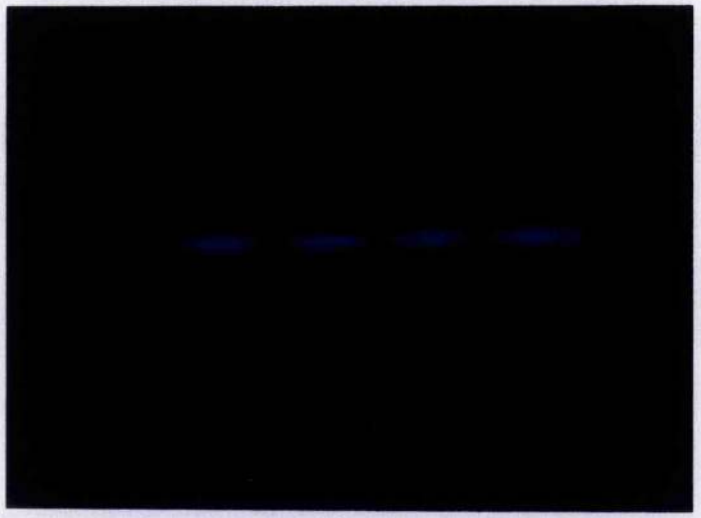

Chapter I.

Introduction

Since the first observation of stimulated emission under pulsed optical pumping in Neodymium doped Yttrium Lithium Fluoride (Nd:YLF) at 1047 and 1053nm was reported by Harmer, Linz et al. [1] in 1967, 29 years ago, Nd:YLF has come a long way in becoming one of the leading diode pumped solid state laser materials of recent years. It took another 6 years before the material quality of this anisotropic laser material was sufficient to allow the growth of a 5cm long c-axis rod, to enable comparison with the then already matured Neodymium doped Yttrium Aluminium Garnet (Nd:YAG) in a flashlamp pumped laser [2]. At this stage Nd:YAG was still the superior laser material, with better optical quality.

By then the spectroscopic data of Nd:YLF was well documented [3], and in particular its lower crossection (by a factor of two), combined with its 2.5 times longer upper state lifetime, set Nd:YLF aside as a medium gain material when compared to the high gain material Nd:YAG. The strength of medium gain materials are in their energy storage capability. The reduced crossection has distinct advantages in amplifier design, due to the later onset of amplified spontaneous emission, while the longer fluorescence lifetime is an important advantage in repetitively or quasi-cw pumped Q-switched lasers. The relation between the average output power, P_{av}, of a repetitively Q-switched laser and its cw output power level, P_{cw}, can be approximated by:

$$P_{av} = P_{cw} f\tau \left\{1 - \exp\left(-1/f\tau\right)\right\} \xrightarrow{f\tau \ll 1} P_{av} = P_{cw} f\tau \qquad (1.1)$$

where f is the repetition rate and τ the lifetime of the laser transition.

For low repetition rates ($f\tau << 1$) the energy per pulse stays constant, while the average power decreases linearly with the repetition rate and the upper state lifetime defines the maximum extractable pulse energy.

The first cw flashlamp pumped operation of Nd:YLF was reported in 1982 by Chicklis, Jensen et al. [4]. In that comparison with Nd:YAG the advantage of an expected lower cw threshold in Nd:YLF was confirmed. The cw threshold of a laser material scales with the inverse of the product of crossection and lifetime, assuming identical experimental conditions and pumping efficiencies.

$$\frac{P_{Thres.}(YLF)}{P_{Thres.}(YAG)} = \frac{\sigma\tau(YAG)}{\sigma\tau(YLF)} \qquad (1.2)$$

The predicted ratio of 0.65 was somewhat lower than the measured ratio of 0.85, and Nd:YAG still exhibited substantially higher slope efficiencies in multi-mode operation (0.75% as compared to 0.4% for Nd:YLF). This difference in slope efficiency was attributed to a lower pumping efficiency into the upper laser level caused by a lower integrated line strength and/or quantum efficiency of the pump bands under flashlamp pumped conditions. More important, however, was the superior performance of Nd:YLF under TEM_{oo} operation, enforced by intra-cavity aperturing, due to its higher single spatial mode volume, which was a factor of four times larger than that of Nd:YAG. Jensen et al. therefore concluded that the combination of weaker thermal lensing, polarised output and higher fluorescence lifetime would make Nd:YLF an exceptional Q-switched laser material, especially with regard to non-linear conversion schemes, due to the intrinsic polarisation properties of the material. A prognosis which has now been fully realised, due to high power, diode pumping of Nd:YLF.

The transition from flashlamp to diode-pumping of Nd:YLF lasers started in 1986 with Fan, Byer et al. reporting a cw single-stripe diode end-pumped Nd:YLF laser [5], with sub mW threshold, overall conversion efficiencies approaching 30%, and 8mW of output power for 1047nm operation. Temperature tuned intracavity doubling in Lithium Niobate ($MgO:LiNbO_3$) achieved 150μW at 523.5nm and indicated the future advances which could be expected from the combination of highly efficient diode pumped solid state lasers and non-linear optics.

The use of narrow bandwidth (typical 2-3nm FWHM for high power arrays) semi-conductor diode lasers as the pump source for Nd:YLF removed the problem of the lower pumping efficiency in YLF, as compared to YAG under flashlamp pumping, by pumping directly into one of the two main absorption lines of Nd:YLF at 791 and 797nm. With the advances in the output power of GaAlAs diodes, the next major step in diode-pumped solid-state laser

development was the use of a 10W cw linear diode array for end-pumping Nd:YAG, by Shannon & Wallace in 1991 [6]. The strong asymmetry in the output of the diode bar, which had an aperture of 10mm x 1μm, was transformed by a 3-element focusing optic in order to allow end-pumping.
Pump power densities of several kW concentrated within a few cubic millimetres of the neodymium host crystal places extreme demands on the host crystal quality. The high efficiency of the end-pumped design started to suffer setbacks at these pump power levels, due to changes in the optical properties of the host crystal, caused by the thermal gradients within the gain region [7]. As thermal stress fracture of the host crystal at these pump densities becomes a real concern, the early high power work concentrated on YAG lasers, which have the important advantage over YLF of a much better thermal shock parameter, R, which is a figure of merit for the thermo-mechanical properties of a crystal.

At the start of this work, in the beginning of 1992, St. Andrews University took delivery of one of the first couple of 20W cw-diode array-bars commercially available in Europe. Even at pump power levels of 20W, only 10mJ of energy are delivered into the pump bands within the fluorescence lifetime of Nd:YLF. In the case of Nd:YAG this value more than halves and compares even more unfavourable to pulsed diode pumping, where several tens of mJ are easily available within 400μs [8]. This underlines again the importance of medium gain materials with high energy storage capability, especially in cw-diode pumped, repetitively Q-switched lasers.
The work in this thesis pioneered high power, diode-bar, end-pumping in Nd:YLF, resulting for example in the generation of 3W of green radiation at 5KHz repetition rate (25ns pulse durations) in a simple, external single pass KTP doubling scheme, with conversion efficiencies around 60% [9]. These results were state of the art until the development of side pumped Nd:YLF systems in 1995 [10], which avoided the strongly aberrated thermal lensing, characteristic of strongly end-pumped, monolithic laser designs. Currently, the above mentioned work by Harrison, Moulton et al. has demonstrated up to 6.8W of green at 10kHz (pulse durations 50ns) by external, single pass doubling in temperature tuned LBO. The table below summarises the chronological development of Nd:YLF laser.

Year	*Important experimental advances*
1960	Demonstration of the first optical maser in the form of a flashlamp pumped Ruby laser [10a]
1961	First stimulated emission from Nd^{3+}:Glass [10b]
1964	First stimulated emission from Nd^{3+}:YAG [10c]
1967	First stimulated emission from Nd^{3+}:YLF [1]
1970	Several 100W cw output from a flashlamp pumped Nd:YAG rod laser [10d]
1973	First pulsed Nd:YLF laser operation. [3]
1982 [4]	First CW operation of Nd:YLF. YLF starts to fulfil some of its promise and compares favourably to YAG in specialised areas.
1986	First diode pumped operation of Nd:YLF [5]. Excited state absorption noted, which gives rise to visible fluorescence. [5/27]
1991	Start of high power diode bar end-pumping (10W) in Nd:YAG rod laser. [6]
1993/94	High power end-pumping of Nd:YLF slab (≤40W). High repetition rate source at 523.5nm with 3W TEM_{oo} at 5kHz (25ns pulses) for 20W diode pump power. [9]
1995	Diode bar, side pumped (40W) Nd:YLF slab with 13W TEM_{oo} cw and 6.8W green at 10kHz (50ns pulses). [10]

Table 1.1: *Development of the material Nd:YLF from the beginning to the present, in which Nd:YLF has established itself as one of the leading diode pumped, repetitively Q-switched laser materials, superseding the traditional high power material Nd:YAG in this application.*

The table includes the first realisation of a laser by Maiman in Ruby ($Cr:Al_2O_3$) [10a] and the first observation of stimulated emission with Nd^{3+} in Glass [10b] and Yttrium Aluminium Garnet ($Y_3Al_5O_{12}$) [10c], to set the start of the Nd:YLF development into its historical context. Although there is only a time lapse of three years between the appearance of Nd:YAG and that of Nd:YLF, the strong dependence of solid state laser development on the mainstream growing community, which is mainly located in the USA, is indicated by the fact that it then took almost 20 years for YLF to catch up with the domination of YAG . YAG development made rapid strides right from the beginning and Nd:YAG lasers covered a range from several 100W cw output [10d] to mW thresholds within 6 years of its appearance.

In this thesis is demonstrated the extraction of up to 12W cw multimode output, from a crystal volume of less than a tenth of a cubic centimetre, at a total conversion of 30%, giving testimony to the dramatic improvement in the quality and reliability of Nd:YLF.

The two main classifications in terms of pump geometry for diode pumped lasers are side-pumped and end-pumped designs. At the beginning of cw diode pumping only end-pumping was of relevance, due to the high prices for these first generation semiconductor pump diodes and their, by today's standards, low power abilities. Focusing into the path of the resonator mode guarantees virtually TEM_{oo} operation, low thresholds and high conversion efficiencies. This direct deposition of the pump energy into the mode volume was the crucial difference from flashlamp pumped systems, making improved efficiency of more than a magnitude possible. In contrast to this, diode side pumping mainly deposits the energy close to the edge of the gain medium, due to the short (typically a few mm) absorption length. This causes reduced efficiency and transversal mode control problems, which are both connected to the difficult mode matching situation.
One of the advantages of side-pumping is the comparatively straightforward pump power scalability of this approach, by elongating the active medium to gain more room for additional pump modules. The main advantage, however, is the reduced pump power density, reducing the problems of highly aberrated thermal lensing in strongly pumped solid state lasers.

Figure 1.2 illustrates variations on the classical longitudinal and transversal pump schemes. It becomes obvious that gain media in the form of a slab are best suited to either increase the efficiency of side pumped systems (a), d)) or to scale the pump power of end-pumped configurations (b), c)), because of their ability to fold the resonator path within the gain medium. The more advanced side-pumped systems utilise a rod lens to collimate the diode emission in the high divergence plane, in order to provide a sheet of gain within the plane of the resonator path. The configuration depicted in figure 1.2a utilises total internal reflection, to keep the resonator mode within the high inversion region close to the surface [12], while the steeper reflection angle in the zig-zag resonator path in figure 1.2d increases the interaction (pumped) length [13].

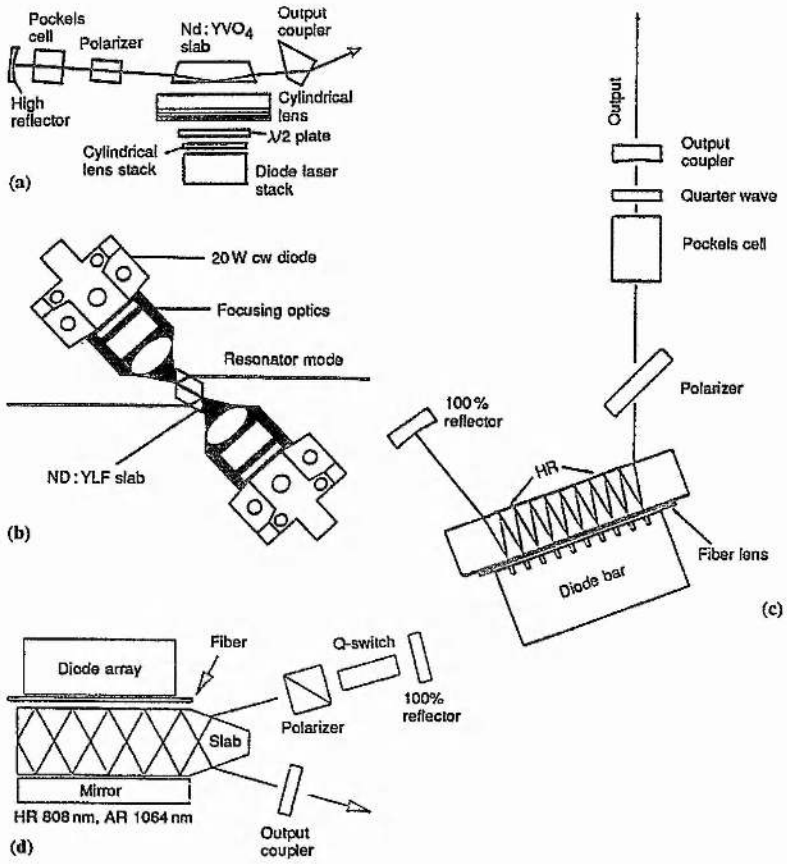

Fig. 1.2: *Different diode pumped slab configurations based on internal reflections of the laser beam [11]: **a)** Slab with grazing angle at the pump face, **b)** end-pumped geometry in Nd:YLF, as proposed in this thesis, **c)** tightly folded resonator design, and **d)** slab with folded zig-zag path.*

The pump configuration 1.2b of this thesis [14] is based on the scalable, end-pumped configuration first proposed by H.P. Weber et al. in 1990 [15], which was originally demonstrated with four, and later with eight [16], low power diodes (0.5W) in Nd:YAG. The zig-zag path is utilised to de-couple the resonator path from the pump path, thus allowing multiple, longitudinal pump positions.

The tightly folded resonator ('TFR') design by T. Bear reported in 1992 [17], which compares the merits of Nd:YAG and Nd:YLF in this pump configuration, is a very interesting hybrid of end- and side-pumping techniques. The spacing between the reflection points mirrors the emitter distance of the diode array, so that each fold can be thought of as end-pumped.

One of the main problems with these slabs designs in general is their susceptibility to parasitic oscillations, because of the high degree of symmetry in these slab geometries, with parallel, high quality surfaces. These problems are especially severe in the 'TFR' design, and if operation on low gain lines, such as, for example, the 1.321μm line in Nd:YLF which is characterised in this thesis, is necessary. Parasitic oscillations can be controlled by destroying the symmetry through wedging of the slabs and paying attention to the coating specifications.

A common characteristic of all four slab designs is the use of Brewster windows, making anti-reflection (AR) coatings obsolete, while enforcing a linear polarisation of the resonating field. The advantage of a linearly polarised output is especially important in non-linear optical applications, as described in the second part of this thesis. The need to maintain a linearly polarised output in the presence of high thermal gradients, as are typical for high power diode pumped lasers, is also responsible for the increased interest in naturally birefringent materials such as Nd:YLF and Nd:Vanadate (YVO_4). The natural birefringence of these materials overwhelms the thermally induced stress birefringence, which is the dominant effect in Nd:YAG [18], as it is isotropic at room temperature .

The non-linear conversion schemes described in this thesis, such as frequency doubling, tripling and OPO's [19], are all three-wave interaction processes, dependent on the χ^2 susceptibility of the material. The generation of new frequencies is caused by the interaction of the fundamental, electro-magnetic wave with the matter through which it is passing. When the electro-magnetic waves pass through the crystal, the electrons within the crystal are excited into dipole oscillations with an amplitude x, which themselves generate radiation. The resulting induced polarisation, P, can in most cases be approximated to be linear with the strength of the exciting field, E.

$$\vec{P} = Ne\vec{x} = \varepsilon_o \chi^{(1)} \vec{E} \quad ; \quad \text{with} \tag{1.3}$$

ε_o := Permittivity of free space

N := Volume density of atoms ex := dipole moment

The linear part of the induced polarisation is itself the origin of a new electromagnetic wave, $E_3^{(1)}$, which is constituted only of the frequency

components of the two incident waves and no new frequencies are generated.

This linear behaviour of the induced polarisation only holds strictly true if the electrons are subjected to a parabolic potential. All real potentials, however, deviate from this idealised linear dependence of binding force and excited amplitude. The assumption of a parabolic potential is then only accurate for small elongations. With the arrival of laser sources the high intensities necessary to ionise even molecules arose, making the amplitude of the dipole oscillation comparable to the range of the potential well. The linear relation in eqn. 1.3 has therefore to be replaced by a Taylor expansion in E, to include second and higher order effects, which are responsible for the generation of new frequencies.

$$\vec{P} = \varepsilon_o(\chi^{(1)}\vec{E} + \chi^{(2)}\vec{E}^2 + \chi^{(3)}\vec{E}^3 + \ldots) \qquad (1.4)$$

The coefficients, χ, are tensors and the magnitude of their components strongly decreases with the order of the non-linear effect. Typical numerical values for characteristic components of the χ coefficients are [20]:

$$\chi^{(1)} \sim 1 \; ; \; \chi^{(2)} \sim 10^{-10}\,\mathrm{cm/V} \; ; \; \chi^{(3)} \sim 10^{-17}\,\mathrm{cm/V}$$

Given these low values, only the spectral purity and high intensities available through laser radiation made experimental proof of non linear effects in the optical region possible. Non-linear optics started with the frequency doubling of a pulsed ruby laser, using Quartz as the non-linear material, by Franken et al. [21] in 1961. This first proof of useful non-linear coefficients was reported within a year of the first demonstration of a laser, while the first tunable OPO experiment in $LiNbO_4$ followed quickly in 1965 [19].

Today, conversion efficiencies in excess of 60% for frequency doubling from the infra-red to the green can be routinely achieved, if materials such as Potassium Titanyl Phosphate (KTP) or Lithium Triborate (LBO) are used. Such high conversion efficiencies, even at kHz rates, as achieved in this thesis for single pass doubling in a 10mm long KTP crystal, are somewhat fascinating, bearing in mind that only a second order effect of the induced polarisation is the origin of this frequency doubling of the fundamental radiation.
The extension of non-linear optics to high repetition systems requires strong focusing of the pump beam to achieve the required intensities or electrical field

strength within the crystal, because the energy per pulse at kHz repetition rates is very limited (typical ~1mJ). Also required is high non-linearity in the material, which again places high demands on the crystal quality. A good figure of merit t for crystals is therefore the non-linear coefficient (d_{eff}), damage threshold product ($d_{eff}^2 x P_d$).

Material	BBO	LBO	KTP	$LiNbO_3$	KDP	$LiIO_3$
Figure of merit	41.4	12	5.2	1.7	1.1	0.42

Table 1.3: *Comparison of non-linear materials according to their non-linear coefficient (d_{eff}), damage threshold product ($d_{eff}^2 x P_d$) [in $GWcm^{-2} \cdot pmV^{-1}$] [22].*

In the late 70 and 80's new materials such as KTP, BBO and LBO [23-25] were developed, with much higher figure of merits and extended transparency ranges, than the older materials such as KDP or $LiNbO_3$. The damage threshold of the converter crystals is a very important characteristic. Other parameters, dictated by the phase matching conditions, such as the effective interaction length of the three waves within the crystals and the effective non-linear coefficient , are, however, also of paramount interest in high repetition rate conversion schemes in order to secure reasonable pump depletions despite the low energy per pulse available. Therefore materials like KTP or LBO are preferable to BBO, which exhibits the highest damage threshold, making it an excellent material for high energy, pulsed laser sources [26].
After optimisation of conversion efficiency by choosing reduced or walk-off free phase matching schemes with high non-linear coefficients, advances in non-linear crystal growth techniques and laser development are the driving forces in the field of high repetition rate non-linear optics. In particular, the short pulse durations of diode pumped, repetitively Q-switched lasers, being one of the hallmarks of the diode end-pumped design as compared to flashlamp pumped systems, combined with their diffraction limited beam quality, are of crucial importance on the pump laser side.

This thesis describes the development of such a diode end-pumped, repetitively Q-switched Nd:YLF slab laser from scratch and demonstrates the abilities of the pump laser system with a variety of conversion schemes ranging from frequency doubling and tripling to frequency down conversion of the infra-red pump beam with optical parametrical oscillators. These schemes broaden the

spectral cover of the infra-red laser at 1047nm to certain wavelengths, ranging from the near UV (349nm) to the near mid-infrared (3.44μm).
The work divides into two major sections, a laser and a non-linear optics section. The first chapter within the laser section deals with the development of the laser system itself. Special attention is dedicated to thermal problems. This chapter includes details of the pump geometry, dimensions and thermal lensing properties at 1047nm of the Nd:YLF slabs, as well as some technical remarks discussing the cooling problems of the laser diodes and Nd:YLF slabs themselves. In particular the mounting of the YLF slab needs careful attention, in order to attain reliable operation at high pump power levels.
The third and fourth chapters describe the experimental results at 1047 and 1321nm, for cw as well as for Q-switched operation. In both cases attention has been paid to the linewidth properties of the laser emission. To supplement the linewidth measurements under lasing conditions the fluorescence spectra in the 1 and 1.3μm regions have also been briefly characterised. A drastic increase in the thermal lensing strength at 1.321μm and pronounced changes in the transversal mode control at 1.047μm under Q-switched conditions triggered an investigation of excited state absorption (ESA) of laser radiation in Nd:YLF, which is described in chapter five.
Chapter five therefore presents detailed measurements of the fluorescence in the visible and near UV, which is caused by the up-converted laser emission under Q-switched operation for 1.047 and 1.321nm. The analysis of the fluorescence was both time dependent, with the pulsed laser emission as a reference point, as well as spatially resolved, discriminating in that case only between the UV and visible emission bands. The main interest of this chapter is the question in how far these up-conversion processes limit the operation of Nd:YLF under lower repetition rates (500Hz to 3kHz) in high density diode pumped configurations.
This chapter concludes the characterisation of the developed laser system.

The sixth and seventh chapter describe the non-linear optical experiments with the Nd:YLF laser as the pump source at 1047nm. The good results in the frequency doubling and tripling chapter confirm the good beam quality properties, short pulse width and high degree of linear polarisation, independently of the earlier measurements. As a sideline the high average power and repetition rates make possible an aesthetically pleasing demonstration of coherence length under varying degrees of phase mismatch within a KTP crystal.

For the frequency down conversion of the infra-red pump beam both a KTP and a KTA-OPO were used. Due to absorption of the idler in the KTP crystal only the signal wave at 1.54μm could be extracted at an average power in the 1W range. To overcome this limitation of KTP in the 3μm region, an identical NCPM typeII KTA-OPO was compared in its performance to the KTP-OPO. In addition to the anticipated advantage of an idler output of a few 100mW both OPO's were compared with regard to their linewidth and transversal mode structures under identical pump conditions. By switching on a cw background, simulating self seeding of the laser, the influence of the pump linewidth on the OPO output could be analysed. Attention was also paid to the inconsistency of the existing Sellmeier equations for KTA. The different KTA Sellmeier equations were also discussed in the doubling chapter, in view of using KTA as a non-critical doubling crystal.

The conclusions take a more general look at the laser and non-linear optical development with suggestions for future work. A more specific summary and conclusion can be found at the end of each experimental chapter. As this thesis covers a broad range of different topics, no single theory chapter was compiled. The necessary background information is given for each chapter at the time of interest.

References

[1]: A.L. Harmer, A. Linz & al. - **Fluorescence of Nd^{3+} in YLF ($LiYF_4$)** - Bull. Am. Phys. Soc. 12, 1068 (1967)

[2]: E.J. Sharp, D.J. Horowitz & J.E. Miller - **High-efficiency Nd^{3+}:$LiYF_4$ laser** - J. Appl. Phys. 44, No.12, 5399 (1973)

[3]: A.L. Harmer, A. Linz & D.R. Gabbe - **Fluorescence of Nd^{3+} in Lithium Yttrium Fluoride** - Phys. Chem. Solids 30, 1483 (1969)

[4]: T.M. Pollak, E.P. Chicklis, H.P. Jensen & al. - **Cw operation of Nd:YLF** - IEEE J.-QE. QE-18, No.2, 159 (1982)

[5]: T.Y. Fan, G.J. Dixon & R.L. Byer - **Efficient GaAlAs diode-laser-pumped operation of Nd:YLF at 1.047μm with intracavity doubling to 523.6nm** - Opt. Lett. 11, No.4, 204 (1986)

[6]: D.C. Shannon & R.W. Wallace - **High power Nd:YAG laser end-pumped by a cw, 10mm x 1μm aperture, 10W laser-diode bar** - Opt. Lett. 16, No.5, 318, (1991)

[7]: S. C. Tidwell, J. F. Seamans, M. S. Bowers, & A. K. Cousins - **Scaling cw diode-end-pumped Nd:YAG lasers to high average powers** - IEEE Journal of Quantum Electronics QE-28, No.4, 997 (1992)

[8]: Quasi-cw stacked diode bars of the SDL 3230/50 series **SDL 1994 laser diode product catalogue**

[9]: C.Rahlff , M.H.Dunn, B.D.Sinclair & W.Sibbett - **High power end-pumped effects and applications in Nd:YLF at 1047 and 1321nm** - Paper CThG4, Conference on Lasers and Electrooptics , Anaheim, May 1994

[10]: J. Harrison, P.F. Moulton & G.A. Scott - **13W, M^2<1.2 Nd:YLF laser pumped by a pair of 20W diode laser bars** - Paper CPD-20, Conference on Lasers and Electrooptics , Baltimore, May 1995

[10a]: T.H. Mayman, Nature 187, 493 (1960)
R.J. Collins & al. - **Coherence, narrowing, directionality and relaxation oscillations in the light emission from Ruby** - Phys. Rev. Lett. 5, 303 (1960)

[10b]: E. Snitzer; Phys. Rev. Lett. 7, 444 (1961)

[10c]: J.E. Geusic, H.M. Marcos & L.G. van Uitert - **Laser oscillations in Nd-doped Yttrium Aluminium, Yttrium Gallium and Gadolinium Garnets** - Appl. Phys. Lett. 4, 182, (1964)

[10d]: W. Koechner - **Multi hundred Watt Nd:YAG continuous laser** - Rev. Sci. Instr. 41, 1699 (1970)

[11]: W. Koechner **"Solid-State Laser Engineering"** , p. 365
4th. Edition (1995), Springer-Verlag

[12]: C.E. Hamilton, R.J. Beach, W.F. Krupke & al. - **1W Average power levels and tunability from a diode-pumped 2.94μM Er:YAG oscillator** -
Opt. Lett. 19, 1627 (1994)

[13]: J. Richards & A. McInnes - **Versatile, efficient, diode-pumped miniature slab laser** - Opt. Lett. 20, 371 (1995)

[14]: C.Rahlff , M.H.Dunn, B.D.Sinclair & W.Sibbett
- **Scalable cw diode end-pumped Nd:YLF slab system** -
Poster at the UK Quantum Electronics Conference 11, Belfast, August 1993

[15]: P. Albers, C. Pfistner & H.P. Weber
- **Highly efficient diode laser multiple end-pumped Nd:YAG slab** -
Paper CMF4, p.24-25 CLEO Technical Digest 1990
C. Pfistner, P. Albers & H.P. Weber - **Efficient Nd:YAG slab longitudinally pumped by diode lasers** - IEEE J-QE. QE-26, No.5, (1990)

[16]: B. Neuenschwander, P. Albers & H.P. Weber - **Efficient multiple-longitudinally diode laser pumped Nd:YAG slab laser** -
Optical and Quantum Electronics 24, 363, (1992)

[17]: T.M. Bear, D.F. Head, S. Hutchison & al. - **Performance of diode-pumped Nd:YAG and Nd:YLF laser in a tightly folded resonator configuration** -
IEEE J.-QE. QE-28, No.4, 1131, (1992)

[18]: Y. Kaneda, M. Oka, S. Kubota & al. - **7.6W of continuos-wave radiation in a TEM_{oo} mode form from a laser-diode end-pumped Nd:YAG laser** -
Opt. Lett. 17, No.14, 1003 (1992)

[19]: J. A. Giordmaine & R.C. Miller - **Tunable coherent parametric oscillation in $LiNbO_3$ at optical frequencies** - Phys. Rev. Lett. 14, No.24, 973 (1965)
S.E. Harris - **Tunable optical parametric oscillators** -
Proceedings of the IEEE 57, No.12 (1969)

[20]: H. Weber **"Nichtlineare Optik"**
Lecture notes, Optisches Institut, T.U.-Berlin

[21]: P.A.Franken, A.E.Hill, C.W.Peters & G.Weinreich - **Generation of optical harmonics** - Phys. Rev. Lett. 7, 118, 1961

[22]: V.G.Dmitriev, G.G.Gurzadyan, D.N.Nikogosyan - **"Handbook of nonlinear optical crystals"** - Series in optical sciences 64 ; Springer-Verlag (1991)
G.Robertson - **"Optical parametric oscillators: A comparison of new materials"** Ph.D. Thesis, University of St. Andrews, May1993

[23]: F.C. Zumsteg, J.D. Bierlein & T.E. Gier - **$K_xRb_{1-x}TiOPO_4$: a new non-linear material** - J. Appl. Phys. 47, 4980 (1976)
J.D. Bierlein & H. Vanherzeele - **Potassium titanyl phosphate: properties**

and new applications - J. Opt. Soc. Am. B 6, No.4, 622 (1989)

[24]: D.Eimerl, L.Davis, S.Velsko et al. - **Optical, mechanical and thermal properties of barium borate** - J. Appl. Phys. 62, No.5, (1987)

[25]: C.Chen & Y.Wu - **New nonlinear-optical crystal: LiB_3O_5** - J.Opt.Soc.Am.B 6 , No.4, 616 (1989)

[26]: G. Robertson, A. Henderson & M.H. Dunn - **Efficient, single-axial mode oscillation of a ß-BaB_2O_4 optical parametric oscillator pumped by an excimer laser** - Appl. Phys. Lett. 62, 123 (1993)
G.Robertson, A.J.Henderson, Y.Tang, M.H.Dunn et al. - **Comparison of lithium triborate and b-barium borate as nonlinear media for optical parametric oscillators** - J. Opt. Soc. Am. B 10, No.9, 1737 (1993)

[27]: T. Chuang & H.R. Verdun - **Energy transfer up-conversion and excited state absorption of laser radiation in Nd:YLF laser crystals** - IEEE J. QE. QE-32, No.1, 79 (1996)

Chapter II.

Slab-laser development

This section describes the development of the cw Nd:YLF slab laser system, which was the platform for the Q-switched system and non-linear conversion schemes described in this thesis. Beginning with the basic design considerations needed to achieve an efficient TEM_{00}-multiwatt laser source, this chapter concentrates on the efforts undertaken to compensate for the adverse effects of a high thermal load on the laser host.

Thermally induced stress fracture and thermal lensing were the main problems in achieving a multiwatt, near diffraction limited laser source. The sections 'slab design' and 'thermal lensing' give more details on these thermally related problems.

As the set-up of this end-pumped laser is very compact due to its folded resonator geometry, the space for the diodes, focusing optics and cooling blocks was always very restricted. These more technical issues of the set-up are dealt with in the section 'pump modules'.

2.1 Basic design ideas

At the start of the project diode prices for the 20W cw laser diodes were £ 9,000 a piece. For this reason laser efficiency had a high priority. It is well known that the end-pumped diode laser configuration combines high efficiency with preferred TEM_{00} selection, as the pump and resonator mode volumes overlap well. The benefit of these advantages is especially obvious if only low powered pump diodes of up to a few watts of output power are used. At higher pump powers side effects resulting from the absorption of high pump energy in a small volume begin to deteriorate the performance of the laser.

The refractive index changes caused by thermal gradients, together with thermal expansion, give rise to an overall thermal lensing, which consists of a bulk lensing component (dn/dt changes) and end-effect governed lensing (thermal expansion). Only in the case of a uniformly heated and cooled rod is the overall thermal lensing equivalent to that of a spherical lens, since only in this case do the resulting thermal gradients have parabolic curvature [1].

This idealised picture of a flashlamp pumped rod laser obviously does not hold in the case of a diode end-pumped laser. Here the strongly localised pump causes non-uniform heat distribution, and the cooling is also non-uniform, especially when using a slab geometry. The resulting deviation from a parabolic temperature profile introduces phase distortions, which lead to increased losses in the TEM_{00} mode and finally make diffraction limited operation impossible. These imaging faults in the thermal lens, mainly introduced by the distortions of the pumped surfaces, are ultimately the problem, not the idealised spherical lensing of the bulk material under uniform pumping and cooling conditions, as this can be compensated for by an appropriate stable resonator geometry.

In comparison, the laser diode side pumped approach does not suffer as much from imaging faults of the thermal lens, if it is designed to approximate quasi flashlamp pumped conditions. This would include a circularly multiplexed side pumped rod (with 3 or more stripes per full circle) to give uniform energy storage in the centre of the rod, surrounded by a water cooled flow-tube, to realise uniform cooling. An additional precaution might be to ensure sufficient separation (~5mm) between the pumped area and the end faces of the rod to prevent any deterioration of the quality of the cavity. The main disadvantage of this scheme is, however, the low efficiency (of about 10%) into a TEM_{00} mode [2].

Given the high prices for the pump diodes and the aim of around 5W near diffraction limited output in a repetitively Q-switched mode, an end-pumped scheme was preferred, to ensure that the 40W total of pump power would be more than enough. In a traditional side pumped rod set-up this pump power level would be barely adequate to reach the goal. The results published in 1991 of a 10W diode end-pumped Nd:YAG laser with high efficiency (total of 20% into TEM_{00}, slope efficiency: 28%) [3] was motivation for extending the end-pumped approach to higher powers.

With a high thermal load on the laser host the choice of material became even more important. The scaling limit of an end-pumped laser is given by the maximum pump power which can be focused into the mode matched volume without causing thermal stress fracture. A suitable high power material should exhibit strong thermo-mechanical properties. A figure of merit for high power laser host materials is therefore the thermal shock parameter R [1], which is dependent on various material constants and is given by:

$$R = \frac{k(1-\nu)}{\alpha E}\sigma_{max} \; ; \quad \text{with R in [W/cm]} \quad \text{and} \tag{2.1}$$

k:= thermal conductivity
ν:= Poisson's ratio
α:= thermal coefficient of expansion
E:= Young's modulus
σ_{max}:= surface fracture stress

YAG, with a high thermal shock parameter of 7.9W/cm as a laser host materials, compared to Glass at 1W/cm, at the low end of shock resistivity, is therefore the standard choice for high pump power applications. In realising a linearly polarised and repetitively Q-switched laser other material properties such as the upper state lifetime and thermally induced birefringence become of importance, so that YLF as an alternative laser host is of interest. The table below shows properties of the materials YAG and YLF which are of importance in selecting the most promising crystal for an end-pumped, repetitively Q-switched laser with linearly polarised, high average output power. The properties of glass as a host material are added to show the contrasting values of a non suitable material for the application.
The very good thermal properties of YAG are obvious in its high values for thermal conductivity and shock parameter, but there are some significant drawbacks attached to this material.

Material	dominant birefringence type	thermal conductivity K [W/cmK]	thermal shock parameter R [W/cm]	fluorescence lifetime τ [μs]
Nd:Glass	dependent on host	0.01 (cf. --> Cu is 3.84)	1	~300 (host dependent)
Nd:YLF	natural	0.06	1.8	480
Nd:YAG	stress	0.14	7.9	230

Table 2.1 : *Material properties of different laser hosts.*

The cubic, and therefore isotropic structure of YAG, changes to an anisotropic, stress induced, birefringence in the presents of thermal gradients. The radially and azimuthally polarised components of the E-field would suffer losses if a linear polarisation enforcing component such as a Brewster plate were inserted into the cavity. The amount of loss would change from point to point over the cross section of the resonator mode and the intensity pattern of radiation coupled out would resemble the form of a 'Maltese cross' in the case of a rod geometry [4].

As the aim was to achieve a linearly polarised output in the presence of high thermal gradients, due to the end-pumped conditions, this thermally induced birefringence is a problem. In contrast to this, YLF is naturally birefringent and the two, orthogonal, linearly polarised components are not disturbed by the weaker stress birefringence.

Depending on the orientation of the low loss cavity E-field relative to the crystal **c**-axis, wavelength and linear polarisation can be selected and maintained without polarisation losses in the presence of thermal gradients.

An additional advantage of Nd:YLF is the approximately double upper state lifetime as compared to Nd:YAG, which influences its energy storage capability in the Q-switched case. This is an important aspect for repetitively Q-switched cw systems as the pump energy per lifetime is very limited. Even in the case of 20W of cw pump power, only approximately 10mJ or 5mJ are delivered in the respective fluorescence lifetimes of Nd:YLF and YAG. This should be compared to pulsed systems, where a total of 72mJ (in 400μs) is readily available from 3-bar stacks. However, the fluorescence lifetime advantage of YLF over YAG only comes strongly into play if the pump intervals are longer than the fluorescence lifetime of YAG. This makes a Nd:YLF laser especially useful in operation at repetition rates below 5kHz.

Choosing Nd:YLF as the laser material in an end-pumped configuration gave priority to efficiency and Q-switched performance, as opposed to a more secure route, which would have meant a side pumped Nd:YAG or YLF system. The high risks arising from the inferior thermo-mechanical properties of Nd:YLF had to be compensated by careful choice and design of the crystal geometry. The details of this problem will be given in the paragraph entitled 'slab design'.

A technical consideration in the design concerned the problem of cooling. Both the laser diodes as well as the slab had to be cooled. A 20W cw diode with a total efficiency of roughly 30% generates close to 40W of heat under full load conditions. To remove this amount of heat, two basic options can be used:

- Peltier elements, which are used as temperature controlled heat pumps against an unregulated cold reservoir, commonly cold tap water, or
- Direct, temperature controlled, water cooling.

Peltier elements are a convenient way of controlling temperatures with a wide range of 'off the shelf' solutions. However, the transfer of more than 30W of heat towards the hot side of the Peltier element requires Peltier driving units with a high current delivery capability, which leads to equally high prices for these units. The main reason for developing a direct water cooling solution was the compactness of this approach, with the cooling block no bigger than the diode itself.
This is an important advantage as the available space in a multi-diode end-pumped set-up will always be restricted. An additional benefit is the moderate cost. The details of the cooling of the laser diodes and slab are described in the section 'pump modules and cooling'.

2.2 Slab geometry

In the case of more than one pump diode for end-pumped systems, the usual approach of close coupling the pump module directly against the laser medium aperture and in line with the resonator axis has obviously to be changed. There are two different methods used to reach a scalable end-pumped geometry:

- The off-axis circularly multiplexed configuration [5], where the pump modules are only slightly offset from the linear resonator axis, allowing access to the laser gain medium apertures. Rods are usually used for this set-up, and both rod ends can be used this way for pump purposes. Further scaling is possible by adding more rod elements to the linear cavity.
- Folded resonator configurations allow end-pumping conditions at the folding points. The pump module is so oriented that the pump beam is refracted into the resonator path [6]. Slabs are usually used for this approach. The folding of the resonator axis can be achieved in a monolithic set-up within one slab, or alternatively by discrete end-pumped slabs or rods at each folding point.

An interesting case of the folded multiple end-pumped resonator is the tightly folded resonator concept by T. Baer et al. [7]. This concept combines the mechanical simplicity of the side-pumped technique (no coupling optics) with the high efficiency of the end-pumped technique. This is achieved by utilising each of the laser diode emitters in one cw diode stripe as discrete pump sources at the folding points, which are close to each other. Due to the very tight folding angle, a good mode match between pump and resonator mode is achieved. However, the single emitters have to be placed at a certain distance (wider than available in a commercial package) to allow for wide enough mode diameters in order to achieve good efficiency (overlap). Another drawback of this rather elegant approach is the problem in controlling the parasitic oscillations between the highly reflective parallel surfaces. A discrimination by the coating characteristic as a function of the incident angle is not possible, due to the very steep folding angle of the resonator path.

A folded resonator concept, based on that proposed by H.P. Weber et al. [6], was chosen and modified for the anisotropic laser material Nd:YLF. This included choosing the right crystal axis orientation with regard to the pump and resonator E-fields, and giving special attention to the thermal breakage problem in end-pumped Nd:YLF by choosing the right dimensions of the slab

geometry. A schematic diagram of the pump configuration is shown below.

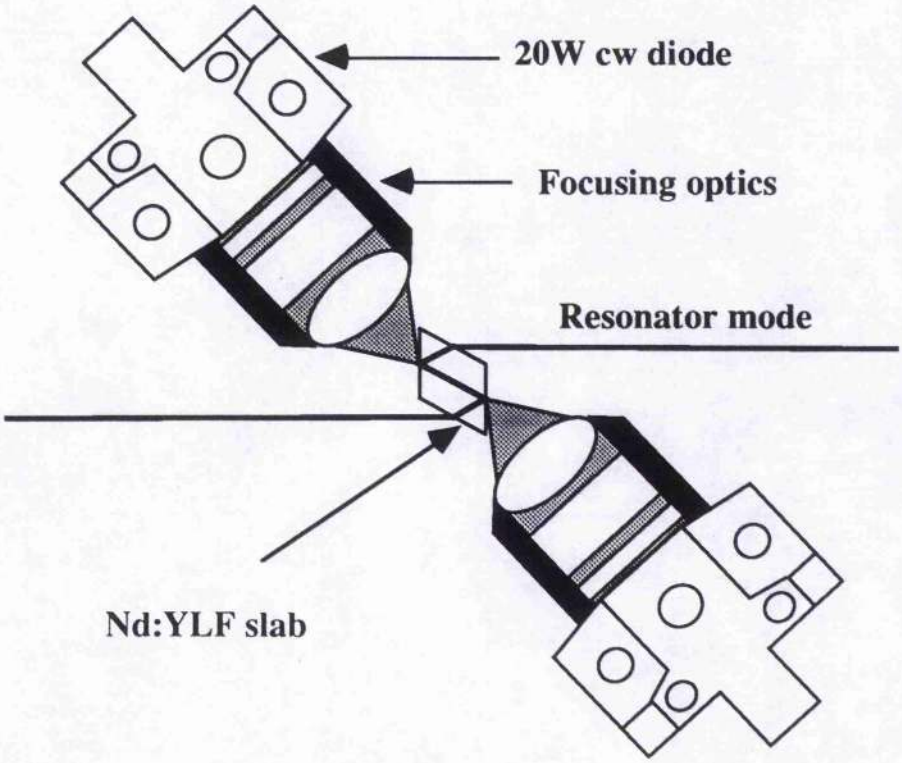

Fig. 2.2: *Nd:YLF slab with end-pumped folded resonator path and pump modules consisting of 3 element focusing optics and 20W cw laser diodes.*

The beam path, into which both pump diodes focus, is in the folded section inside the slab parallel to the Brewster entrance windows. The pumped surfaces are dielectric coated and provide high reflection (R > 99.9%) for the laser mode and high transmission for the pump wavelength (T > 90%). Using Brewster cut entrance surfaces makes an antireflection coating unnecessary and defines, in combination with the c-axis orientation of the crystal, the laser wavelength selection in the anisotropic YLF. In table 2.3 some of the important laser parameters of the two polarisation dependent wavelengths in Nd:YLF are given.

By orienting the c-axis normal to the pumped path inside the crystal (see figure 2.4) and in the plane defined by the incident E-field, the high gain line at 1047nm is selected. The p-component of the electrical field in the pumped region is parallel to the c-axis under these conditions. With the same c-axis orientation effective optical pumping is also possible, because the pump polarisation is parallel to the c-axis, utilising the higher absorption under these

conditions, as compared to the case of the orthogonal polarisation orientation.

	Wavelength λ [nm]	**Refractive index** n	**Stimulated emission cross section** σ [cm^2]	**Absorption coefficient @797nm** α [cm^{-1}]
π (E | | c)	1047	$n_e = 1.45$	1.8×10^{-19}	~10
σ (E | | a)	1053	$n_o = 1.47$	1.2×10^{-19}	~6

Table 2.3: *Polarisation dependent laser parameter of the anisotropic Nd:YLF for the* $^4F_{3/2}$ ---> $^4I_{11/2}$ *transitions.*

The parallel polarisation orientation of the pump radiation is easily achieved by using the laser diodes in the horizontal position (i.e.: the long dimension of the diode laser aperture (10mm x 1µm) is again in the plane of incidence, which coincides in figure 2.2/2.4 with the plane of the paper). The horizontal position of the pump modules matches well with the constraints in thickness of the slab, which are dictated by thermal fracture problems, as discussed later in this section. The longer half axis of the elliptical fluorescence profile after focusing falls in the plane of incidence, whereas the restricted dimension of the slab, the thickness, coincides with the short axis of the fluorescence profile. This makes it possible to optimise the mechanical strength of the slab, by minimising its thickness, without suffering premature clipping losses.

The horizontal dimensions of the slab are determined by the size of the fluorescence profile and the orientation of the c-axis towards the Brewster-cut entrance window. The exact dimensions and angles of the Nd:YLF rhombus are shown on the next page in figure 2.4 .
By choosing a 90°-angle of the c-axis towards the Brewster window the pumped path becomes parallel to the entrance windows. This orientation of the c-axis was chosen to give a reasonable magnitude for the angle of incidence of the pump beam and to simplify manufacturing, test procedures and alignment of the slab. The pumped area exhibits a visible fluorescence so that parallelism between the pumped path and the Brewster surfaces can be more easily detected than with other orientations. The width, *a*, of the entrance surfaces is determined by the width of the fluorescence profile. As an extra safety margin the width was chosen to avoid clipping losses in a Gaussian beam with a $1/e^2$ width equivalent to the fluorescence profile.

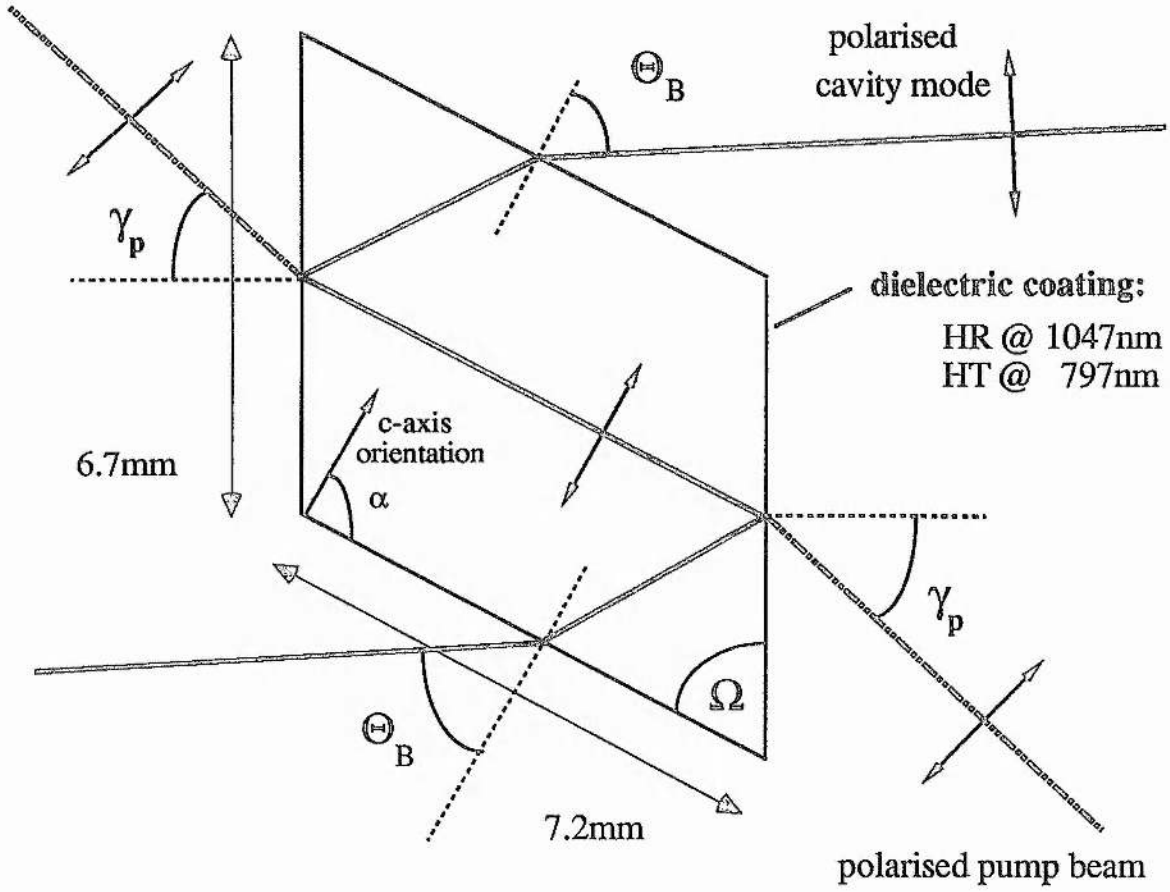

Slab Dimensions

a = **7.2mm**

b = **6.7mm**

c = **2.0mm** (thickness)

Ω = **62°**

α = **90°** (c-axis orientation)

Coating Specification

The two surfaces with the dimensions 6.7 x 2mm^2 were coated as follows:

i) **HR @ 1047nm**, p-polarisation, **angle of incidence: 28°** Θ_B = **56.1°**

ii) **HT @ 797nm**, p-polarisation, **angle of incidence: 43.7°** γ_p = **43.7°**

Surface Quality

i) surfaces 7.2x2mm^2 (Brewster windows) and 6.7x2mm^2 (pumped windows)
flatness and parallelism: λ/10 **scratch and dig: 10/5** **no chamfer**

ii) surfaces 7.2x6.7mm^2 (cooling surfaces)
optical polish **scratch and dig: 60/30** **slight wedge form**

Fig. 2.4: Exact drawing of the Nd:YLF slab used.

With these constraints the geometry of the slab is determined. The slab angle Ω and length *b* of the slab result from the Brewster angle condition. As the p-polarised 1047nm transition chosen is the extraordinary wave in the crystal it does not behave according to Snell's law. The exact calculation is given in RARDE Report II [8] (Appendix IV) . The difference between the exact solution and the approximation used here (Snell's law) of 0.3° is, however, unlikely to cause problems under practical alignment conditions.

The remaining undetermined value is the thickness of the slab. To get an idea about the temperature differences which occur, and which finally limit the pump power because of stress fracture, a simple one-dimensional heat conduction model was developed. To simplify the model the end-pumped crystal was divided into a directly pumped and a non-pumped region. Figure 2.5 illustrates this in a sketch and introduces the co-ordinate system used.

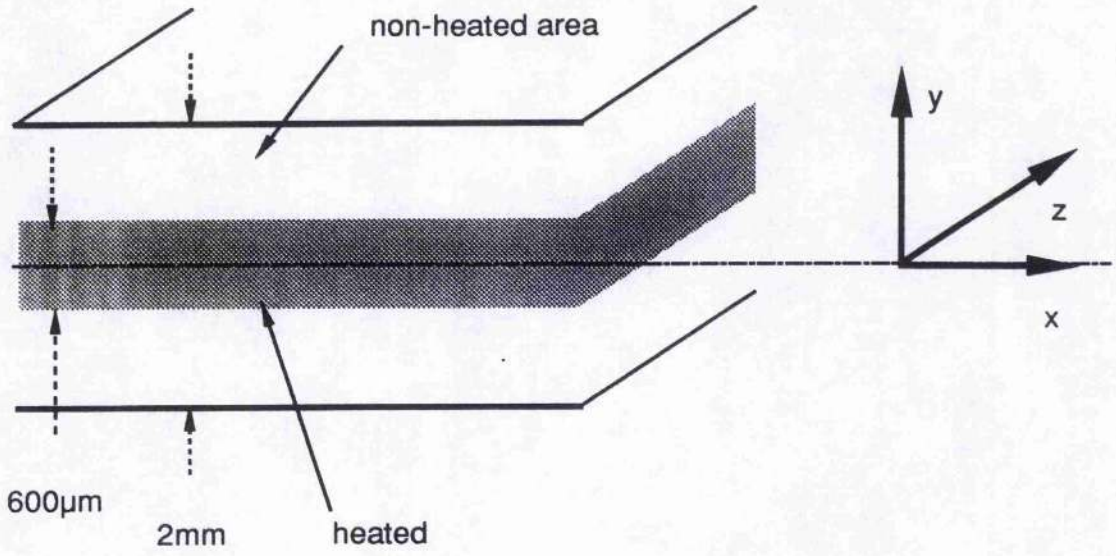

Fig. 2.5: *Side view of the end-pumped slab surface showing the modelling conditions of assumed uniformly heated and non-heated areas.*

The assumptions of the model are as follows:

- No temperature gradients along the x- and z- directions, because of the assumed thermal uniformity in these directions.
- The uniformly heated volume is assumed to be similar to the optically pumped volume.
- Steady state conditions prevail.

The parabolic temperature profile along the y-coordinate is described by [9]:

$$\frac{d^2T}{dy^2}+\frac{Q_0}{k}=0 \qquad (2.2)$$

where Q_0 is the constant rate of heat production per unit volume, and k is the thermal conductivity. The maximum temperature occurs in the centre of the slab and results in a temperature difference across the heated region of:

$$\Delta T_{para}=\frac{t^2}{8k}Q_0 \qquad (2.3)$$

where t is the thickness of the heated area.
The non-heated area exhibits an expected linear temperature gradient, described by:

$$\frac{d^2T}{dy^2}=0 \quad \text{where} \quad \Delta T_{lin}=\frac{f}{k}\Delta y^*, \quad \Delta y^*=y-t/2 \qquad (2.4a/b)$$

The temperature difference ΔT_{lin} in the non-heated region is dependent on the heat flux, f, necessary to remove the deposited heat through the remaining, non-pumped crystal thickness Δy^*, with a heat conductivity, k.

It is obvious that the reduced heat conductivity of Nd:YLF ($0.06W/cm^2$ as compared to that of Nd:YAG, $0.14W/cm^2$) causes higher temperature gradients under the same pump conditions. Furthermore, the absolute temperature difference which can be tolerated across the slab is only a function of the material constants. Here again Nd:YLF loses out with its lower tensile strength as compared to Nd:YAG. To estimate the maximum permissible temperature difference across the slab the approximation for a uniformly pumped slab, as given by Koechner [1], was used.

$$\Delta T_{max}=\frac{3(1-\nu)\sigma_{max}}{2\alpha E}=\frac{3R}{2k} \quad \text{and} \quad \Delta T_{max}\geq\Delta T_{slab}=\frac{f}{k}\Delta y^*+\frac{t^2}{8k}Q_0 \qquad (2.5a/b)$$

The maximum permissible temperature difference does not depend on the thickness of the slab (Eqn. 2.5a). However, the unpumped crystal region does add substantially towards the total temperature difference ΔT_{slab}. By reducing the unpumped thickness Δy^* to its minimum the disadvantages of the low thermal conductivity and tensile strength of Nd:YLF can be reduced in this geometry.

In calculating the temperature differences the assumption of which volume is heated has a critical influence on the result. Two extreme cases were assumed:

- Worst case: Only the pumped volume is heated uniformly. This leads to the maximum thermal flux needed to dissipate the heat, as only a small part of the two slab cooling surfaces contributes to the cooling.
- Best case: The whole slab surfaces are used for the extraction of the absorbed power. This leads to a minimum thermal flux through the crystal and corresponds to the picture of a uniformly heated crystal slice sandwiched between the purely heat conducting parts of the slab.

With these assumptions the calculations indicated that a thickness of between 1 and 2mm would probably be sufficient to withstand the thermally induced stress of 40W diode pump power focused into a fluorescence profile of 1.2mm x 0.6mm diameter.

As thermally induced fracture will occur as failure at the surface, due to uncompensated tension, the two cooling surfaces were also specified to be inspection polished. This should strengthen the surface, as scratches might act as seeding points for surface fracture. To avoid parasitic oscillations between the inspection polished faces (which were also low quality polish instead of laser quality 1/10-polish) a slight wedge form of approximately 10mrad was specified.

At a later stage in this work it was of interest to test in how far these first assumptions corresponded to the real temperature conditions. Fabry-Perot fringes were used to measure the temperature rise inside a block of Nd:YLF subjected to the same pumping geometry, ($E_p \parallel c$), as was used in the actual Nd:YLF slabs itself. This block was 3mm thick and had sufficient parallelism between its faces to allow its use as a interferometer. The method is based on detecting the number of reflected maxima, m, which occur during thermal contraction, due to scanning through the resonances of the Fabry-Perot etalon [10]. The temperature change per detected maximum, DT/m, is related to the optical path length change and is inversely proportional to the separation, l, of the Nd:YLF surfaces.

$$\frac{\Delta T}{m} = \lambda \Big/ 2l\left\{\frac{dn}{dT} + n\alpha_{th}\right\} \qquad \text{with} \qquad (2.6)$$

α_{th} := thermal expansion coefficient $\qquad$ l := wavelength of test beam

dn/dT := temperature dependent refractive index change

An example of an interferometric trace recorded is given in figure 2.6. Due to the relatively short length of the crystal, which gives a temperature change of several degree per recorded maximum, the accuracy of the method is limited to approximately ±1°C.

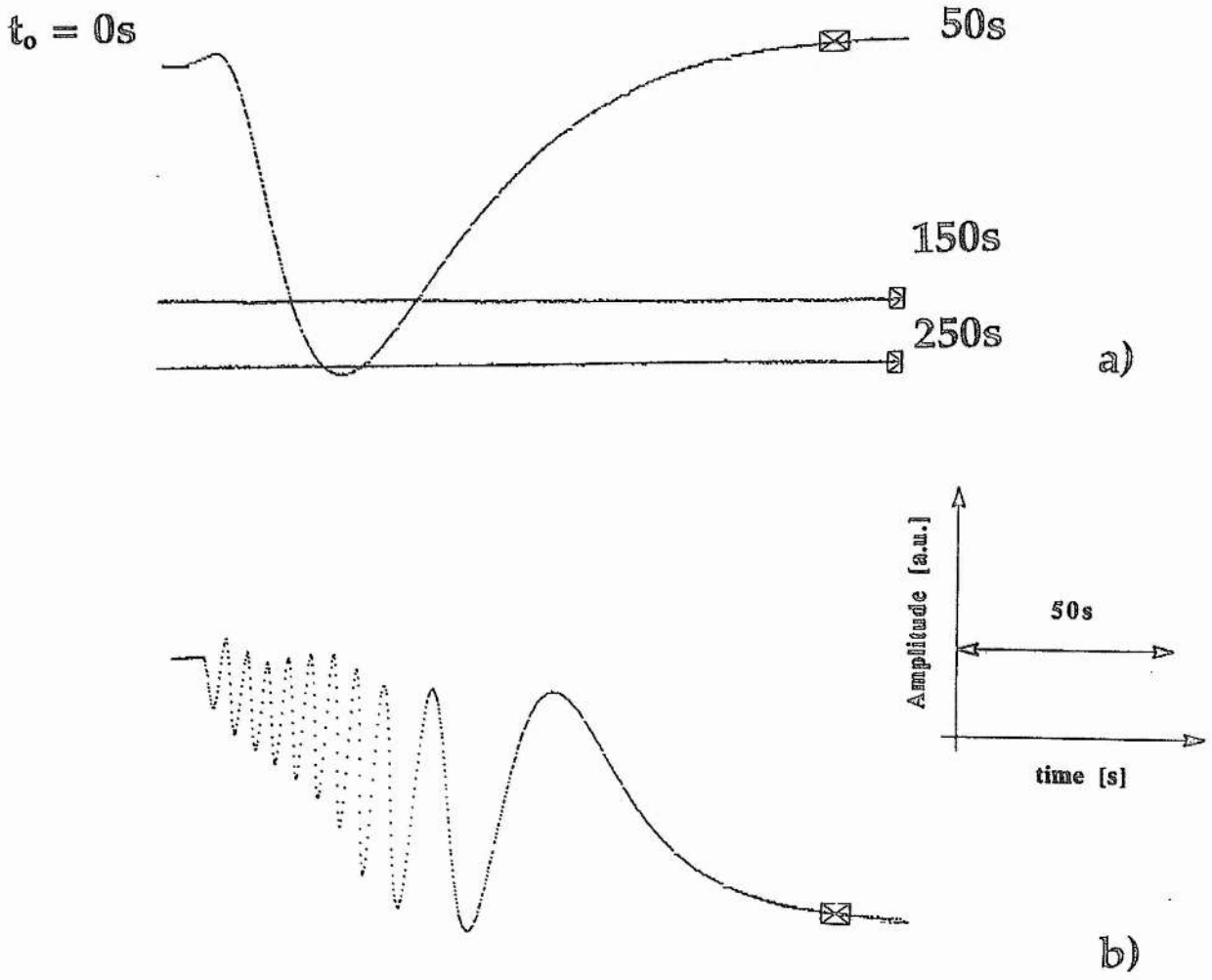

Fig. 2.6: *Interference pattern recorded during the cooling period from room to cooling water temperature , with no load on the slab (**a**)) and for an absorbed pump power level of 7.5W down to the slab cooler temperature (**b**)). The observed number of 10.5 maxima in **b**) indicates a temperature change of 38°C inside a 3mm thick Nd:YLF block. The trace (**b**))was recorded over a time interval of 50 seconds. The additional traces in (**a**)) are indicating the slow approach to a thermal equilibrium situation, stretching the observation time up to 250s.*

A good test of the accuracy of this method was to record the temperature reduction for the change from room to cooling water temperature with a

known temperature difference (fig. 2.6a), and without placing a heat load on the YLF slab. The calculated temperature change per maximum was 3.6°C when a Helium Neon laser (632.8nm) was used as the test beam. The measured temperature difference in 2.6a was therefore 5.4°C (allowing for 250 seconds to establish a thermal equilibrium). This is in acceptable agreement with the expected temperature change of 6.8°C, taken by subtracting the cooling water temperature from the room temperature.

Using this technique to scan the horizontal temperature distribution (x-axis) makes it possible to give a better estimate of the heated region.

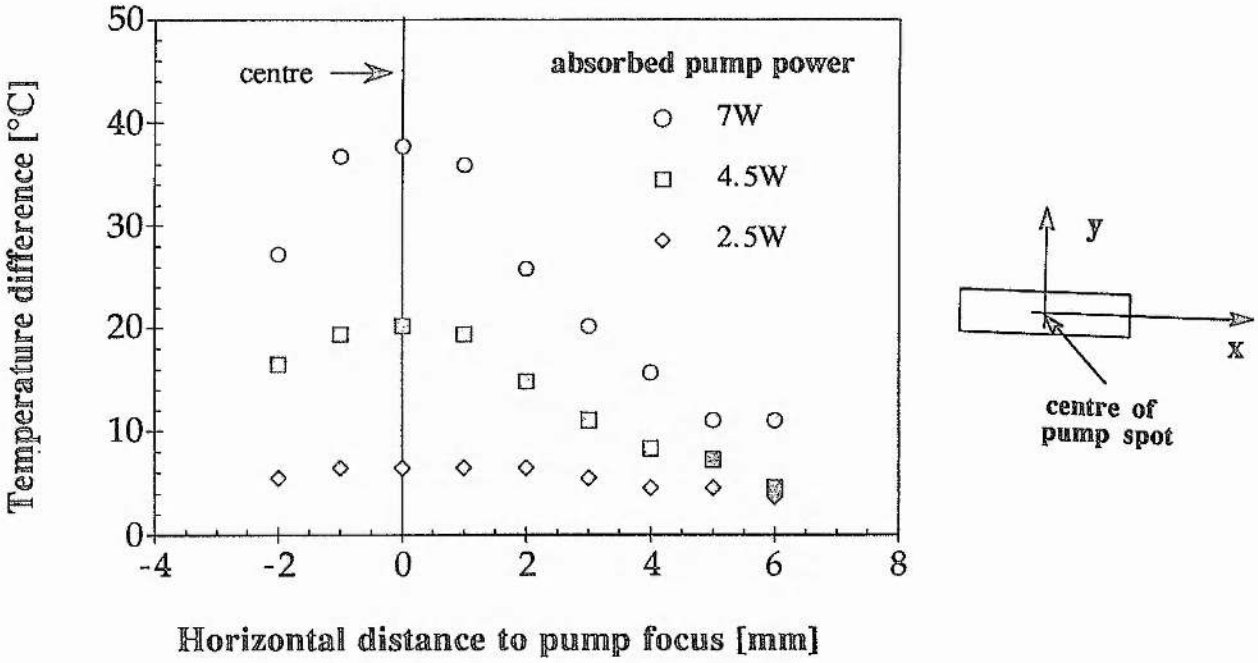

Fig. 2.7: Measured temperature difference as a function of varying horizontal distance (along x-axis) from the pump focus for different absorbed pump power levels. The YLF block used was 3mm thick.

The experimental results shown in figure 2.7 indicate clearly that at higher pump powers a far bigger region is heated then the directly pumped region (1.2 x 0.6 mm^2 (x x y-axis) full width $1/e^2$ intensity reduction, as measured by the IR fluorescence). The FWHM of the horizontal temperature distribution at high pump power levels is approximately 4 times the length of the directly pumped region (1.2mm), as identified by the infra-red fluorescence. The earlier assumption of thermal uniformity along this axis is therefore not unrealistic for the distances of interest (<<5mm).

In terms of the YLF slabs actually used, this means that the whole of their top and bottom surfaces contribute to the cooling of the slab. This is the best case assumption mentioned before, since the big cooling area implies a considerable reduction in stress. For this reason it is not advisable to make a reduction in the width of the slabs, risking fracture at higher pump powers.
The prediction of the temperature profile across the slab according to equation (2.5b) was also compared with the experimental results of scanning along the y-axis of the crystal as shown in the sketch in figure 2.5. The agreement between the predicted temperature rise, assuming that the whole slab area contributes to the cooling, and measured temperature lies within a margin of 20%, with the two measured locations along the 3mm wide aperture indicating a shallower and lower temperature profile than predicted.

From the beginning of this work it was, however, clear that a one-dimensional model is not sufficient to describe the details of stress in a 3-dimensional, non-uniformly heated, anisotropic crystal. The details of comparison between model and experiment have therefore been omitted at this stage.
The motivation and benefit of this preliminary model was to give a reasonable estimate of the thickness of the YLF slabs to be ordered. It has succeeded in this, as these Nd:YLF slabs have never suffered stress fracture, under any conditions of operation (including a blocked resonator path), even with pump powers of up to 40W, which corresponds to 20W per surface. The contactless interferometric temperature measurements are a valuable experimental technique for comparing different cooling set-ups, or to ensure reproducible cooling conditions. This is important for an experiment in which the thermal stress limit of Nd:YLF is approached .
For this reason a more detailed technical section follows, describing the cooling requirements of the laser diodes and the Nd:YLF slab.

2.3 Pump modules and cooling issues

The article by Shannon and Wallace [3], which was one of the first publications to use multi-emitter bar high power diodes for end pumping motivated us to explore the possibilities of extending this approach to higher pump powers, and the different material Nd:YLF. In this publication they employed a three element focusing optic to transform radiation from the 10mm x 1μm wide emitting aperture into a small confined gain area inside the crystal. This focusing optic was duplicated, as Cameron Rae, also at St. Andrews University, had already found this design to be particularly successful in previous work on a miniature, end-pumped, pulsed Nd:YLF laser [11].

The interesting point in the design is the use of three lenses to achieve focusing. Although it would be enough to use one lens to collimate the highly divergent vertical component of the emitted radiation, two lenses were used to achieve this. The advantage of this approach lies in the reduced spherical aberration, as the first lens with 1.2mm focal length can be brought extremely close to the aperture (a few 100μm), thus reducing the imaging faults in the strongly curved rod lens (diameter: 1.6mm). The second cylindrical lens collimates the now slightly divergent component, which is then focused along with the uncorrected horizontal component by an aspherical condenser.

To optimise the fluorescence profile in the Nd:YLF slab, every lens was mounted independently, each on two translation degrees. This was only necessary for the prototype and had the additional benefit of reducing the amount of precision needed to manufacture the whole pump module. The main problem in constructing the pump modules was the tight constraint on the available space. The folded and end-pumped geometry made it necessary that all the mounting posts and translation stages had to be on one side of the laser diode (see figure 2.2), as they otherwise would interfere with the folded resonator path. Additionally, the pump modules had to be flush with the condensing lens to leave room for the Nd:YLF slab as well as the slab cooler. This made it necessary to position most of the translation stages behind the laser diode and mount the lenses on extended holders, which gave the pump modules a characteristic oil-rig-like appearance. A detailed picture of a pump module is shown in figure 2.8.

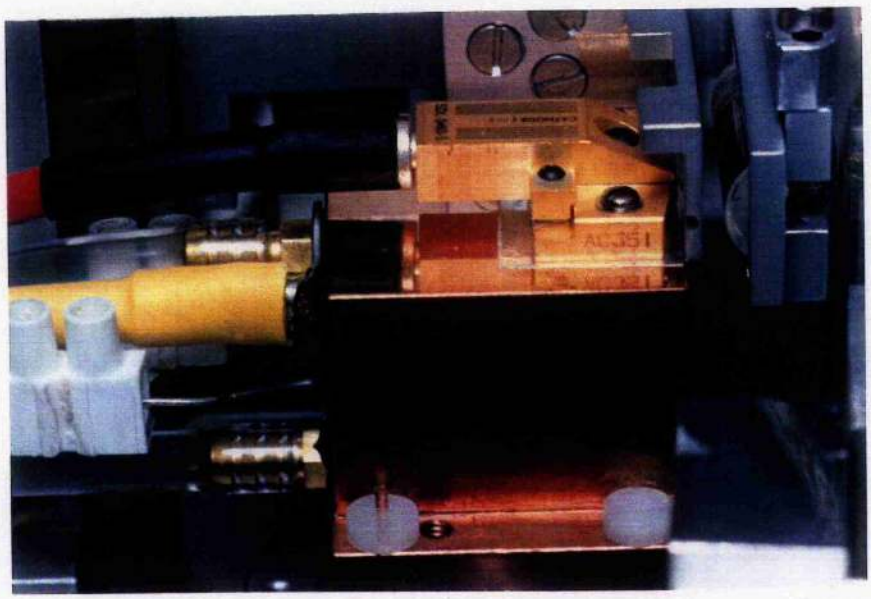

Fig.2.8: *Laser diode mounted on water cooled copper block and independently adjustable focusing optic. The very compact set-up is a consequence of the end-pumped and folded pump geometry. Note the cut-out in the condenser lens mount to ensure resonator mode clearance.*

The highest degree of freedom was given to the alignment of the rod lens with the diode aperture. As the diode aperture is only 1μm thick, a rotation and degree of tilt were utilised to ensure that diode aperture and rod lens surface were parallel. For the performance of the whole laser system it was vital that the rod lens was close enough to the diode aperture, as well as at the right height, to ensure an optimum inversion profile. The separation and height of the remaining two lenses was not as critical, and a variation in distance between the two cylindrical lenses could be compensated for with a slight adjustment in the distance of rod lens and laser diode aperture. In the following list the most important degrees of freedom are given:

- Distance and height of the rod lens from the diode laser aperture.
- Distance between rod and cylindrical lens: 1mm ± 0.5mm

  Distance between cylindrical lens and condenser; close coupled

  All optical axes on centre.
- Parallel movement of the whole pump module, including the focusing optics, with regard to the pumped surface of the slab.
- Height and distance movement of the whole pump module with regard to the pumped surface of the slab.

Under these conditions the neglected degrees of freedom had to be replaced by mechanically ensured square mounting. A well aligned diode pump module should have an integrated fluorescence profile, as measured along the pumped path, of approximately 1.2mm x 0.6mm FWHM. This was achieved using the first generation of Spectra-Physics 20W cw laser diodes (48 times 100µm long emitter-stripes ; SDL 3460-S). The ellipticity of the pump spot could be influenced by alignment of the rod lens - laser aperture distance.

The restricted space conditions made direct water cooling a good choice. The benefit of water cooling is given by the possibility of designing cooling units which have the same size as the object which is to be cooled. This cannot be said about the Peltier coolers (as available in early '92) usually preferred, especially if large amounts of heat are to be dissipated, as in the case of laser diodes. Additional benefits of direct water cooling are the reduced costs and the fact that Peltier elements also need a closed cycle refrigerating unit if independence of tap water supply is needed.

The advantage of water as a coolant, its high heat capacity, turns into a problem if small but fast temperature changes are needed to fine control the laser diode wavelength. To make fast temperature changes possible an ohmic resistor was implanted inside the cooling blocks, and driven by a temperature controller. The feedback thermistor was placed as close as possible to the laser diode, to improve the temperature stability. A sketch of the cooling blocks developed is shown in figure 2.9 on the next page.
To optimise the heating power of the resistors the water inlet is at the bottom of the cooling block. The partially preheated water cools the laser diode and leaves through the outlet at the top of the cooling block. The cooling water temperature has to be at around 4 to 6°C to ensure stabilised diode temperatures of around 20°C (diode 1 operated at 17°, diode 2 at 23°C). The temperature stability of ±0.2°C achieved is more than enough, as changes of 1°C in the operating temperature of the diodes are not critical.

In the case of the slab cooler the cooling water temperature was raised to 10 - 12°C to avoid condensation on the slab surfaces. The cooling channel is in a straight line to minimise vibrations in the slab mount. Routing the water through a U-turn might be a disadvantage for laser pointing and output stability, due to the increased turbulence. A list of the cooling equipment used can be found in Appendix 2.

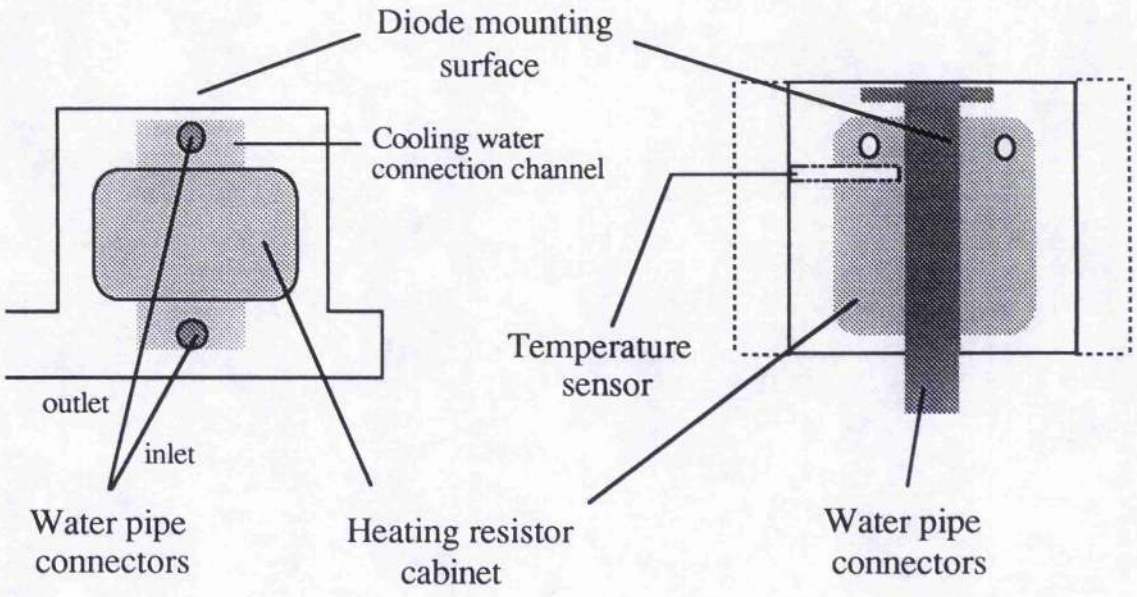

Fig. 2.9: *Sketch of the cooper cooling blocks with temperature controlled heating resistors. The temperature stability is better than ± 0.2 °C.*

The mounting of the slabs is an important factor. At the initial stage of the project the Nd:YLF slab was sandwiched between two hand polished aluminium plates, a base cooler and a spring loaded top-cooler. Both cooling plates had an elevated, polished plateau with the shape and dimension of the slab (slightly oversized) to pre-align the slab position. To optimise thermal contact, thin indium foil (125μm thick) was used to bridge the cooler-crystal surface gap. This double sided cooling technique was in use to measure the previously mentioned temperature profiles and for most of the cw experiments. Pump powers of up to the full available 40W into 2mm thick slabs did not cause any problems.

However, the need to readjust the resonator path under high pump power conditions without having visual feedback was an experimental disadvantage. Removing the top-cooler, which prevented a check of the visible pump fluorescence, indicating the position of the pump modules towards each other, simplified the alignment procedure significantly. Even under these single sided cooling conditions total pump powers of up to 35W were applied to the slab without stress fracture. Higher pump powers were not attempted, as 17W per surface represents the upper pump power limit in terms of reasonable laser performance. Obviously this unexpected result gives rise to questions about

the thermal properties of YLF and the stress distribution inside a non-uniformly pumped and cooled slab. This case cannot be accounted for in the basic model described in section 2.2. A different approach, such as a finite elements model would be better suited to this problem. With such an approach it might be possible to determine if the thermal shock parameter of the Nd:YLF used is higher than the one generally quoted in the literature. However, the amount of material constants involved and the influence of the surface quality on the surface stress limit makes such an attempt a project in its own right.

To achieve safe operating conditions with up to 35W pump power, attention should be given to the following points. Single sided cooling with indium foil as the bonding material then proves to be a reliable and reproducible method:

- The cooling area has to be flat, without visible scratches. Polishing on a glass plate in a figure of eight pattern reduces the risk of polishing the cooling surface round instead of flat.
- The indium foil should be bonded with an uncontaminated, flat surface to the aluminium. A clean glass plate is well suited to press the indium onto the aluminium.
- The slab is bonded to the indium by a slight pressure from the top, again utilising a microscope slide.

At this stage careful brushing around the windows of the slab, to remove dust, will not alter the position of the slab. Later, under high pump power conditions, the slab will adhere more strongly, so that removal of the slab is not easy and best done by tapping the cooler firmly. The sign of a well adhered slab is a silvery, metallic shine to the Indium foil.

2.4 The resonator and thermal lensing

An important effect of the high thermal load on the laser material is the change in its optical properties, inducing intra-cavity lensing effects. Depending on the material constants of thermal expansion (α_{th}) and the temperature dependence of the refractive index (dn/dT), the pumped laser crystal can be described in a zero-order approximation as a positive or negative thin lens. The overall thermal lensing consists of a bulk lensing component (dn/dT changes) and an end-effect governed lensing component (thermal expansion).

The prevailing lensing mechanism relies on the pump conditions. The thermal lensing of flashlamp pumped systems, with their side pumped, quasi homogeneous illumination of the gain material, is governed by the optical properties of the bulk material. Nd:YAG with a positive dn/dT exhibits positive lensing, while Cr:GSGG has a negative thermal lens because of its negative dn/dT. End-effects are generally negligible under homogeneous flashlamp pumped conditions, assisted by the fact that the geometrical length of the gain medium is considerably longer than the pumped length, keeping distortion of the ends to a minimum.

Diode side pumped systems are comparable in their lensing behaviour to flashlamp pumped systems, given homogeneous cooling conditions. The transition to diode end-pumped systems makes the end-effect component of the lensing more important, due to the strongly inhomogeneous and localised energy deposition. Connected to these inhomogeneous pumping and cooling conditions are distortions of the pumped surfaces, which cannot be treated as spherical lenses (or mirrors) and thus cannot be corrected for by spherical cavity mirrors. Although these aberrations of the thermal lens finally limit the performance of an end-pumped laser due to increased losses, especially for TEM_{00} operation [12], they are not the object of this section. The methods of thermal lensing measurement described always assume an aberration-free thin lens in determining the stability condition of the cavity or propagation of a TEM_{00} resonator mode.

It is obvious that an intra cavity lens, with a pump power dependent refractive power, needs to be characterised to ensure:

- **resonator stability** under changing pump power conditions,
- **constant beam diameter** in the pumped region of the Nd:YLF crystal, for optimum mode matching regardless of the pump power level, and
- **safe operating conditions** for the Q-switch, by being able to determine the changing intra-cavity peak intensities.

An example of the changing TEM_{00} spot sizes inside the lens resonator sketched in figure 2.15 is given below for the unpumped and pumped (20W) case. This resonator configuration satisfies all of the afore-mentioned conditions and has been used in these experiments.

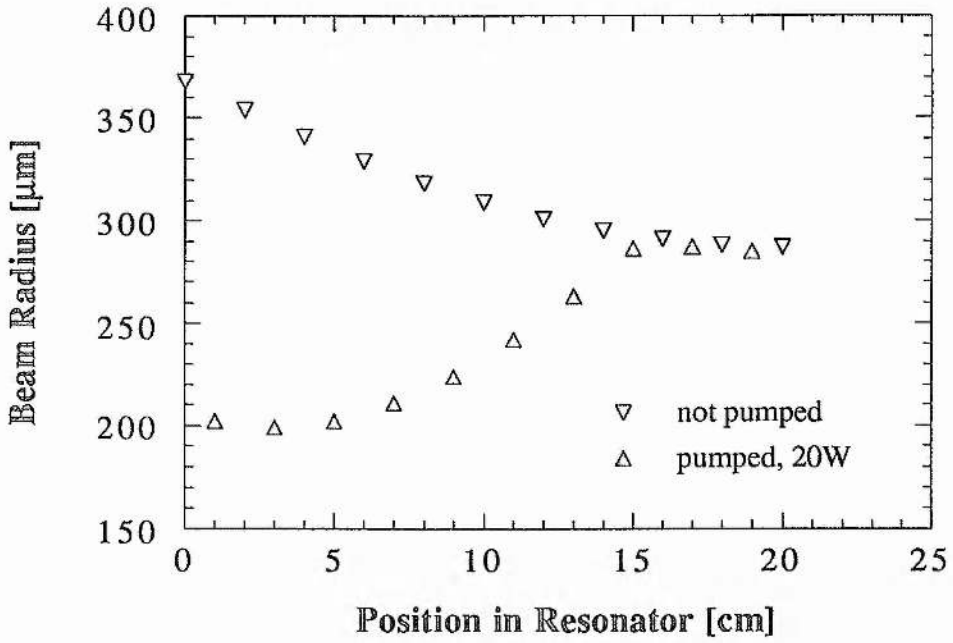

Fig. 2.10: *Beam waist sizes, ω, as a function of the position inside the resonator sketched in fig. 2.15. With higher pump powers focusing on the left mirror (0cm) starts. This effect is limited by the stability condition. The transition from the stable to the unstable region is determined by the change of the beam waist, ω, from a real to an imaginary value on this mirror surface.*

The relatively small spot size on the left mirror surface under 20W pump power conditions indicates that the resonator is close to its stability border. The g-diagram displaying the changing g-parameter of the equivalent resonator in Fig. 2.16 for this resonator configuration confirms this move towards the stability border.

The importance of thermal lensing measurements is further emphasised by the choice of Nd:YLF as the end-pumped material. At the beginning of the project no experience or published results existed of YLF systems in a high power end-pumped set-up. This reflected the inferior thermo-mechanical properties of YLF, making it second choice to YAG in the relatively new approach (starting with Shannon & Wallace '91) of utilising high power (≥10W), strongly

asymmetric, multi-emitter cw bars for end-pumped lasers. Thus, even the sign of the lensing was uncertain, due to the opposing signs of the bulk (negative dn/dT [13]) and end-effect (positive) lensing. Nor was known the pump power dependent magnitude or the influence of the anisotropic crystal structure on the lensing.
To measure the refractive power of the thermal lens under cw and Q-switched conditions two basically different methods were employed. Either the propagation properties of a TEM_{00} test beam through the Nd:YLF crystal or the pump power dependent stability criterion of the resonator were used to describe the magnitude of the lensing. The details of these methods for cw thermal lensing measurements are outlined below:

◦ **Helium-Neon test beam method**
The advantage of this method is the possibility of resolving different thermal lensing effects depending on the polarisation orientation along the two crystal axes in the anisotropic YLF. In using a Helium Neon test beam it is assumed that the wavelength dependent change of the refractive index is not critical. Similar results should be obtained if a Nd:YAG or Nd:YLF test beam were used.

To carry out measurements, the Helium-Neon laser beam must be aligned coaxially to the resonator mode. As the test beam is then propagating through the centre of inversion in the crystal the thermally induced lens can be calculated by measuring the test beam's waist radii at different distances behind the YLF crystal. The mirrors and thermal lens inside the resonator were treated as thin lenses (the pumped length inside the YLF is approximately 7mm). The lensing observed with the Helium-Neon laser method was

+0.45 diopters per watt of input power.

No anisotropic lens could be observed within the accuracy of ±10% for this method. The integrated fluorescence profile during these measurements was 0.6 x 1.2mm^2 (diameter); this is of importance as the amount of anisotropic lensing is also dependent on the ellipticity of the pump spot.
These very high positive values indicate totally end-effect governed lensing, as the negative thermal bulk lensing is entirely cancelled by the positive lensing of the concave mirror-like pumped surfaces. The unexpected strength of positive lensing is the reason for verifying this lensing behaviour through different

measuring methods and operation conditions (cw and Q-switched).

◦ **Instability method**

In this method the laser is driven under varying resonator geometries into the instability regions of the g-diagram, thus reaching unstable round trip conditions for different thermal lens (or pump power) values. One way of describing resonators with an internal pump power dependent lens was introduced in [14], and uses the concept of the equivalent resonator.

This concept is based on the comparison of the round trip ABCD-Matrix [15] for a cavity with and without a thermal lens. The Gaussian beam diameters on the mirrors of the lens resonator and equivalent empty cavity are identical, if the parameters of the equivalent, no lens containing, resonator are altered to $g_{1,2}^*$ and L^*.

It is important to notice that the internal beam diameter of the lens and equivalent resonator are totally different, as can easily be seen by the appearance of two possible internal foci in the lens resonator, compared to only one possible beam waist in an empty cavity. Furthermore, the right/left symmetry of the beam divergence is in the case of the lens resonator no longer valid. The internal lens transfers two Gaussian beams into each other, with the possible result that the divergence on one side could increase, while the other side could show decreasing divergence under pump power changes.

It is, however, possible to reconstruct the beam parameter inside the lens resonator utilising the known beam radii on the mirror surfaces of the equivalent resonator. This is due to the fact that in both resonator configurations the radius of the phase front at the location of the mirror has to be equal to the radius of curvature of that mirror. This enables a step by step transformation of the so determined complex beam parameter, q_m, through the ABCD-law, where the matrices are represented by the elements of the lens resonator.

The concept of the equivalent resonator is used here only to visualise the stability behaviour within the g-diagram. It does not replace the necessary step by step analysis of the lens resonator needed to gain information about the beam properties inside and outside the cavity, as was done for the results displayed in figure 2.10.

To introduce the notation necessary to describe the equivalent resonator a general sketch of a lens resonator is given in the figure below:

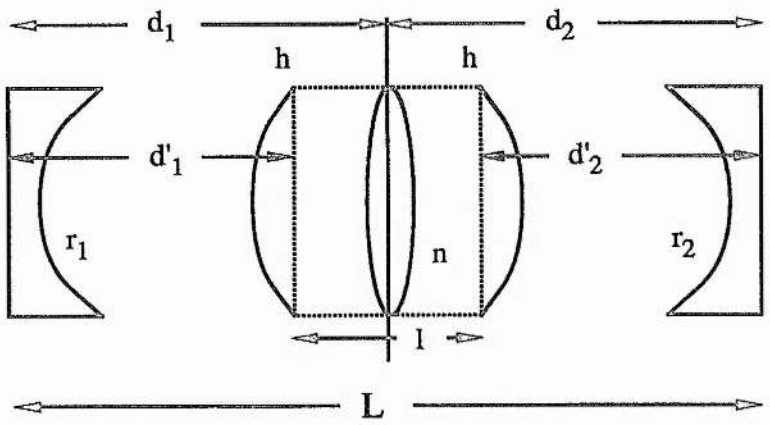

Fig.2.11: *Lens resonator with notation used to describe the equivalent resonator parameters g_i^* and L^*.*

These equivalent resonator parameters are then functions of the lens resonator parameters g_i, L_{opt} (optical length), and refractive power D, as shown below:

$$g_1^* = g_1 - Dd_2\left(1 - {}^{d_1}\!/_{r_1}\right) \quad \text{with} \quad g_i = 1 - {}^{L_{opt}}\!/_{r_i} \qquad (2.7a/b)$$

$$g_2^* = g_2 - Dd_1\left(1 - {}^{d_2}\!/_{r_2}\right) \qquad (2.8)$$

$$L_{opt}{}^* = L_{opt} - Dd_1d_2 \quad \text{with} \quad L_{opt} = d_1 + d_2 = L_{geo} - (n-1){}^{\ell}\!/_{n} \qquad (2.9a/b)$$

For diode pumped systems the shortening of the optical path by the few mm long gain material can often be neglected (thin lens approximation), depending on the geometrical resonator length (L_{geo}). The distances $d_{1,2}$ therefore denote the centre to centre distance between the gain material and the respective mirror with radii of curvature $r_{1,2}$. Without this approximation, $d_{1,2}$ denotes the distance from the main focal planes of the thick lens. Equations (2.7) to (2.9) therefore describe the position of the equivalent resonator in the g-diagram as a function of the refractive power, which in itself is dependent on the pump power. A path through the g-diagram is given on the next page.
Entirely symmetric resonators (mirror curvature, and gain material position) scan through the origin of the g-diagram. The length of the resonator controls the stability range and the sign of the lensing determines the direction of movement along the path.

movement along the path.

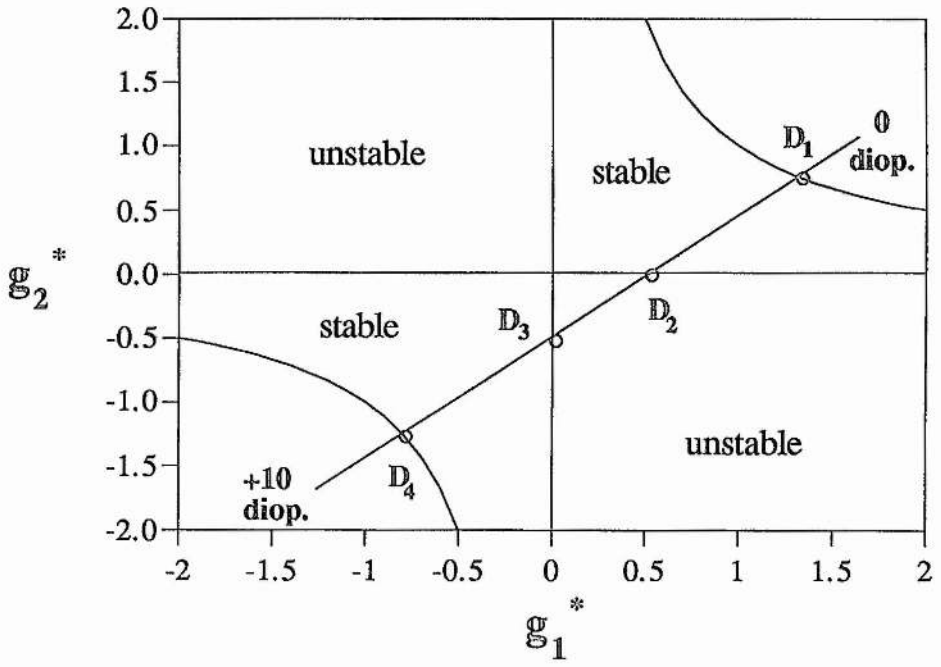

Fig. 2.12: The stability consequences of a changing refractive power (pump power) in the laser material can be displayed as a line in the equivalent g-diagram. The gradient of the path is also dependent on the position of the gain material in the resonator.

The stability borders are the crucial points, as they allow one to link the experimentally observed pump power at the stability transition with the refractive power necessary to reach this transition stage. A maximum of four transitions are possible, where the critical refractive power as a function of the cavity geometry is given below:

$$g_1^* g_2^* = 1 \text{ and } g_1^* > 0 \qquad D_1 = -\frac{1}{r_1 - d_1} - \frac{1}{r_2 - d_2} \tag{2.10}$$

$$g_1^* = 0 \qquad D_2 = -\frac{1}{r_1 - d_1} + \frac{1}{d_2} \tag{2.11}$$

$$g_2^* = 0 \qquad D_3 = \frac{1}{d_1} - \frac{1}{r_2 - d_2} \tag{2.12}$$

$$g_1^* g_2^* = 1 \text{ and } g_1^* < 0 \qquad D_4 = \frac{1}{d_1} + \frac{1}{d_2} \tag{2.13}$$

The thermal lensing dependence on the pump power can be obtained by comparing these experimentally observed pump powers with the calculated

diopter values of the thermal lens at the respective stability borders (figure 2.12). To measure the lensing 8 different flat/flat resonators, with different lengths and geometries were investigated. An average of the results obtained was :

+0.36 diopters per watt of input power.

The highly end-effect governed nature of the lensing is underlined by the discrepancy between the magnitude of the thermal lensing amount per watt of input power measured by this method and that measured by the Helium-Neon method.
In the case of the Helium-Neon method it is essential that the pumped region and test beam overlap totally. The refractive power value so measured is then the highest possible, as the full focusing effect of the distorted YLF interfaces comes into account. However, a handicap of this method is the unrealistic beam diameter of the test beam. The test beam is a factor of two larger in diameter than the resonator mode diameter (~1mm).
In the case of the instability method it is also of importance to take the spatial behaviour of this end-effect governed lensing into account. With higher gains the resonator path and gain area no longer have to overlap exactly in order to maintain the stability of the resonator configuration. Under very high pump power conditions it is advantageous for the mode to avoid the deformed YLF interfaces, and still end up with a net reduction of losses, even after taking losses at the Brewster windows into account.
For this reason the lensing observed depends strongly on the resonator path. To simulate the conditions of the Helium-Neon test beam measurement no realignment from threshold onwards was permitted in the second method, hence ensuring maximum overlap between pumped region and resonator path, thus maximising the thermal lensing.
When permitting realignment from threshold onwards, thus optimising the output power, the refractive power per watt of input power is considerable smaller than in the case without realignment, namely:

+0.36 diopters per watt pump power (no realignment)
+0.25 diopters per watt pump power (with realignment).

The plane/plane resonator geometries used for these measurements permit only transitions from stable to unstable regions in the g-diagram. A better way of measuring the thermal lensing under threshold conditions and high pump

powers (i.e. conditions as found in the test beam method) is by utilising unstable to stable transitions in the g-diagram of a convex/plane resonator configuration. To reach threshold the pumped volume and mode volume have to overlap in the most effective way, thus forcing the resonator mode path onto the pump power distorted YLF surfaces. The calculated g-diagram describing the route of the equivalent resonator under pump powers of between 0 to 20W (reaching stability at 7W of pump power), as well as the measured output power along this path are displayed in figure 2.13a/b.

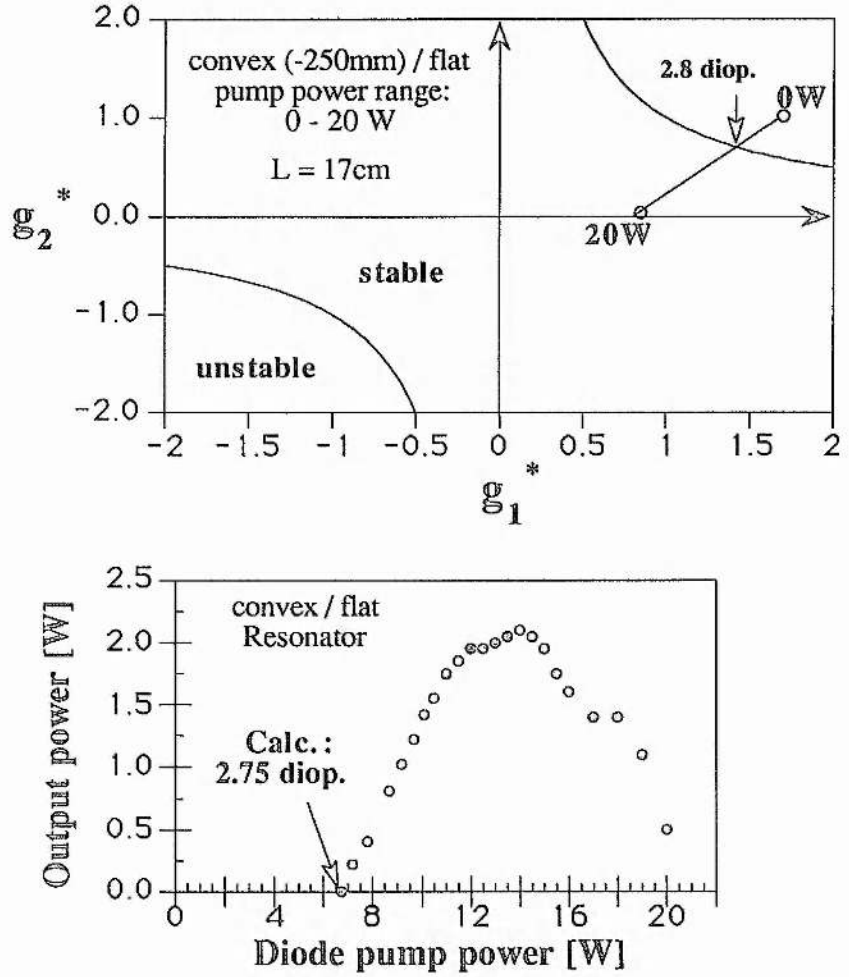

Fig. 2.13a/b: *Equivalent g-diagram of a convex/plane cavity configuration. The respective output power trace is shown below. The comparatively low output power is due to the unmatched resonator mode size.*

The table on the next page summarises the magnitudes of the thermal lensing measured by the different methods under cw operation conditions.
A factor of almost two in the magnitude of the lensing can be detected, depending on the measurement conditions.

Helium-Neon method	**Instability method** unstable-stable transition	**Instability method** stable-unstable transition, threshold optim.	**Instability method** stable-unstable transition, output optimised
0.45 dp/W	**0.42 dp/W**	**0.36 dp/W**	**0.25 dp/W**

The thermal lensing value closest to realistic operating circumstances at high pump powers can be found in the right hand column. Towards the left of the columns the lensing value more and more reflects the situation around threshold. Effects such as an unrealistic beam diameter in the Helium-Neon test beam method, and non mode-matched conditions in the instability method, might also exaggerate the lensing value in the two left columns. The strong variation of the thermal lensing reflects the end-effect governed properties of diode-end-pumped Nd:YLF, where the amount of compensation for the negative bulk thermal lensing depends on the resonator path and the pump power level.

To cross-check these cw results the thermal lensing was also investigated under Q-switched conditions, utilising the emission of the laser itself for the test beam method. This was possible because the beam quality of the Q-switched laser is close to diffraction limited even under high pump powers, so that TEM_{oo} propagation behind the output coupler is a reasonable assumption. The measured and fitted beam radii as a function of the distance propagated are shown in figure 2.14 on the next page.
With thermal lensing values of around +0.3 diopters/Watt, these experiments under Q-switched conditions confirm the interpretation of the varying cw results. The difference in thermal lensing between the 10W and 20W pump power levels again confirms the dependence of the strength of the positive thermal lensing on the resonator path, with the 10W lensing values per watt being higher than the 20W ones.
This tendency to avoid the directly pumped YLF surface under high pump powers, leading to a reduction of the overall positive lensing, can be directly observed during the alignment procedure. A horizontal movement of the pump modules towards each other ensures high output power and good beam quality, by separating the pumped YLF surface slightly from the reflection points of the resonator path on the YLF surface.
A more detailed characterisation of the dependence of thermal lensing on the

resonator path with respect to the pumped crystal surfaces can be found in the following 1.3μm chapter. The lower crossection of the 1.3μm transition renders it much more sensitive to changes in pump and resonator mode overlap, so that the connection between lower thermal lensing and reduced efficiency can be clearly demonstrated.

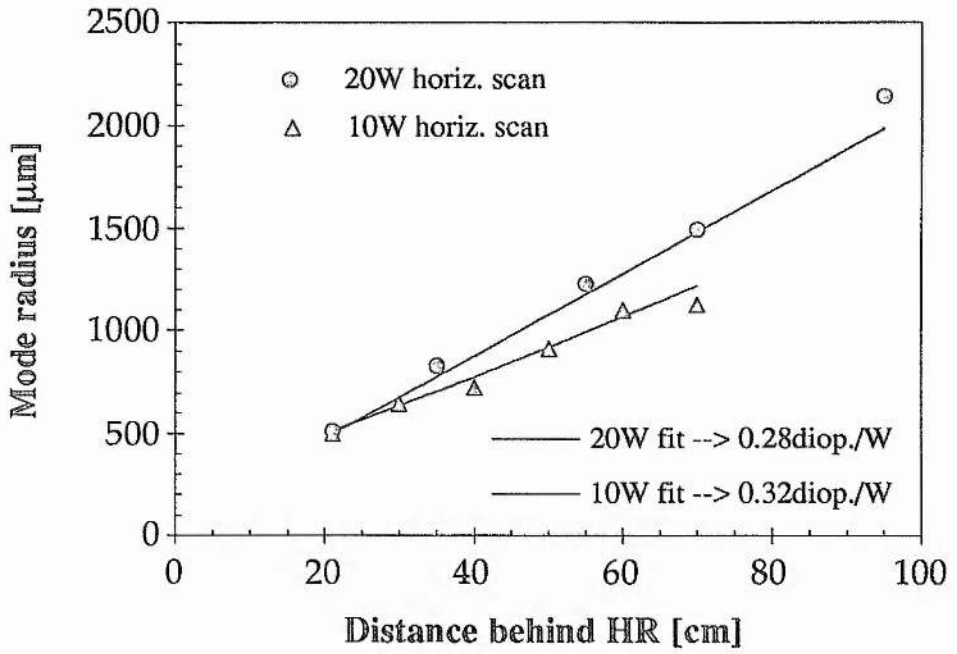

Fig. 2.14: *Thermal lens values under Q-switched conditions for different pump power levels. The measured mode radii are fitted to an assumed $TEM_{0\,0}$ propagation. The repetition rate at 10 and 20W pump power was 2 and 5kHz respectively.*

The similar thermal lensing values between cw and Q-switched operation is also of interest in connection with the later investigation of the relevance of the loss mechanism caused by excited state absorption of laser radiation in Nd:YLF (Chapter 5). These results indicate that the non-radiative decay of the up-converted inversion under 1.047μm operation does not significantly change the thermal lensing behaviour under excitation rates of approximately 5mJ per lifetime. Higher thermal loads, however, would be expected for repetition rates of, for example, 2kHz and 20W pump power, according to the effective lifetime reduction under these operating conditions (figure 5.11).

With these measurements, performed under Q-switched operation, finishing the thermal lensing characterisation at 1047nm, a resonator geometry could be found which ensured,

- almost constant beam diameter in the pumped region, in order to sustain optimum mode matching independent of the pump power level, and
- decreasing beam diameter at the Q-switch location with increasing pump power. In case of an acousto-optical Q-switch this would accelerate the switching time when needed most, namely under high gain conditions. This positive effect has to be balanced with possible damage problems to the Q-switch.

A sketch of the resonator geometry used is pictured in figure 2.15.

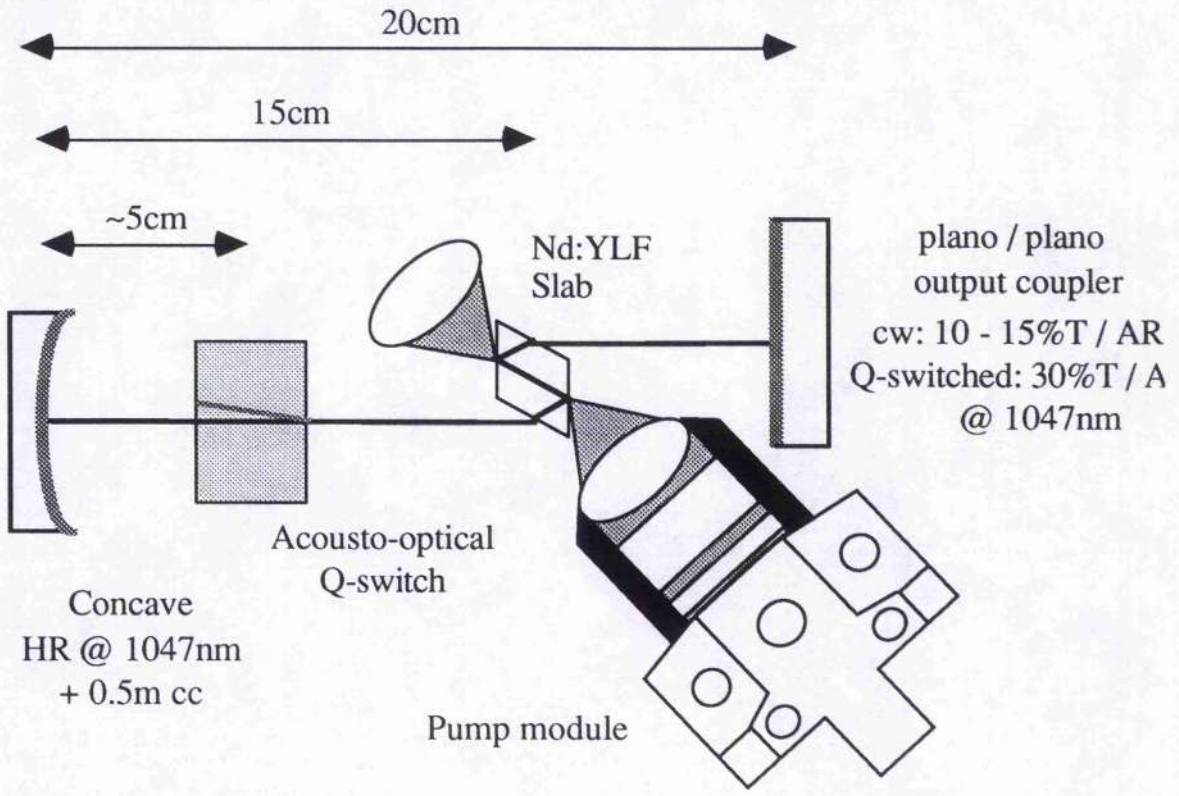

Fig. 2.15: *Sketch of the resonator set-up employed for most of the cw and Q-switched experiments.*

The short distance between flat output coupler and Nd:YLF slab is one of the factors needed to ensure a constant mode diameter in the pumped region. To achieve this close spacing an extension on the mirror mount was necessary, which can be seen later in this thesis, in Chapter 3. The placement of the Q-switch at the far end of the cavity, close to the high reflecting mirror optimises

the switching time of the acousto-optical device. The changing mode size, ω, inside the cavity under the varying pump power has already been displayed in figure 2.10. Under high pump powers (20W) the set-up is near the first stability border, which is equivalent to a tight beam radius on the HR concave mirror (+0.5m), thus giving a decreasing mode diameter in the Q-switch with increasing pump power. The path of this lens resonator through the equivalent g-diagram is displayed in the figure below:

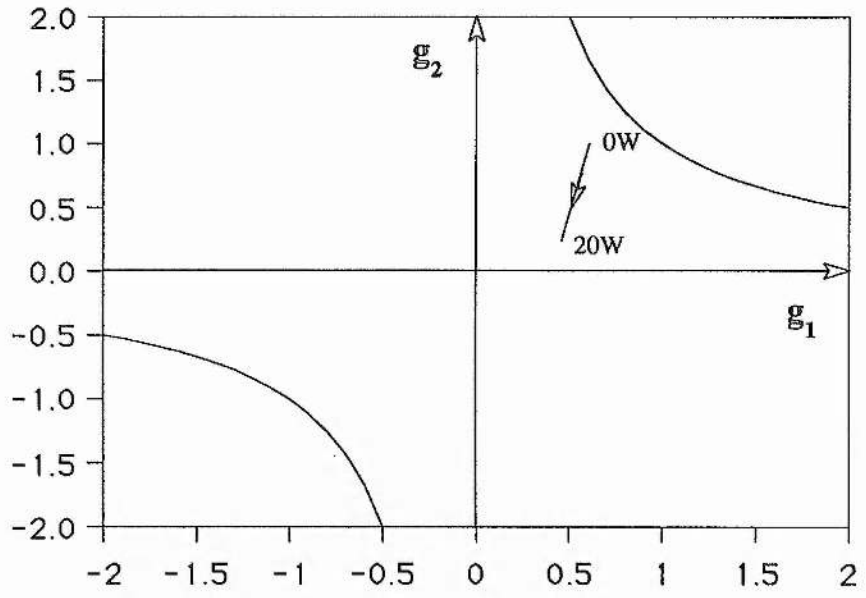

Fig. 2.16: *The changing stability condition of the lens resonator in figure 2.15 for pump powers of between 0 and 20W. A lensing coefficient of +0.25 diopters per Watt diode pump power was assumed.*

The mode radius of 250μm is under mode matched when compared with the dimensions of the fluorescence profile (600μm x 1.1mm diameter). An increase in the mode diameter from 500μm to 600μm does not improve the efficiency of the laser system. On the contrary, efficiency decreases slightly. This is attributed to increased losses if the whole of the pumped region is used as cavity mode volume, decreasing the freedom to move the cavity mode in the surrounding pump volume in the output optimising manner, as described above.

Similar behaviour was reported in a fibre coupled diode end-pumped Nd:YAG laser [16]. Even in the best case of a circularly symmetric inversion profile, only a value of 0.6 for the mode overlap integral was reported. Larger cavity

modes, although supposedly better mode matched, resulted in higher diffraction losses, under high pump power conditions. As the edge of the hard pumped region is the reason for the increased losses it is advantageous to concentrate most of the pump energy into the centre of the rod.
The approach of Kaneda and Kubota [16] utilised a fibre bundle combining the pump power of 19 diode pairs. This set-up made it possible to temperature tune the emission wavelength of the fibre bundle across the aperture.
Detuning along the radius of the aperture away from the centre absorption at 809nm in Nd:YAG would help to maximise the centre inversion, which is less susceptible to the diffraction losses caused by the aberration of the thermal lens.

This advantage of an under mode matched cavity (in one dimension) is the motivation for not trying to improve the conversion efficiency by way of an anamorphic intra-cavity expansion in the other, well under matched direction of the fluorescence profile (1.2mm length). Keeping in mind that the anamorphic expansion with two intracavity prisms would cause extra losses, which are critical in a cw pumped system, and that the expansion ratio should be smaller than two, it is questionable if any gain in performance would result. Another reason against these additional intra-cavity components is the increased complexity in the alignment of the laser. With the presence of pump power induced end-effects altering the resonator path and increasing the losses, the aim was to keep the set-up as simple as possible.

2.5 Conclusions

The combination of pump geometry, orientation of the c-axis and dimensions of the slabs make it possible to use Nd:YLF for high density end-pumping purposes. The folded cavity design in combination with Nd:YLF has the following advantages:

- Natural birefringence of the material which suppresses any pump power induced depolarisation losses.
- End-pumped scheme which favours TEM_{oo} operation at high efficiencies and short Q-switched (typical 25ns) pulse durations.
- c-axis orientation which selects high absorption and high gain line in Nd:YLF with a linearly polarised output at 1047nm.
- Longer upper state lifetime as compared to Nd:YAG which gives better energy storage in the case of repetitive Q-switching for repetition rates below 5kHz.
- Compensation for the inferior thermal properties of Nd:YLF by choice of the appropriate dimensions of the slabs.

With regard to the thermal lensing under these end-pumped conditions, the following key points are of importance:

- YLF exhibits a very strong positive thermal lensing.
- Given the negative bulk thermal lensing ($dn/dT < 0$) in YLF the resulting positive thermal lensing must be highly governed by positive end-effects at the pumped surface.
- Thermal lensing will depend on the alignment of the resonator path, due to the dominant end-effects .
- No anisotropic lensing was observed with the Helium-Neon test beam method. However this method had an accuracy of only 10%.
- A value of **+0.25 to 0.3 diopters/Watt** is a good guidance value for the lensing under high pump power conditions using the pump modules described earlier.

In particular, the absence of any measurable anisotropic lensing - under beam quality optimised alignment conditions - is as unexpected as it is advantageous at high pump powers. A correlation between the pump spot geometry and the thermal lensing properties caused directly by this end-effect is therefore suspected. This hypothesis has to be investigated at a later time (see also

Chapter 4 and 'Conclusions & Future work'), especially if at a later stage the use of fibre coupled diode pump modules is undertaken.

Although a considerable amount of effort was concentrated on thermal lensing characterisation, only a working knowledge exists for the laser described here, which was, however, sufficient to optimise the laser. A more general understanding of end-effect governed lensing in diode end-pumped Nd:YLF would need a different approach. In that case the performance of the laser would not be the centre of attention, as in this work. Instead, extremely controlled experimental conditions, through restricting the degrees of freedom in the cavity, would have to be enforced, to simplify a more analytical approach.

This work was one of the first experiments to extend the high power diode end-pumped approach successfully to Nd:YLF and different views exist about the strength and anisotropy of the lensing. An overview of the thermal lensing results from two other groups working in this field is shown below in table 2.17.

Author	**lensing coefficient** 1047nm, $\|\|c$	**lensing coefficient** 1047nm, $\|\|a$	**integrated fluorescence profile**
Magni et al. [17]	**- 0.042 diop./kW**	**- 0.147 diop./kW**	homogeneously flashlamp pumped
L.Marshall [18]	**+0.03 diop./W**	**-0.08 diop./W**	2.0 x 0.4mm^2
P. Moulton [19]	**+0.25 diop./W**	**+0.1diop./W**	1.2 x 1.8mm^2
This work	**+ 0.25-0.3 diop./W**	**+ 0.25-0.3 diop./W**	0.6 x 1.2mm^2

Table 2.17: *Comparison of different thermal lensing results in Nd:YLF under diode end-pumped conditions, giving the (probably) important parameter of the fluorescence profile used. The flashlamp pumped thermal lensing results are mentioned to highlight the totally different behaviour of YLF under these circumstances.*

The Fibertek work [18] reports anisotropic lensing with a negative lens in one plane and a weak positive lens in the other plane. This result, in particular the residual negative lensing, is difficult to agree with given the results and

experience gained during the experiments described in this thesis.

Similar lensing values have been found by both the Schwartz Electro-Optic publication [19] and this work, although only for one plane. Moulton et al. report weaker positive lensing (by a factor 2) for the other orientation.

A future aim is to understand which pump and cavity parameters are responsible for the observed compensation of the generally anisotropic thermal lensing in Nd:YLF. In particular, the changed thermal lensing behaviour at 1.321μm and its expected connection to excited state absorption is interesting and will be discussed in the 1.3μm chapter later on. That chapter also provides more insight into the difficulties of characterising thermal lensing in strongly end-pumped solid-state lasers, with implications beyond the device actually used .

References

[1]: W. Koechner **"Solid-State Laser Engineering"** , p. 400
4th. Edition (1995), Springer-Verlag

[2]: I. Freitag, D. Golla, H. Welling & al. - **Amplitude and frequency stability of a diode-pumped Nd:YAG laser operating at a single-frequency continuous-wave output power of 20W** - Opt. Lett. 20, No.5, 462 (1995)

[3]: D.C. Shannon & R.W. Wallace - **High power Nd:YAG laser end-pumped by a cw, 10mm x 1μm aperture, 10W laser-diode bar** -
Opt. Lett. **16**, No.5, 318, (1991)

[4]: Bergman Schaefer **"Lehrbuch der Experimentalphysik, Band 8 Optik"**
Walter de Gruyter, 8. Auflage (1987)
W. Koechner **"Solid-State Laser Engineering"** , p. 406
4th. Edition (1995), Springer-Verlag

[5]: S. C. Tidwell, J. F. Seamans, C.E. Hamilton & al. - **Efficient, 15W output power, diode-end-pumped Nd:YAG laser** - Opt. Lett. **16**, No.8, 584 (1991)
S. C. Tidwell, J. F. Seamans & M.S. Bowers - **Highly efficient 60-W TEMoo cw diode-end-pumped Nd:YAG laser** - Opt.Lett. **18**, No.2, 116 (1993)

[6]: B. Neuenschwander, P. Albers & H.P. Weber - **Efficient multiple-longitudinally diode laser pumped Nd:YAG slab laser** -
Optical and Quantum Electronics **24**, 363, (1992)

[7]: T.M. Baer, D.F. Head, S. Hutchison & al. - **Performance of diode-pumped Nd:YAG and Nd:YLF laser in a tightly folded resonator configuration** -
IEEE J.-QE. **QE-28**, No.4, 1131, (1992)

[8]: **"Frequency agile holosteric lasers II"** (Apr. 92 - Oct. 92), Appendix V1
Report compiled by C. Rahlff

[9]: H.S. Carslaw & J.C. Jaeger **"Conduction of heat in solids"**
Oxford Science Publications, 2nd. edition (1959)
S.P. Timoshenko, J.N. Goodier **"Theory of elasticity"**
Mac Graw-Hill Book Company, 3rd. edition (1970)

[10]: K. Mann, H. Weber - **Surface heat transfer coefficient, heat efficiency and temperature of pulsed solid state lasers'**
J. Appl. Phys. **64**, No.3, 1015 (1988)

[11]: C.F. Rae, J.A.C. Terry & M.H. Dunn - **Single-frequency, end-pumped Nd:YLF laser excited by a 12mJ diode laser array** -
Opt. Lett. 17, No.23, 1673 (1992)

[12]: Y. Kaneda, M. Oka, S. Kubota & al. - **7.6W of continuos-wave radiation in a TEM_{oo} mode form from a laser-diode end-pumped Nd:YAG laser** - Opt. Lett. 17, No.14, 1003 (1992)

[12a]: S. C. Tidwell, J. F. Seamans, M. S. Bowers, & A. K. Cousins - **Scaling cw diode-end-pumped Nd:YAG lasers to high average powers** - IEEE Journal of Quantum Electronics QE-28, No.4, 997 (1992)

[13]: T.M. Pollak, E.P. Chicklis, H.P. Jensen & al. - **Cw operation of Nd:YLF** - IEEE J.-QE. QE-18, No.2, 159 (1982)

[14]: H. Kogelnik - **Imaging of optical modes - Resonators with internal lenses** - Bell Syst. Tech. J. 44, 455 (1965)
H.P. Kortz, R. Iffländer & H. Weber - **Stability and beam divergence of multimode lasers with internal variable lenses** - Appl. Opt. 20, No.23, 4125 (1981)
G. Herziger & H. Weber - **Equivalent optical resonators** - Appl. Opt. 23, No.10, 1450 (1984)
D. Metcalf, P. de Giovanni, J. Zachorowski & M. Leduc - **Laser resonators containing self-focusing elements** - Appl. Opt. 26, No.21, 4508 (1987)

[15]: A. Siegman "Lasers" University Science Books 1st. edition (1986)

[16]: L.Y. Liu, M. Oka, W. Wiechman & S. Kubota - **Longitudinally diode-pumped continuous-wave 3.5W green laser** - Opt. Lett. 19, No.3, 189 (1994)

[17]: G. Cerullo, S. de Silvestri & V. Magni - **High efficiency, 40W cw Nd:YLF laser with large TEMoo mode** - Opt. Commun. 93, 77 (1992)

[18]: L. R. Marshall, A. Kaz & H. Verdun - **Cw-diode, end-pumped Nd:YLF laser with an astigmatic resonator** - Paper CMF5, CLEO Digest, p.642, Baltimore 1993

[19]: G.A. Rhines, R.A. Schwarz & P.F. Moulton - **Diode-laser-pumped, cw, Nd:YLF laser with efficient intracavity second harmonic generation** - Paper ATuD3-1, Advanced Solid State Lasers p. 178, Salt Lake City, Feb. 1994

[20]: J. Harrison, P.F. Moulton & G.A. Scott - **13W, M^2<1.2 Nd:YLF laser pumped by a pair of 20W diode laser bars** - Paper CPD-20, Conference on Lasers and Electrooptics , Baltimore, May 1995

Chapter III.

CW and Q-switched performance at 1047nm

In this chapter an overview is given of the experimental results for operation at 1047nm of the laser system developed during this thesis. This chapter contains the main experimental achievements, which are in providing a reliable, diffraction limited, high repetition rate pump laser at output powers of up to 5W (5 to 6kHz, M^2~1.3). With relaxed beam quality requirements (M^2~2) up to 8.5W at 15kHz are possible. This beam parameter product still represents an acceptable focus quality for material processing purposes. The short pulse width (~25ns), high average power and excellent beam quality lay the foundations for the non-linear conversion schemes, which stretch from the near UV at 349nm to 3.44μm in the mid-infrared. These are described in later chapters.

Beginning with the characterisation of cw operation of the laser with the π-polarised transition at 1047nm, the output power and beam quality as well as the problems of maintaining a TEM_{00} mode at high pump powers are discussed. With the cw laser laying the foundation, the transition towards repetitive Q-switching was only a comparatively small step, after a decision was made on a suitable Q-switch technique. The characterisation of the Q-switched system includes average power, mode quality and pulse width behaviour under different pump power conditions and resonator configurations. Also, some of the limitations of this Q-switched system, given by the combination of short pulse build up time and the relatively slow switching characteristics of the acousto-optical Bragg-cell will be mentioned.

Towards the end of the chapter a brief characterisation of the fluorescence and lasing linewidth properties in the 1μm region is given. These results are particular of interest in comparison with the 1.321μm linewidth characteristics of Nd:YLF in the next chapter. A narrow linewidth pump laser is of specific importance with regard to non-linear conversion schemes, as the pump source linewidth is often the dominant factor, depending on the phase match configuration and non-linear material choice, in the total linewidth of the conversion process.

3.1 CW performance at 1047nm

At the start of the project a polarisation dependent output coupling scheme was employed, which allowed flexible experiments with only a few standard high reflecting mirrors, due to its adjustable degree of output coupling. These experiments proved to be very valuable in achieving a first intermediate characterisation of pump power related parameters such as thermal lensing, losses and gain of the new system. However, during these experiments the thin-film polariser proved to be the reason for additional intra cavity losses, of the order of ~2% as determined by the standard Finlay-Clay method [1] used for cw systems, while the AR-coated $\lambda/4$-waveplate was virtually loss free. Compared with the equivalent fixed output coupler cavity (10% transmission), these losses caused a reduction in output power of more than 25% in the case of a TEM_{00} mode (5W pump power level).

As a consequence all the high pump power experiments were done with fixed output couplers, whose selection was greatly helped by the preliminary experiments. The performance achieved for pump powers of up to 20W is displayed in figure 3.1.

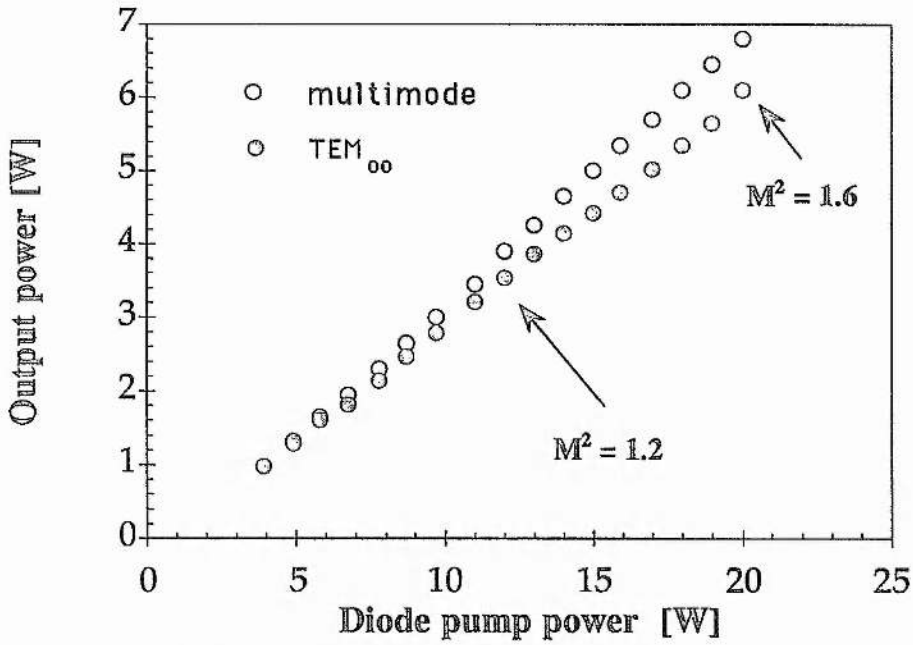

Fig. 3.1: *Multimode and TEM_{00} performance at 1047nm for pump powers of up to 20W (both pump modules used). For pump powers above 15W intra cavity aperturing was necessary to maintain acceptable beam qualities, hence the increasing difference between multi mode and TEM_{00} output.*

The beam quality measurements reflect the increased problems in achieving close to diffraction limited output at higher pump powers. Beam quality improvement could be achieved by two methods:

- Parallel shifting of the two pumped regions, by aligning the pump modules horizontally towards each other, in order to achieve the best overlap between the straight resonator path and both pumped regions.
- Intra-cavity aperturing to achieve a more circular inversion profile, by inserting, for example, a knife edge to cut down on the long axis of the elliptical pump profile.

Due to the 2:1 eccentricity of the elliptic fluorescence profile (with the long axis in the horizontal direction) the cavity mode has the tendency to be multi-mode along the axis with the wider fluorescence profile. In the vertical direction, which coincidences with the short axis of the fluorescence profile, the aperturing of the 2mm thick slab prevents multi-mode operation. For lower pump powers (10 to 12W) it is sufficient to align the pump modules horizontally, and parallel to the pumped surface. Under higher gain conditions it is necessary to insert the knife edge and additionally realign the horizontal orientation of the pump modules towards each other in order to optimise the gain profile. As the TEM_{xy} modes are radially symmetric in their intensity distribution, a single sided restriction still results in a symmetric mode pattern. Following this procedure, 6.3W TEM_{oo} with a measured beam quality of M^2=1.6 could be achieved at 20W diode pump power. The insertion of the knife edge gives rise to extra diffraction losses, as well as a reduced mode volume, so that the output power drops by ~1W from the multimode case of 7.4W. A similar, if slightly reduced (especially at higher diode pump powers), performance was achieved, as displayed in figure 3.1, using one pump module and applying 20W of pump power to only one of the two folding points (~5.2W TEM_{oo}). As with the intermediate $\lambda/4$-waveplate and polariser output coupling scheme, this experiment was run with only one pump module for over half a year. This was partly to verify the anticipated thermal damage resistance and partly due to the time necessary to construct the second pump module. However, the symmetric pump geometry is clearly preferable, as it stays far below the pump power limit per surface, reducing the breakage risk and allowing improved mode control by parallel shifting of the pump modules. The multi-mode performance for the whole pump power range of up to 40W is shown in figure 3.2 on the next page.

The turning point in the output power curve at 36W pump power designates the practical scaling limit for this end-pumped laser. At this point distortions of the pumped surfaces are so high that even high order modes suffer greater diffraction losses than can be compensated for by the increased gain. This practical pump limit occurs in Nd:YLF before thermal stress fracture, the ultimate barrier for pumping the material harder, destroys the slab. The achievement of 20W pump power per reflection point without thermal stress fracture occurring, gives the security needed to optimise the Nd:YLF system at the lower, sub 20W pump powers per surface.

To make sure that this power drop is not caused by a transition to an unstable round trip condition, the behaviour at the highest pump powers was checked with different resonator configurations, which provide stability even against extreme positive thermal lensing. A symmetric, very short (10cm), plane-plane cavity provides stability over a wider range as the equivalent resonator moves through the origin into the third Quadrant, the second stability area of the g-diagram [2].

Even under these conditions the characteristic turning point occurred at around 35W diode pump power, well within the stability range for that configuration. This confirmed that the output power drop could not be attributed to an incorrect measurement of the thermal lensing coefficient.

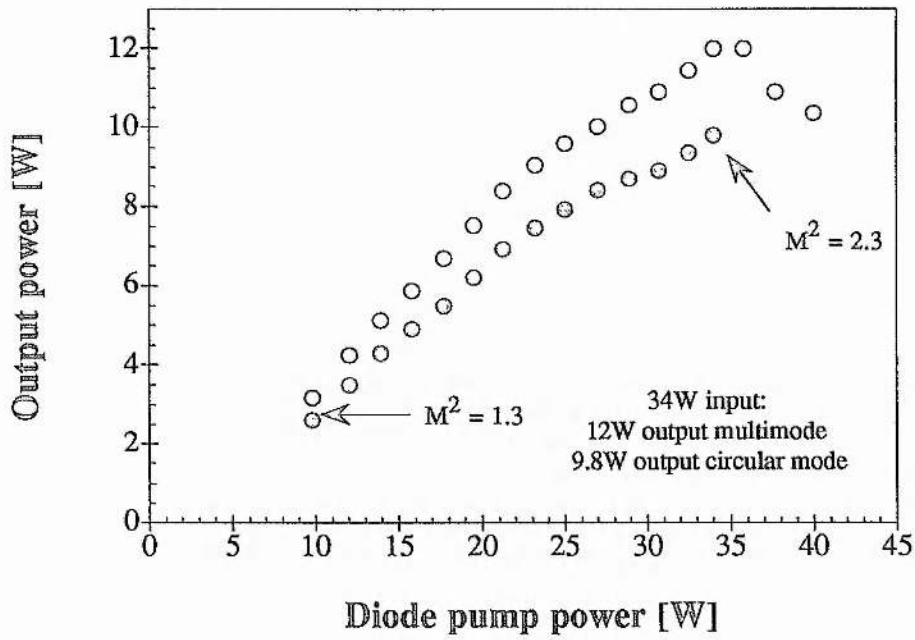

Fig. 3.2: *High pump powers above 20W cause increased losses, due to aberrations of the thermal lens. Above 17W of pump power per surface these losses dominate, and output power decreases despite intensified pumping.*

The selection of the 1047nm line in the anisotropic Nd:YLF was achieved by the combination of two Brewster cut crystal surfaces and the orientation of the c-axis towards the resonating field. By investigating the spectral characteristics of the cw output with an optical spectrum analyser it could be checked that the losses for the vertical polarisation were high enough to prevent parasitic oscillations at 1053nm. The recorded spectrum between 1037nm and 1057nm is shown in figure 3.3.
Only the π-polarised 1047nm transition is detectable; the scattered small peaks are due to noise. A repeat measurement under Q-switched conditions for the same pump power level later confirmed the above result under higher gain conditions.

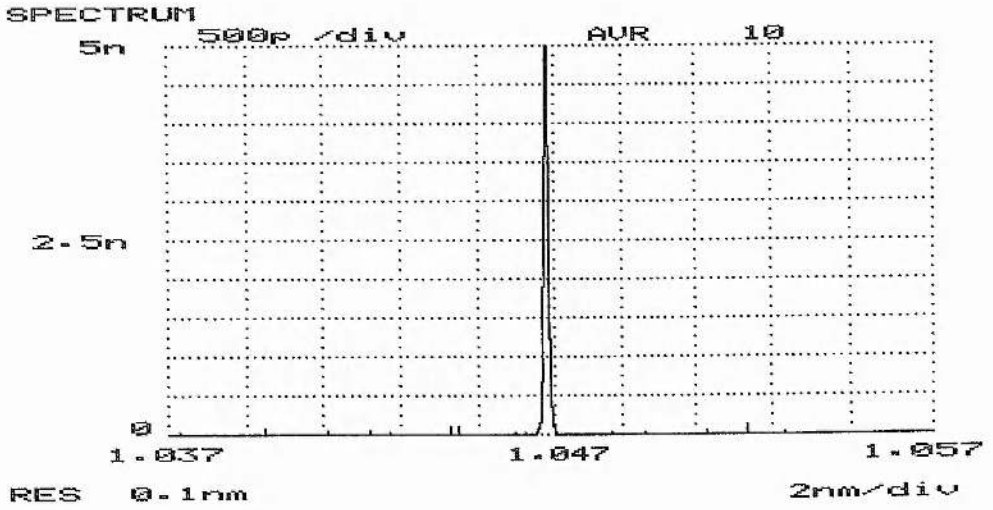

Fig. 3.3: Optical spectrum of the cw Nd:YLF laser output at a diode pump power of 20W. There are no traces of the σ-polarised 1053nm radiation.

In addition to the good wavelength selection properties of the slab design, the second purpose of the Brewster windows also came fully up to expectations, as they provided low loss for the horizontally polarised component, eliminating the need for anti-reflection (AR) coatings on these entrance windows. The loss of the Nd:YLF slab measured according to the Finlay-Clay method was about 2%. As this includes the scattering losses as well as the reflections losses on the Brewster windows under operating conditions near threshold, it is also evidence of the high quality of the Nd:YLF material and coatings.

The polarisation dependent lasing wavelength of Nd:YLF can be directly observed by detecting the fluorescence spectrum in the 1μm region under polarised and unpolarised conditions. The main reason for examining the 1μm

and 1.3μm fluorescence in respect to their linewidths arose during work on the 1.3μm transition (Chapter 4), which exhibited unusually wide linewidths, of up to 1nm, depending on the repetition rate under Q-switched operation.

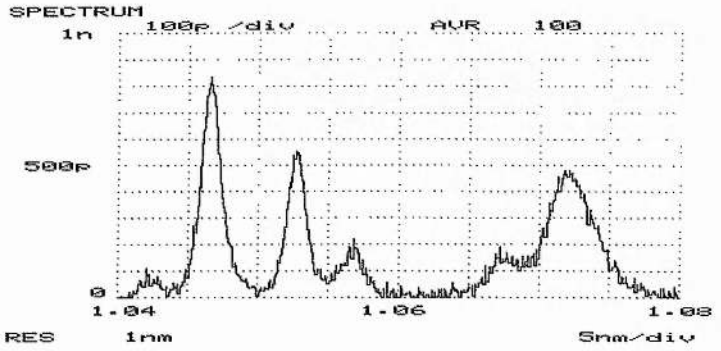

a)

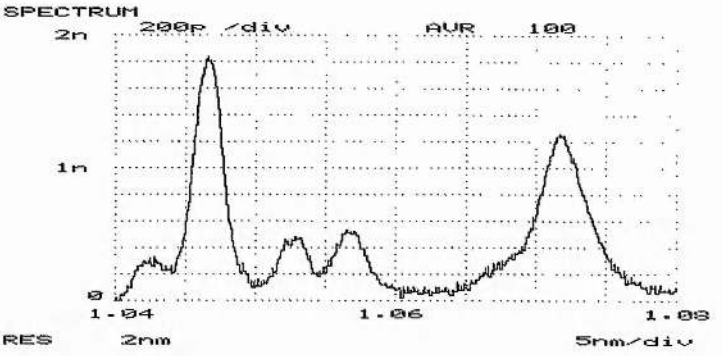

b)

Fig. 3.4: The unpolarised (a)) and polarisation resolved (b)) fluorescence spectra of Nd:YLF (1.1% (weight) doping) at a pump power intensity of ~700W/cm², recorded through one Brewster surface of the slab. As the high transmission of the polariser cube was in the plane of incidence of the Brewster window, the σ-polarised transitions were suppressed.

At a first glance the two main lines in Nd:YLF at 1047 and 1054nm are recognisable. The σ-polarised 1054nm line was suppressed by a polariser with the suitable orientation being inserted into the fluorescence path, which was then coupled into the optical spectrum analyser. The remaining intensity of the 1054nm is π-polarised and it would be possible to achieve lasing on this mainly σ-polarised line, by enforcing π-polarisation within the resonator by suppressing the much stronger, and also π-polarised 1047nm line with a birefringent filter [3].

However, the strength of the more exotic 1072nm line is very surprising, especially as a recent paper by Ryan and Beach [4] calculates the cross-section of this transition as $5 \cdot 10^{-20}$ cm², with the calculated crossections being based on

calibrated emission spectra. This low cross section value for 1072nm is comparable to the 1321nm line in Nd:YLF. According to Ryan and Beach the line at 1043nm would even have a higher crossection ($7 \cdot 10^{-20}$ cm^2) than the 1072nm transition, but in the spectrum above this line is much weaker than the measured 1072nm intensity.
On the simplified assumption that the stimulated emission crossection is linear with the fluorescence intensity, a much higher value would have been expected given the measurement above. Taking the ratio of the unpolarised peak fluorescence intensities at 1047nm and 1053nm in figure 3.4 confirms the crossection ration of these transitions as being in good agreement with the calculated crossection ratio of Ryan and Beach:

$$I_{1053nm} / I_{1047nm} = 0.78 \qquad \sigma_{1053nm} / \sigma_{1047nm} = 0.73$$

To check that the high fluorescence intensity at 1072nm is not caused by two superimposed lines of different polarisation, the ratio of the 1047 and 1072nm lines was taken in each case for the polarised and unpolarised spectrum.

$$I_{1072nm} / I_{1047nm} = 0.59 \qquad I^{p}_{1072nm} / I^{p}_{1047nm} = 0.67$$

These two ratios are only slightly different, indicating that both lines are, dominantly and to a similar degree, π-polarised. The remaining time did not permit the achievement of lasing on the π-polarised 1072nm transition, by using a prism to suppress the 1047nm line, in order to resolve this puzzling disagreement. The reason for the interest in the 1072nm emission is in its potential use for doubling purposes. With the longer wavelength it might just be possible to realise a temperature tuned, NCPM type II doubler in KTA/KTP. This would have especially interesting consequences for cw intra-cavity doubling applications, where CPM type II phase matching schemes in KTP have well known disadvantages, such as walk-off and depolarisation of the fundamental [5]. More about this potential scheme, in connection with the 1072nm line in Nd:YLF, can be found in the frequency doubling and tripling section.

The linewidth of the 1072nm fluorescence, at approximately 3nm, is comparable to the 1.3µm transition widths, which would give rise to an estimated Q-switched linewidth in the 0.6nm region, as encountered with the

1321nm transition in Chapter 4. In contrast to this is the fluorescence linewidth of 1.1nm at 1047nm, which corresponds to a lasing linewidth of 0.1nm for this transition, as measured towards the end of this chapter.
The following table gives all the resolvable lines in the 1μm region, with their dominant polarisation orientations, as measured in figure 3.4.

Centre wavelength [nm]	*Dominant polarisation*	*Centre wavelength [nm]*	*Dominant polarisation*
1043	π	1057	π
1047 (1.1nm)	π	1067	σ
1053 (1.3nm)	σ	**1072** (3.2nm)	π

Table 3.5: *Overview of the fluorescence transitions and dominant polarisations in the 1μm region for Nd:YLF. The lines with comparable high fluorescence intensities are printed in bold figures. The fluorescence linewidths (FWHM) for these lines have been measured down to 0.2nm OSA resolution.*

3.2 Repetitive Q-switching and beam quality improvement at 1047nm

The transition from the cw system to the Q-switched system was comparably straightforward, as only a decision about the Q-switching technique was necessary. As a high average output power was the main objective of this cw pumped system, the ability to give high repetition rates, beyond the 1kHz mark, was an essential requirement for the Q-switch technique selected.

With the decision to use an acousto-optical Q-switch, the established switching technique for cw-pumped lasers was chosen. This way a trouble free high repetition capability was ensured. The associated disadvantages of this approach such as,

- slow switching time (dependent on the mode diameter, ~100ns in this cavity configuration),
- low damage threshold and
- hold off problems due to limited diffraction efficiencies

did not cause any practical problems. The exception was the switching time limitation under extreme operating conditions. These limitations of the system will be discussed towards the end of the chapter. Table 3.6 gives an overview of some of the measured Q-switch characteristics.

RF driving requirements	80 MHz ; 2.5 to 3W to avoid hold-off problems Damage limit of transducers: ≤ 4W
Q-switch material (3mm high, 10mm wide 16mm along optical axis)	Not $PbMO_4$, otherwise no information from 'Isle Optics'. Measured data matches: SF6 Glass Bulk damage limits: between 200 and 500MW/cm^2
Diffraction efficiency	~80% (3W RF driving power) measured at 633nm
Speed of sound	2950 m/s
Switching time characteristics	Resonator beam diameter: 300µm in ~100ns Transducer to optical axis distance: 4.5mm --> ~1.5µs delay to input pulse Rising edge on signal generator: 10ns

Table 3.6: Driving requirements and measured characteristics of the Isle Optics Q-switch QS 080.

However, after overcoming some initial alignment problems, such as realigning the housing aperture of the Q-switch with regard to the centre of the ultrasonic wave propagation and boosting the RF driving power up to between 2.5 and 3W, in order to optimise the diffraction efficiency of the switch, reliable Q-switching with average output powers of more than 8W at 1047nm could be achieved.

A picture of the very compact Q-switched laser configuration, including the pump modules, can be seen on the next page. In between the pump modules the rhombic form of the Nd:YLF mini-slab is clearly recognisable, sitting on the water cooled Aluminium finger. The long output mirror extension of the right hand mirror mount is necessary to ensure good mode matching independent of the pump power level (as described in section 2.4). The acousto-optical Q-switch (Isle-Optics) is placed between the slab and the left hand high reflector. Initial experiments with this set-up were carried out at low pump powers of up to 10W, utilising the same resonator geometry as in the cw case (cavity length of 20cm, output coupling 15% transmission). The gain governed dependence of the pulse length, given by pump power and repetition rate, is clearly shown in figure 3.8 .

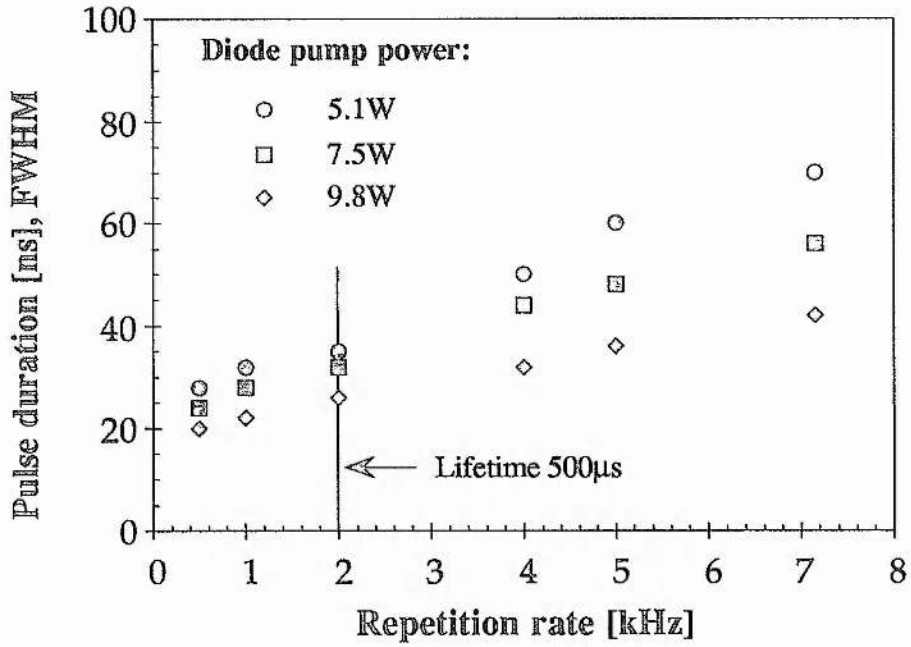

Fig. 3.8: A comparison of pulse durations achievable under low pump power conditions (10W pump power ; geometrical length of resonator: 20cm).

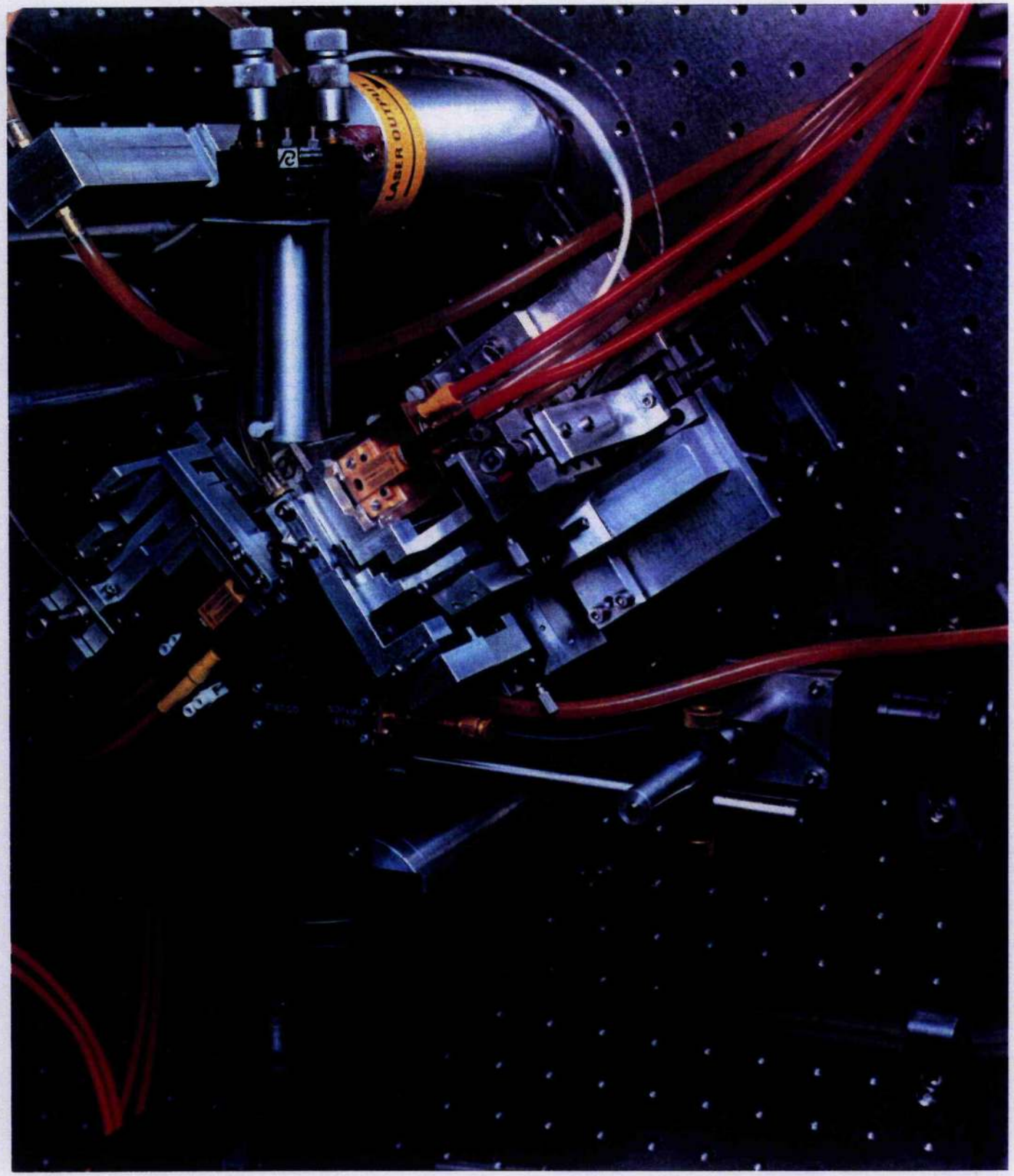

Fig. 3.7: *Photo of the Q-switched, cw diode-pumped, Nd:YLF laser.*

During these experiments for the first time signs of damage were encountered, for repetition rates around 1kHz and 10W pump power. This corresponded to an intra-cavity intensity of 80MW/cm^2 and caused the beginning of damage on the Nd:YLF slab coatings (20% drop in output power), as a later inspection of the cavity elements confirmed.
This unexpectedly low damage threshold of the coatings (at least 200 to 500MW/cm^2 would be expected) could be a direct consequence of the end-effect governed lensing, with its increased stress on the coatings. However, in order to avoid this critical intra-cavity intensity of just below 100MW/cm^2, a change of output coupling was indicated. By doubling the output coupling transmission from 15% to 30% the intra-cavity elements could be effectively protected against damage for output peak powers of 40kW, while the average output power was only marginally reduced (~15% compared to the low output coupling). This insensitivity against a change in output coupling is a consequence of the higher gain under Q-switched conditions, with the optimum output coupling curve having a broad maximum.

A positive side effect of this slightly over-coupled cavity is a more compact pulse form, however the pulse width, measured according to the 'Full Width Half Maximum' (FWHM), remains essentially constant. The compact pulse shape is due to the sharper falling edge of the pulse, as the fall time is directly connected to the decay time of the cavity.

The second parameter used to improve the performance of the Q-switched system is the geometrical cavity length. By reducing the length of the cavity, the round trip time decreases and the stored energy can be extracted within a shorter period. However, the practical importance of a short cavity is lessened by the damage limitations of the slab coatings. In order to stay within the limited safe peak power per pulse, short cavities can only increase the average output power and repetition rates at which these maximum permissible peak powers can be extracted. At high pump powers this increase of average power due to cavity shortening decreases more and more as the 40kW limit is reached for repetition rates close to the quasi-cw saturation level. In order to shorten the standard 20cm long resonator down to 11cm, modifications of the slab cooling mount were necessary. A comparison of achievable peak powers per pulse, due to shorter pulse durations, with these two cavities is shown in figure 3.9a/b .

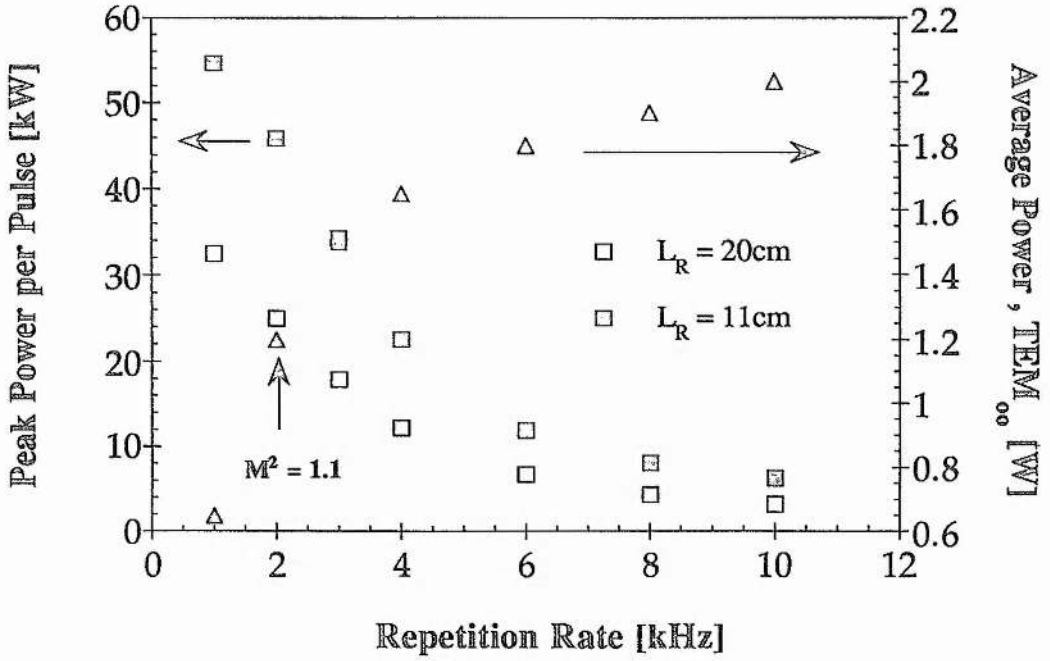

Fig. 3.9a: *Influence of the cavity length on the peak power per pulse for 10W of diode pump power. The pulse duration is roughly halved in the case of the shorter cavity.*

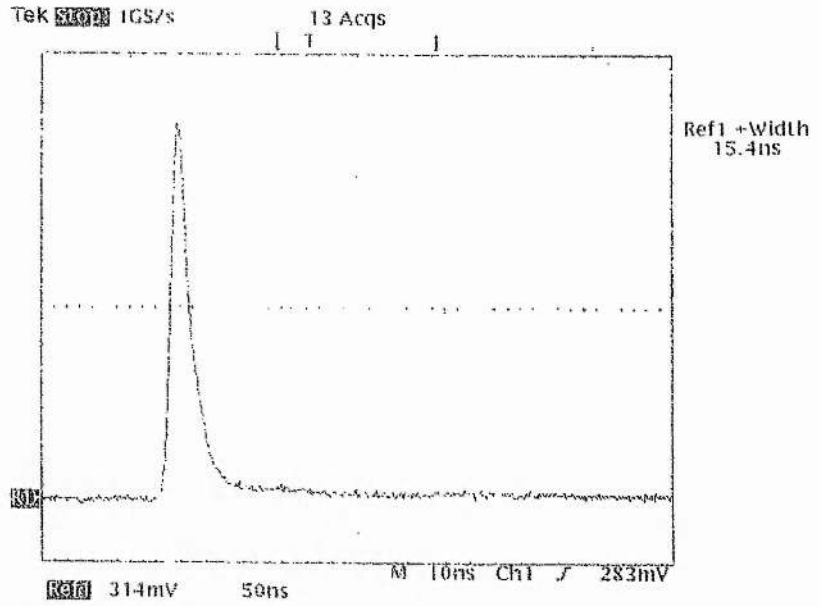

Fig. 3.9b: *A typical pulse shape with 15ns FWHM for a 3 kHz repetition rate is shown above (11cm long cavity).*

The beam quality achieved was almost diffraction limited and had a measured M^2 of 1.1 for a repetition rate of 2kHz (20cm long cavity). Remarkably the beam quality improvement under Q-switched conditions is substantial when

compared to the cw case, especially considering the comparative experimental ease of achieving these good beam qualities. No aperturing was necessary to achieve these close to diffraction limited outputs, even under high pump powers of 20 to 30W. This improved beam quality is a substantial advantage over the cw operation mode, and it should be strongly emphasised that Q-switching is the preferred mode of operation for this end-pumped Nd:YLF system. A comparison of the characteristic beam parameter products for cw and Q-switched operation is shown in figure 3.10.

The improvement from a M^2 value of 1.6 to 1.3 at the 20W pump power level, although not terribly impressive on paper, makes an enormous difference, if the laser system is used as a pump laser. The stated cw beam quality is much more difficult to realise, with a tendency to sudden instabilities of the transverse mode structure, and therefore demands full attention to be on the laser system, which makes it by definition a very poor pump laser. The Q-switched beam qualities are, however, readily achievable and, once the alignment is established, very stable in time.

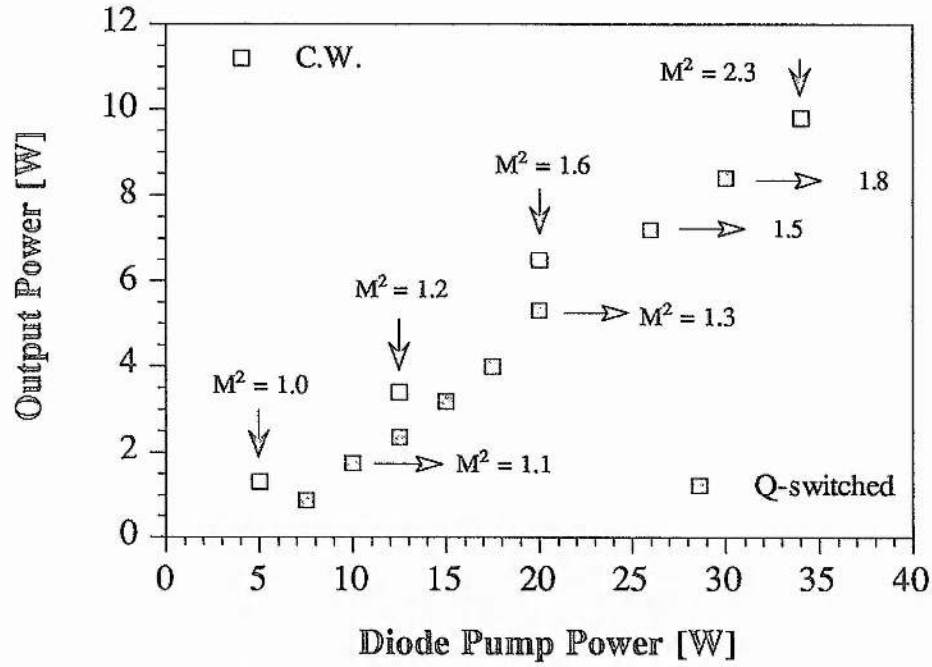

Fig.3.10: *The measured beam quality of the cw and repetitively Q-switched laser system for different diode pump power levels. The improvement in the beam quality is dependent on the repetition rate and increases with prolonged pump intervals. The best M^2 value, at the lowest possible Q-switching rate, is used in this comparison.*

Although in general the Q-switched beam quality is an improvement on its cw counter part, the beam parameter products converge towards the same value for the lowest (5W) and highest (30W) diode pump power levels for this end-pumped laser system. At low pump powers the beam parameter products of the cw and Q-switched systems are identical because of the negligible thermal influence, while at the highest pump powers the thermal distortions of the pumped surfaces were the dominant effects in defining the transverse mode structure. In between these extremes the transverse mode structure is always noticeably improved, as the Q-switched induced effect overwhelms the deteriorating influence of the increasing diode pump powers. The beam quality improvement is illustrated in the pictures below. The multi-modish cw beam is cleaned up under Q-switching and transferred into a circularly symmetric TEM_{oo} mode.

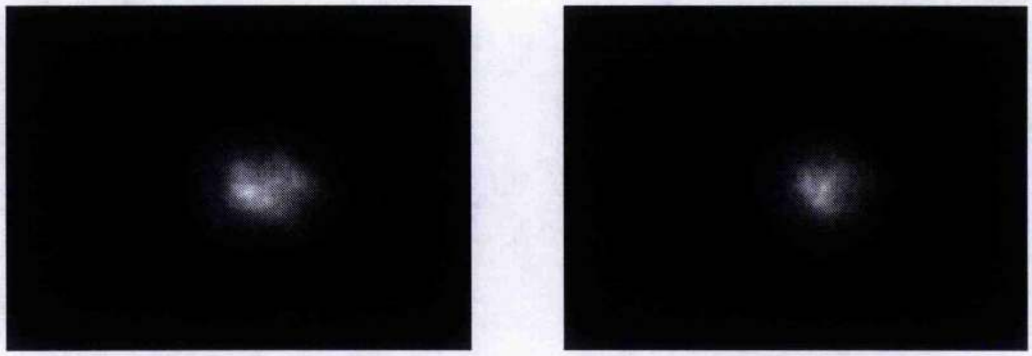

a) **b)**

Fig. 3.11: *Comparison of the transverse mode structure under cw (4W) (**a**)) and Q-switched conditions (4kHz, 2.7W) (**b**)). The diode pump power is 15W. The elliptic shape of the cw mode structure is due to a tendency to prefer multimode operation along the wider axis of the fluorescence profile.*

At this point the question arises as to which mechanism improves the transverse mode selection under Q-switched conditions, when the longitudinal mode selection definitely decreases, due to the increased gain. The increasing linewidth with repetition rate under Q-switched conditions could be clearly demonstrated for the 1.321μm transition (Chapter 4) and is also present during 1μm operation. The different behaviour of the transverse mode structure at 1μm, which in fact improves with the repetition rate (fig. 3.13) could be explained by a spatially varying loss mechanism, which is provided by parts of the excited state absorption process, inherent to Nd:YLF. This hypothesis and

the up-conversion properties into the visible and near UV bands under 1 and 1.3μm operation in Nd:YLF are described in greater detail in Chapter 5.
The 20W pump power level, previously at the limit in terms of maintaining an acceptable cw-mode quality, is now the best compromise between high average output power and beam quality. An almost diffraction limited beam, with a measured M^2=1.3 for a typical average output power of 4.8W (up to 5W), at 5 to 6kHz repetition rate could be achieved. The comparative ease of alignment required to achieve this result, and the beam quality improvement when compared to the cw case (M^2 = 1.6) makes this operation mode well suited for non-linear conversion schemes, as proved in the frequency conversion schemes at the end of this thesis. The changing output characteristics as a function of the repetition rate is shown in figures 3.12/13.

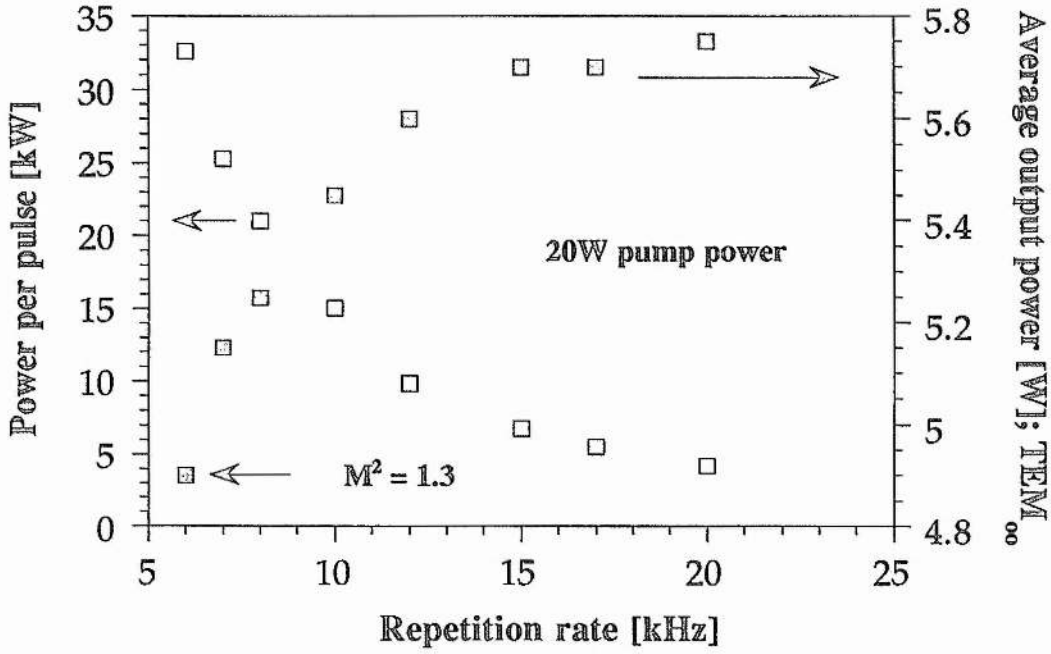

Fig. 3.12: Average output power and peak power per pulse as a function of the repetition rate at 20W diode pump power. The geometrical cavity length is 20cm, the output coupling 30%.

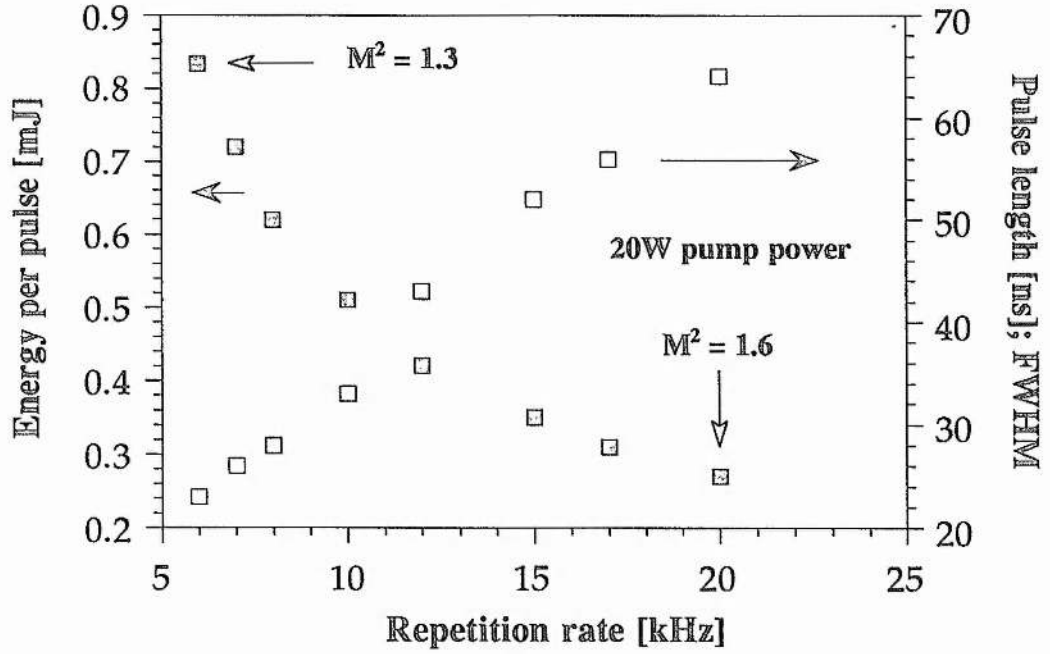

Fig.3.13: Energy per pulse and pulse duration as a function of the repetition rate. Note the beam quality dependence on the repetition rate.

The beam quality reaches its optimum value for low repetition rates. The lower limit for the repetition rate is dictated by the damage threshold of the slab coatings, as discussed in detail previously for the 10W pump power level. This restricts the repetition rate to 6kHz, with 0.8mJ per pulse and a typical pulse duration of 26ns. Pulse forms and durations under the conditions of these high repetition rates are very stable. A single pulse and the overlaid shapes of 124 pulses, sampled over a period of 10 seconds, are shown in figure 3.14.
The repetition rate is 6kHz and the Q-switched output averages 4.8W in near diffraction limited beam quality ($M^2 = 1.3$), linearly polarised at 1047nm.

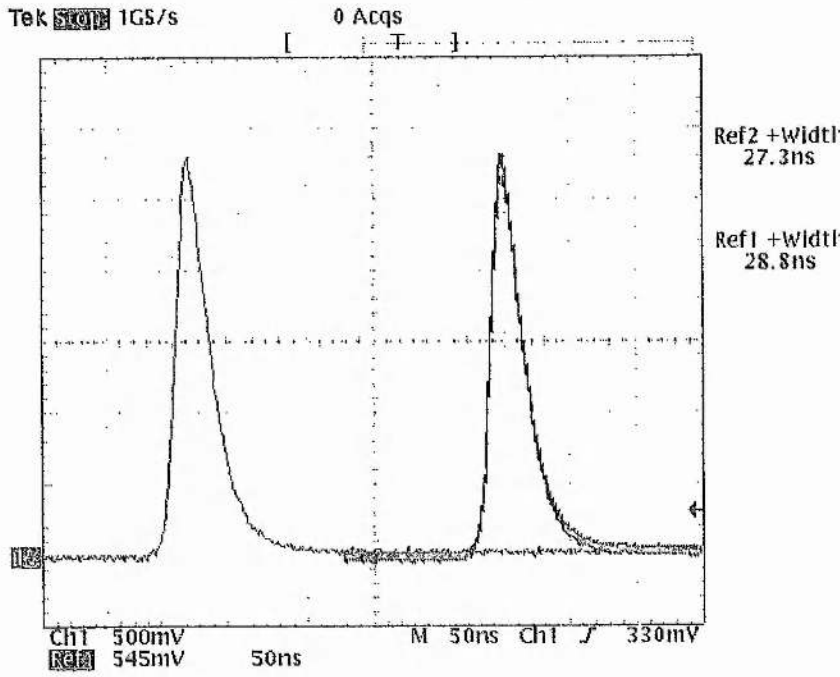

Fig. 3.14: Sampled trace of a single pulse and 124 non-consecutive pulses, observed during approximately 10 seconds (6kHz, 4.8W, M^2=1.3)

These results represent the objective of the laser development which was;

To provide an efficient, high average power, high repetition rate and near diffraction limited, linearly polarised laser source with sufficient peak power due to short pulse durations in the 25ns region.
The combination of these attributes is due to the use of Nd:YLF under high diode pump powers in an end-pumped geometry. This combination, which was previously avoided, due to the low thermal shock parameter of Nd:YLF, was in 1994 state-of-the-art for high repetition rate systems, and found its expression in an invited talk at CLEO 94 [6].

I.E. Optomech packaged this system into a commercial laser system, which was presented at CLEO 95 in Baltimore. A picture of the 'DAYlight' laser is shown below.

Fig. 3.15: *A picture of the commercial version of the laser developed during this thesis and now marketed by I.E. Optomech and Uniphase. The footprint of this laser is, including the cooling and power supply, at a minimum, due to the excellent packaging abilities of I.E.*

Around the same time, in mid 1995, several other manufacturers such as Spectra Physics (fibre coupled, end-pumped Nd:Vanadate system), Schwartz Electro-Optics [7] and Light Solutions [8] (both diode bar, side pumped Nd:YLF systems) had developed similar (Spectra Physics, product stage, Light Solutions; lab-system at the time) or superior systems (Schwartz, lab-system). From the viewpoint of this thesis the side pumped Nd:YLF systems, especially the one developed by Schwartz Electro-Optics, are very interesting and will be discussed in the conclusions of this thesis.

3.3 System limitations and linewidth characterisation

An obvious route to improve the performance of this end-pumped slab system is to shorten the cavity, in order to optimise the pulse duration. An attempt along these lines, by reducing the resonator length down to 11cm, did not succeed, as the resulting pulse-build-up times proved to be too fast for the switching times of the acousto-optical Q-switch. The opening time of the switch is given by the travelling time of the acousto-optical wave to leave the mode-waist region. In the cavity configuration used this amounts to approximately 100ns. This is a direct consequence of the Q-switch material used, which has a high damage threshold but comparatively low ultra-sonic speed of sound (approximately 3km/s opposed to 4km/s ($PbMO_4$) or 5km/s). If the pulse already builds up during the opening phase of the Q-switch, higher losses and bad mode quality in the form of high order modes are the experimentally observed consequences. This limitation is not too great a disadvantage in the current set-up, as the peak power per pulse is already limited by the damage threshold of the slab coatings.

The previously mentioned safe peak power limit of 40kW per pulse for the slabs can be stretched to ~70kW without immediate coating damage. However this grey zone was only an option because one slab had already shown signs of coating damage and total failure of this slab would not have been a big loss. With the present coatings this operational mode is not advisable, especially at higher pump powers.
By pushing the short cavity system with low repetition rates and slightly higher pump powers (12W) to pulse widths below 10ns, a rising edge in the falling flank of the Q-switched pulse starts to appear. This pulse shape is shown in figure 3.16.
This unexpected behaviour could be an indication of a bottleneck effect, either caused by the lifetime of the lower laser level being comparable to the very short pulse durations of around 10ns [9], or a repopulation of the upper laser level, due to relaxation of population from higher excited states, which were previously up-converted by excited state absorption of laser radiation .

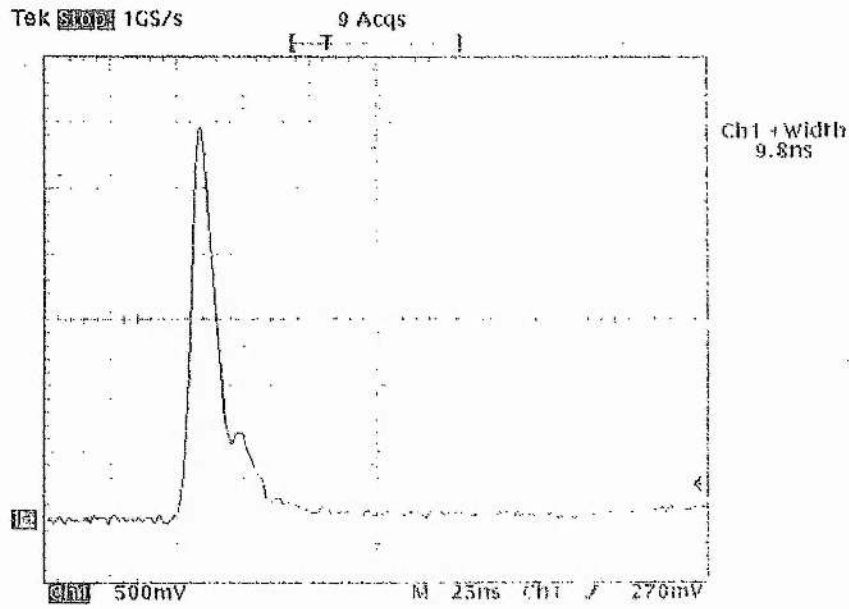

Fig. 3.16: *An unwanted deviation of the pulse shape appears for very short pulses. The rising edge in the falling flank of the pulse starts to appear for pulse durations around 12 - 15ns (see fig. 3.9b). With shorter pulse durations this after-pulse becomes more pronounced, as the 10ns pulse shape above exposes.*

In contrast to this there have been reports of pulse widths approaching 3.5ns at 1047nm in Nd:YLF [10], but without displaying the pulse form. These short pulse results were achieved by utilising extremely short resonator configurations (2 to 3cm) and low cw pump powers, of about 500mW. A comparison of such different systems is difficult, as the form (or even appearance) of an after-pulse also depends on the time dependent intra-cavity losses during Q-switching.
However, in the present system the 10ns pulse width region is clearly a lower limit in terms of pulse duration and could not be circumvented by careful alignment of the Q-switch or cavity mirrors.

Higher pump powers than the 20W so far used lead to a further decrease in mode quality. Pumping at the 30W level represented a system limitation, as the degraded beam quality at this level could not be used to increase the diffraction limited green or UV output. For other applications, such as, for example, material processing, the high average output powers in the 8W region are an interesting alternative. The change of the output power with repetition rate for diode pump powers of 30W is shown in figure 3.17 .

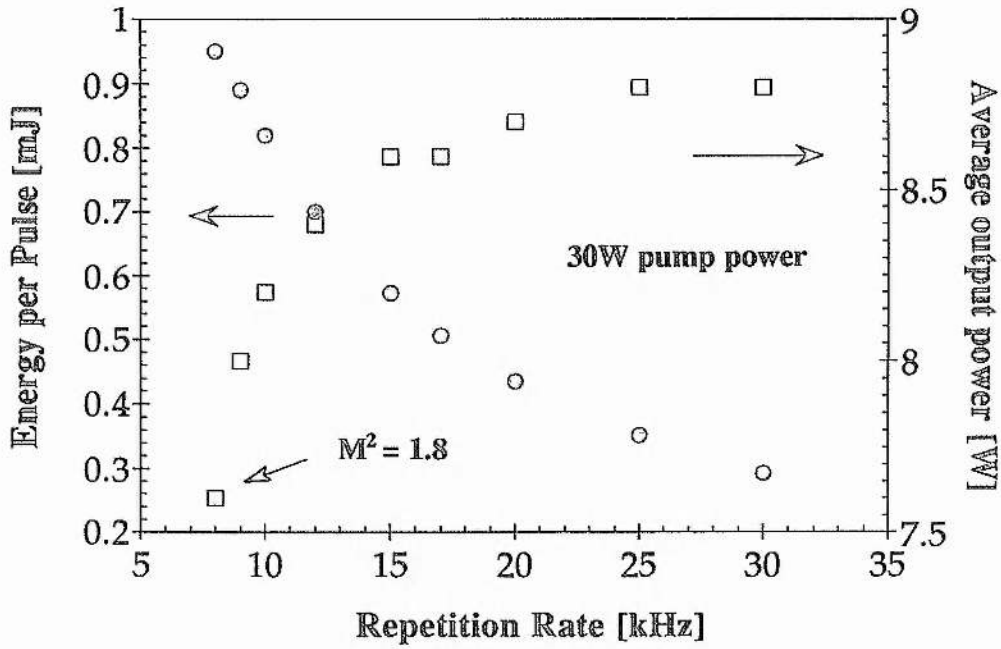

Fig. 3.17: *In the case of 30W diode pump power the beam quality decreases to M^2 = 1.8 at 8kHz. The average output power and peak power per pulse is displayed as a function of the repetition rate.*

Although average powers of up to 8.7W were achieved, the beam quality decreased to an M^2 of 1.8 at 8kHz repetition rate, and the efforts needed to control and maintain these moderate mode properties also increased. This high power operation is an interesting alternative if the beam quality of the fundamental or converted radiation is only of secondary interest. For example, the conversion efficiency for doubling does not necessarily drop dramatically for beam parameters approaching M^2 = 2, so that the advantage of higher average infrared powers at the 30W pump level can be transferred into the converted green radiation.

However, the mediocre beam quality does not improve in the frequency doubled case. This is reflected in the frequency tripling results, where the mixing process of two beams with decreased transversal mode properties notably affects the conversion efficiency into the UV . The details of the single pass doubling and tripling experiments will be discussed in Chapter 6. As the main interest was in near diffraction limited beam qualities, the Q-switched experiments were limited to the 30W diode pump power level. Higher pump powers would only have increased the average output power of the system at

the further expense of the beam quality.
So far the linewidth of the laser system has not been described satisfactorily, as the recorded linewidth of 0.2nm in figure 3.3 is just at the resolution limit of the optical spectrum analyser. Even a single frequency Helium-Neon laser with a linewidth better than 0.002nm (1GHz), did not record a much improved linewidth (~0.15nm), than the definitely multi-longitudinal 1.047μm laser source. To obtain a meaningful value for the 1μm spectrum a Fabry-Perot etalon has been used to analyse the frequency doubled infra-red radiation. Frequency doubling has the advantage of easy control of the Fabry-Perot alignment. The etalon mirrors used have a reflectivity of R=80% in the green, and the separation of the mirrors was 1mm. The short separation was necessary to account for the broad spectrum of the free running laser.
The free spectral range (FSR) of this set-up was 150GHz and, given the finesse of F~14, the resolvable linewidth was 12GHz. Three clusters of longitudinal modes within the free spectral range could be resolved and were imaged with a 100mm lens onto the CCD Camera (figure 3.18).

By switching on a cw background, a generally undesirable mode of operation under normal Q-switching conditions, the fringe pattern could clearly be sharpened. In this self seeded mode of operation, although only improvised, the linewidth could be reduced down to 3-5GHz in the green. The reduction of the hold-off, by detuning the Q-switch away from the Bragg-angle, is a demonstration of the well known line narrowing technique by pre-lasing [11].
No relevant improvement in the spectral brightness could be achieved with this very crude seeding, as the output power drops by at least a factor of two, while the pulsewidth broadens and the pulse to pulse fluctuations strongly increase. However, this improvised line narrowing is of use to characterise and demonstrate the linewidth dependence of OPO's, when pumped with this Q-switched laser operating in the infra-red (Chapter 7).
The main reason for the measurements was to determine the linewidth at 1047nm. Taking into consideration that the fringe pattern was observed in the green, the linewidth of the Q-switched laser is in the region of

~0.1nm (25GHz).

This corresponds to ~35 longitudinal modes about threshold. The strength of the clustering, as observed through the Fabry Perot etalon, can be slightly varied, without introducing after-pulses, and depends on the alignment of the Q-switch. The characteristic three clusters can also be observed in the signal output of a NCPM KTP-OPO, as shown in Chapter 7.

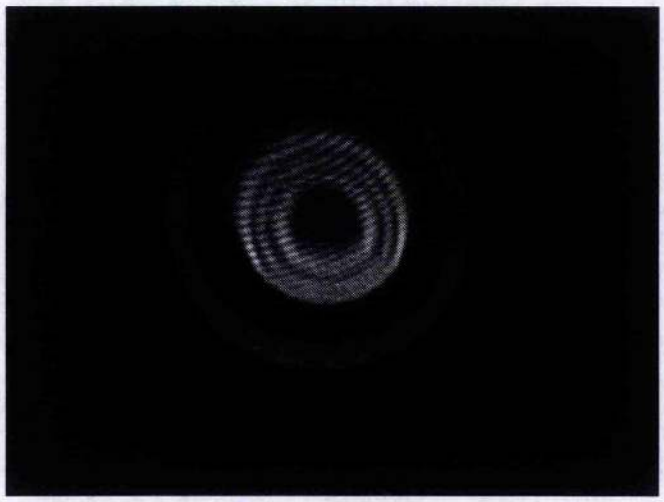

a)

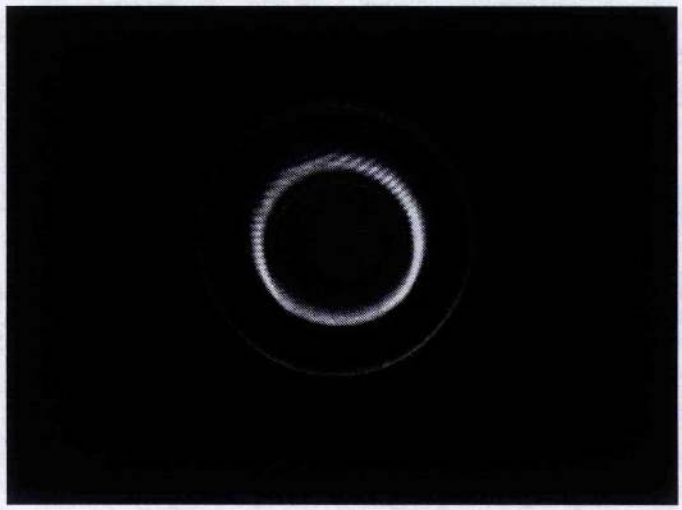

b)

Fig. 3.18: *Fabry Perot fringes of the frequency doubled, Q-switched output (**a**)). The separation between fringes within one spectral range is ≥12GHz. Line narrowing could be achieved by switching on a cw background (**b**)). The reduced hold-off in this case causes irregular after pulses.*

3.4 Conclusions

The cw operation proved that the design aims for the Nd:YLF slabs were reached.

- The poor thermal properties of the material could be compensated for by choosing the right dimensions of the slab, making it feasible to end-pump it with up to 20W per surface (e.g. 40W total).
- The geometry of the slab combines wavelength selection in the anisotropic material and low losses without additional AR-coatings.
- The end-pumped approach ensures high efficiency into the TEM_{oo} mode. An all-optical slope efficiency of 32% into TEM_{oo} has been achieved.

The table below gives a summary of the important experimental results and data.

Maximum output power	Multimode		12W @ 36W pump
	TEM_{oo}	$M^2 = 1.6$	6.2W @ 20W pump
		$M^2 = 1.2$	3.0W @ 10W pump
Slope efficiencies	TEM_{oo}	32%	all optical
		35.5%	absorbed power
	Multimode	36.5%	all optical
		40.5%	absorbed power
Optimum output coupling	10%		10W pump level
	15%		20W pump level
Intra-cavity losses	~2%		near threshold (i.e.: up to 2W output)

Table 3.19: *Summary of the key results and experimental data under cw operation at 1047nm.*

The limitations of the end-pumped approach in a monolithic slab laser, utilising focused linear diode arrays, also became evident. Thermal distortions of the pumped surfaces introduce diffraction losses into the cavity and ultimately limit the maximum achievable TEM_{oo}, as well as multi-mode, output powers.
These aberrations of the thermal lens could not be compensated for by using spherical mirrors. Only the idealised parabolic part of the thermal lensing could be offset by choosing the right curvature and geometrical length of the cavity.

The scalability of these folded resonator geometries is therefore dependent on the pump power density per folding point and the total number of folding points. In the case of the proposed two pump module scheme, the limit was 17W at each reflection point and therefore below the available pump powers. Introducing more folding points by scaling the slab in length would reduce this pump power per folding point further, as the distortions, if uncorrected, add up, so that not too much might be gained. Furthermore, additional degrees of freedom would be introduced, which might render the scheme impractical in terms of alignment. The proposed geometry therefore seems a good compromise in terms of output power and complexity.

The preferred mode of operation is repetitive Q-switching of the cw pumped Nd:YLF laser, as it enhances its capabilities as a pump laser. In particular, the beam quality, which is the most critical parameter of high power end-pumped lasers, is improved, as well as the reliability in achieving this high quality performance.
The combination of pump geometry, laser material and acousto-optical Q-switching are responsible for the positive characteristics of this laser system:

- Short pulses and efficient TEMoo mode operation are a consequence of the end-pumped approach.
- Efficient linearly polarised output at high pump powers, without depolarisation losses, and with good energy storage, leading to short pulses and relatively high energy levels per pulse, are the consequences of the natural birefringence and long upper state life time of the chosen Nd:YLF laser material.
- Unproblematic high repetition rate operation, which is inherent to the acousto-optical switching technique, is reflected in the good pulse to pulse stability of the Q-switched system. The flawless performance of the Q-switch is one of the foundations of the accomplished results.

Depending on the pump power level and resonator configuration, three different modes of operation, optimising either beam quality / pulse duration (10W pump) or beam quality / average power (20W pump) or average power (30W pump) have been investigated. The results and important experimental parameters are shown in the table on the next page.

Maximum output power	$M^2 = 1.8$ 30W pump power	7.6W @.8kHz, 25ns Cavity: $L_{geo.} = 20cm$
Maximum efficiency (i.e.: Best compromise between M^2 and P_{out})	$M^2 = 1.3$ 20W pump power	5W @ 6kHz, 27ns Cavity: $L_{geo.} = 20cm$
Shortest pulses	$M^2 = 1.1$ 10W pump power	1W @ 2kHz, 12ns Cavity: $L_{geo.} = 11cm$
Output coupling	T = 30%	

Table 3.20: *Results and experimental data at characteristic pump power levels for the Q-switching experiments.*

The most restrictive limitation in the present set-up is the coating damage on the Nd:YLF slab. This restricts the safe operating peak power to 40kW per pulse ($80MW/cm^2$ intra-cavity). The onset of coating damage is not clearly defined and this grey zone reaches up to 70 - 80kW per pulse. These levels are possible to sustain for short periods of time. This technical problem should be cured with harder coatings, possibly at the expense of slightly higher losses, which are associated with this type of coating.

Finally, the switching time of the acousto-optical Bragg-cell will set the peak power limit. This is a principal restriction, which can only be lessened by minimising the mode size at the location of the Bragg-cell. However, a resonator set-up approaching the optimised configuration - close to the stability border, with the Q-switch as close as possible to the mirror on which the cavity mode will focus during its transition into the unstable region - is already employed. Therefore, a further reduction of the mode size, and thus switching time reduction, will only be marginal and is also limited by the damage threshold of the Bragg-cell ($\leq 300MW/cm^2$, estimate by supplier).

Despite these restrictions under extreme modes of operation, a reliable, high average power, near diffraction limited, coherent light source has been achieved with the present system.

References

[1]: D. Findlay & R.A. Clay - **The measurement of internal losses in 4-level lasers** - Physics Letters 20, No.3, 277 (1966)

[2]: H. Kogelnik - **Imaging of optical modes - Resonators with internal lenses** - The Bell System Technical Journal, 44, 455 (1965)

[3]: HH. Zensie, E.P. Chicklis, M. Knights & al. - **Non-linear conversion of 1.3μm Nd:YLF emission** - "Tunable Solid State Lasers II" p.364 (Springer, 1986)

[4]: J.R. Ryan & R. Beach - **Optical absorption and stimulated emission of neodymium in yttrium lithium fluoride** - J.Opt.Soc.Am.B 9, No.10, 1883 (1992)

[5]: Z.Y.Ou, S.F.Pereira, E.S.Polzik & H.J.Kimble - **85% efficiency for cw frequency doubling from 1.08 to 0.54μm** - Opt. Lett., 17, No.9, 640, 1992

[6]: C.Rahlff , B.D.Sinclair , W.Sibbett & M.H.Dunn - **"High power end-pumped effects and applications in Nd:YLF at 1047 and 1321nm"** Paper CThG4, Conference on Lasers and Electrooptics, Anaheim, May 1994 Laser Focus World, 30, No. 6, p. 20, (1994) - **Diode-pumped slab lasers operate at high frequencies** -

[7]: J. Harrison, P.F. Moulton & G.A. Scott - **13W, M^2<1.2 Nd:YLF laser pumped by a pair of 20W diode laser bars** - Paper CPD-20, Conference on Lasers and Electrooptics , Baltimore, May 1995

[8]: L. Marshall, A. Johnson & al. - **Efficient 2-5μm KTP, KTA and $ZnGeP_2$ optical parametric oscillators** - Paper PDP14 , Advances in Solid-State Lasers, San Francisco, January 1996

[9]: T.Y. Fan - **Effect of finite lower level lifetime on Q-switched lasers** - IEEE J.QE. QE-24, No.12, 2345 (1988)

[10]: W. Grossman, M. Gifford & R.W. Wallace - **Short-pulse Q-switched 1.3- and 1-μm diode-pumped lasers** - Opt. Lett. 15, No.11, 622 (1990)

[11]: A.J. Berry, D.C. Hanna & C.G. Sayers - **High Power single frequency operation of a Q-switch TEMoo mode Nd:YAG laser** - Opt. Commun. 40, 54 (1981)

C.F. Rae, J.A.C. Terry & M.H. Dunn - **Single-frequency, end-pumped Nd:YLF laser excited by a 12mJ diode laser array** - Opt. Lett. 17, No.23, 1673 (1992)

Chapter IV.

CW and Q-switched performance at 1321nm

Encouraged by the performance of the slabs coated for the 1μm transition, we decided to use the same slab geometry to achieve lasing with the π-polarised 1321nm transition. The initial intention was to double this output into the red, in order to provide an alternative pump wavelength to the frequency doubled 1μm green source. This aim proved to be difficult to realise due to the strong sensitivity of this low cross-section transition to the intra-cavity losses of the Q-switch inserted (~2%), and the disproportionately higher thermal lensing at 1.3μm, as compared to the 1μm transition.

Although good slope efficiencies (23%) and 2.8W at 15W of pump power could be reached, higher pump powers than 15W were only possible if a much shorter resonator configuration than in the 1μm experiments was used. With this short resonator ($l_{geo.}$ = 8cm), up to 3.75W could be extracted for 20W pump power radiation. Subsequent Q-switching was therefore limited to the 10W pump power level due to the geometrical constraints of the cavity components. At this level peak powers of up to 6kW could be achieved, which were too low for efficient frequency doubling of the 1.3μm line [1]. In addition, the limited average output power conditions of the 1.3μm transition could not compensate for the low efficiency doubling process by means of a high repetition rate.

Nevertheless, the opportunity to compare the 1μm and 1.3μm transitions in an identical experimental set-up was important, and has been investigated in some detail. A comparison of the 1321nm transition with the 1047nm line [2,3] is still

of interest as there is not a lot of published information about the use of the 1.3μm lines in Nd:YLF in cw or Q-switched diode pumped systems.
Of particular practical concern in this system are the disproportionately higher thermal lensing values of the Nd:YLF slab under 1.321μm operation, as well as the wide linewidth of the Q-switched emission (up to 1nm), as compared to the 1μm operation. The higher heat load under lasing conditions could be attributed to a reabsorption of the laser wavelength, this being detectable as it is part of an upconversion process, involving the upper laser level $^4F_{3/2}$.
The spectroscopic measurements which are necessary to characterise these fluorescence effects are incidentally greatly helped by the polished cooling surfaces of the slab, a design criterion originally added to improve the fracture resistance. This gives excellent optical access to the pumped and unpumped parts of the folded resonator path within the crystal. These first indications of a different up-conversion and loss behaviour at 1.3μm led to a detailed comparison of up-conversion processes between 1 and 1.3μm operation in Nd:YLF, as presented in Chapter 5.

Although this thesis does not present any applications in non-linear optics for the 1.3μm source, its main benefit was to force a more detailed investigation of the above characteristics, resulting in guidelines for a hopefully improved diode end-pumped, repetitively Q-switched 1.3μm source at a later date. This is discussed in the conclusions of this chapter.

4.1 CW performance and thermal lensing of the 1321nm transition

Figure 4.1 shows the output power with changing pump power under the condition of an optimised output coupling of 3% transmission for two different resonator lengths.

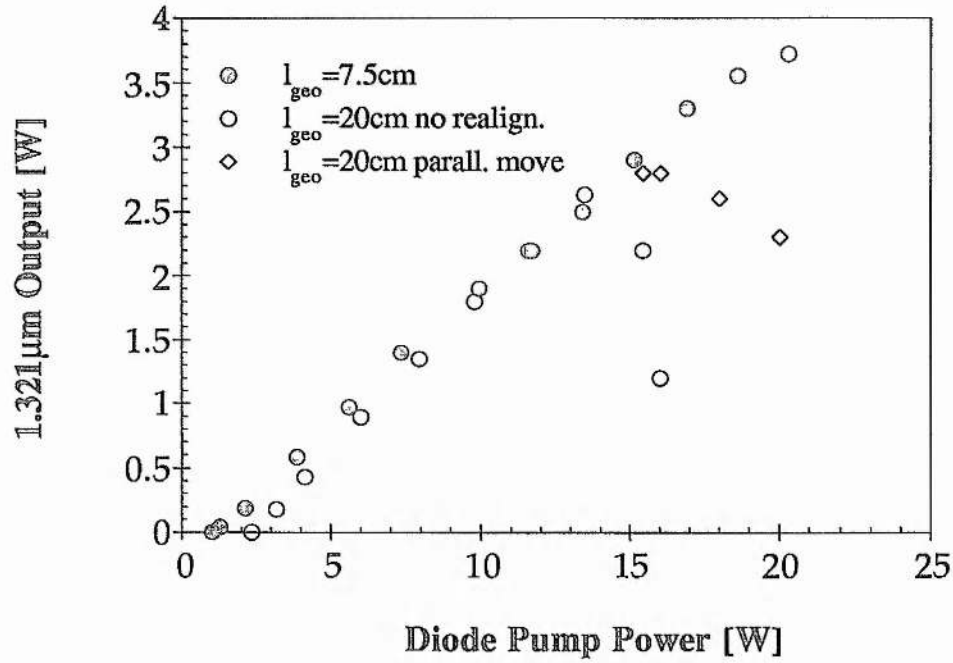

Fig. 4.1: *Output power and instability of the standard longer resonator geometry (l_{geo}: 20cm) under 1.3µm operation in comparison with an extended pump power range, stable, short resonator ($l_{geo.}$: 7.5cm). A parallel realignment (fig.4.6) of the pump modules can change the output power between the two extremes, for the longer, partly unstable resonator.*

The above figure, 4.1, summarises the high thermal lensing encountered under 1.3µm operation, as well as the strong dependence of the overall thermal lensing on the alignment of the cavity. Despite a good slope efficiency of 23%, and a maximum output power of 2.8W at 15W pump power, when using the standard 20cm cavity (figure 2.15), it was not possible to pump with higher diode powers without experiencing the output power drop shown.
At first this power drop was wrongly attributed to pump power introduced losses, which would have a stronger influence on the smaller crossection transition at 1.3µm. This high sensitivity to changing round-trip losses is shown for the case of varying output coupling losses in figure 4.2.

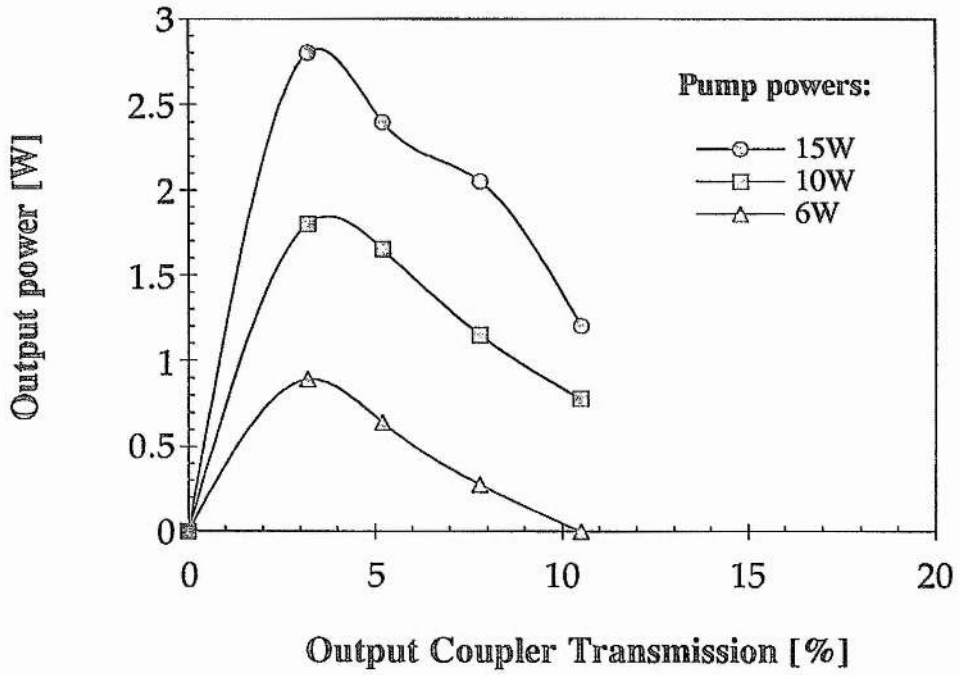

Fig. 4.2: Output power as a function of the transmission of the output coupler for different pump power levels. The cavity is of the standard geometry displayed in figure 2.15 ($l_{geo.}$ = 20cm).

A small variation of only a few percent from the optimum output coupling loss (~3%) leads to a pronounced drop in 1.3µm output coupling. A comparison of this with a possible variation of ± 5% around the optimum output coupling of 15% at 1047nm, which does not change the output power dramatically (it is a less than 10% drop), caused the wrong interpretation of the pump power induced losses which cause the power drop in figure 4.1.

Later results suggest strongly that the 1.321µm operation in Nd:YLF gives rise to a much stronger thermal lensing than for the 1µm transition. The considerable rise in the thermal lensing coefficient from 0.3 diopters/Watt pump power (@ 1µm) to 0.7 diopters/Watt (@1.3µm) is totally unexpected, as the positive lensing in Nd:YLF is entirely dependent on the mirror-like deformation of the pumped surfaces.

However, the higher thermal load obviously present during 1.3µm operation is a bulk effect and it is remarkable that this bulk effect (with a negative dn/dT) does have such a strong influence on the surface deformation. The higher lensing coefficient at 1.3µm was for this reason not expected or recognised in the earlier stages of these experiments.

Subsequent shortening of the cavity down to 8cm removed the instability at 15W pump power, and a cw output of 3.75W multimode at 20W pump could be extracted (fig. 4.1). Given the very short cavity length necessary to maintain stability, Q-switching at high powers is difficult due to the limited available free space for the Q-switch. The minimum cavity length including the Q-switch is about 10cm.

Measurement of the thermal lensing coefficients was done by utilising the 'instability-method', as has been described earlier in Chapter 2. The main advantage of this method is that it measures the thermal lensing under the actually chosen operating conditions, by utilising the laser emission as the test beam. This is a very important point, as the thermal lensing depends heavily on the alignment of the resonator path towards the pumped, and lensing defining, surface of the Nd:YLF slab. The strong dependence of the measured thermal lensing on the alignment will be demonstrated after the actual thermal lensing measurements.

In order to standardise the operating conditions, no substantial realignment of either mirror or pump module orientation was allowed, after an output power optimised set-up at low to medium pump power levels (3 to 5 Watts) was found. To reach the instability border at different pump power levels, the longer arm of the resonator configuration was varied between 25cm and 4cm, resulting in a total geometrical length of 29 to 8cm for the cavity. A sketch of the resonator used is shown below.

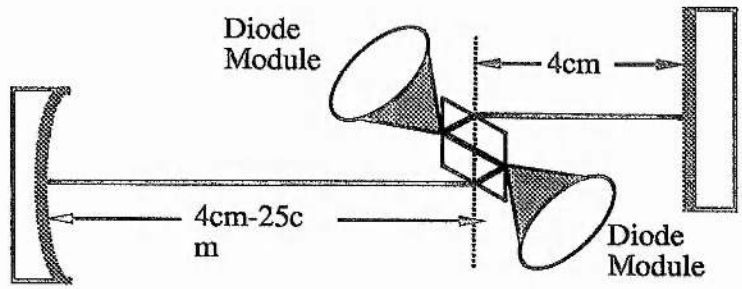

Fig. 4.3: Sketch of the resonator configuration. With an increasing arm length, a, the pump power necessary to reach instability will decrease.

Dividing the pump power at instability by a lensing value determined through an ABCD formalism, results in an average lensing coefficient for a range of values, a. This averaging is based on the assumption that the lensing strength, dominated by the distortion of the surface, scales linearly with the pump power, as has been shown in greater detail in the 1µm lensing section, and is again confirmed by these experiments . The coefficient so determined is

$$\zeta = \frac{D}{P_{dp}(D)} \qquad \zeta_{1321\text{nm}} = 0.7 \text{ diop./W} \tag{4.1}$$

This value is surprisingly large if compared to the lensing coefficient of $\zeta_{1047\text{nm}}$ = 0.3 diop./W earlier determined. The expected proportional rise, due to the reduced efficiency of this low cross-section transition resulting in an increased heat dissipation at the same pump power level, would give rise to an expected lensing coefficient, ζ^*_{1321nm} of

$$\zeta^*_{1321nm} = 0.43 \text{ diop./W} < \zeta_{1321\text{nm}} . \tag{4.2}$$

This can be estimated by relating the lensing strength, D, at the stability border, not to the pump power as in eqn. (4.1), but to the heating power ($P_{dp}(D)$ - $P_{out}(D)$). The lensing coefficient, ζ^{heat}, so defined should be largely independent of efficiency changes induced either by intracavity losses of the 1µm, or the change to a lower cross-section wavelength, as it is the case with the 1.3µm transition.

$$\zeta^{heat} = \frac{D}{P_{dp}(D) - P_{out}(D)} \qquad \zeta^{heat} = 0.43 \text{ diop./Watt} \tag{4.3}$$

Where the different parameters are given as follows:
D := Diopter value at stability border, which depends on the cavity geometry
$P_{dp,\,out}$ (D):= Diode pump power and laser output power at the stability border

Knowing the output power as a function of the pump power (fig. 4.1 ; i.e. 1.8W for 10W_p) defines the heating power, and thus the expected lensing value under these pump conditions according to δ^{heat}, resulting finally in the estimated value δ^*_{1321nm} for 1321nm operation in (4.2).
The fact that this value strongly underestimates the measured lensing indicates that the heating mechanism under 1.3µm operation is more efficient than that

under 1μm operation. Keeping in mind that the heating mechanism is a bulk effect, while the measured positive lensing is entirely dependent on surface effects, this suggests that the bulk heating effect under 1.3μm operation is probably spatially different, in order to induce the non-proportional rise (if related to δ^{heat}) in the lensing values. This postulated explanation will be backed up by the reabsorption evidence at the end of this chapter.

Being aware that a basically totally different (by a factor of more than two) lensing coefficient at 1.3μm will be definitely questioned with regard to its correctness, the very clear evidence of this abnormal lensing is shown below, again in terms of the simple measurement of output power behaviour for different cavity geometries.

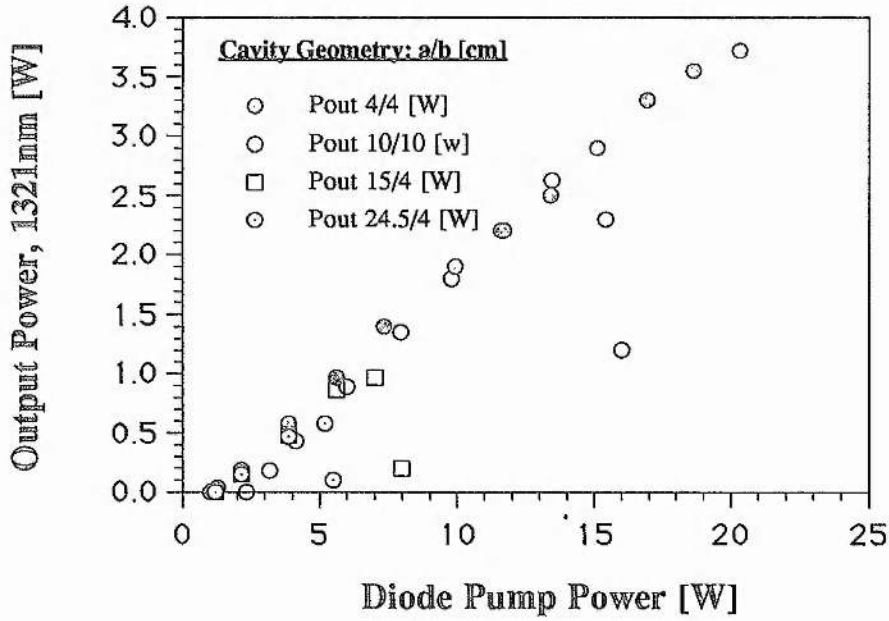

Fig. 4.4: *The different pump power values needed to reach the instability border, due to a change in one of the cavity arm lengths (see fig. 4.3), which defines the transition value for an unstable round trip condition.*

In comparison with the 1μm transition it is obvious that the instability, measured by the power drop, at 1.321μm is reached far earlier. The standard 20cm long cavity (15/5cm), if used for the 1047nm transition, is stable without pronounced realignments for pump powers past 25W. Whereas, under 1.321μm operation, significant realignment becomes necessary even in the 6W diode pump power region (fig. 4.6). This is significant, as the slab geometry, the resonator dimensions, and, more importantly, the slab cooling conditions as

well as the pump modules, all of which define the thermal lensing conditions, are identical.

The only source of error is the strong dependence of the measured lensing on the resonator path with regard to the pumped slab windows. To minimise this error only 'minimal' realignment during this thermal lensing measurement was allowed. The high thermal lensing at 1.321μm and the strongly localised surface deformation, makes it an ideal transition to demonstrate the influence of the alignment on the lensing behaviour, and to describe the term 'minimal realignment', as often used before in the 1.047μm and 1.321μm lensing chapters.

Given the high pump powers available in this end-pumped scheme, deviations from the output power optimised zig-zag path were possible, as there was enough gain to support non-optimum mode matched paths. The penalty of higher losses at the Brewster windows and reduced extraction efficiency was balanced by reduced thermal lensing. As in the 1047nm chapter, the additional losses caused by lens aberrations at high pump powers can be even higher than the above losses of moving away from ideal mode matching. This resulted in general in a reduction of the lensing coefficient, if the alignment was optimised for output power, the higher the pump powers were.
Two alignment moves were used to cause deviation from the optimum mode matched alignment. Either by:

- tilting the resonator path in the plane of the paper in figure 4.5 through mirror rotation, while keeping the pumped volume fixed within the crystal, or by
- translating the pump modules in parallel to the pumped slab window, while keeping the resonator path fixed.

To simplify the measurements and interpretation, parallel displacement of only one pump module was chosen to demonstrate the alignment sensitivity of the end-effect governed lensing. The second pump module was not used during these experiments. Figure 4.6 shows the comparison between a short cavity (8cm), stable over the whole pump power range with longer cavities (20-28cm), where the parallel displacement was used to maintain stability. This displacement in the case of the longer cavities reduced the positive thermal lensing, and subsequently also reduced the extraction efficiency.

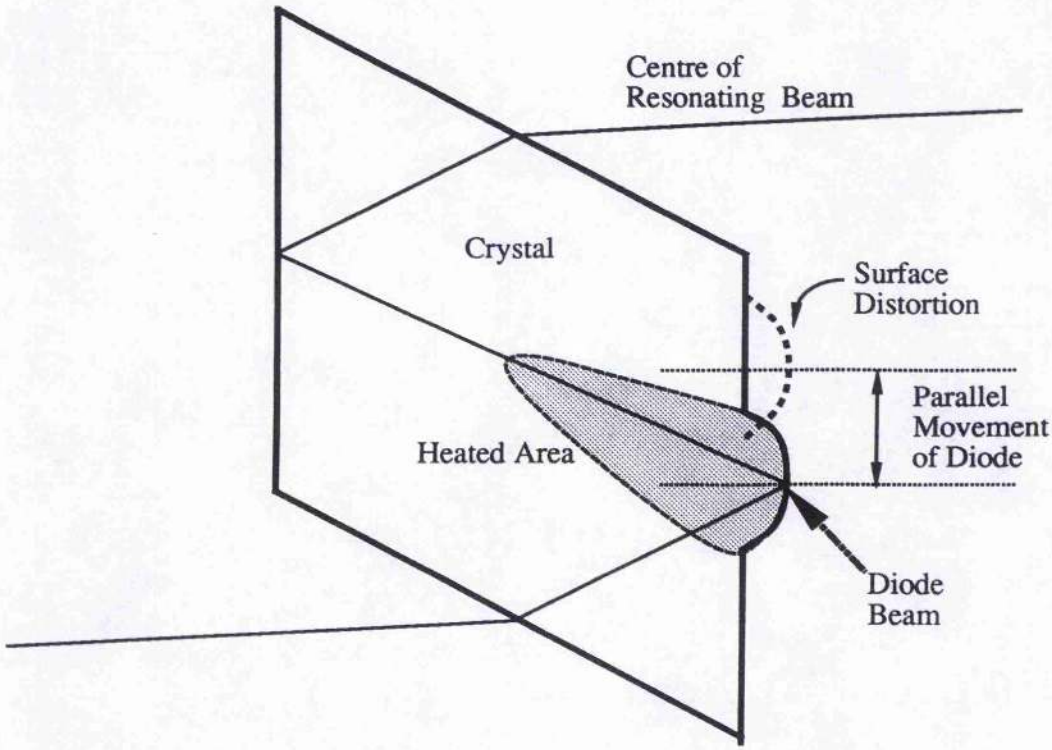

Fig. 4.5: *Sketch of the Nd:YLF slab with the parallel movement chosen to misalign the optimum mode matched set-up. The displacement needed to maintain stable round-trip conditions with rising pump powers is a centre to centre measurement of the respective gain profiles, as measured by the translation stage in the pump module.*

The ability to maintain stability for almost any cavity geometry and pump power level, by reducing the positive lensing component caused by surface deformation, highlights the problem of describing thermal lensing in high pump power end-pumped configurations in general. This thesis takes the practical approach, that relevant thermal lensing coefficients describe the system under beam quality and output power optimised conditions. A deviation from the optimised situation is always accompanied by a drop in the slope efficiency and substantial realignment of the cavity in general, or the pump module in this specialised case.

In this context the extraordinarily high lensing coefficient at 1321nm, of 0.7diopters/Watt, makes more sense, as this low gain transition is strongly dependent on an optimum mode matched alignment. It is thus especially affected by any localised surface lensing mechanism, which is unfortunately enhanced by a spatially selective reabsorption process close to the pump window.

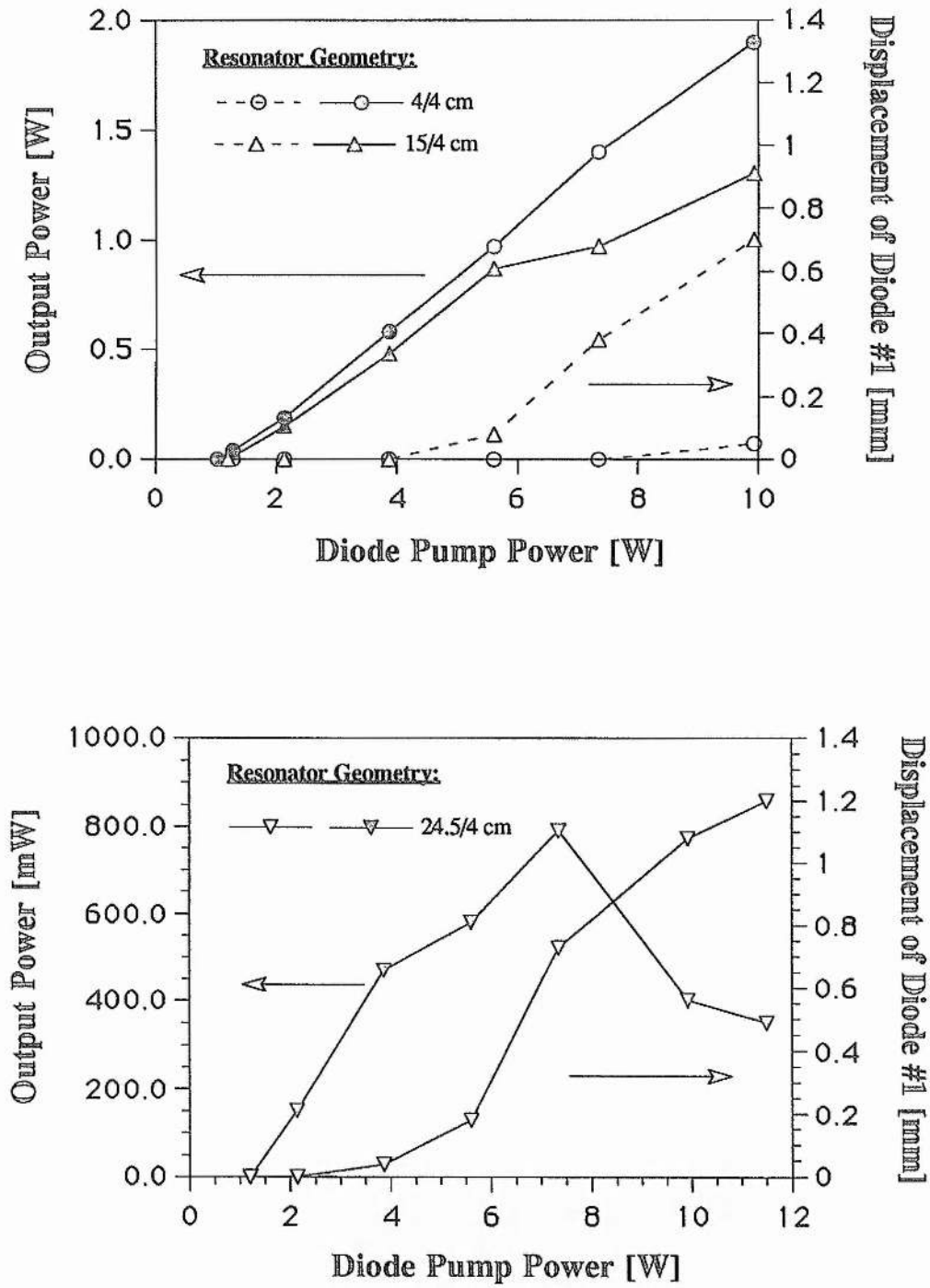

Fig. 4.6: *Output power and displacement of diode pump module No.1 as a function of the pump power for three different cavity lengths. The shortest cavity is stable under optimum mode match conditions, while the longest cavity becomes unstable for these conditions at pump powers around 5 to 6W.*

The above figures also illustrates that 'minimal realignment' corresponds to movements of the pump modules in the region of 0.2mm. Above minimal realignment, the displacement needed to compensate for higher pump power induced lensing values (6 to 10W pump power region, 28.5cm cavity in fig. 4.6b) rises dramatically. The localised positive surface lensing-effect becomes obvious at higher pump powers (above 10W in fig. 4.6b), as then the surface deformation is practically removed from the reflection point on the pumped surface. At this stage the mode overlap factor rapidly decreases, as shown in the quick drop in output power (8 to 12W pump, fig.4.6b). The levelling out of the displacement necessary at around the 1.2mm mark (centre to centre) is in reasonable agreement with the earlier temperature measurements along this line in Chapter 2 (fig. 2.7). Both experiments confirm that the affected (heated and distorted) area is considerably larger than the fluorescence spot size diameter in the plane of the parallel movement (integrated fluorescence profile diameter in the direction of the pump is 1.2mm in this plane) .

This is only one of the problems, which in this case can be solved with reasonable care, in determining the lensing value. Not addressed during this thesis was the characterisation of anisotropic lensing in Nd:YLF, which is likely to depend on the pump spot geometry. The problems are then even greater than before. While the Brewster windows introduce the first and only defined astigmatism [4], the two thermally induced mirrors within the folding section complicate the situation drastically. The resulting astigmatism of these surfaces is very likely to depend on the following:

- pump spot astigmatism (circular or elliptical fluorescence profile),
- pump power level
- laser transition and
- alignment of both pump modules towards the folding points inside the slab.

With anisotropic expansion coefficients along the a and c-axes, astigmatic lensing in flash lamp pumped as well as diode-pumped YLF is generally the rule, as was reviewed in the conclusions of the 1.047nm chapter. The astigmatism for the laser developed during this thesis was always controllable by parallel movements (fig. 4.5) of the pump modules to an extent that, for example, frequency doubled beams in the green could be propagated over a distance of 3 meters without losing their circularly symmetric appearance. This warrants the use of an isotropic lensing value throughout this work, although this is clearly not a general property of lensing in Nd:YLF.

However, generalised and valid thermal lensing coefficients for high power diode end-pumped solid-state lasers are very difficult to come by, as has been illustrated above and in the earlier lensing characterisation of the 1047nm transition.

To complicate matters further, pronounced astigmatism complicates thermal lensing measurements even more, as the field component with the higher lensing coefficient reaches unstable round-trip conditions earlier than its orthogonal counterpart. This is a well known fact for flashlamp pumped Nd:YAG systems. Stress birefringence introduces anisotropic lensing coefficients for the radially and azimuthally polarised components, where the radial component is subjected to a 20% higher lensing [5,6] than its azimuthally polarised counterpart. This behaviour introduces further complications and error margins in determining the stability border for thermal lensing measurement purposes. Figure 4.7 shows such a split in the output power curve of a flashlamp pumped Nd:YAG rod laser approaching the stability borders at different pump power values.

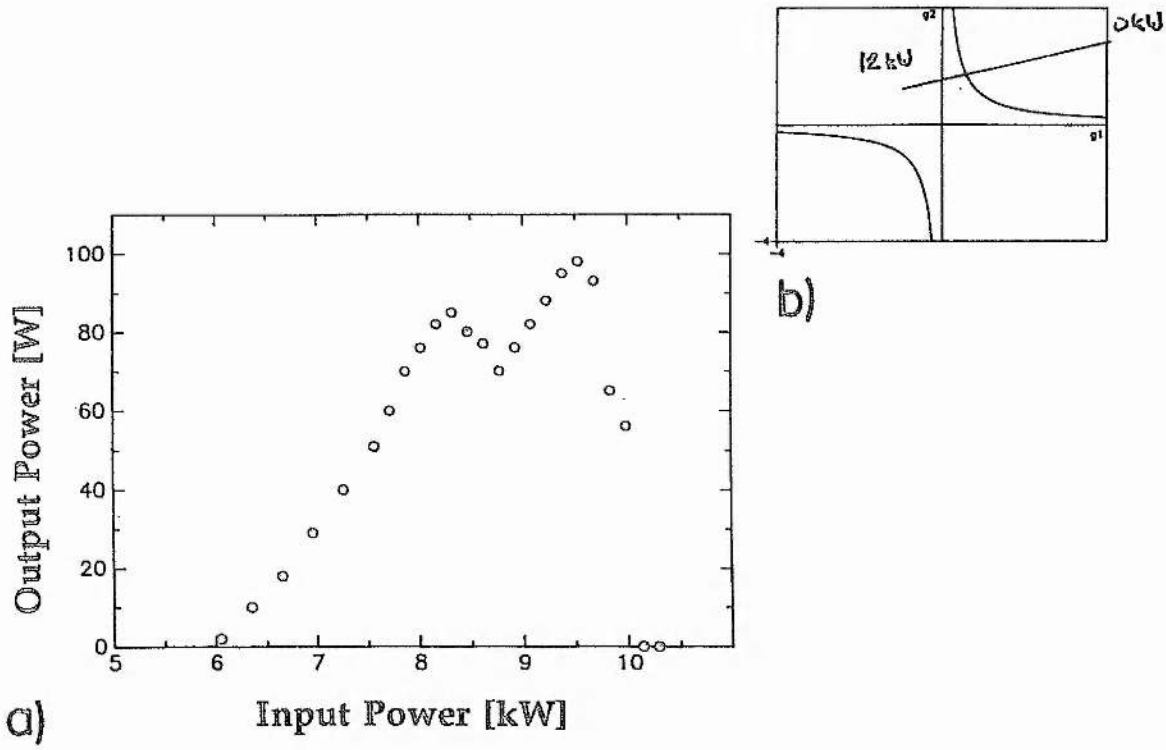

Fig. 4.7: The two local maxima in the output power curve [6] (a)) while approaching the stability border in the first Quadrant of the g-diagram (b)). The ratio of the input powers at these maxima agrees well with the expected refractive power ratio $D_r/D_\Phi = 1.2$ (assuming linear scaling of D with P_{in}).

The absence of any intermediate and resolvable power drops when coming near to a stability border in the diode pumped Nd:YLF slab experiments, at both wavelengths, emphasises that anisotropic lensing with refractive power ratios of D_a/D_c (@1047nm) = 1.8 [7] can be avoided by a combination of chance (in having the 'suitable' pump spot ratio and gain material geometry) and a well chosen degree of freedom in the alignment of the pump module towards the pumped slab surface.

The disproportionately high thermal lensing values at 1.321µm causes practical problems with the components available for the Q-switched cavity. An alternative to the existing cavity design in order to ensure stability and sufficient room for the cavity components during later experiments with higher pump powers than the 10W used here would be:

- A reduction of the stable pump power band, by using a cavity which reaches stable conditions only at higher pump powers. This cavity would still be situated in the 1st. quadrant of the stability diagram.
- Making use of the stability area in the 3rd. quadrant of the g-diagram under higher pump powers. This method would maximise the stable pump power band, having an unstable region only during the cross over from the 1st. to the 3rd. quadrant.

Both methods are unproblematic in view of cw operation. Using the 3rd. Quadrant of the stability diagram avoids in general very short cavities, which might cause problems due to space restrictions.

With regard to optimising Q-switch operation, the shortest possible cavity is the most desirable solution for reducing the pulse width of the 1.3µm laser system. For this reason the first suggestion, using cavities within the 1st. Quadrant of the g-diagram, is going to be the preferred configuration. Optimising the switching time of the acousto-optic device, damage thresholds permitting , can be achieved by operating near to the stability borders, which are at the transition to the 2nd. or 4st. Quadrant. This results as before in the earlier, but longer set-up, with a small intra-cavity beam diameter at the position of the Q-switch, if it is placed within the longer arm of the cavity close to the high reflecting and now of convex curvature cavity mirror. Switching time restrictions, as in the 1µm operation, are not an issue, as the pulse build up time is greatly increased under operation of the low gain line at 1.3µm. In order to secure enough high cavity Q time during each Q-switch cycle, the opening time of the pulse generator was increased to typically 4µs, instead of the standard 1µs under 1µm operation. An insufficient opening time of the Q-

switch leads to incomplete Q-switching or even halving of the pulse repetition rate, as compared to the driving frequency of the pulse generator.

Using identical slab geometries, pump conditions and resonator set-ups (at least at low pump powers) for the 1 and 1.3μm transitions makes a relative comparison of the cross-sections easy by utilising the Finlay-Clay method and comparing the slope efficiencies of both transitions. According to this the ratio of the cross-sections, σ, is:

$$\sigma_{1047}/\sigma_{1321} = 5.2$$

The losses of the Nd:YLF slab with the 1.3μm coating are ~2% (round-trip) and thus comparable with the earlier results of the 1μm slabs. The Q-switch coated at 1.3μm added another 2% round-trip loss to the cavity. These additional losses, comparable to the optimum output coupling in the cw case, were a severe limitation to the Q-switched 1.3μm operation, and incurred an output power drop by a factor of almost 2 as compared to the cw cavity without the Q-switch. Given the limitations of the coated Q-switch under Bragg-angle, a Brewster-cut Q-switch for the cavity field, which is polarised anyway, would be a better solution in a future improved set-up. To achieve the desirable round trip losses of less than 0.5% it might also be advisable to change the Q-switch material. According to Isle Optics the advantage of higher damage thresholds has been traded against increased scattering losses within the SF6 glass(extra dense flint glass). The traditional Q-switch material Lead Molybdate might be a better approach, damage threshold limitations permitting. An additional advantage of $PbMO_4$ is the slighter faster switching times (~25%), as compared to the used flint glass Q-switch.

A closer look at the Finlay-Clay measurements shows that the threshold power over the logarithm of the output reflectivity shows a deviation from the expected straight line for very low values of output coupling (T≤ 2%), as shown in figure 4.8. This is uncharacteristic behaviour for the losses of a diode end-pumped laser. The general problem of varying losses during a Finlay-Clay measurement set has already been addressed in the 1μm chapter. In general, constant losses are only present for low pump powers, corresponding to low output coupling, while pump power induced losses become increasingly

detectable at high output coupling.

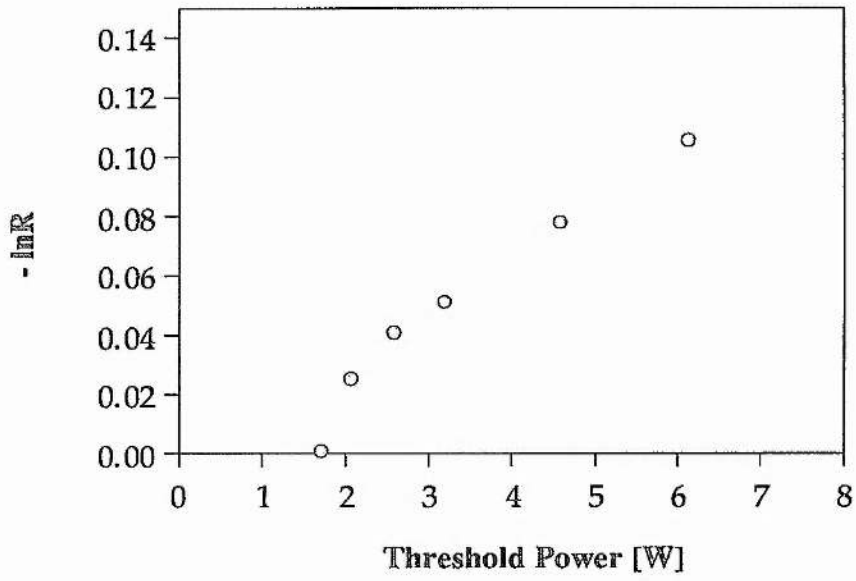

Fig. 4.8: Finlay-Clay diagram for the 1.3μm Q-switch cavity. The Q-switch, when inserted, causes an additional round-trip loss of 2%, as compared to the cw cavity. The deviation from the expected linear relation between the threshold pump power and -lnR for high intracavity intensities (low output coupling) is unexpected, when compared to the 1μm experiments.

The deviation from the straight line for low output coupling could be interpreted as higher losses under high intra-cavity intensities, which might be caused by a reabsorption of the 1.3μm wavelength in Nd:YLF. The threshold measurements at low output coupling were repeated several times , to ensure that the higher than expected values were reproducible.

A clearly visible indication of reabsorption problems with the lasing transition at 1321nm is the visible fluorescence along the unpumped paths of the Nd:YLF slab. This weak fluorescence signal, together with the strong fluorescence in the pumped region, traces along the whole folded resonator path, as long as the cavity is aligned. Figure 4.9 shows this reabsorption in the unpumped path of the Nd:YLF.

The fluorescence along the unpumped path is only a property of the 1321nm operation. The 1047nm transition exhibits different up-conversion behaviour in the cw as well as the Q-switched case. A discussion of the different up-conversion mechanism under Q-switched operation is given in the next chapter, including a spatial as well as a time resolved spectral analysis of the fluorescence signal. These experiments will verify that the upper laser level,

$^4F_{3/2}$, is the lower level of the up-conversion process by reabsorption of the 1321nm radiation, and that this process scales linearly with the intra-cavity intensity.

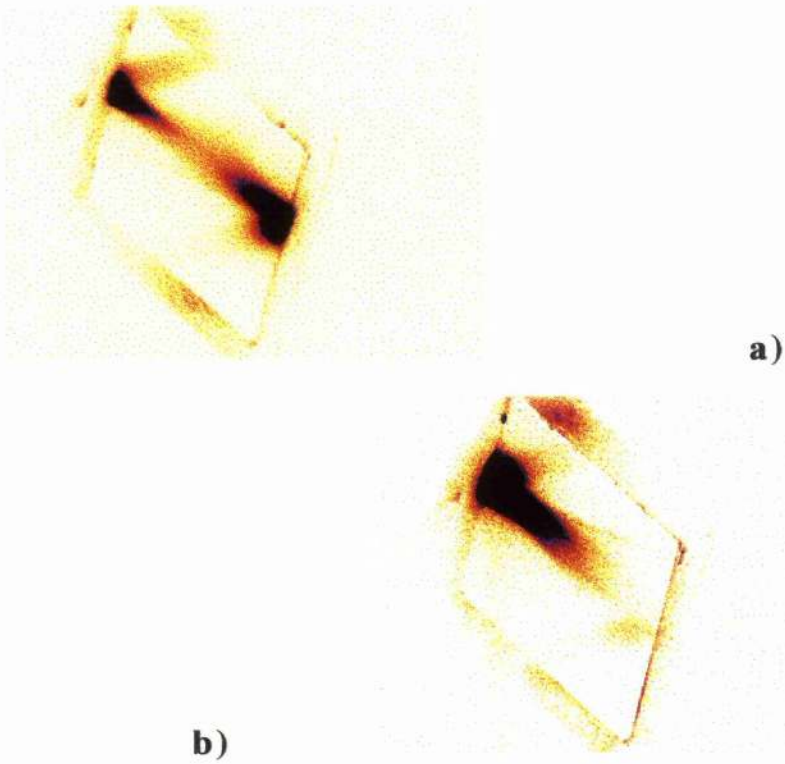

Fig. 4.9: *The mainly green-yellow fluorescence under cw 1321nm operation traces the whole of the folded resonator path under aligned cavity conditions (**a**)). Even under single sided pump conditions is a fluorescence signal on the opposite side of the slab detectable (**b**)).*

The significance of the fluorescence in the indirectly pumped area is that only scattered pump radiation can contribute to any of the population necessary to maintain the up-conversion process.

Another experiment to demonstrate the reabsorption is to detect the laser emission at threshold pump levels and very low output coupling (HR≥99.9%), in order to achieve high intra-cavity intensities. Reabsorption should give rise to output oscillations, due to the increased losses, as soon as threshold is reached. A periodic off-on behaviour, with the typical spiking of the laser output during the on-periods, could be recorded. However, most of these traces showed a 50Hz period (or multiples of it), probably stemming from the output fluctuations of the diode driver, making these measurements not

significant. With the stability of the pump diode output questionable, no further time was spent in changing output coupling and intra-cavity losses to possibly get around this problem.
The measured higher thermal lensing coefficient and the reabsorption problem at the laser wavelength, as indicated by the fluorescence behaviour, denotes the higher thermal load present during 1.3μm operation. As a final consequence, the thermal stress induced breakage limit under lasing conditions should be lower than in the 1μm case.
This effect appears not to be of practical concern, as beam quality degradation limits the useful pump power range to a maximum of ~20W (as compared to ~30W for the 1047nm transition) for 1.321 μm operation in the present set-up , while up to 40W pump power under non-lasing conditions are possible. However, as mentioned before, the diopter value per Watt heating power for 1.321μm lasing operation is comparable to the non-lasing diopter value, which is by definition per Watt heating power, as there is no laser output in the energy balance. This can be explained by a change in the spatial heat deposition due to the reabsorption under 1.3μm lasing conditions, as compared to the heating mechanism at 1μm, which are each responsible for the lensing value.

Up-conversion as the source of the additional heating effect resolves the somewhat paradoxical situation of a higher heat load being generally a bulk effect, which, with a negative dn/dT, increases the negative lensing, while any increase in the positive lensing is only due to a dominant surface effect with a positive expansion coefficient. With the up-conversion process being dependent on the population of the undepleted upper laser level, $^4F_{3/2}$, and scaling linearly with the intracavity intensity, this will shift the additional heat load further towards the surface of the pumped window. It thus deforms the pumped surface more effectively than the same amount of additional heating in the centre of the crystal.

This unusual behaviour could lead to a reversal of the well known effect in flashlamp pumped systems, that laser materials, i.e. Nd:Glass, which are operated close to the thermal fracture limit, fracture if the cavity is blocked, due to the increased heat load. In diode end-pumped Nd:YLF operated at 1.321μm, unblocking the cavity under pump power conditions close to the fracture limit, and then achieving laser action, could fracture the crystal. This is in spite of the reduced total heat load, but with a now more critical spatial distribution, which increases the surface stresses on the pumped crystal facets.

These increased surface stresses are documented in the disproportionately higher thermal lensing values of Nd:YLF under 1.321μm operation, as measured before.

Only some effects of the up-conversion in the 1.321nm cw-operation in Nd:YLF have been mentioned here. More about the influence of the up-conversion processes under Q-switched operation on the intracavity losses, effective upper laser level life time and transverse mode control will be discussed in detail for the 1 and 1.3μm transitions in the next chapter.

4.2 Q-switched performance and linewidth attributes at 1321nm

The Q-switched performance has been hindered by the high insertion losses of the Q-switch, as mentioned before. Due to the higher thermal lensing at 1.321μm, and the restrictions on the cavity length, only pump powers of up to 10W total diode pump power was used. The alternative cavity designs mentioned above have been not realised, as the extra expense of the required mirrors and for a Brewster angled Q-switch were still questionable, in view of achieving a more suitable pump laser performance (i.e. higher energies and shorter pulses). The main focus of the 1.3μm work carried out has therefore been a characterisation of this wavelength in comparison to the better known 1047nm transition.

Figure 4.10 shows the characteristic energy per pulse and average power curves as a function of the repetition rate. The optimum output coupling for this experiment was T~3%. No coating damage to the slab was encountered for repetition frequencies down to a 500Hz repetition rate.

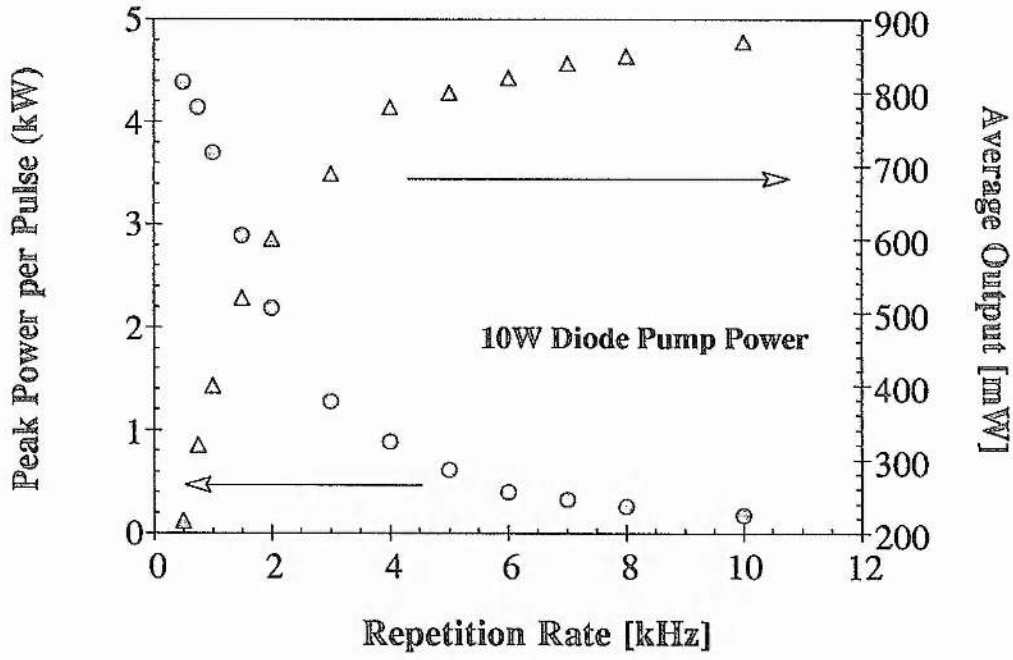

Fig. 4.10: *Average power and energy per pulse as a function of the repetition rate. The geometrical cavity length is 15cm and output coupling transmission, T~3%.*

The shortest pulse length at 500Hz repetition rate was around 80 to 85ns FWHM for the 15cm long cavity. Shortening the cavity down to 10cm reduced

the pulse width, by approximately a factor of 1/3, as expected by the length ratio of the two cavities. These shorter pulse durations made peak powers around 6kW at 1kHz possible. The changing pulse width as a function of the repetition rate range for both cavities is shown below.

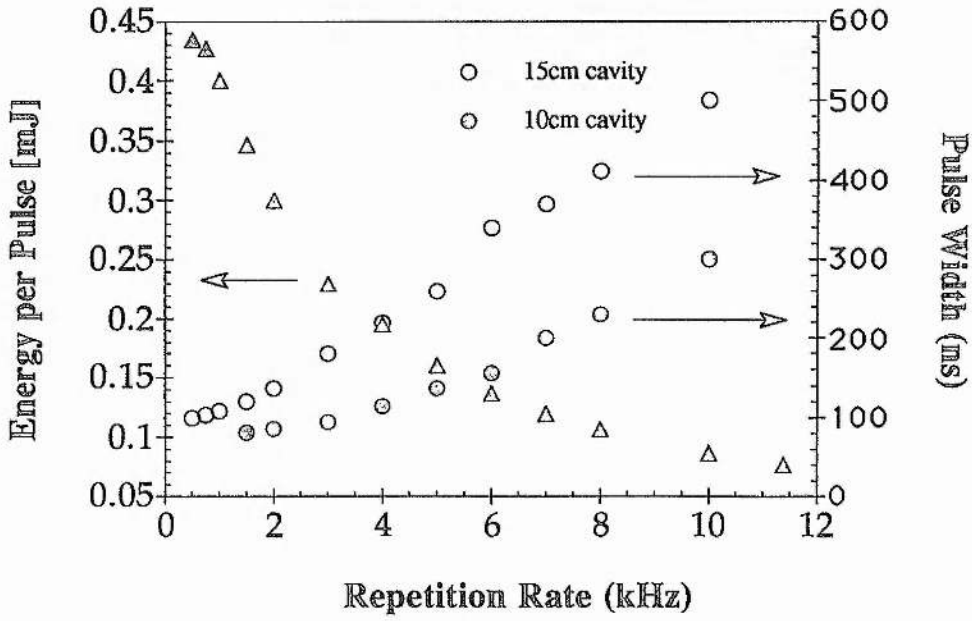

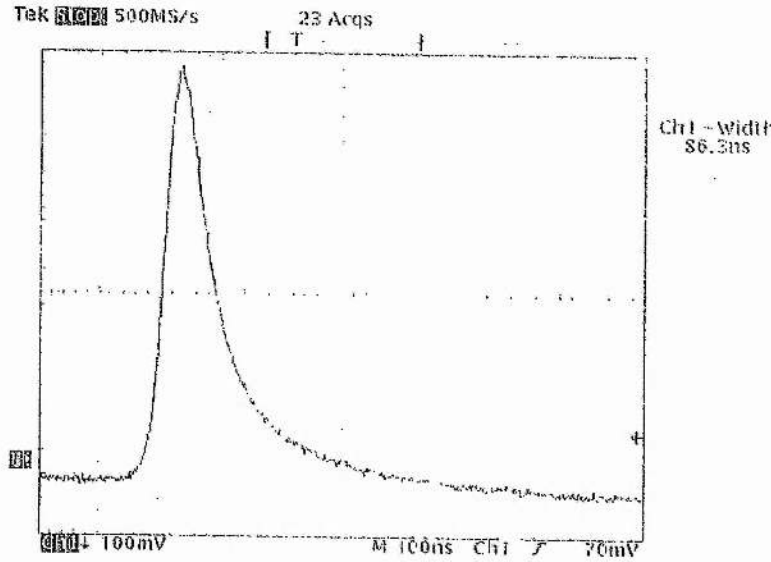

Fig. 4.11: *Typical pulse shape at 2.5kHz (10cm long cavity) and the pulse widths and energies per pulse of the 10 and 15cm long cavity as a function of the repetition rate.*

The transverse mode structure in the above Q-switched experiments was TEM_{oo} ($M^2 = 1.4$). However the quality and stability of this mode structure was inferior to the results at 1047nm. This is another drawback of this lower cross-section transition when compared to the 1μm operation. Higher pump powers than the 10W level will cause severe problems in maintaining TEM_{oo} operation even under Q-switched conditions, which again limits its use as a pump laser for non-linear optics experiments.

The spectral width of the π-polarised 1321nm line is shown in figure 4.12 below. Compared to the cw linewidth, again a broadening of the spectrum under Q-switched conditions can be observed, as before in the case of the 1μm operation.

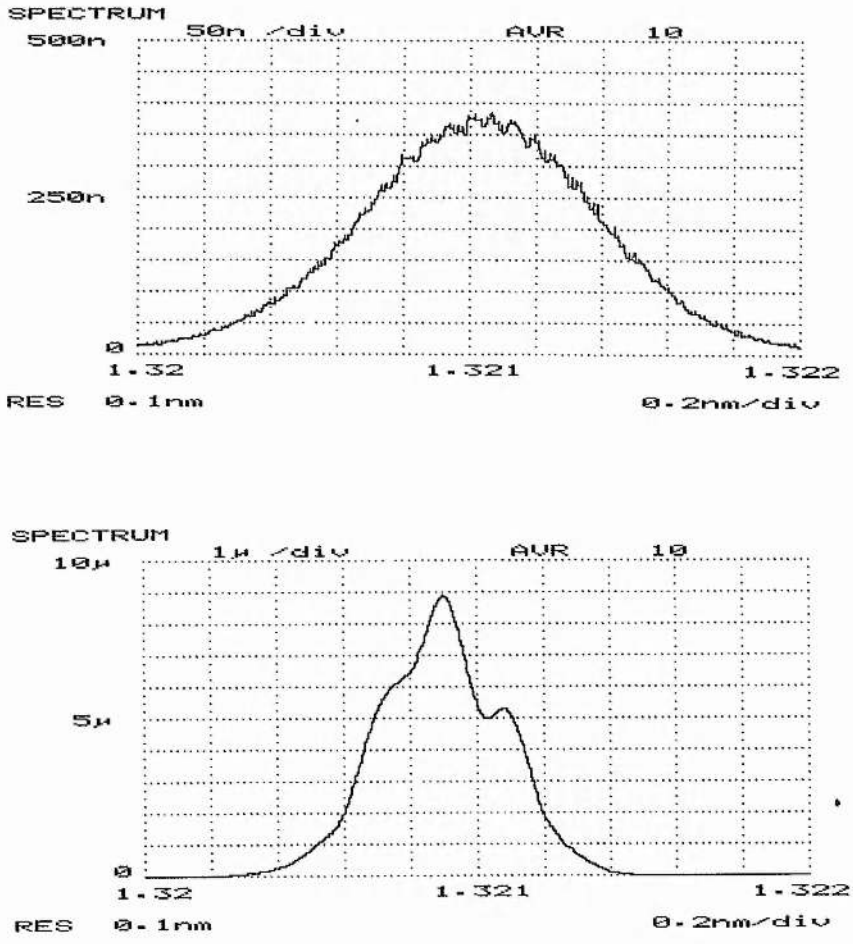

Fig. 4.12: *The higher gain under Q-switched conditions (2kHz) reduces the longitudinal mode selection. This leads to a broadening of the linewidth. The spectrum below shows the cw linewidth at the same 10W diode pump power level as a comparison.*

Two changes in the spectrum as compared to the 1047nm line are remarkable:

- The much wider linewidth of the 1321nm transition at 0.7nm, as compared to the 1047nm, which has a measured resolution limited width of ≤ 0.2nm.
- The striking smoothing of the spectral line under Q-switched conditions, as compared to the ragged line form in the cw case. Only the Q-switched 1321nm line shows the smooth, expected, line shape, as does the 1047nm line in both modes of operation, cw as well as Q-switched.

The structure on the cw spectrum is probably due to a Fabry Perot effect of the output coupling mirror (HR/uncoated @ 1.3μm, Finesse F≤1), providing feed-back into the cavity. This gives rise to an equally spaced, small modulation of the spectrum, as observed above. The free spectral range of the planar 6.5mm thick BK7 substrate is 15.3 GHz (0.09nm @ 1321nm), according to

$$\Delta\nu = \frac{c}{2nd} \qquad \text{n(BK7 @ 1321nm)} = 1.504 \qquad (4.4)$$

which is half the modulation actually observed in the spectrum. The reason for this is the resolution limit of the OSA, which is slightly worse than the quoted 0.1nm of the specifications. A safe lower limit for the resolution is therefore 0.2nm, especially for signals with a small modulation in the intensity.

Under cw operation a modulated signal could always be detected, but no change in alignment could achieve a modulated spectrum under Q-switched conditions, certifying that a change in the input conditions of the OSA is not responsible for the different behaviour. At this stage the most likely explanation for the absence of the spectrum modulation is that the feed-back effect from the Fabry Perot is not strong enough to establish mode selection under Q-switched conditions, as the fast pulse built up does anyway not encourage longitudinal mode selection. Another possibility is an averaging effect from different Fabry-Perot patterns at a pulse repetition rate of several kHz, while being scanned by the cw optical spectrum analyser. In general the use of the cw spectrum analyser has not been a problem with regard to the recorded line form, if outputs with repetition rates above 1kHz were analysed. Below 1kHz the envelope over the detected wavelength showed missing intervals, as the input stopped being quasi-cw, if compared to the scanning speed of the analyser.

The FWHM-width of ~1nm (0.4nm cw) at 1321nm is very broad if compared to the resolution limited 0.2nm in 1047nm operation (cw and Q-switched). Both

transitions share the same upper laser level and the results were taken at the same pump power level. However, the higher thermal load present during 1.3μm operation could lead to a slightly bigger thermal broadening component of the total linewidth. The main reason for the broadening is most likely to be caused by the width of the lower level $^4I_{13/2}$. To confirm this, the fluorescence spectra of Nd:YLF were taken in the 1 and 1.3μm regions. The fluorescence was recorded in the resonator beam path, behind the Brewster window of the slab. For the 1 and 1.3μm fluorescence measurements, the high reflection coated slabs were used, in order to maximise the intensity on the fibre coupled optical spectrum analyser.

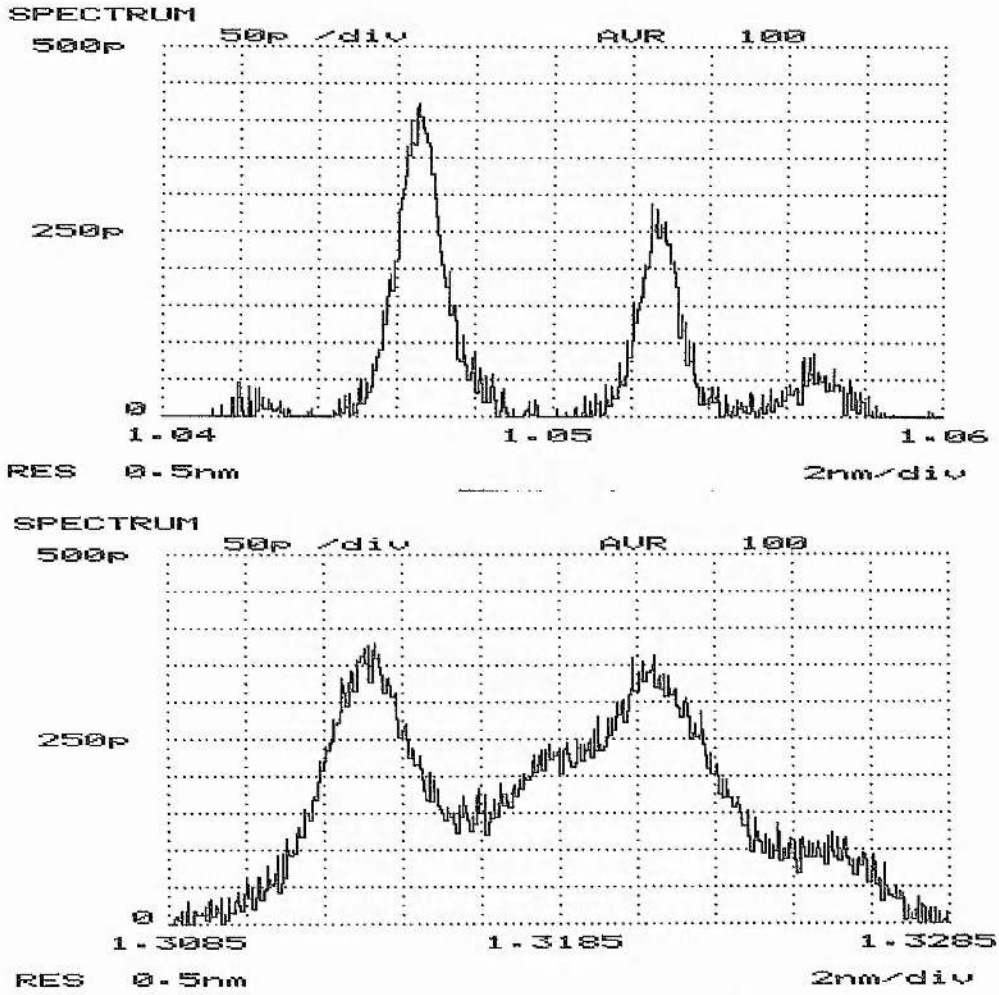

Fig. 4.13: *Comparison of the fluorescence linewidths in the 1.3μm and 1μm regions of the Nd:YLF-slab. The pump conditions are in both cases identical (10W) and the fluorescence spectra were recorded through the Brewster window of the Nd:YLF slab. This results in a single pass reduction of the σ-polarised components by ~16%, according to the Fresnel equations.*

The 1321nm fluorescence linewidth (3.8nm) is much broader than the 1047nm width (1.1nm). Compared to this even the orthogonally polarised 1314nm line is comparatively narrow (2.6nm), and has a slightly higher emission crossection, as the fluorescence intensity equals the 1321nm line intensity, despite the ~16% loss on the Brewster surface. The very broad, feature less linewidth of the 1321nm line is not of advantage, when it comes to reduced longitudinal mode selection under Q-switched conditions. This disadvantage under Q-switched operation turns into an advantage if this transition is used in a mode locked laser [8a]. The wider gain bandwidth makes shorter pulse durations possible and the 1321nm line is therefore preferable to the 1314nm transition. This paper by J. Lincoln, M.J.P Dermott & A. Ferguson is also remarkable in terms of the 166cm long resonator [8b]. At first glance this is a very long cavity, given the extremely high thermal lensing coefficient which is encountered in the slab laser system. A further analysis of the mode locked cavity is pending, but the probable discrepancy in thermal lensing encountered in both systems is at the time not understood.

The figure below shows the changing FWHM linewidth of the 1321nm emission as a function of the repetition rate. Under high gain, corresponding to four times lifetime pumping, the FWHM rises to ≥1nm, as compared to 0.4nm under high repetition rates or cw operation.
Mode cluster effects as during 1047nm operation might be present, however the uncertainty about the presence of averaging effects through a changing longitudinal mode selection during the slow scanning process makes it impossible to distinguish between a complete set of longitudinal modes or quickly varying clusters. To resolve this question a Fabry-Perot interferometer, set-up for the frequency doubled output, to make it detectable with Silicon sensors, and imaged onto a CCD-camera with a fast exposure time (≤500μs) would be necessary to resolve the spectrum of one pulse.

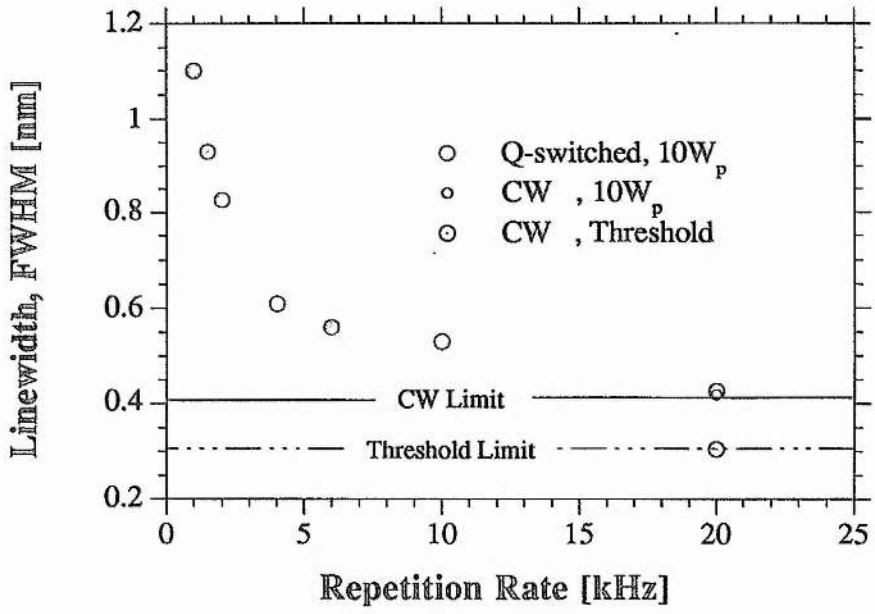

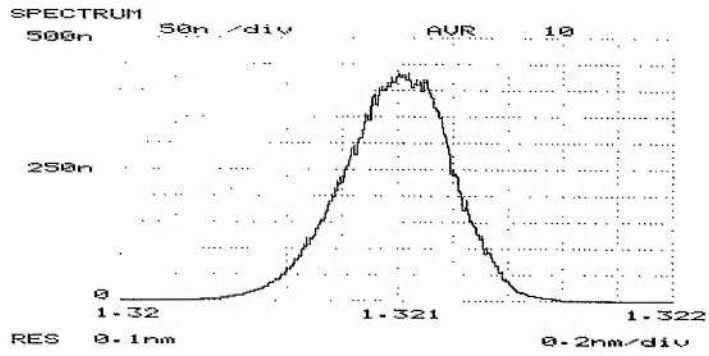

a)

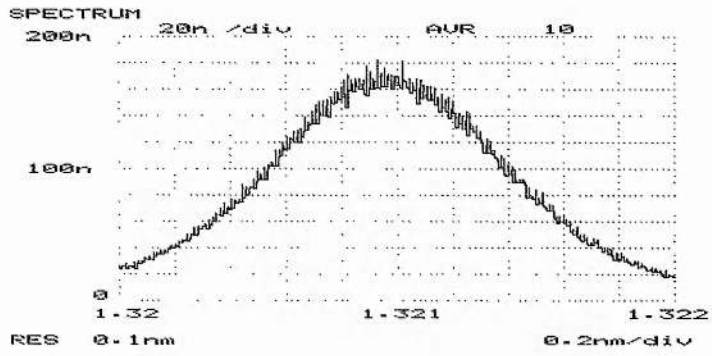

b)

Fig. 4.14: *Reduced longitudinal mode selection as a function of the repetition rate. The wide lasing linewidth for a homogeneous broadened line of up to 1.1nm (189 GHz, FWHM) is equivalent to ~250 longitudinal modes above threshold (**b**)). For short pumping cycles (20kHz) the linewidth comes close to the cw value of 0.4nm (**a**)).*

In order to prove the assumption that thermal vibrations of the YLF-lattice are the main mechanism for a predominately homogeneously broadened transition, fits have been applied to the measured fluorescence lineshapes. The Lorentzian lineshape describes the homogeneously broadened response, while a Gaussian lineshape is the response for an inhomogeneously broadened system like Nd:Glass or gaseous gain media. The lineform function describes the fluorescence intensity through the following relation:

$$I(\nu) = I \cdot g(\nu) = \left(\frac{\mu_o}{\varepsilon_o}\right)^{-\frac{1}{2}} E(\nu)^2 \qquad \text{and} \qquad I = \int_{-\infty}^{+\infty} I(\nu)\,d\nu \tag{4.5}$$

The equations used for the line forms $g(\nu \approx \nu_0)$ are:

Lorentzian line form:
$$L(\nu - \nu_o) \propto \frac{1}{(\nu - \nu_o)^2 + (\Delta\nu/2)^2} \tag{4.6}$$

Gaussian line form:
$$G(\nu - \nu_o) \propto \exp\left\{-\left(\frac{\nu - \nu_o}{\Delta\nu/2}\right)^2 \ln 2\right\} \tag{4.7}$$

With ν_0 as the centre frequency of the resonance and $\Delta\nu$ the half width of the lineshape. Only one fit factor, the half width, $\Delta\nu$, was used, with no allowance for an off-set in the intensity. This reduction to only one fit factor was necessary to prevent Gaussian fits with unrealistically high off-sets also delivering a relative good fit (with the off-set being at the second variable).
For both wavelength regions around 1 and 1.3µm, the Lorentzian lineshape described the measured intensities very accurately, while the Gaussian fit with the linewidth as the variable was not satisfactory. Representative traces for 1047nm, 1314nm and 1321nm are shown in figure 4.15. The measured central wavelengths of the transitions are shown for each trace.
According to the calibration sheet of the optical spectrum analyser the absolute readings in the 1 to 1.3µm region will be 0.2 to 0.3nm higher than the measured ones. An additional advantage of the fits to the measured fluorescence data points is that the linewidths can be more accurately determined than is possible by trying to measure the width in a superimposed spectrum as before. By using only parts of the undisturbed single line intensities a good fit and linewidth estimate can still be achieved.

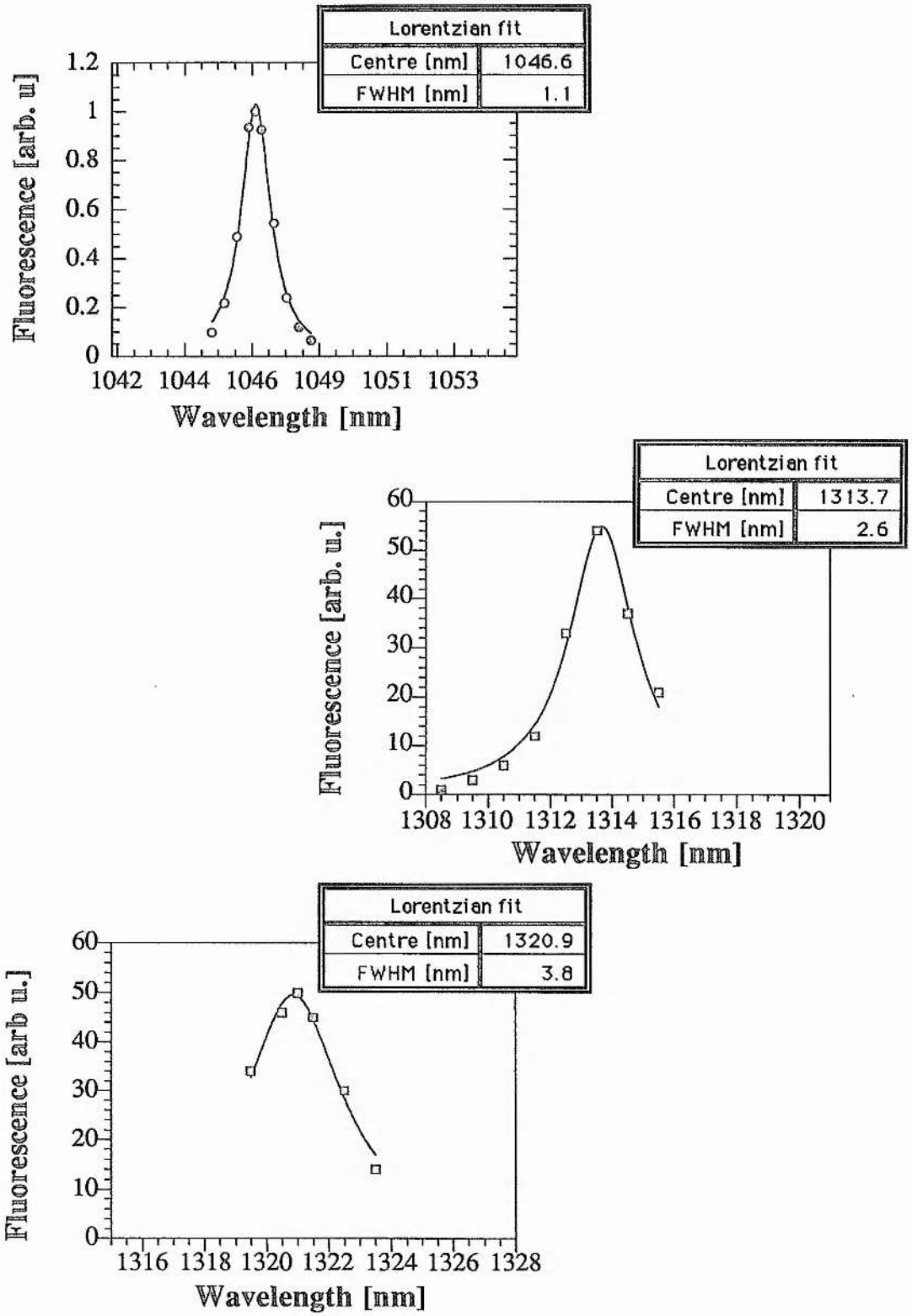

Fig. 4.15: Lorentzian lineshape fits to the measured fluorescence data at 1047nm, 1314nm and 1321nm. Despite the broad fluorescence linewidth of several nm in the 1.3μm region, the lines are predominantly homogeneously broadened. All plots cover a range of 13nm to make the different linewidths obvious.

The spectrum and table below summarises the central wavelengths, polarisations and fluorescence linewidths, as well as lasing linewidths (as applicable) for the main lines of Nd:YLF, as measured with the optical spectrum analyser. The complete spectrum of Nd:YLF in the 1.3μm region is given to compare the fluorescence signal strength of the different lines.

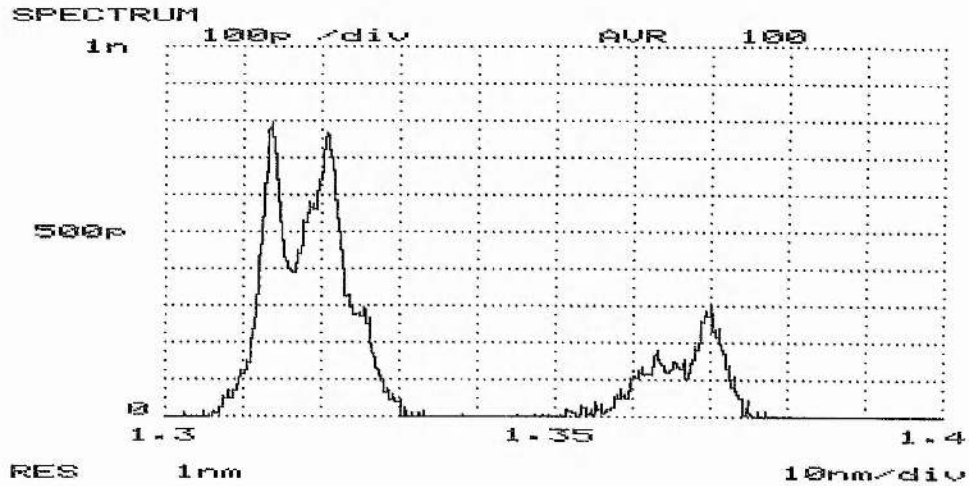

centre λ_F [nm]	Polarisation	Fluorescence width [nm]	Lasing width [nm] Q-switched	CW
1046.9	π	1.1	~0.1	~0.1
1313.9	σ	2.6	-	-
1321.1	π	3.8	0.4 - 1.1	0.3 - 0.4
Main: 1363 (1361, 1366)	π	≥3nm	-	-
1372	π	2.9	-	-

Table 4.16: *Complete fluorescence spectrum around 1.3μm and comparison of fluorescence data and lasing linewidth of transitions in the 1 and 1.3μm regions. The quoted width are all FWHM.*

The dominant polarisation orientation for each fluorescence line was determined with the help of a polariser, as was demonstrated for the fluorescence spectra in the 1μm region earlier (figure 3.4). The lines for the band around 1363nm, and the 1370nm line, have been added to give some basic information on the more exotic wavelengths in Nd:YLF, which are an option if the need arises for a special application. The cross-sections achievable

in this wavelength region makes the 1321nm line, which has been problematic in this work, look like a high gain line.
Interestingly, E.Chicklis, P.Knights & al. have used the band around the 1363nm line to obtain 455.5nm, a resonant line in Cs, by frequency tripling the 1366.5nm fundamental of a flashlamp pumped laser [9]. Up to 90mJ at 1366.5nm could be extracted, being proof of the high parasitic oscillation threshold of the medium gain material Nd:YLF, with an extremely small signal gain ratio at 1047nm/1366nm of

$$g_o^{1047} / g_o^{1336} = 28 \qquad \text{(compared to } g_o^{1047} / g_o^{1321} = 5.2 \text{ in this experiment).}$$

Given these crossection ratios, gain competition from the π-polarised lines at 1321nm, and even 1370nm, becomes a problem, which was solved with birefringent filters, making continuous tuning in the broad 1.363nm band possible. The 1μm competition was suppressed with wavelength selective silicon Brewster windows. With such an arrangement effective single pass gain ratios of half a million to one could be suppressed within this two stage flashlamp pumped oscillator set-up.

4.3 Conclusions

The 1321nm transition in Nd:YLF is problematic mainly because of its disproportionately higher thermal lensing, as compared to the 1μm operation, due to a reabsorption of the laser wavelength. This reabsorption, which depends on the undepleted $^4F_{3/2}$ population and the intracavity intensity, shifts the additionally generated heat towards the pumped window. This hypothesis, which explains the undoubtedly higher lensing values by means of a spatial redistribution of the heating power, removes the paradoxical situation that similar total amounts of bulk crystal heating, as encountered under 1 and 1.3μm operation (even though the 1.3μm dissipated heat is slightly higher), give rise to a totally changed surface effect, which in turn defines the increased, positive thermal lensing.
These increased surface distortions magnify the standard problem and limitation of high power end-pumped laser systems, as already described in the 1μm chapter. The aberrations introduced by the thermal lens result in increased losses for TEM_{oo} operation.

This, in hindsight, combined with the low gain of the 1321nm transition, makes the choice of this transition for a high repetition rate system, dedicated to pump non-linear optical experiments, somewhat unfortunate. The lack of pump laser suitability has been compensated for by the luck of exceptional optical access to the pumped and unpumped regions within the slab, which made these physically identical 1 and 1.3μm systems ideal for up-conversion investigations and comparisons (see Chapter 5). A summary of important performance results and measured laser parameters is given in the following table:

CW output characteristic	$10W_p$: 1.6W TEM_{oo}, 1.9W TEM_{2o} ; $T_{opt.} = 3\%$ $20W_p$: 3.75W $TEM_{20/30}$
Q-switched output	$10W_p$: 4kHz - 800mW, 110ns ; 1kHz - 400mW, 75ns
Crossection	relative: $\delta_{1047} / \delta_{1321} = 5.2$ absolute: $\delta_{1321} = 0.38...0.69 \cdot 10^{-19} cm^2$ [10,11]
Lensing coefficient ζ	ζ~0.7 diop./W_p (@ 1047nm: ζ~0.25-0.3 diop./W_p)
τ_{eff} *(Q-switched)*	τ_{eff} = 450μs ($10W_p$ level) (see Chapter 6)

Table 4.17: Summary of the 1321nm experiments with emphasis on the measured laser parameters.

The 1321nm line in Nd:YLF investigated in this set-up, besides the anticipated low gain, quite a few additional undesirable laser parameters, such as:

- wide lasing linewidth (up to 1.1nm)
- reabsorption at the laser wavelength
- high thermal lensing,

which made it an interesting transition to investigate, although it is only of limited use for high repetition rate, non-linear pump purposes. To achieve (in a future set-up) an improved high repetition rate 1.3μm source, the first and easiest alteration is the change to a Brewster cut Q-switch, which is preferable in order to achieve the required very low insertion losses (≤ 0.5%). A more important change would be a different c-axis orientation to access the 1314nm line within this slab geometry.
The fluorescence measurements in figure 4.16 indicate that the orthogonally polarised transition at 1314nm, would probably have been a better choice for Nd:YLF operation in the 1.3μm region. However, with the resonator field then being parallel to the a-axis of the crystal, and propagation along the c-axis, the pump polarisation would be parallel to a for end-pumped configurations. This would reduce the absorption crossection of Nd:YLF by a factor of ~1.8 [10] and is, at least for diode array end-pumped lasers, a drawback, due to their strongly different divergence in the two pump planes. Fibre-coupled diode modules are better suited, as they provide greater flexibility in imaging the output, in order to optimise the fluorescence profile over a longer absorption length, while the loss of the pump polarisation, one of the possible disadvantages of fibre coupling, is in a-axis cut Nd:YLF not of relevance. Fibre coupled diode-pumping through an external mirror substrate onto an AR coated, c-cut, Nd:YLF crystal would be the preferred pump configuration in a future 1.314μm set-up.

The main reason for using the 1314nm transition is not that the cross-section is slightly bigger and the fluorescence linewidth smaller. More important is the fact that reabsorption is a resonance phenomenon, so that a change of 8nm in the emission wavelength would present at least the chance of avoiding reabsorption problems. The disproportionately high surface deformations for 1.321μm cause a real limitation for this transition in diode end-pumped set-ups, as they degrade the beam quality, as compared to the 1μm operation, and it could be hoped that the 1314nm transition would not suffer from the same problem.

References

[1]: G.R. Morrison, C. Rae, M.H. Dunn & al. - **Diode-pumped, Q-switched, 1.321μm Nd:YLF laser and its frequency doubling** - Opt. Communications 118, 55 (1995)

[2]; N.P. Barnes, D.J. Gettemy, R.E. Allen & al. - **Comparison of Nd 1.06 and 1.33μm operation in various hosts** - IEEE J-QE QE-23, No.9, 1434 (1987)

[3]: W. Grossman, M. Gifford & R.W. Wallace - **Short-pulse Q-switched 1.3- and 1-μm diode-pumped lasers** - Opt. Lett. 15, No.11, 622 (1990)

[3a]: T.M. Bear, D.F. Head, S. Hutchison & al. - **Performance of diode-pumped Nd:YAG and Nd:YLF laser in a tightly folded resonator configuration** - IEEE J.-QE. QE-28, No.4, 1131, (1992)

[3b]: H.Y. Shen, R.R. Zeng, Q.J. Ye & al. - **Simultaneous multiple wavelength laser action in various neodymium host crystals** - IEEE J-QE QE-27, No.10, 2315 (1991)

[4]: H.W. Kogelnik, E.P. Ippen, A. Dienes & al. - **Astigmatically compensated cavities for cw dye lasers** - IEEE J-QE QE-8, No.3, 373 (1972)

[5]: K.B. Steinbruegge, E.P. Riedel, G.W. Roland & al. Appl. Opt. 11, 999, (1972)

[6]: C. Rahlff - **Polarisation properties of high power Nd:YAG lasers** - Diplomarbeit, Technische Universität Berlin, Oktober 1990

[7]: G.A. Rhines, R.A. Schwarz & P.F. Moulton - **Diode-laser-pumped, cw, Nd:YLF laser with efficient intracavity second harmonic generation** - Paper ATuD3-1, Advanced Solid State Lasers p. 178, Salt Lake City, Feb. 1994

[8]: J.R. Lincoln, M.J.P Dymott & A.I. Ferguson - **Femto second pulses from an all-solid-state Kerr-lens mode-locked Cr:LiSAF laser** - Opt. Lett. 19, No.16, 1210 (1994)
J.R. Lincoln & A.I. Ferguson - **All-solid-state intra-cavity doubled Nd:YLF laser producing 300mW of 659nm light** - Opt. Lett. 19, No.16, 1213 (1994)

[9]: HH. Zensie, E.P. Chicklis, M. Knights & al. - **Non-linear conversion of 1.3μm Nd:YLF emission** - "Tunable Solid State Lasers II" p.364 (Springer, 1986)

[10]: J.R. Ryan & R. Beach - **Optical absorption and stimulated emission of neodymium in yttrium lithium fluoride** - J.Opt.Soc.Am.B 9, No.10, 1883 (1992)
T.M. Pollak, E.P. Chicklis, H.P. Jensen & al. - **Cw operation of Nd:YLF** - IEEE J.-QE. QE-18, No.2, 159 (1982)

[11]; E.J. Sharp, D.J. Horowitz & J.E. Miller - **High-efficiency $Nd^{3+}:LiYF_4$ laser** - J. Appl. Phys. 44, No.12, 5399 (1973)

Chapter V.

Excited State Absorption in Diode Pumped Nd:YLF

It is well known, that under high density diode pumping Neodymium doped host materials like YAG, YLF or Yttrium Vanadate (YVO_4) exhibit a more or less bright visible fluorescence. This chapter will compare the different fluorescence properties in the visible and near UV under cw and repetitively Q-switched operation for both of the π-polarised transitions at 1.047 and 1.321μm in Nd:YLF.

The first mention of the visible fluorescence in Nd:YLF under diode end-pumped operation was in a paper by Fan & Byer [1]. They later investigated the possibility of the excitation of an UV transition in Nd:YLF pumped by a two step resonant up-conversion mechanism [2]. These results are of direct relevance for the fluorescence behaviour of the Q-switched 1047nm line.

More recently the fluorescence behaviour has again been of interest as the source of a loss mechanism, limiting the energy extraction capacity of Nd:YLF under low repetition rates and high pump power densities [3,4,5]. This possible loss problem in Nd:YLF would reduce one of the main advantages of this host material when compared to YAG, namely the higher upper laser level lifetime, which is of importance for repetition rates below the 4 to 5kHz region.

Other questions of interest attached to the fluorescence behaviour relevant to these experiments at 1047nm are, in addition to the loss mechanism through up-conversion, the following two areas:

- The beam quality improvement under Q-switching of the 1047nm line.
- Appearance of an after pulse, beyond a certain pulse width ($\Delta t \leq \sim 15$ns), during 1047nm operation.

Both possible explanations for these effects are related to the loss mechanism through excited state absorption of laser radiation (ESALR). The beam quality improvement could be due to a spatially varying loss, while the appearance of an after pulse characterises the time constants of parts of the up-conversion process, through re-population of the upper laser level.
The analysis and comparison of the visible and near UV fluorescence was done with a time dependent spectral analysis as well as with a spatially resolved spectrum of the Nd:YLF crystal, operating at 1047nm and 1321nm.

An additional experimental advantage of the system developed during this work is that it is extremely well suited to investigate the up-conversion fluorescence properties, as the pumped area is very accessible for probing purposes through the polished cooling surfaces. Furthermore, the internal folding section makes a distinction between up-conversion in the pumped and unpumped area possible. This accidental advantage made the observation of some unusual properties during 1.321µm operation possible. In general the up-conversion mechanism involved during 1.321µm operation has not been reported so far and these first results presented here might lead to a better understanding of this not very often used transition. Of special interest is the connection between the much higher thermal lensing values under 1.321µm operation, as shown in the previous chapter, and the suspected higher reabsorption crossection of the laser radiation.

CW 1047nm

Q-switched 1047nm

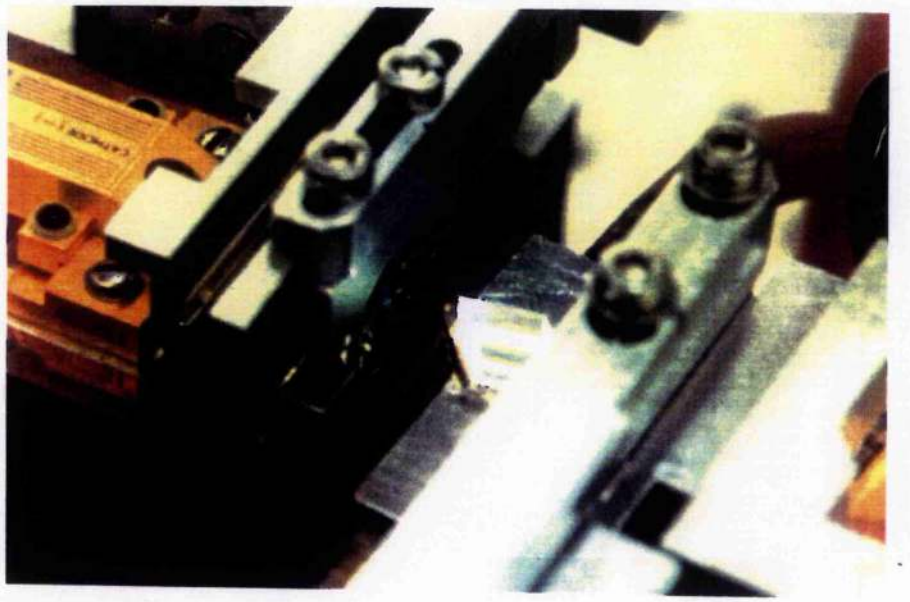

Fig. 5.1: *Under cw-operation the up-converted fluorescence has the characteristic yellow-green appearance, which changes to a blue-whitish emission under Q-switched conditions, caused by a second step ESALR excitation into blue/UV emitting Nd:YLF energy levels.*

5.1 Fluorescence properties under 1047nm operation

The most obvious property in the visible fluorescence is the change induced by repetitively Q-switching the cw pumped Nd:YLF laser. The fluorescence in the pumped path changes from a yellow-green to a bright blue-whitish appearance. This is due to a resonant two step excited state absorption (ESA) process of the 1μm emission, giving rise to near UV transitions with radiative lifetimes in the μs-region. The blue and near UV parts of the spectrum mixing with the green-yellow-red bands cause the overall white impression to the eye. Figure 5.1 shows the Q-switch induced colour change of the fluorescence as well as the gain in brightness, as compared to cw operation.

Under cw conditions the yellow-green fluorescence shows strong depletion as soon as lasing is established (Fig. 5.2). The pictures below were taken with a CCD camera and a frame grabber. Unwanted scattered pump radiation at 797nm was blocked by a Schott (GB 38) filter .

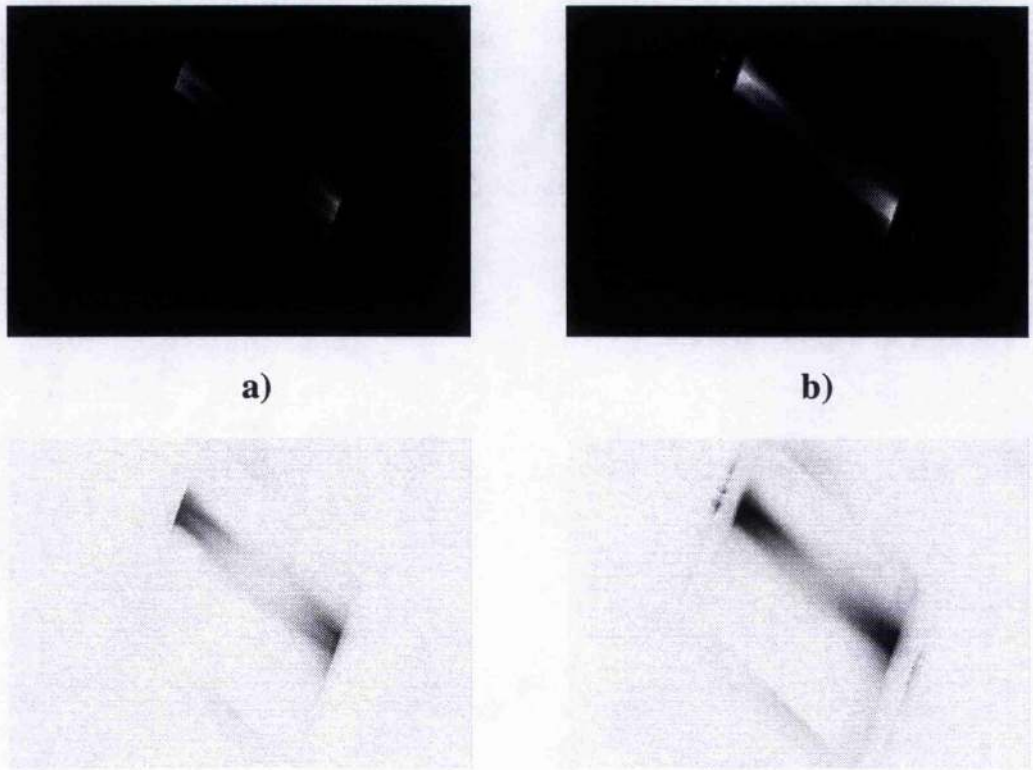

Fig. 5.2: *Spatial depletion along the resonator path of the visible fluorescence for lasing conditions (**a**)). As a comparison, the full fluorescence under non-lasing conditions (blocked resonator) along the pumped path is shown (**b**)). The laser operates in TEM_{00}. The row below is in an inverted representation.*

This is a clear indication that the upper laser level $^4F_{3/2}$ is involved in this up-conversion process. Under non-lasing conditions the origin of the fluorescence is due to energy transfer up-conversion (ETU). This is where the excited state relaxes, radiationless, into the ground state, transferring its energy to a neighbouring excited state, which is thus excited to the $^2G_{9/2}$ manifold (for energy level diagram and notation see figure 5.3). After radiationless relaxation into the $^4G_{7/2}$ level this manifold becomes the main origin for optical transitions into the $^4I_{13/2}$ to $^4I_{9/2}$ levels.
Under Q-switched conditions ETU is replaced by ESA of the 1μm photons from the $^4F_{3/2}$ level, thus competing with the laser transition for the same inversion. This process leads as before to a population of the $^4G_{7/2}$ level (via $^2G_{9/2}$). The transitions from there into the lower ^4I levels coincide with the measured peak wavelength of the green (532nm, $^4I_{9/2}$), yellow (584nm, $^4I_{11/2}$) and red (656nm, $^4I_{13/2}$) fluorescence bands.

The observed UV transitions while Q-switching could be attributed to a population of the $^4D_{3/2}$ manifold. This is the same level which was pumped by a resonant two-step excitation at 587.4nm, involving the upper laser level as an intermediate storage level [2]. Subsequently identical UV transitions could be detected in this work, as in the paper by Fan and Byer. The excitation route into the $^4D_{3/2}$ level is again by ESA, but this time by reabsorption of laser radiation and with $^2G_{9/2}$ as the intermediate level, which is already populated by a single 1μm photon ESA process. The different intensity dependence of the one and two step excitation processes for the visible and UV fluorescence respectively, is shown later in order to confirm the different excitation routes.

The time resolved spectrum under Q-switched operation was measured using a photo multiplier (RCA 931B) as a detector in combination with an 0.25m monochromator. The fluorescence signal was picked up through the top cooling surface, deflected through 90° by a broadband Aluminium mirror and imaged onto the monochromator slits with an uncoated f=100mm lens. The orientation and size of the fluorescence imaged into the entrance slit was such that only parts of the total fluorescence were recorded. Optimising for the highest possible signal to noise-ratio always meant that the crystal area pumped from one diode fell onto the entrance slit. More details about the photo multiplier tube and monochromator can be found in the appendix "Equipment (A2)".

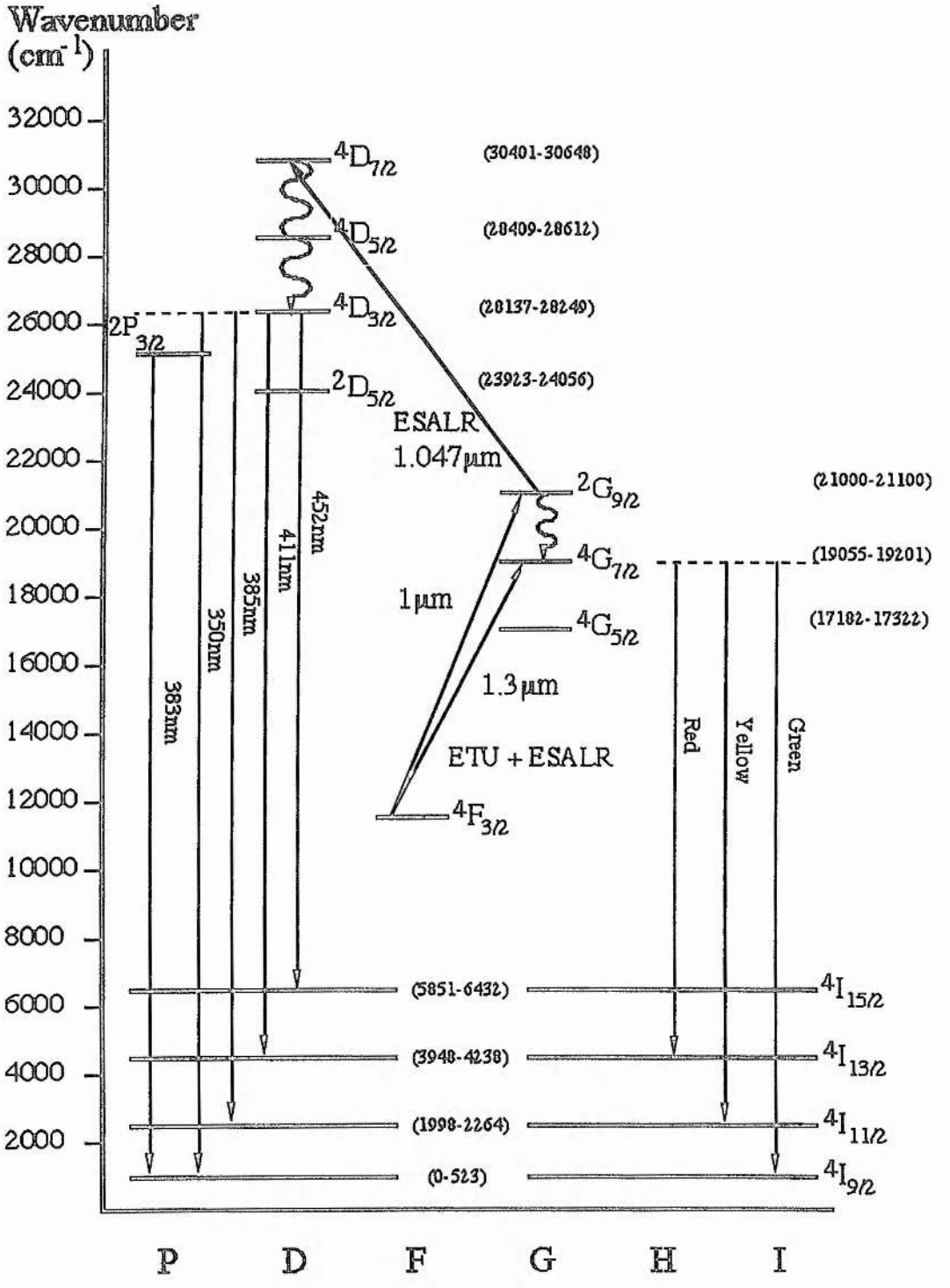

Fig. 5.3: *Simplified energy level diagram of Nd:YLF, with attention to energy levels involved in the energy transfer up-conversion (ETU) and excited state absorption (ESA). Spectroscopic data was taken from de Gamma et al. [6a].*

The low intensity of the fluorescence and difficult imaging conditions made the use of a photo-multiplier in combination with the short, efficient monochromator necessary. The downside to the much needed sensitivity was limited resolution and absolute accuracy, which is the drawback of the 0.25m monochromator.

As an overview, figure 5.4 shows the visible and near UV parts of the spectrum in one graph, with fully open entrance and exit slits of 2mm (resolution: ~2nm). As the sensitivity of the photo multiplier drops strongly towards the red region the measured intensities have been scaled to correct for the non-linearity of the detector.

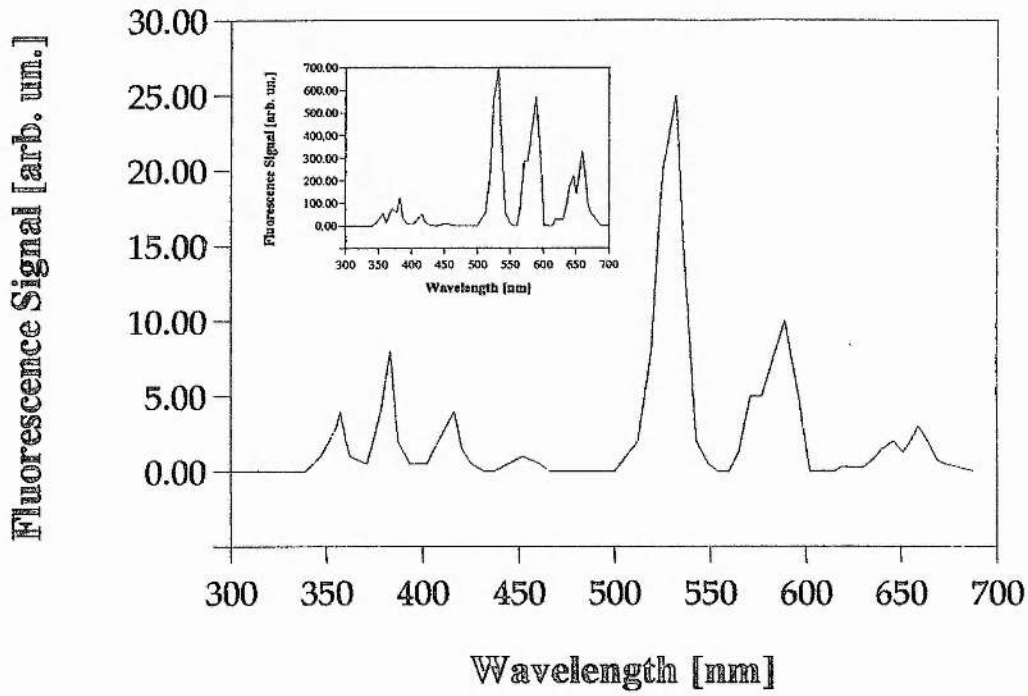

Fig. 5.4: *Low resolution scan of the entire detectable fluorescence spectrum under Q-switched conditions (2kHz rep.-rate, 10W pump power). The inset with the scaled intensities is given to allow a rough comparison of the relative intensities of the bands.*

The absolute intensities of the near UV part of the spectrum are likely to be underestimated, as no correction for the grating characteristic of the monochromator, which tails of in the UV region (50% cut-off: 350nm & 750nm, 1200 lines grating) was applied.

The time response connected to the Q-switched laser pulse is very different for the visible and blue/near UV bands. While the visible emission follows the laser pulse shape with a delay of approximately 20ns (i.e.: fluorescence lifetimes of some 10's of nanoseconds), the near UV bands have a substantially longer lifetime, ranging from 1μs up to ~10μs, depending on the specific transition. A higher resolution spectrum for most fluorescence wavelength bands (intensities permitting), with the characteristic time response of each transition, is given in figures 5.6/7.
With these transition measurements the likely energy levels which correspond to each fluorescence peak can be identified. The table below gives, for each peak wavelength, the upper and lower level as well as the fluorescence lifetimes and excitation mechanism responsible for populating the upper levels.

Δ λ [nm]	upper level	lower level	lifetime	excitation
Visible				**single photon excitation**
532 (green)	$^4G_{7/2}$	$^4I_{9/2}$	25ns ($^2G_{9/2}$)	1μm ESA :
589(yellow)	$^4G_{7/2}$	$^4I_{11/2}$	25ns ($^2G_{9/2}$)	$^4F_{3/2}$ to
656 (red)	$^4G_{7/2}$	$^4I_{13/2}$	25ns ($^2G_{9/2}$)	$^2G_{9/2}$
Near UV				**two step excitation**
357	$^4D_{3/2}$	$^4I_{9/2}$	~1μs	1μm ESA:
383	$^4D_{3/2}$	$^4I_{11/2}$	~1.5μs	$^2G_{9/2}$ to
411	$^4D_{3/2}$	$^4I_{13/2}$	~1μs	$^4D_{3/2}$
452	$^4D_{3/2}$	$^4I_{15/2}$	~15μs	(via $^4F_{3/2}$)

***Fig. 5.5:** Table of fluorescence transitions and lifetimes during 1047nm operation.*

The identification of the energy levels involved was done by matching the measured wavelength with the possible Nd:YLF energy transitions. Although the wavelength measurement was not as accurate as desirable (± 2nm, absolute accuracy), an empirical identification was possible by elimination, by starting with all the possible transitions according to the Nd:YLF energy diagram and excitation energies for up-conversion.

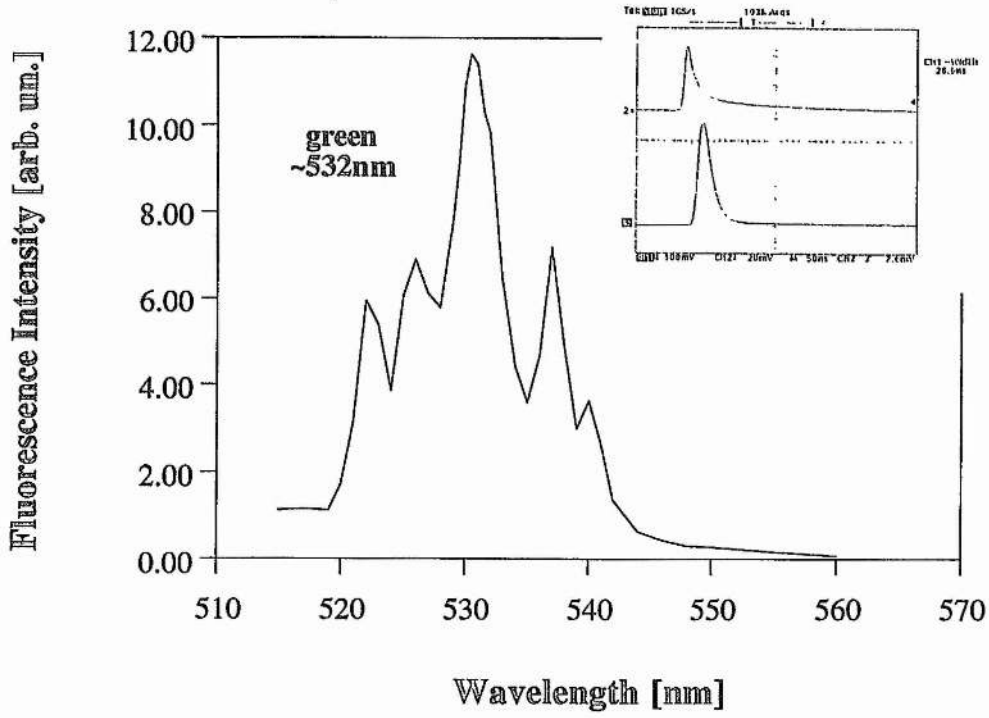

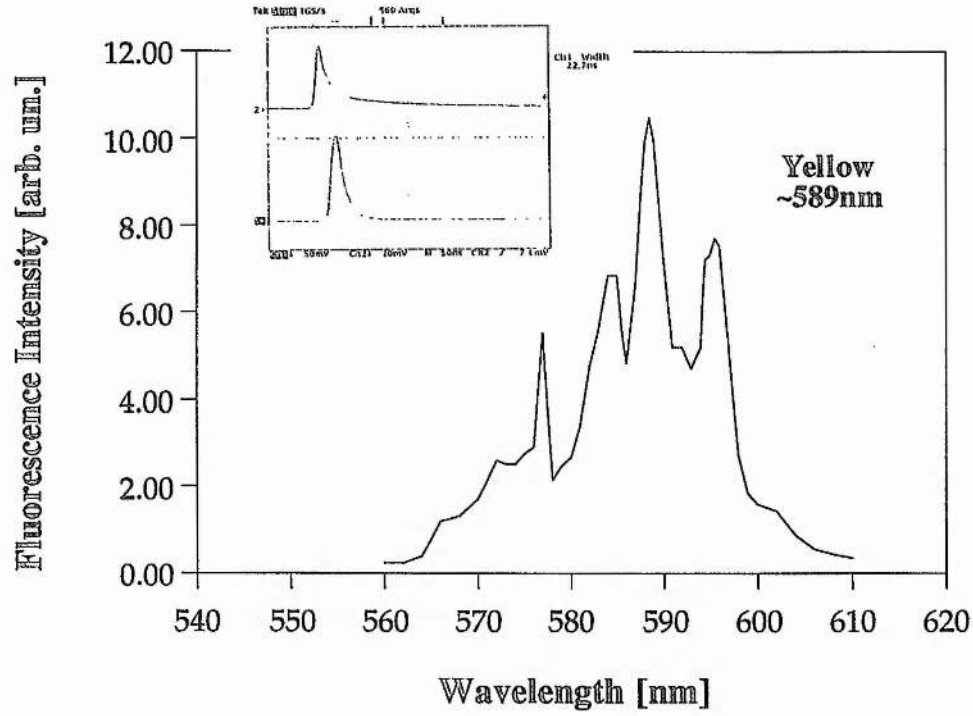

Fig. 5.6: *'High' resolution (resolution limit: ~0.5nm) of the green and yellow, up-converted fluorescence in Nd:YLF under Q-switched conditions. For each dominant fluorescence peak is the time response of the fluorescence (lower trace) is given with respect to the 1μm laser pulse (upper trace in the inset).*

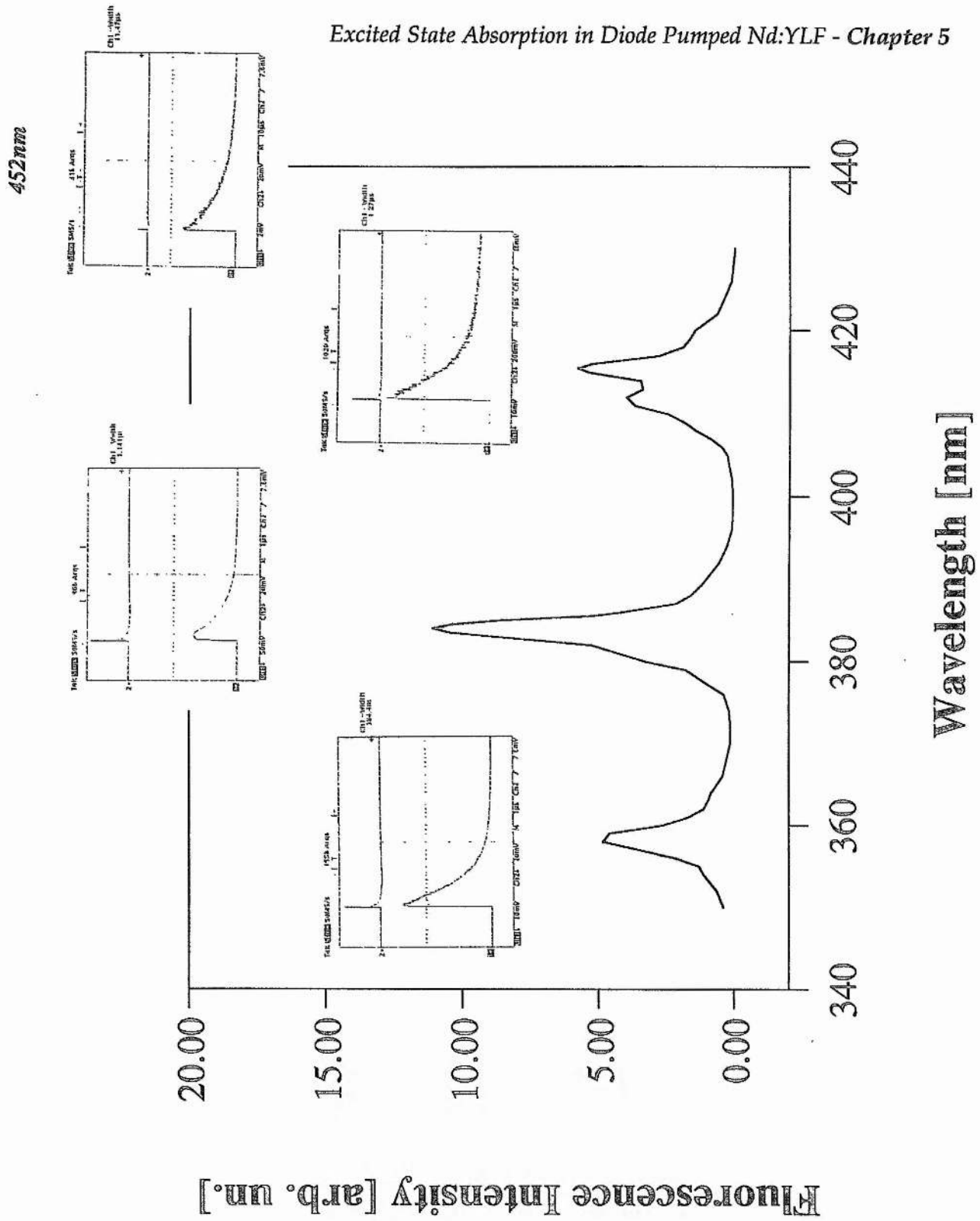

Fig. 5.7: *'High' resolution (resolution limit: ~0.5nm) of the up-converted UV fluorescence in Nd:YLF under Q-switched conditions. In addition to each main fluorescence peak, the time response of the fluorescence is given with respect to the 1μm laser pulse.*

The visible transitions with their very short lifetimes are an ideal probe of the upper laser level state of inversion, as all visible transitions appear to have the same upper laser level as a starting point for ESA in common. The ability to probe the state of inversion of the laser transition makes a distinction of the mechanism which causes an after pulse possible, if the pulse duration of the main pulse is below approximately 15ns. Three mechanisms have been taken into account:

- Repopulation of the upper laser level by a recirculating inversion from the $^2G_{9/2}$ or $^4G_{7/2}$ states.
- A bottleneck effect caused by the lower laser level, caused by the lifetimes of this transition into the ground state being in the range of 10ns, thus temporarily terminating the laser transition [7].
- Incomplete Q-switching due to hold-off problems.

This chapter works on the assumption, that the observed fluorescence bands represents only a fraction of the $^4G_{7/2}$ population, while the main decay route will relax radiationless, so that a repopulation of the upper laser level becomes a distinct possibility. The main concern of this chapter is to investigate if excited state absorption of laser radiation is a loss mechanism of practical concern in high power diode-end pumped Nd:YLF systems. Accepting the above working hypothesis of mostly radiationless transitions from the G and D states, it concentrates instead on experimental evidence of this circulating population.

The delay of this repopulation mechanism from the peak intensity of the laser pulse could give rise to an after pulse, which occurs within a certain delay of the first intensity peak. The pulse duration of the main pulse is therefore critical if the after pulse is to be resolved. For longer pulses the second pulse could be hidden in the falling flank of the Q-switched pulse. A clear second pulse will only be registered if the decay of the first pulse has reached almost zero level before repopulation of the upper laser level causes a second gain switched pulse. To achieve sufficiently short pulse durations the shortest possible resonator length was employed ($l_{geo.}$ = ~12cm) during the following experiments. This arrangement permits pulse lengths of just below 10ns FWHM, but is however limited to pump powers in the 10W range, to avoid opening time problems of the acousto-optical Q-switch, as noted before.
The after pulse intensity peak delay from the main peak has to be the same (or roughly the same) time constant as observed between the fluorescence peak and the main peak. The exact timeconstant depends on the nature of the

relaxation process by a radiationless transition into the $^4F_{3/2}$ upper laser level. Pulse build-up time effects can be neglected, as there are still sufficient photons around. The corresponding time delays between laser pulse peak and fluorescence peak, as well as the main peak and the second gain switched after pulse of the laser emission are pictured below in figure 5.8.

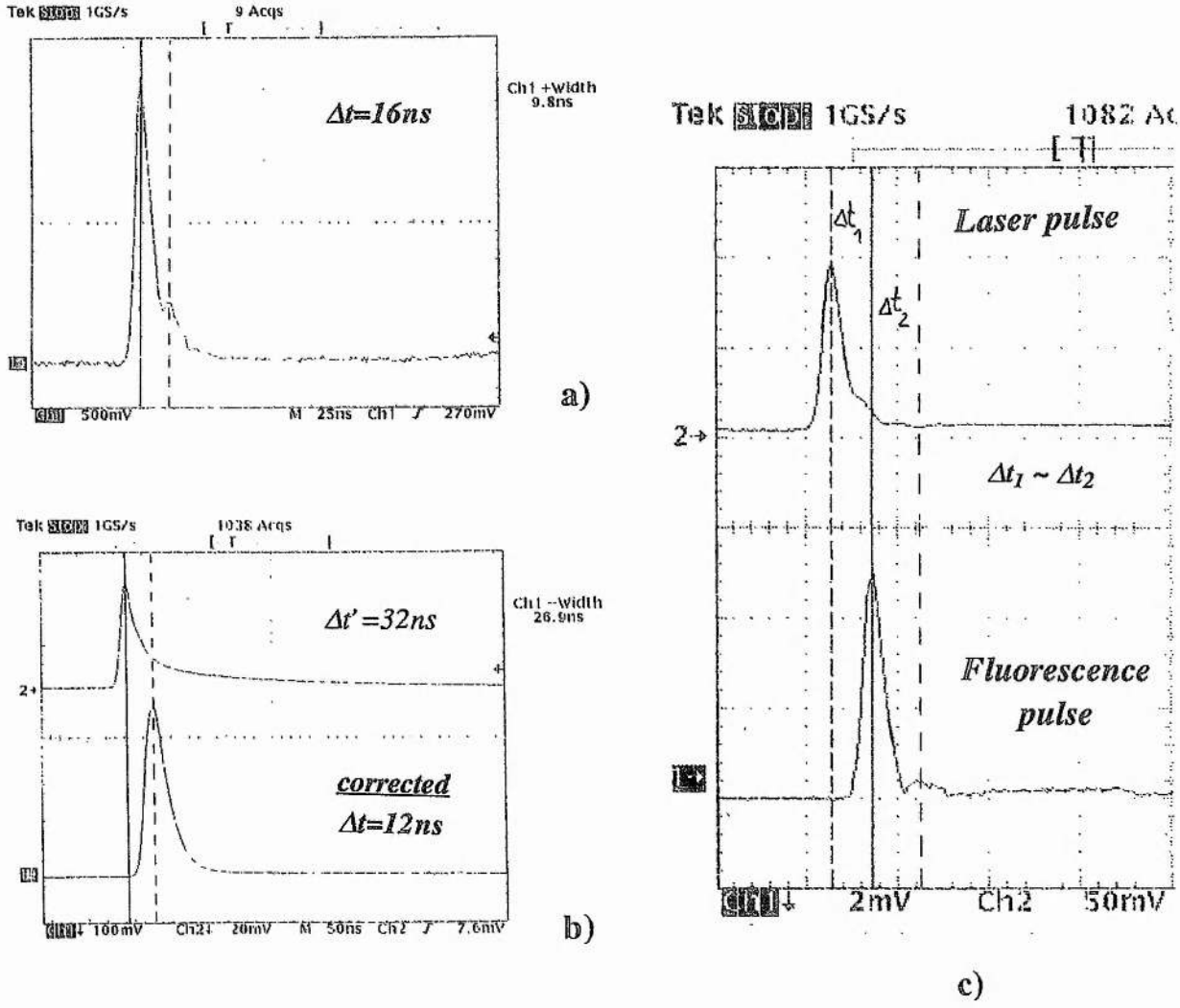

Fig. 5.8: *The peak of the gain switched after-pulse, due to the repopulation of the upper laser level, appears 16ns after the main intensity peak in figure a). This temporal response in the infrared is mirrored in the behaviour of the visible fluorescence (532nm) (b)). The non-radiative decay of the major part of the population, associated with the visible fluorescence peak, repopulates the upper laser level, giving rise to the gain switched after pulse. Two visible fluorescence peaks are detectable at 479nm (c)), both being ESA-echoes of main and after pulse.*

The very weak fluorescence signature of the 479nm decay route ($^4G_{9/2}$ --> $^4I_{9/2}$) shows a much faster decay behaviour than the other visible transitions, which makes it possible to detect the fluorescence decay of the excited state absorption during the after pulse (5.8c). This accounts for the two fluorescence peaks, each delayed by ~22ns (uncorrected by the multiplier response) to the respective laser pulse.

As the photo-multiplier tube adds a time delay, due to the amplification process, the time response of the photo-multiplier used has to be calibrated relative to the Silicon and Germanium photo-diodes, which were used to generate the trigger signal on the rising edge of the Q-switched pulse. The measured time delay of the multiplier tube RCA 931B (1kV, negative cathode voltage) was 15 to 20ns (Ge:20ns, Si:15ns), depending on the type of photo-diode compared to, and thus in good agreement with the data sheet quoting 20ns delay. With this correction the repopulation of the upper laser level coincided with the peak of the visible fluorescence in figures 5.8b/c.
This coincidence in time makes repopulation of the upper laser level the more likely mechanism for the after-pulse than a bottleneck effect caused by the lower laser level life-time.

After-pulses can also be caused by insufficient hold-off of the Q-switch. However, these pulses appear later when compared to the main peak (up to several 100ns) and also have a constantly changing delay and broad pulse-width ($\geq$ 100ns), due to the switching on a low, varying cw background. The after pulse caused by the recirculating population connected to the up-conversion process has a fixed time delay from the main Q-switched peak and a short pulse duration, as is usual for gain switched pulses. To demonstrate the transition from a cleanly Q-switched pulse with a hidden after-pulse in its tail, to a short pulse duration, allowing one to see the rising edge of the after-pulse, the following sequence of pulse forms were taken:

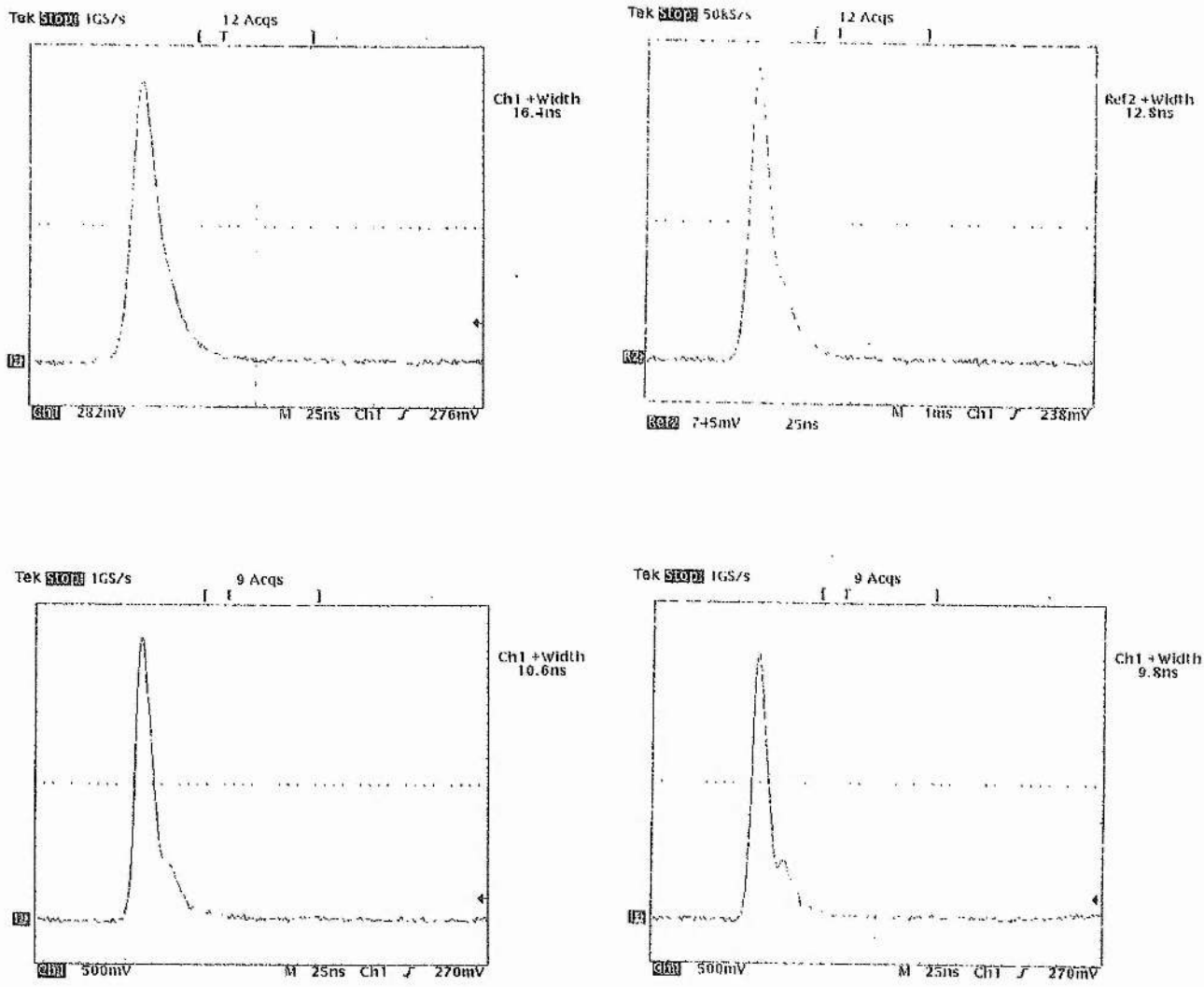

Fig. 5.9: *Changing the repetition rate from 6kHz down to 1kHz shows the gradual appearance of the gain switched after-pulse in the tail of the main pulse. The high temporal stability and short pulse width of the after-pulse sets this gain switched pulse apart from after-pulses due to incomplete Q-switching. No realignment of the cavity or Q-switch was done during this sequence ($l_{geo.}$=12cm, 10W pump).*

The significance of the after-pulse as a loss mechanism is particularly a concern if the second pulse makes a visible change to the shape of the Q-switched main pulse. For very short pulses (≤ 10ns) at low repetition rates a gap or separation of the two pulses reduces the useful peak intensity for non-linear optics experiments.

Contrary to this, the up-converted parts of the radiation caused by the resonant two-step reabsorption, which populates the UV emission states, always cause losses in the 1μm output, due to the μs-life times connected to these transitions. Both loss routes have in common that they are only likely to become a significant loss mechanism at low repetition rates combined with higher pump powers (i.e.: ≤ 2kHz and 20W diode pump powers). Unfortunately damage limitations for the slab coatings prohibited a detailed investigation of this low repetition rate, high pump power operation regime. Improved coatings were made available in a second batch of Nd:YLF slabs, made for I.E Optomech, which developed the packaging of the 1μm laser system into a product. Based on these slabs (courtesy of I.E.) a few results could be taken under low repetition rates and higher pump powers to determine the effects of excited state absorption as a loss mechanism on the effective life-time of the upper laser level in Nd:YLF . This effect is described in the next section in greater detail.

5.2 Up-conversion as a significant loss mechanism

A very simple and reliable method to determine the effective life-time, with reasonable accuracy, is given in a method proposed by Seelert and Kortz [3]. In this method they apply the following fit to the extracted energy per pulse as a function of the repetition rate:

$$E = E_0\left(1 - \exp(^{-\tau_{pump}}/_{\tau_{eff}})\right) \tag{5.1}$$

With E_o being the maximum pulse energy for an infinite pumping time, τ_{pump}, and τ_{eff} denoting the effective fluorescence life-time. Equation 5.1 describes the stored energy in the upper laser level per pump cycle as a function of the pump and fluorescence life-times. In order to make the transition to the extracted energy per pulse the main assumption of this fit has to be that the extraction efficiency of the stored energy remains constant, an approximation which is fulfilled in the case of operation well above threshold [9]. For operation twice above threshold an extraction efficiency of ~80% is reached.

The important advantage of this simple method is that this fit describes the normalised pulse energy, E/E_o, over a wide range, independently of changes in the loss behaviour, which depends on the pump power level and slab used, the slabs being from different batches as explained before.
The analysed pulse energies in the pump power range between 5 and 20W, corresponding to pump intensities of 0.7 to 2.8 KW/cm^2, clearly indicate that the up-conversion process is a substantial loss mechanism reducing the effective storage time of the Nd:YLF gain medium.

The effect of a reduced fluorescence lifetime is most pronounced at pump intervals equal or longer than the effective fluorescence life time, which in this case are repetition rates around the 3kHz margin. At pump power levels beyond 10W these repetition rates could not be accessed with the original batch of 1µm coated slabs, without incurring coating damage. At up to 5 kHz repetition the extracted energy per pulse between the measured 270µs (Fig. 5.10) and expected 480µs lifetimes is negligible. The results in the 1kHz region only were taken by I.E Optomech on the DAYlight laser system, all other results were taken on the original system developed in this work.

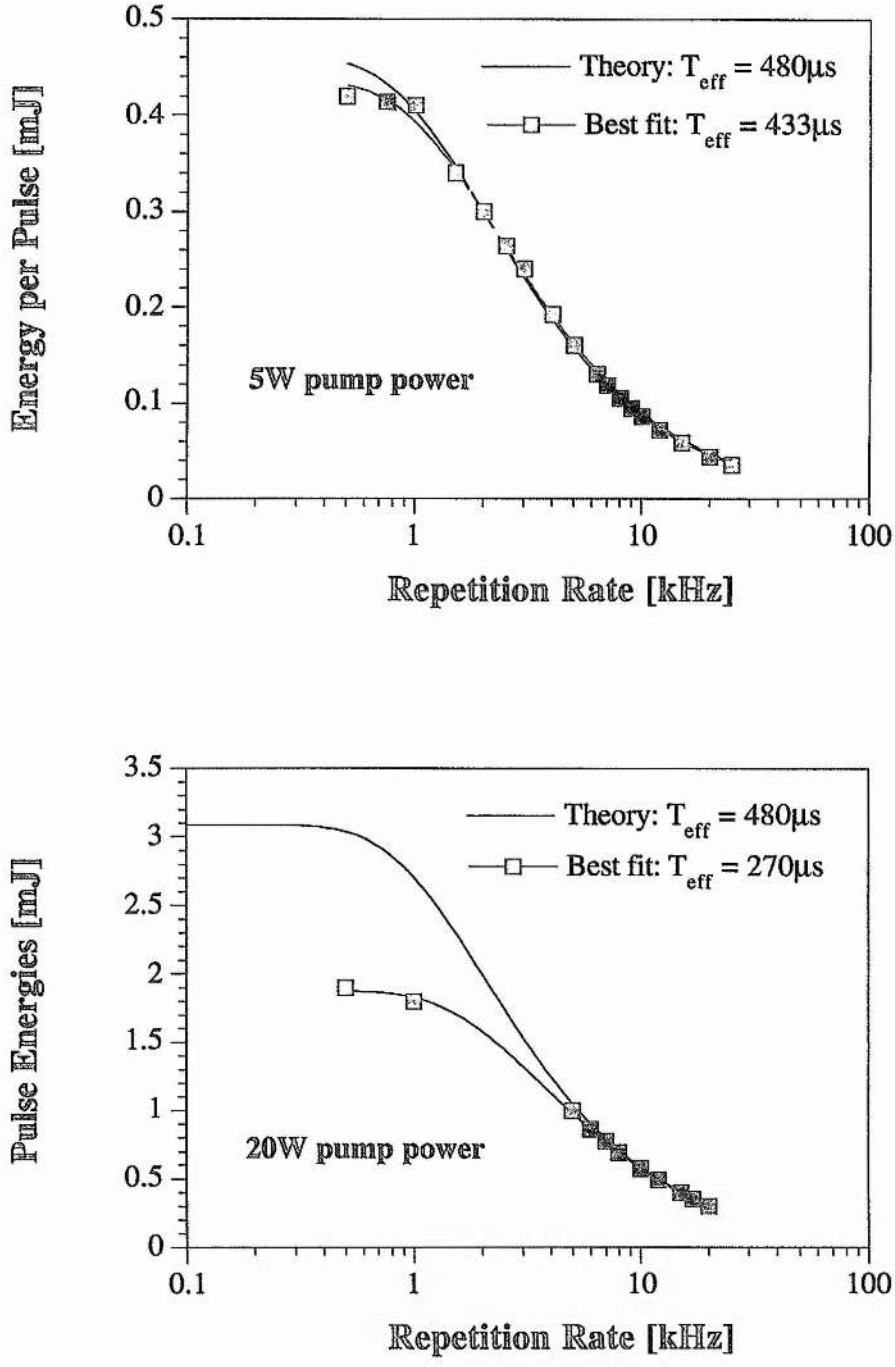

Fig. 5.10: *Comparison of pulse energies as a function of the repetition rate at low and high excitation densities. The deduced upper state lifetime decreases from 450µs at the 5W pump power level to 270µs at 20W pump. Free parameters for the fit were E_o and τ_{eff}. In the case of the extrapolated energies for a 480µs life-time, only the first 5 high repetition data points have been used, with only E_o as the free parameter.*

This considerable decrease in lifetime could be cross-checked and verified at least in tendency with the same slab used in the DAYlight laser, but this time as part of the system at St. Andrews. Evaluating that slab for I.E. Optomech on the system developed during this thesis and at a pump power level of 15W led to a reduced life time of 410µs for the corresponding excitation density of 2 KW/cm^2. An overview of the effective fluorescence life-time as a function of the diode pump power is given below.

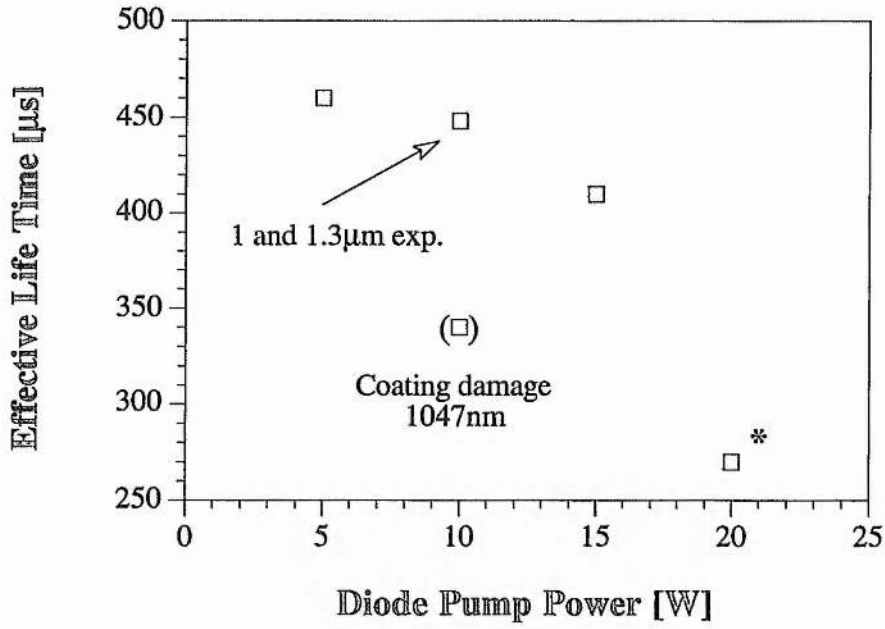

Fig. 5.11: *The decreasing effective storage capacity of the upper laser level $^4F_{3/2}$ under high excitation densities at 797nm, with the pump polarisation parallel to the c-axis of the Nd:YLF slab. (*:= Results by I.E. Optomech [8])*

The 20W pump power result is denoted with a star, because of the non-identical experimental conditions. Even an assumed extracted energy per pulse of 2.3mJ at 1kHz (a more than optimistic assumption, given the fact that the DAYlight prototype at I.E matched the average power results of the original system), corresponding to a life time of 380µs, would decrease the storage capacity by 20% as an estimated upper limit under excitation intensities of the order of 2.8 KW/cm^2.

One problem with the lifetime results at the 10W pump power level was finally resolved, as being caused by the start of damage to the coated slab surfaces. To improve the accuracy of the lifetime fit, repetition rates below 2kHz were desirable and attempted, although 2kHz is the known safe, long-term operation limit at this pump power level. The reduced energies per pulse at 1.5

and 1kHz suggested an upper-state life-time of 340μs, and are in contradiction with the fluorescence lifetime results at 15W pump power, which are higher.

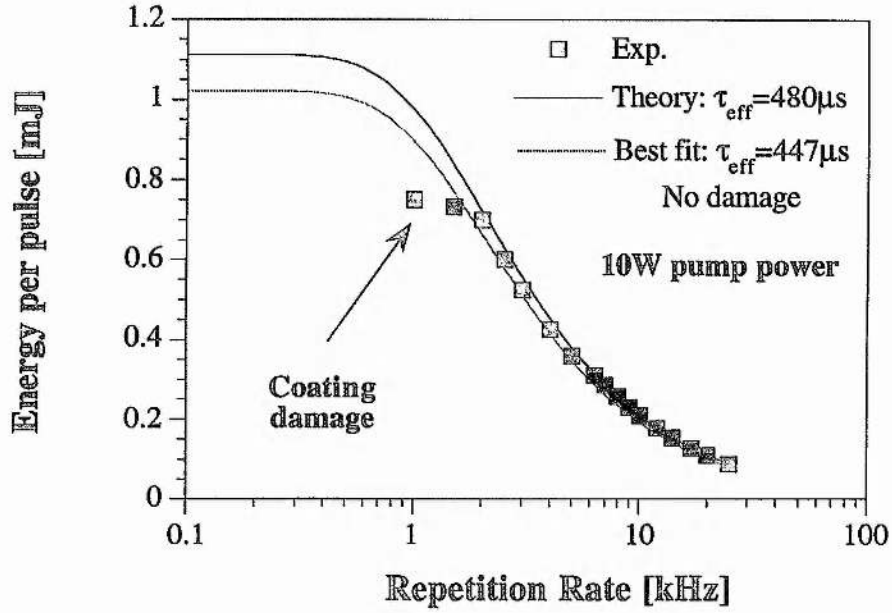

Fig. 5.12: Damage to the slab coatings can reduce the pulse energy at the low repetition rates, which are important to get an accurate fit. Up to 2 kHz the pulse energies are in line for lifetimes of 450μs. Damage to the coatings was confirmed by a 15% drop in cw output. This is a characteristic sign of the beginning of coating damage.

Removing the damage suspect results at 1kHz corrected the lifetime to 450μs, as assumed in figure 5.11. To confirm this fluorescence lifetime at 10W pump power the same fit was applied to the energies of the repetitively Q-switched 1321nm line (Fig. 5.24 in the next section). This time the lifetime determined was 447μs, which is in agreement with the 1μm transition result above. This is an expected result as both transitions share the same upper Stark split sub-level of $^4F_{3/2}$.

The coating damage problems with operation at 1μm, as compared to the damage-free operation at 1.3μm, despite higher intracavity intensities, highlights that it is most likely the UV intensities below 400nm which are responsible for the coating failure. According to the suppliers, Lightning Optical Corporation, the coating composition used starts to absorb below 400nm. This damage mechanism might also explain the unusual fact that a total coating failure was never experienced, only power drops in the region of 10 to 20%, as a rule. By clamping the maximum extractable energy through this damage, the

UV intensities during the Q-switched pulse appear to be restricted to tolerable levels, causing no further degrading of the coating.

The measured reduction of the effective fluorescence lifetime confirms the earlier assumption that the visible and UV transitions are only a faint echo of the present total up-converted population. A significant amount of population appears to cycle in the upper G and D manifolds under higher pump densities of 2 kW/cm^2, as encountered under 15W and higher cw pump conditions with the focusing arrangement used.

5.3 Beam quality improvement under Q-switched operation

The up-conversion process cannot only have an impact on the laser performance by reducing the accessible population in a spatially uniform manner. A radially varying loss mechanism, with higher losses towards the edges of the transversal mode structure, could be responsible for the improved TEM_{00} operation under Q-switched conditions. To investigate the spatial reabsorption behaviour it was again very helpful to capture the fluorescence through the top cooling surface of the Nd:YLF slab with a CCD camera and frame grabber. To resolve the two fluorescence wavebands of interest, which are the visible and near UV bands, coloured filters were used (Schott BG37 (green pass) & VG6 (blue/UV pass)) in order to block the unwanted parts of the spectrum. In addition the scattered pump radiation was always blocked with a couple of Schott BG38 filters.

The spatially dominant up-conversion region can be determined by looking at the time delay between the visible fluorescence peak and the laser peak intensities. Experimentally this time delay remains constant at 15ns (if corrected by the multiplier delay of 20ns) for the 1μm transition. The delay is independent of the repetition rate, which changes the value of the initial inversion from just around threshold condition to several times (≤ 10) above threshold inversion. This is an indication that the main up-conversion intensity, as recorded by the photo-multiplier in the visible spectral region, is in the area of the undepleted inversion towards the edge of the transversal mode structure. It thus scales linearly with the peak 1μm intensity on an almost constant inversion background.
An up-conversion process subjected to a strong competition between depletion of the inversion through the laser transition and 1μm reabsorption, as found in the centre of the transversal mode structure, would show a varying time delay between the two peaks, depending on the inversion ratio. The figures below show the varying time delay of the product of inversion and 1μm photon densities (which is the driving excitation of the visible fluorescence peak) in relation to the Q-switched pulse, by solving the standard coupled Q-switch equations [9] under the assumption of a constant inversion profile (as opposed to radially varying gain under realistic pump conditions).

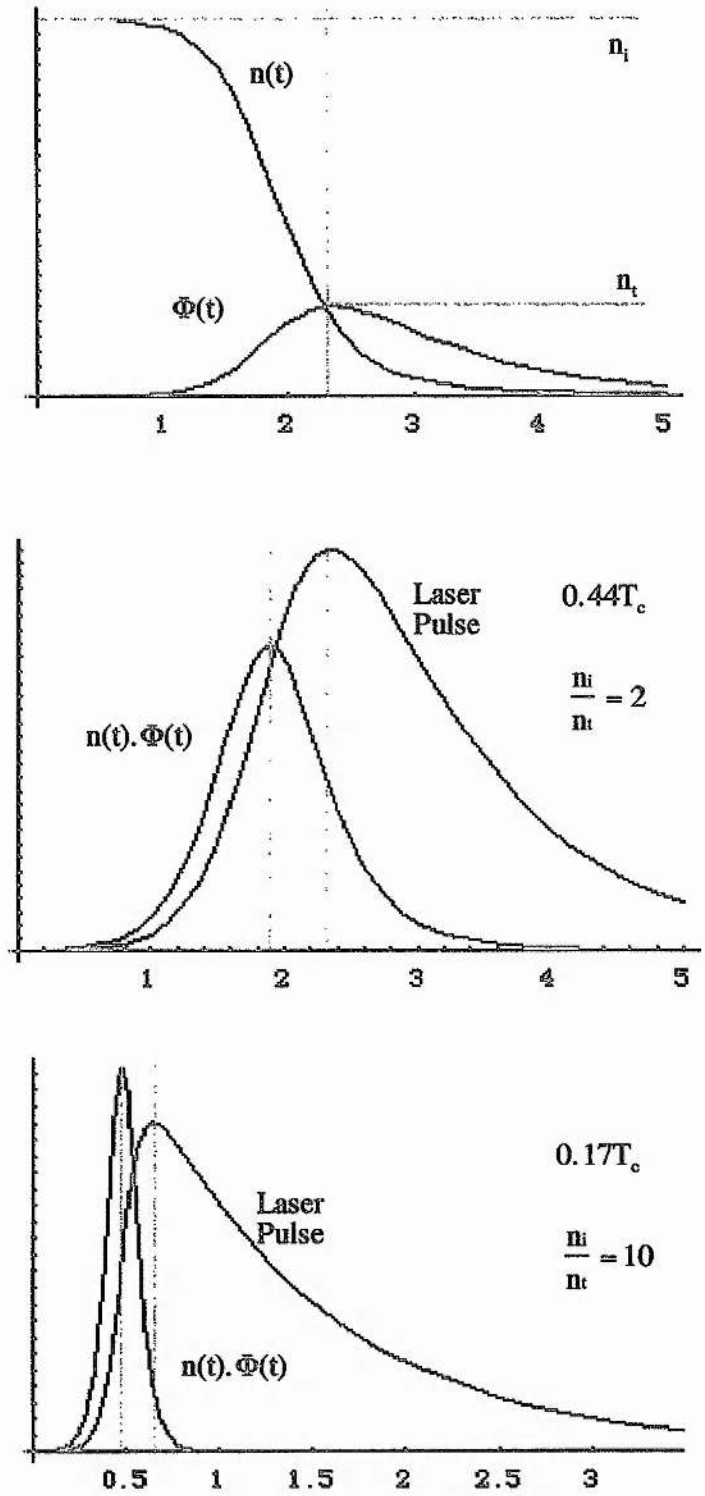

Fig. 5.13: *The changing time delay between the peak intensity of the laser pulse and the product of inversion with photon density ($n(t)x\Phi(t)$) for different initial inversion densities. The time scale is normalised in units of the photon decay time of the resonator [9].*

The lifetime of the $^2G_{9/2}$ level, which is approximately 15ns, adds a constant delay to the actually observed fluorescence pulse (from $^4G_{7/2}$ into the ^4I-levels) and broadens the falling edge. Despite the change introduced by the lifetime of the $^2G_{9/2}$ level, a varying peak to peak delay, which is comparable to the laser pulsewidth, would have to be obvious. Pictures of the green-yellow fluorescence band under Q-switched operation, with a maximum of the ESALR at the edge of the 1µm mode, confirm the above hypothesis and agree with the observation of a constant fluorescence peak delay, independent of the repetition rate.

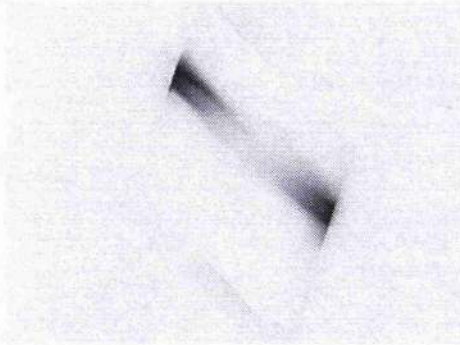

a)

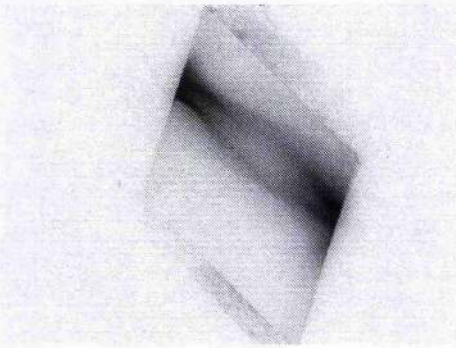

b)

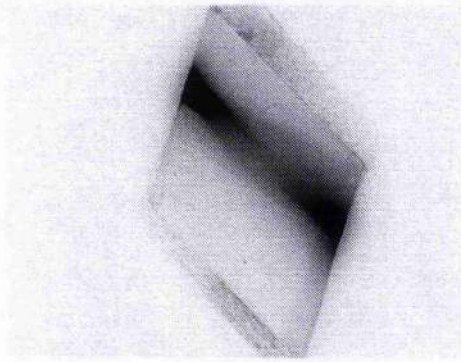

c)

Fig. 5.14: *Comparison of the spatial up-conversion distribution under Q-switched operation (2kHz) for the visible (**a**)) and infra-red (**b,c**)) fluorescence. The IR fluorescence under Q-switched (**b**)) and blocked resonator conditions (**c**)) is given as a comparison, to confirm that the maximum of the inversion is in the centre of the pump region. Scattered pump and near UV radiation is suppressed with filters.*

As predicted, the visible fluorescence has its peak activity at the edge of the mode structure (a), while the centre shows almost no up-conversion activity. It is important to keep in mind that the CCD camera has an exposure time of 20ms, which thus averages the fluorescence during the Q-switched (ESALR) and non-lasing time intervals (ETU). Despite the different time intervals (20ns pulses interrupted by ≤500μs non-lasing intervals (2kHz)) the high intensity during the ESA up-conversion at the edges of the transverse mode is still the dominant fluorescence activity region in the visible.

The up-conversion under 1.047μm operation is therefore a loss mechanism, which benefits the transversal mode control by suppressing intensities towards the edge of a TEM_{00} mode during the pulse build-up. In particular, TEM_{01} modes are effectively suppressed, as they have a minimum of their field intensity where the TEM_{00} mode has its maximum. Under high inversion ratios (low repetition rates) the pulse build-up will preferably start in the centre of the inversion with a TEM_{00} profile.
This spatially varying loss mechanism ties in well with the observation of improved beam quality under Q-switched conditions as opposed to the beam quality under cw conditions.

The second stage up-conversion process is again an ESA process of the 1μm laser emission, involving the previously up-converted population at $^2G_{9/2}$, as the photos below demonstrate. The other possible route, an ESA up-conversion involving the visible fluorescence emission itself from the upper laser level at $^4F_{3/2}$, can be ruled out, since the UV emission shows an inverted pattern to the green-yellow emission bands under Q-switched conditions shown in the figure above.

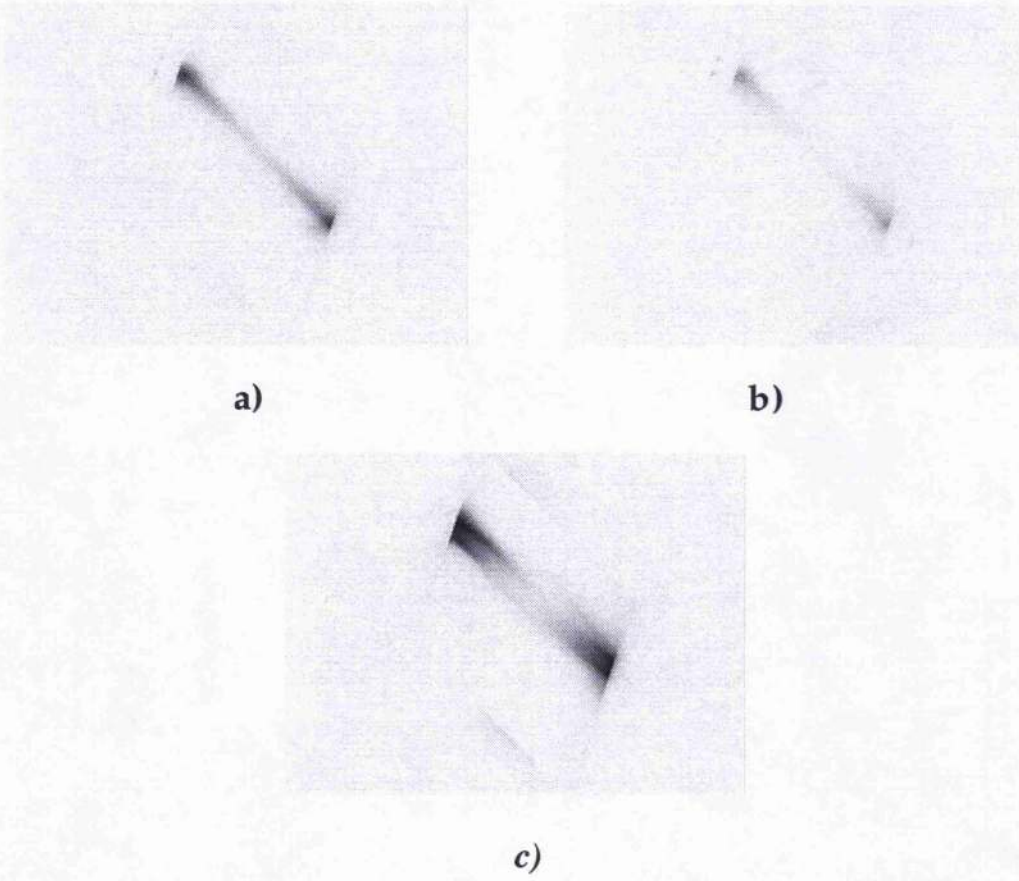

a) b)

c)

Fig. 5.15: *Comparison of the spatial up-conversion regions for the UV-bands (**a**),**b**)) and green-yellow fluorescence (**c**)). In both cases the laser operates in TEM_{00}. The two step up-conversion (UV) has its maximum in the centre of the mode structure, contrary to the visible fluorescence (**c**)) . The gain settings on the CCD camera are the same, with a common 20ms sampling time.*

The two step up-conversion process shows a typical quadratic dependence on the laser intensity at 1047nm. This non-linear dependence is obvious in the increasing intensity of the UV, depending on the repetition rate of the Q-switch, demonstrated for repetition rates of 1 and 6kHz in the figures a), b) above. Contrary to this is the linear scaling of the visible fluorescence components with the intracavity intensity, as they are due to a single step excitation process. The measured intensities of both fluorescence bands are presented below, verses the intracavity peak intensity under Q-switched conditions.

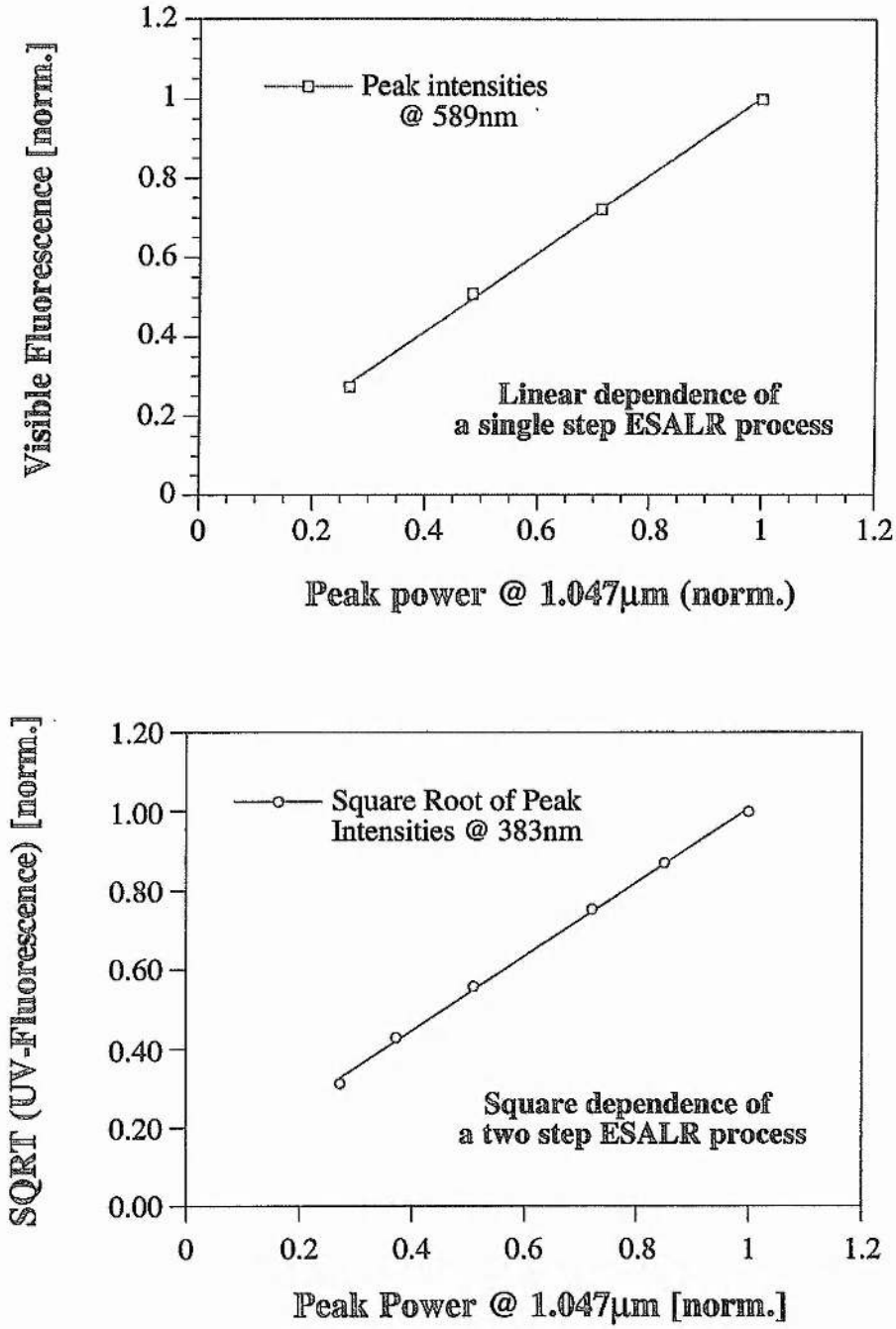

Fig. 5.16: *Normalised peak fluorescence intensity in the UV (383nm) and visible (589nm) as a function of the normalised peak power per pulse. The curves show the expected quadratic and linear dependency for the UV and visible emission, corresponding to two- and single step excitation respectively (10W pump power, output coupling:30%).*

The same relation could be found for the other wavelength bands, however small changes from an ideal slope of 1 for the normalised intensities were

present to a varying degree. This indicates the presence of possible cross-relaxation mechanisms or saturation effects, influencing the measured fluorescence intensities towards higher pulse intensities. A pulse form in the UV, indicating such an exchange of population between excited states, which increases the absolute fluorescence intensity, is shown below.

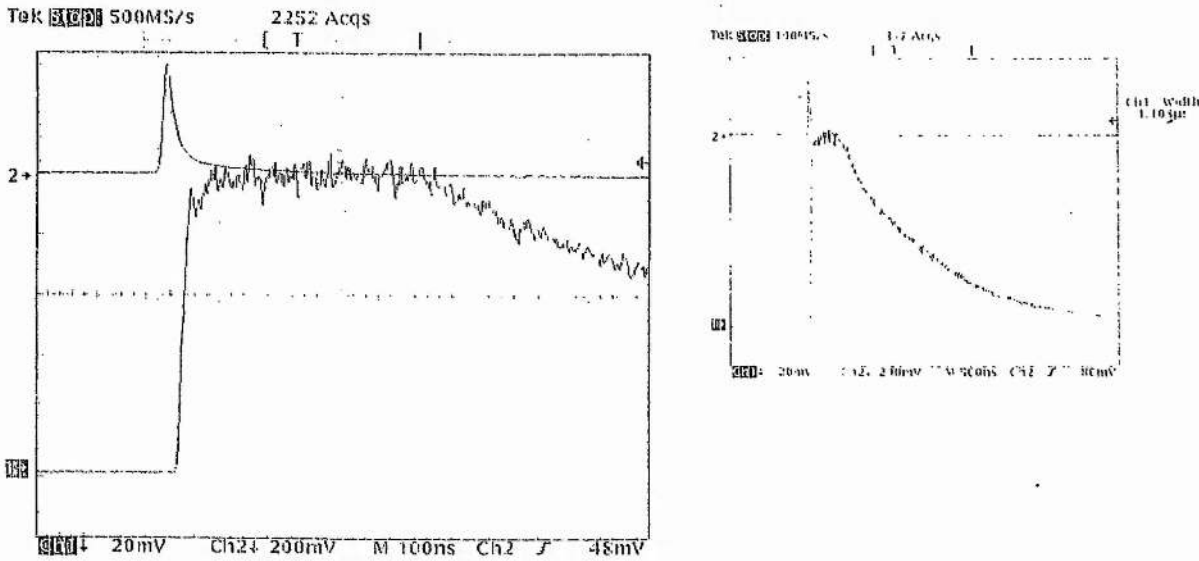

Fig. 5.17: *Temporal response of the 383nm line after two-step up-conversion of the 1047nm emission. The sharp rising edge is due to the initial up-conversion caused by the ~25ns laser pulse, and the following slow rising flank indicates a transfer of population from another UV line, delaying the onset of the exponential decay by some 100ns.*

No further investigation of these effects was attempted, as it would not have changed the significance of the up-conversion as a general loss mechanism, which improves the beam quality due to a spatially varying loss during the critical pulse build-up-time.

5.4 Fluorescence properties under 1.321μm operation

The unexpected fluorescence behaviour of the 1.3μm transition under cw operation continues to be puzzling in the Q-switched mode. Unlike the much brighter appearance of the fluorescence during 1μm Q-switched operation, the intensity of the up-converted radiation remains almost unchanged under both modes of operation in the 1.3μm case. This lack of UV or two-step up-conversion activity does not give any direct hint of an additional loss route, which would be responsible for the higher thermal load experienced under 1.3μm operation. However, having the same stark split upper level of $^4F_{3/2}$ in common with the 1μm line, a comparison of the behaviour of both transitions allows one to verify some of the earlier up-conversion mechanisms.

The fluorescence spectrum in the visible, consisting of bands in the green, yellow and red, remains unchanged as far as the peak wavelengths are concerned, although the absolute intensities are lower for a similar intra cavity intensity and pump power level if compared to the 1μm activities. Only very faint UV bands can be detected with the photo-multiplier set-up. These traces of UV appear at the same centre wavelengths as before, with the 387nm-line again being the most dominant . To the eye only the blue band centred around 450nm was visible and no traces of the blue-whitish emission, characteristic for the 1μm Q-switched operation, could be observed. This, together with the barely noticeable intensity change between cw and Q-switched operation, where no depletion along the centre of the transversal mode path is visible, are the most striking differences when compared visually to the up-conversion under 1μm operation.

The measured fluorescence spectrum could only be recorded for the directly pumped volume of the crystal. Due to the faint intensity in the unpumped region no spectrum could be taken there, however, to the eye this part of the up-conversion process also showed the characteristic yellow-green appearance. Figure 5.18 shows the barely distinguishable visible emission during cw and Q-switched operation. The shutter time on the CCD camera during all experiments was 20ms, which thus averaged the incoming intensity over several tens of pulses, depending on the repetition rate.

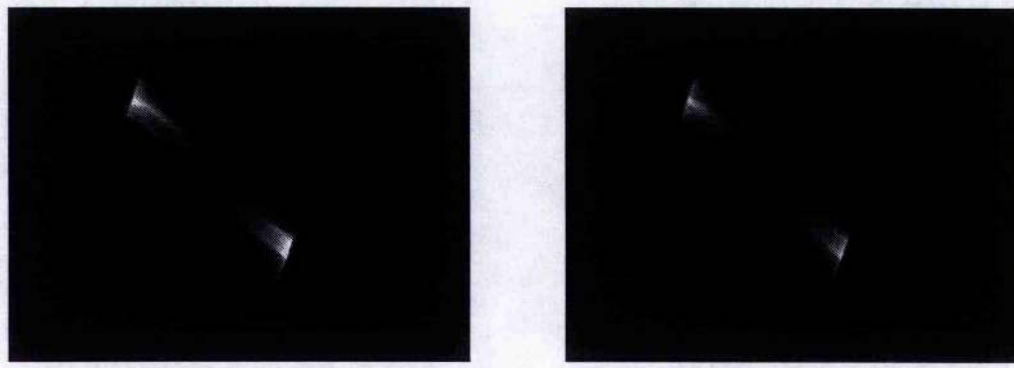

a) **b)**

Fig. 5.18: *Spatially resolved fluorescence intensity comparison between cw (**a**)) and Q-switched (**b**)) operation at 1321nm. The modes of operation are only just distinguishable and do not show the depletion of the visible fluorescence in the centre of the resonator path. UV and scattered pump light components were blocked with filters.*

This would suggest that the fluorescence intensity due to ESA scales with the average intracavity intensity, as the average output power remained in the 800 to 500mW region regardless of the mode of operation (cw (a) or 2kHz (b) switched respectively in figure 5.19). This linear scaling with the pulse intensity is verified in the figures below.

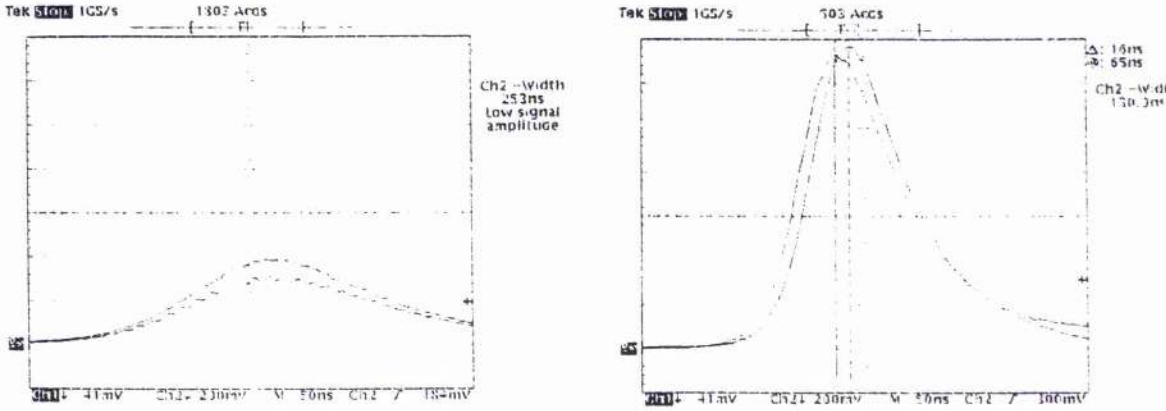

a) **b)**

Fig. 5.19: *Q-switched pulse at 1.321μm and corresponding fluorescence signal at 532nm in the pumped area. The fluorescence linearly follows the Q-switched pulse intensity, as can be seen from the two scope printouts for repetition rates between 6kHz (**a**)) and 2kHz (**b**)). The measured time delay between the laser pulse and fluorescence signal is 16ns (**b**)). This time delay has to be corrected for the measured delay of the photo multipliertube (also 20ns, Si-detector). Therefore the fluorescence immediately follows the laser pulse.*

With the multiplier time delay also being 20ns, the visible fluorescence under 1.321μm operation immediately follows the laser pulse. The absence of the usual ~35ns time delay (corrected:15ns) between laser pulse and fluorescence peak is different to the 1μm spectrum. The likely explanation for the immediate decay of the fluorescence as compared to the 15ns delay during 1μm operation, could be because the level of origin for the visible transitions, the $^4G_{7/2}$ state, is pumped directly under 1.3μm ESA and decays very quickly with a ns lifetime. For the 1μm case, the possible slower radiation less transition from the $^2G_{9/2}$ level, excited under 1μm ESA, into the $^4G_{7/2}$ state is responsible for the characteristic 25ns delay.

The comparatively faint fluorescence intensity in the unpumped area is too small under the gain setting of the CCD camera used above to be resolved and needs over exposure of the directly pumped parts to make it visible, as depicted in the figure below. Interestingly, this area of the fluorescence did not show any intensity gain, either when the cw intensity was compared with the Q-switched one, or between different repetition rates. The picture below shows this almost constant up-conversion intensity in the unpumped area.

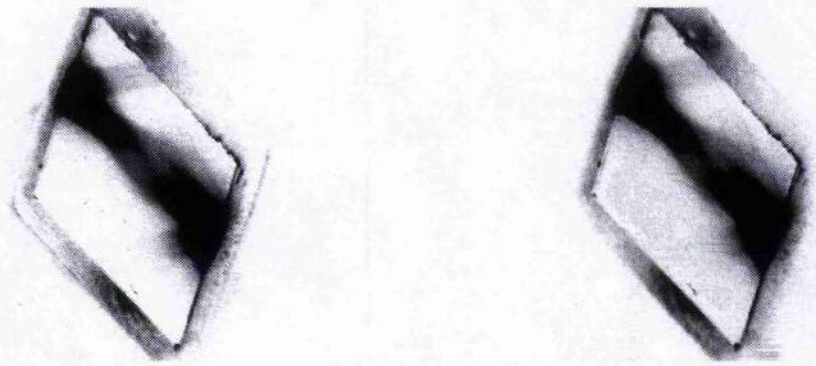

a) **b)**

Fig. 5.20: *Comparison of the fluorescence intensity under 1.3μm operation in cw and Q-switched mode. In particular the intensity in the unpumped area decreases slightly from cw (**a**)) to Q-switched (at 2kHz) (**b**)) operation, when recorded with a CCD camera. The pumped areas are heavily overexposed to make the faint fluorescence intensity in the rest of the resonator path visible.*

The almost constant fluorescence intensity in the unpumped area (Fig. 5.20a/b) is particularly perplexing, as in this case a multi-photon process appeared at

first to be the most likely mechanism for excitation to the visible emission states. Such an excitation route would have to be strongly non-linearly dependent on the 1.3μm intracavity intensity. The absence of this nonlinear behaviour suggests that the same one-photon absorption as in the directly pumped area is responsible for the up-conversion.

Spatial migration of excited $^4F_{3/2}$ states out of the pumped area into the unpumped region, can be neglected, as the diffusion length of such processes would be restricted to a region in the order of 100μm and would not cover the several mm of distance observed in figure 5.21. In order to rule out reflection effects from the coated Nd:YLF crystal sides, the coatings were checked for transmission in the UV and visible with the coating supplier. The result of this check was high transmission in the visible and at the pump wavelength (T≥95%. A.of.I.: 27°) and absorption starting below 400nm. Reflection of the visible fluorescence off the coated surface is anyway unlikely, due to the dependence of the fluorescence on the presence of resonating 1μm photons within the cavity. This leaves the scattered pump light as the only plausible explanation for the observed fluorescence in the not directly pumped region. The extent of the up-conversion within this weakly excited area is amazing, as the picture below underlines:

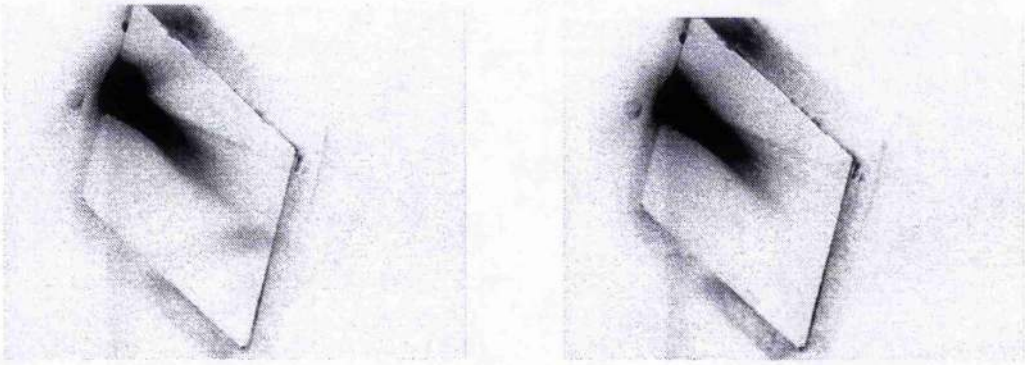

a) **b)**

Fig. 5.21: *Observed fluorescence under cw operation at 1321nm, if only one side of the slab is pumped (**a**)). No fluorescence activity outside the directly pumped area is recorded for a blocked resonator (**b**)). The other diode module is shorted out (pump power:10W, T=5%).*

Following the hypothesis that these excited states are due to scattered pump radiation, means that the same spatial spread should be present when the 1μm

slabs are pumped. However, no up-conversion in the unpumped region could be observed under 1μm operation. This is an indication that the up-conversion process during 1.3μm operation has a higher crossection, assuming that the branching rate into the radiative decay route, the only signal which is monitored, is similar for the 1.047 and 1.321μm up-conversion processes.
This higher reabsorption crossection at 1.321μm would be in agreement with the drastically higher thermal surface load present in the slab under this mode of operation, as was discussed in the thermal lensing section of the 1.3μm chapter. The higher thermal load could be attributed to radiation-less transitions from $^4G_{7/2}$, which would be the dominant decay route for repopulation of the upper laser level. Again the fluorescence is only a faint indication of the population actually circulating in the higher Nd:YLF energy levels. As the reabsorption process is detectable even in areas where only scattered pump radiation populates the excited states (unlike in the 1μm operation), it is obvious that the maximum heat deposition will be closest to the pumped window, where the density of excited $^4F_{3/2}$ states is at its maximum value. This spatially selective heating effect maximises the surface governed lensing effect in Nd:YLF and resolves the confusing fact that similar total heat deposition under 1.047 and 1.321μm operation, within identical experimental conditions, gives rise to totally different lensing coefficients.

The faint UV lines detected during 1.3μm operation exhibit the same non-linear intensity rise with repetition rate as is familiar from the 1μm experiments. A comparison of the cw and Q-switched UV intensities, as recorded with a CCD camera through the top cooling surface, is shown below.
This non-linear behaviour is typical of the two-photon absorption process, which leads to the UV lines. The recorded intensities are very faint, as can be seen from the UV generation due to ETU (c), showing comparable intensities to the emission under Q-switched conditions. The very faint UV emissions under Q-switched operation are different in their up-conversion route to the UV conversion in the Q-switched 1047nm transition shown before.
This is due to the lower energy of the 1.3μm photons, making the second stage up-conversion process into the $^4D_{1/2\text{-}7/2}$ manifolds very unlikely, as they require an excitation energy equivalent to the 1μm photons, assuming that the $^4G_{5/2\text{-}7/2}$ states are the starting points for this up-conversion route.

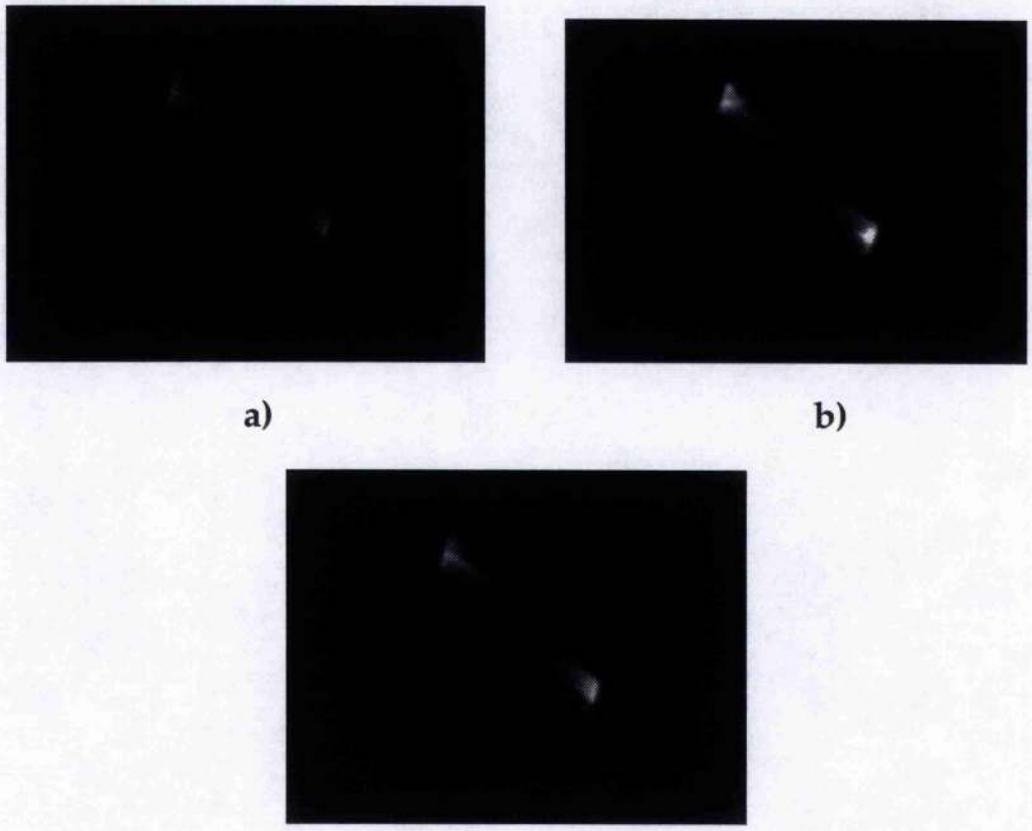

Fig. 5.22: *By using a filter with a broad pass UV-band the near UV-lines were isolated from the rest of the spectrum and recorded with a CCD camera. The rise in UV fluorescence intensity due to ESA during the transition from cw (**a**)) to Q-switched (**b**)) operation is clearly visibly. The UV intensities due to ETU under cw pumping and with a blocked resonator(**c**)) are given as a comparison. The diode pump power is 10W in all 3 pictures, with no changes in the gain of the CCD camera settings (output coupling T=5%).*

The second possible up-conversion route into the UV states must therefore be the main contributor to the population. This is the reabsorption of the yellow-green fluorescence lines from the upper laser level, $^4F_{3/2}$. This process is still a two-step excitation process, with its quadratic intensity response, however, the crossection of this up-conversion process appears to be low, as the comparison with the similar cw UV intensities suggests. Given that the up-conversion process through reabsorption of the yellow fluorescence line from the upper laser level is independent of the lasing wavelength (1 or 1.3µm), confirms that the earlier result of a 1µm reabsorption from the $^2G_{9/2}$ manifold is the dominant UV lines excitation mechanism during 1µm operation.

A comparison of the visible fluorescence activities due to ESA, in the directly pumped and unpumped region of the crystal, is helpful in understanding the different behaviour of the 1 and 1.3μm transitions. The table below summarises the differences:

Region of the slab under lasing conditions	Fluorescence activity at: 1047nm	1321nm
directly pumped region	strong reduction of the visible fluorescence due to depletion along the centre of the resonator path	increased up-conversion activity along the resonator path despite depletion of the $^4F_{3/2}$ manifold
'unpumped' region; only scattered pump radiation provides ESA starting points	no visible fluorescence	faint visible fluorescence, due to single photon absorption from $^4F_{3/2}$

Fig. 5.23: *Comparison of the different up-conversion intensities in the pumped and unpumped region of the slab under 1 and 1.3μm operation.*

Both the 1 and 1.3μm laser transitions share the same upper stark-split level of the $^4F_{3/2}$ manifold, giving rise to the same fluorescence lifetime for both transitions.
This was confirmed by applying an exponential fit to the energy per pulse at 1321nm, as described earlier for the 1μm transition, yielding the same lifetime of ~450μs in each case.

The identical results for the fluorescence lifetime indicates only that the losses as a function of the repetition rate are the same for both wavelengths, despite their different up-conversion characteristics. A constant loss, scaling linearly with the intra-cavity intensity, cannot be detected with the above method.

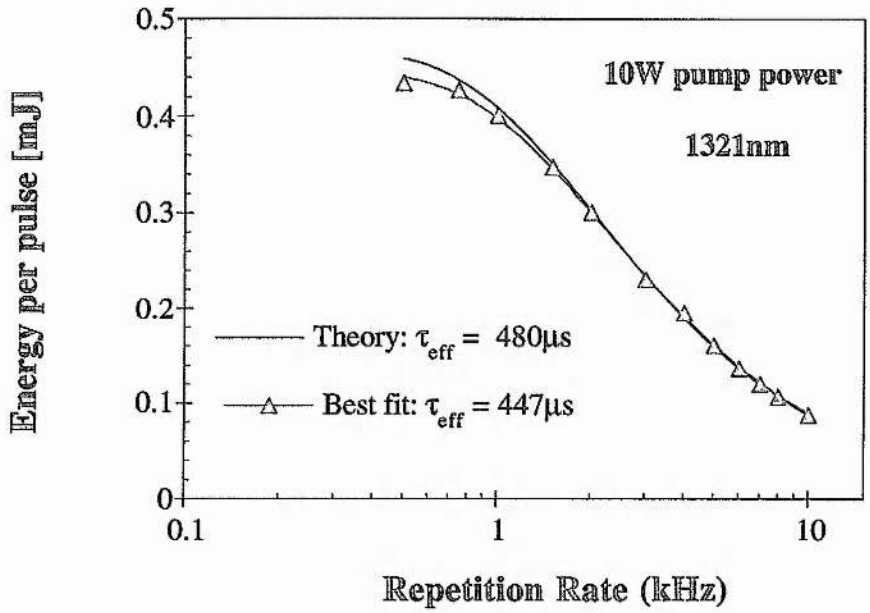

Fig. 5.24: *Deduced upper laser level lifetime of 447µs for the 1321nm transition in Nd:YLF (10W pump corresponding to 1.4KW/cm² excitation density) is in agreement with the 1047nm results. The pump polarisation is parallel to the c-axis.*

The loss factor contributing to the effective fluorescence lifetime shortening of the 1047nm transition is the two-step up-conversion, a varying loss mechanism which depends on the switching rate, due to the quadratic nature of the reabsorption, which populates the D-manifold. The trapping of population in the UV emitting states of the D-manifold, with lifetimes in the µs region, is far too long a delay for repopulation of the upper laser level, in time to provide gain for a 10 to 100ns pulse. The absence of any significant two step excited state absorption of laser radiation, as indicated by the minimum UV activities, suggest that the 1.321µm line in Nd:YLF does not suffer from a reduction of the effective upper state lifetime as in the 1.047µm transition. This appears to be one of the more easily accessible tests of the assumptions made during this chapter and should be followed up a later stage.

Opposed to this are the ns lifetimes of the G-states (populated by the first step up-conversion process), which permit a repopulation of the $^4F_{3/2}$ level, thus contributing gain to pulses with a duration of 10 to 100ns. The up-converted, and quickly circulating population of the G-manifold is an obvious loss

mechanism for very short pulses in the 10ns region, for which a clear separation of main and after pulse exists. An estimate of the magnitude of this up-conversion cross-section for the 1047nm transition can be made by looking at the magnitude of the after-pulse under very short pulse durations (~10ns pulses in Fig. 5.8).
A pronounced difference in the cross-sections for the reabsorption of the laser emission into the G-levels for the 1047 and 1321nm transitions is the proposed reason for the measured higher thermal load under 1.321μm operation. The long pulse durations at 1.3μm (from 80ns up to several 100ns) as compared to the ns-lifetime of the population circulating between the G- and F-levels prevents direct proof of this hypothesis by measuring the magnitude of the 1.3μm after-pulse for pulse durations of ~10ns for the main 1.3μm pulse.

So far the only experimentally accessible differences between both up-conversion activities in the visible is the difference in the spatial up-conversion activity of the green-yellow fluorescence and the strongly enhanced surface deformation under 1.321μm operation, as measured by the increased thermal lensing coefficients.

5.5 Conclusions

The up-conversion properties of Nd:YLF were investigated by resolving the ESA-spectrum in the visible and near UV both by a time dependent spectral analysis as well as a spatially resolved spectrum for two of the π-polarised Neodymium lines in Yttrium Lithium Fluoride.
Both upconversion mechanisms at 1047nm and 1321nm operation in Nd:YLF are a significant loss contributing factor under the high pump power densities encountered in end-pumped, Q-switched laser systems, such as the one developed during the course of this thesis. The 1047nm line is only significantly affected by excited state absorption (ESA) under Q-switched conditions, showing a pronounced reduction in the effective upper state lifetime for low repetition rates. The higher reabsorption of the laser emission at 1321nm also affects cw operating conditions, by giving rise to increased surface deformation, as measured by the drastically increased thermal lensing.

The first up-conversion activity is ESA involving the upper laser level $^4F_{3/2}$ through reabsorption of the laser emission to populate the $^2G_{9/2}$ and $^4G_{7/2}$ levels. This loss mechanism scales linearly with the intra-cavity intensity and the lifetimes involved are in the ns regime.
Opposed to this is the square dependence of the two stage excited state up-conversion on the intra-cavity intensity, significant only under 1047nm operation, involving the previously up-converted population in the $^2G_{9/2}$ band finally populating the $^4D_{3/2}$ level, the origin of the observed UV bands. The µs lifetimes of these levels traps the up-converted population without any chance of repopulating the upper laser level during one Q-switched cycle. This is in contrast to the ns life times in the G-states, where the repopulation of the upper laser level is responsible for the detectable after pulse, when the main pulse duration becomes comparable to the lifetimes of the shifted population in the G-states.

The up-conversion activity cannot only be classified by its time constants and population density dependence on the intra-cavity intensity. Due to the competition between the laser emission and the upconversion, which relies on the population of the upper laser level, the upconversion also varies spatially. In particular the up-conversion process responsible for the visible fluorescence is in competition not only with the lasing transition but also with the two step ESA into the UV emitting states. These two facts account for the spatially

inverted upconversion patterns, with the UV having its maximum value in the centre of the inversion, while the remaining population in $^2G_{9/2}$, undepleted by the UV excitation route, causes the maximum of the visible fluorescence to be at the edges of the transversal mode structure. This radially varying loss mechanism is proposed as the cause for the beam quality improvement in Q-switched Nd:YLF, as compared to the cw-beam qualities.
Increased losses at the edges of the pumped volume will suppress higher order transversal modes, as these higher order modes are characterised by maxima of the field intensity close to the edge of the available inversion, contrary to a TEM_{oo} intensity profile. The table below gives an overview of the experimental evidence gathered in this thesis, which is attributed to ESA up-conversion effects in Nd:YLF under high density end-pumping.

Line [nm]	*Experimental evidence*	*Proposed up-conversion mechanism responsible*
1047	appearance of after-pulse below minimum main pulse duration	up-conversion process with ~20ns lifetime, repopulating $^4F_{3/2}$
1047	improved transversal mode control	up-conversion process with maximum loss towards the edge of the pumped volume
1047	reduced effective upper state lifetime for low repetition rates	two step up-conversion process (µs-lifetimes) scales quadratically with the intra cavity intensity
1321	increased thermal lensing and up-conversion activity in not directly pumped crystal regions	strongly increased reabsorption crossection and surface near heating via radiation less decay from $^4G_{7/2}$

Fig. 5.25: *Experimental evidence of increased losses under cw (1321nm) or Q-switched (1047nm) operation and proposed ESA up-conversion routes in Nd:YLF.*

The characterisation of the up-conversion properties in Nd:YLF has only been qualitative, with the main problem being the lack of knowledge about the spectroscopic crossections for the excitation routes described in this chapter. Of particular interest are the branching ratios between the radiative and non-radiative decays (with exact decay routes) from the excited states in the G and

D energy level bands.
The next step would be a model of the rate equations, incorporating the up-conversion transitions, to simulate the measured intensity ratio between main and after-pulse (figure 5.8), thus gaining a more quantitative understanding of the up-conversion process. A rate equation analysis of some of the up-conversion aspects mentioned here can be found in the recent paper (Jan. 1996) by Verdun et alt. [10]. It is worthwhile to note that this paper does not detect the main UV emission bands, as recorded in this thesis, which are centred at 357 and 383nm. This might be due to a detector cut-off in the UV.
The early paper by T.Y. Fan and B. Byer [2], gives calculated emission cross-sections for all the UV transitions which have been observed in this work. However, the relative strength of these crossections, when compared with the experimental data presented here, do not agree.
These disagreements underline the need for calibrated, high resolution measurements, as only a dedicated spectroscopic work can deliver, in order to come to a finally accurate description of the ESA crossections and radiative and non-radiative decay routes. An incentive to such work could be, to evaluate the idea, presented in [2], of a two-step-excitation pumped near UV/blue laser.

From the viewpoint of this work one could restrict the pump density in end-pumped systems by increasing the pumped volume and matched resonator mode size, in order to minimise the loss incurring excited state absorption in Nd:YLF, which reduces the energy storage capacity by up to 40% for this laser system. With the extraction efficiency of Q-switched lasers only varying strongly close to threshold, this has no dramatic influence on the efficiency of the laser system, but should maintain a high effective upper state lifetime. For thermal fracture reasons big pump volumes in Nd:YLF are only an option for pulsed diode end-pumped systems. In high power cw diode pumped systems, a transition to side pumped schemes is the only alternative. Coincidentally the recently developed cw-pumped, high repetition rate systems in Nd:YLF, which are superior in performance to the system developed here, are side pumped [11] and report an excellent mode quality.
The spatially varying loss behaviour in Nd:YLF, proposed as the likely reason for the improved transversal mode control in end-pumped systems, is likely to reduce the known problems of transversal mode control in side-pumped Nd:YLF systems. This positive side to the losses caused by excited state absorption makes Nd:YLF an excellent material for cw pumped, repetitively Q-switched lasers.

References

[1]: T.Y. Fan, G.J. Dixon & R.L. Byer - **Efficient GaAlAs diode-laser-pumped operation of Nd:YLF at 1.047μm with intracavity doubling to 523.6nm** - Opt. Lett. 11, No.4, 204 (1986)

[2]: T.Y. Fan & R.L. Byer - **Two-step excitation and blue fluorescence under continous-wave pumping in Nd:YLF** - J.Opt.Soc.Am.B 3, No.11, 1519 (1986)

[3]: W.Seelert, H.P. Kortz & W.Yen - **Excited state absorption and $^4F_{3/2}$ lifetime shortening in diode pumped Nd:YLF Q-switched lasers** - OSA Proc. Advanced Solid-State Lasers 13, 209 (1992)

[4]: T. Chuang & H.R. Verdun - **Energy transfer up-conversion and excited state absorption of 1047μm laser radiation in Nd:YLF laser crystals pumped in the 800nm region** - OSA Proc. Advanced Solid-State Lasers 15, 239 (1994)

[5]: W. Grossman, M. Gifford & R.W. Wallace - **Short-pulse Q-switched 1.3- and 1-μm diode-pumped lasers** - Opt. Lett. 15, No.11, 622 (1990)

[6a]: A.A.S. da Gamma, G.F de Sa, P. Porcher & P. Caro - **Energy levels of Nd^{3+} in $LiYF_4$** - J.Chem.Phys. 75, No.6, 2583 (1981)

[6b]: A.L. Harmer, A. Linz & D.R. Gabbe - **Fluorescence of Nd^{3+} in Lithium Yttrium Fluoride** - Phys. Chem. Solids 30, 1483 (1969)

[6c]: M. Malinowski, B. Jacquier, C. Linares & al. - **Laser-induced fluorescence and up-conversion processes in $LiYF_4:Nd^{3+}$ laser crystals** - Phys. Rev. B 41, No.1, 41 (1990)

[6d]: J.R. Ryan & R. Beach - **Optical absorption and stimulated emission of neodymium in yttrium lithium fluoride** - J.Opt.Soc.Am.B 9, No.10, 1883 (1992)

[7]: T.Y. Fan - **Effect of finite lower level lifetime on Q-switched lasers** - IEEE J.QE. QE-24, No.12, 2345 (1988)

C. Bibeau, S.A. Payne & H.T. Powell - **Evaluation of the terminal-level lifetime in sixteen neodymium-doped crystals and glasses** - Paper AWC3, p.236, Advanced Solid State Lasers, Utah, February 1994

[8]: Results courtesy of **I.E. Optomech**, Priv. Com. with Neil MacKinnon

[9]: W.G. Wagner & B.A. Lengyel - **Evolution of the giant pulse laser** - J. Appl. Phys. 34, No.7, 2040 (1963)

A. Yariv - **"Optical electronics"** - Saunders College Publishing, fourth edition (1991)

[10]: T. Chuang & H.R. Verdun - **Energy transfer up-conversion and excited state absorption of laser radiation in Nd:YLF laser crystals** -
IEEE J. QE. QE-32, No.1, 79 (1996)

[11]: J. Harrison, P.F. Moulton & G.A. Scott
- 13W, M^2<1.2 Nd:YLF laser pumped by a pair of 20W diode laser bars -
Paper CPD-20, Conference on Lasers and Electrooptics , Baltimore, May 1995

Chapter VI.

Frequency doubling & tripling

The conversion of the infra-red laser output into the green by single pass external doubling in a KTP crystal was the initial application of this laser as a pump source. It was the first direct test of the focus quality, although the beam quality had been measured before with good results by determining the beam waist and far field divergence in the focus and at the focal length of each spherical lens respectively.
A tight focus is vital for a laser system limited in peak power to still reach the intensities necessary for effective conversion. A decline by a factor of two in M^2, the figure of merit used to describe the beam quality in multiples of the diffraction limited beam parameter product (0.33mm-mrad, for 1047nm), halves the intensity achievable under identical focusing conditions. The advantage in average power for a transition from near diffraction limited to multi-order mode quality ($M^2 \geq 3$ to 4) is typically less than 20% for this laser system, and thus far removed from compensating for the beam quality decline. This underlines the importance of a near diffraction limited pump laser, which is reinforced in the two stage process of the third harmonic generation experiment. Here tight restrictions on the quality of the transversal mode structure apply to both the partly depleted infra-red, and the already frequency-doubled green beam, in order to allow an efficient mixing process (~14% conversion efficiency from the IR has been demonstrated at 5kHz), despite the pulse energies involved being in the sub milli-Joule class (the depleted fundamental and converted 523.5nm radiation are each ~0.5mJ per pulse).

Well established doubling and tripling techniques for 1μm radiation were used in this work and the novelty value of the results presented here is in the high conversion efficiencies, with subsequently high average output power in the green and near UV, at the kHz level (typically 2 to 5kHz) [1].
They are testimony to the improved growth techniques and damage resistance of non-linear crystals such as KTP and LBO as well as the excellent beam quality of the laser system developed in the course of this thesis. In addition to this, the improvement in the tripling efficiency when using two typeII conversion schemes, by compensating the walk-off in the KTP through walk-on in the LBO, can be highlighted, as well as the aesthetically pleasing demonstration of back-conversion under the varying condition of increased phase mismatch in KTP, which allows a clear visual experimental verification of well known doubling parameters.

6.1 Frequency doubling - a short review

The first paper in non-linear optics was on the frequency doubling of a flash- lamp pumped ruby laser, with quartz as the non-linear material, by Franken, Weinreich & al. in 1961 [2]. Since then, conversion efficiency for single pass, external cavity doubling has been improved by many magnitudes, from $\sim 10^{-8}$ in the original experiment to routinely 50-60% nowadays. This remarkable advance has been mostly possible through the development of damage resistant materials with high non-linear coefficients such as KTP, and to a lesser extent by progress in laser development. However, the high repetition rate, low threshold conversion schemes described in this thesis rely on diode pumped solid-state laser systems with excellent beam quality, high average power and short pulse durations in the 25ns regime, characteristic of the Nd:YLF system developed in the course of this work.

The detailed derivation of the doubling efficiency and deduction of the effective non-linear coefficient for different crystal symmetry groups can be found in the literature [3]. The starting point for this review is the second harmonic power as a function of the crystal and pump beam parameters. This form does not account for the depletion of the fundamental wave during the doubling process, which at this point is not of concern, as the equation is only used to discuss the basic physical properties and parameters used to optimise the doubling efficiency:

$$P_{2\omega} \propto \frac{\omega^2 d_{eff}^{\,2} l^2}{n_\omega^{\,3}} \frac{\sin^2(\Delta k l/2)}{(\Delta k l/2)^2} \frac{P_\omega^2}{\pi \omega_o^2} \qquad (6.1)$$

with the different parameters as follows:

$P_{2\omega,\,\omega}$:= power of the second harmonic, fundamental
d_{eff} := effective non-linear coefficient
l := nonlinear crystal length, or effective length as appropriate
n_ω := refractive index at the frequency of the fundamental
Δk := phase mismatch , $\Delta k = k_{2\omega} - 2k_\omega$
ω_o := beam radius in the centre of doubling crystal

The most important parameter in achieving a high doubling efficiency is d_{eff}. The efficiency $\eta_{2\omega}$ is related to d_{eff} and l such that:

$$\eta_{2\omega} \propto d_{eff}^2 l^2. \qquad (6.2)$$

The basic requirement that the effective non-linear coefficient must be non-zero further reduces the possible phase-matched propagation directions in the chosen material. The calculation of the effective non-linear coefficient, being a function of the propagation direction, depends on the symmetry class of the material used, which determines the values and zero elements of the d-tensor. The popular materials KTP and LBO both belong to the mm2 symmetry-class and d_{eff} can be calculated, for example, for both typeII ooe and eeo transitions in the three different tuning planes [4].

Tuning Plane	o <--> oe	e <--> eo
xy	0	$d_{32}\cos^2(\phi) + d_{31}\sin^2(\phi)$
yz	$d_{31}\sin(\Theta)$	0
xz	$-d_{32}\sin(\Theta)$	0

Table 6.1: *d_{eff} for different tuning planes and phase-matching schemes for mm2-class crystals (i.e. KTP, LBO).*

The table above underlines the importance of a non-zero effective non-linear coefficient, as for each tuning plane two possible phase-match options exist, but one is ruled out by its vanishing non-linear coefficient. In KTP this translates into the typeII scheme (e<-->eo) being used for doubling purposes (d_{eff} = 2.92pm/V) [5], to achieve phase-matching in the xy-plane, while the other phase matchable ooe-scheme is ruled out by d_{eff} being zero, as according to table 6.1.

The next important parameter on the laser side is the beam quality of the fundamental pump beam, as the doubling efficiency is proportional to the intensity, I, in the crystal and the square of the interaction length, l, (for a non-depleted pump and a plane wave approximation only).

$$\eta_{2\omega} \propto \frac{P_\omega}{\pi\omega_o^2} l^2 \propto I l^2 \qquad (6.3)$$

Connected to the pump laser parameter related equation above is the influence of the phase mismatch Δk on the conversion efficiency, as it limits the effective conversion length. Also, the optimum focusing arrangement under the

limitations dictated by damage threshold considerations restricts the usable intensity. Both parameters will be discussed in the following section and back-conversion due to phase mismatch will be experimentally demonstrated.

In addition to the conservation of energy, the phase velocities of the interacting waves have to be also matched, to achieve constant energy transfer into the second harmonic. In general the fundamental and second harmonic travel with different phase velocities through the medium, giving rise to the phase mismatch Δk, and severely limiting the effective conversion length. Under non-phase-matched conditions the interaction length would only be a few tens of microns. The standard technique to maximise the conversion is matching the phase velocities, so that Δk is zero, by taking advantage of the birefringence of the anisotropic non-linear crystal.
The match of the refractive indices has to be to a high degree, in the region of $\Delta n \leq 10^{-4}$ (doubling of 1047nm in KTP), to be within the first maximum of the sinc^2 function.

$$P_{2\omega} \propto \frac{\sin^2(\Delta kl/2)}{(\Delta kl/2)^2} \quad ; \quad \Delta k = \frac{4\pi}{\lambda\omega}\Delta n \qquad (6.4)$$

This underlines the necessity for a high degree of accuracy in the knowledge of the refractive indices of the materials used, as a function of the propagation direction and wavelength. The refractive index is described in general by a Sellmeier equation, of which several slight variations in terms of refractive index data and mathematical notation exist for each material. The Sellmeier equations for all the different non-linear materials used during this work can be found in Appendix A.
KTP is different from most other non-linear materials, as two different growth methods exist, flux grown and hydro-thermally grown KTP [6], resulting in materials with distinctively different Sellmeier equations. The typeII phase-matched angle for doubling of 1047nm is 39° in hydro-thermally grown KTP, as compared to 37° in the flux grown variety.
Although hydro-thermally grown KTP is superior in terms of damage threshold and has a better gray tracking resistance, flux grown material was used for the work in this thesis for purely economic reasons. The restriction in growth volume brought upon by the high pressures and temperatures utilised during the hydro-thermal growth process severely limits the KTP boule size , if compared to the less restrictive flux grown technique. These difficulties are

reflected in the approximately 4 times higher price (1995) of the hydro-thermally grown material, even for a doubler in the 5mm length region.

A demonstration of phase mismatch and the accompanying phenomenon of back conversion can be experimentally realised by angle tuning the KTP crystal away from the phase-matched position. Conversion and back-conversion are then observed through one of the grinded side faces of the crystal. A sequence of photos taken with a camera under different phase mismatch angles can be found on the next page in figure 6.2.
Alternatively to taking pictures with the camera a CCD-camera was used to record the green intensities within the crystal, thus giving the possibility to analyse the captured intensity distribution. A Schott GB30 filter was used to block scattered pump light in order to enhance the contrast. The high average power of the system is helpful, as the scattered green radiation within the at this wavelength nominally transparent KTP is detected. A minimum of the sinc^2 function, which describes the frequency doubled output power, is always reached for detuning angles which permit full periods of conversion / back-conversion cycles, with a minimum of green generated at the exit surface.

The intensity profile along the conversion path for a given mismatch angle shows the characteristic $\sin^2$-function for the cycling green intensity as a function of the crystal length, resulting from a fixed Δk phase mismatch.

$$P_{2\omega} \propto \frac{\sin^2(\Delta k l/2)}{(\Delta k l/2)^2} l^2 \quad , \Delta k \text{ constant} \quad \text{---> } \quad P_{2\omega}(l) \propto \sin^2(l) \qquad (6.4a)$$

The expected $\sin^2$ variation as a function of the distance along the conversion path can be confirmed by the intensity profile measured along the conversion path. Figure 6.3 illustrates the sinusoidal variation along the frame pictured in figure 6.2d, with 6 complete conversion / back-conversion cycles clearly visible.

Under the observed tuning angles of less than 0.5° in the xy-plane, the converted green radiation drops dramatically according to the distribution of the sinc-function in the phase mismatch term. The change in output power as a function of the detuning angle ($\phi - \phi_m$) is shown in figure 6.4.

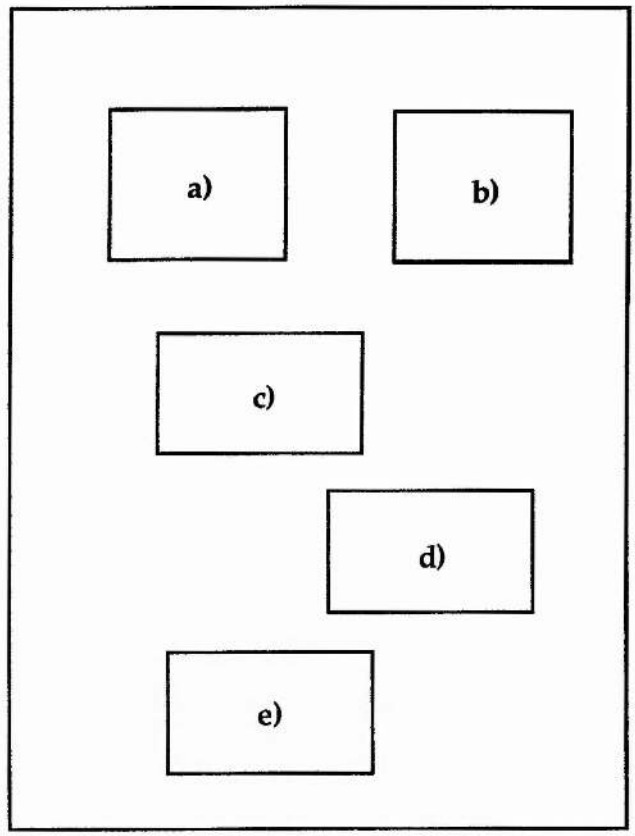

Fig. 6.2: *Figure 6.2a shows the experimental set-up with the infra-red beam propagating from left to right. Within the 10mm long KTP doubler parts of the IR-beam are frequency doubled. The doubling crystal is mounted in a Perspex holder, which enables free access to the top and one of the side surfaces. The remaining four photographs monitor the frequency doubled green beam by looking onto the top surface of the doubling crystal (xy-plane), while varying degrees of phase mismatch are introduced through rotating the crystal in the plane of observation. Starting from the position of perfect phase-matching(**b**)) the tilt angle is slightly increased to introduce phase mismatch. With increasing misalignment more conversion / back-conversion cycles of the green beam can be observed (**c**), **d**),**e**)). At a tilt angle of ~6.5°, 6 cycles can be observed within the 10mm long crystal (**e**).*
*The arrow like structure close to the exit surface of the KTP crystal is due to a linear scattering phenomenon of the coated surface (**b**)).*

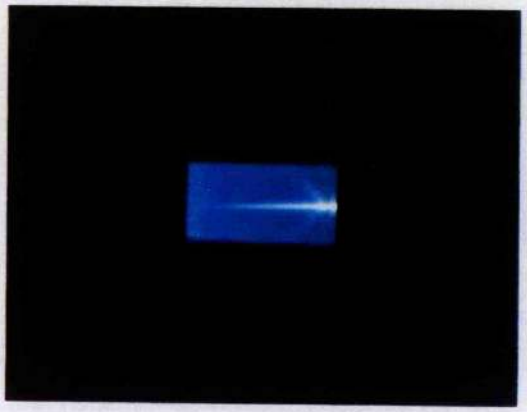

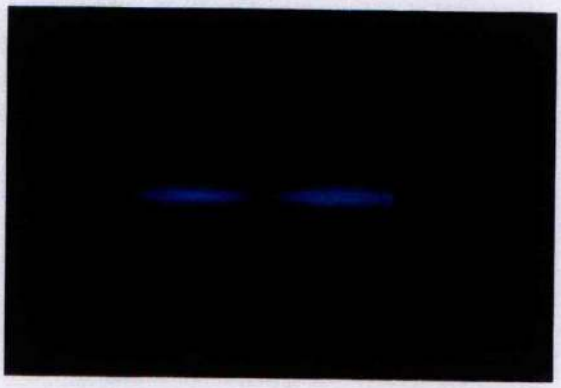

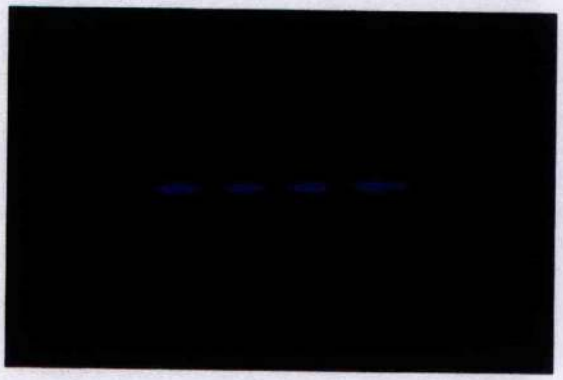

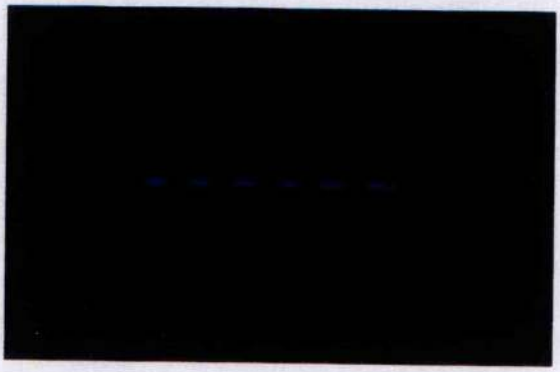

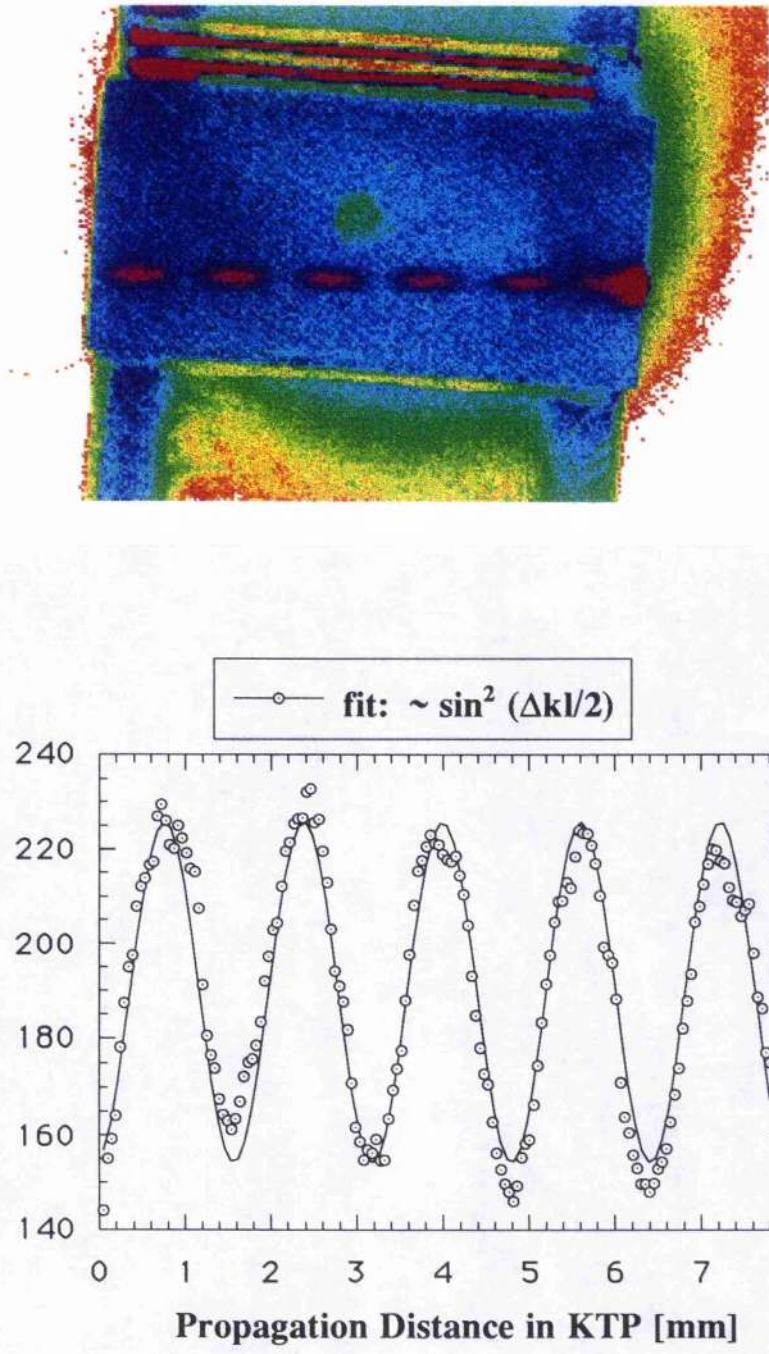

Fig. 6.3: *Plot of the measured $\sin^2$ variation for the frequency doubled intensity within the KTP crystal under conversion / back-conversion cycles. The intensity plot covers 8mm within the crystal as shown in the above false colour representation of the KTP crystal taken with a CCD camera and frame grabber.*

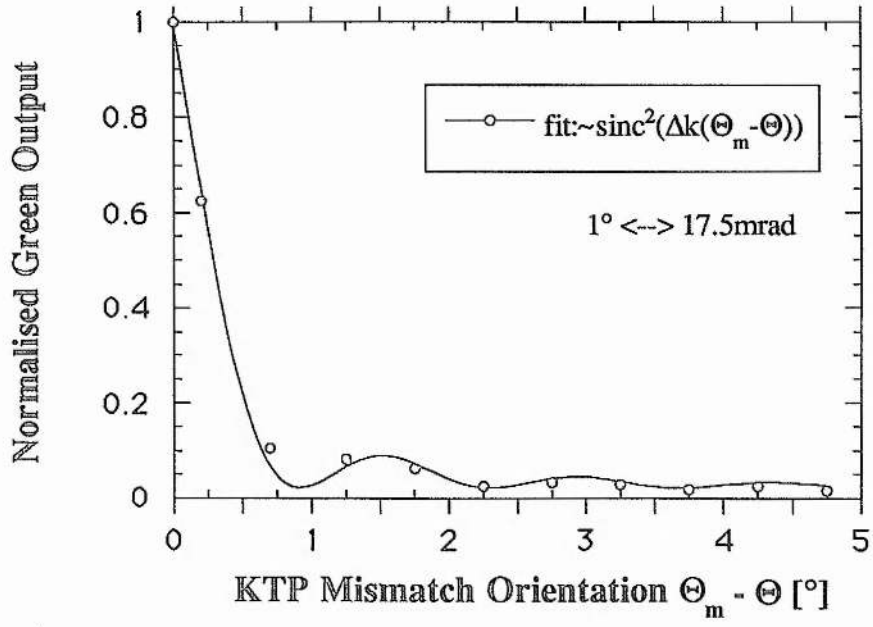

Fig. 6.4: *The green output as a function of the detuning angle (ϕ - ϕ_m) with ϕ_m denoting the phase matched angle. The output is modulated with the sinc function. The second minimum corresponds, for example, with the two completed cycles in figure **6.2b** .*

An interesting side effect is the arrow like structure close to the exit surface of the KTP crystal, which is very well visible in picture 6.2b. While the doubling process is a non-linear process, the arrow structure is due to a linear scattering phenomenon of the surface coating, described by Mie-scattering [19]. The back-scattered pattern is different for the two observable planes (xy- and yz-plane) and the distance of the anchor or arrowhead figure from the exit surface depends on the distance of the frequency doubled beam from the respective plane it is viewed through (see Appendix A3).

The high intensity spot, located exactly on the exit surface is a reflection from the AR coating and not related to the scattering phenomenon and is intensified by the blooming of the overexposed CCD pixels.

With the location of the structure depending on the distance of the doubled beam from the viewing plane it becomes clear that the scattered 3-dimensional pattern resembles an umbrella like shape with different curvatures in the two orthogonal planes. This will complicate any intensity analysis of the exact pattern, as scattering under various angles is observed (the straight green beam is scattering observed under 90°, while the scattered radiation is moving under an angle towards the observation plane , which acts like a screen).

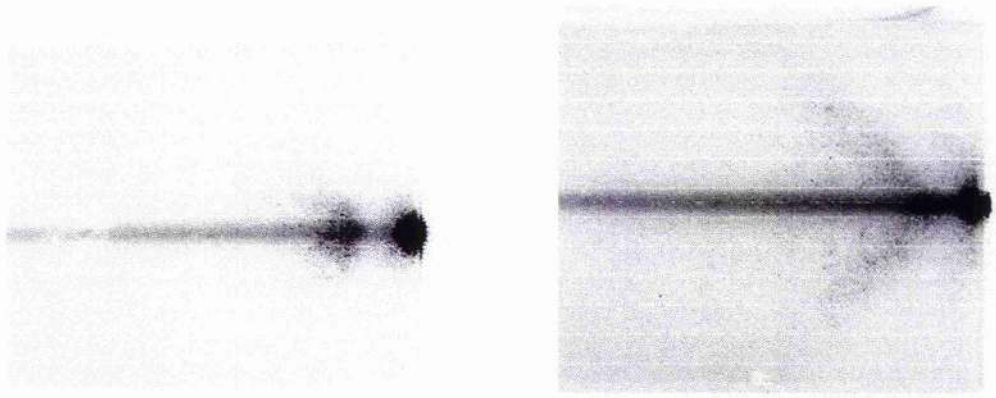

a) **b)**

Fig. 6.5: *Two different scattering patterns, if viewed through the top (xy-plane, **a**)) and side (yz-plane, **b**)) surface of the KTP doubler. The polarisation of the green radiation in each case is within the xy-plane. The beam is very close to the surface (≤0.5mm).*

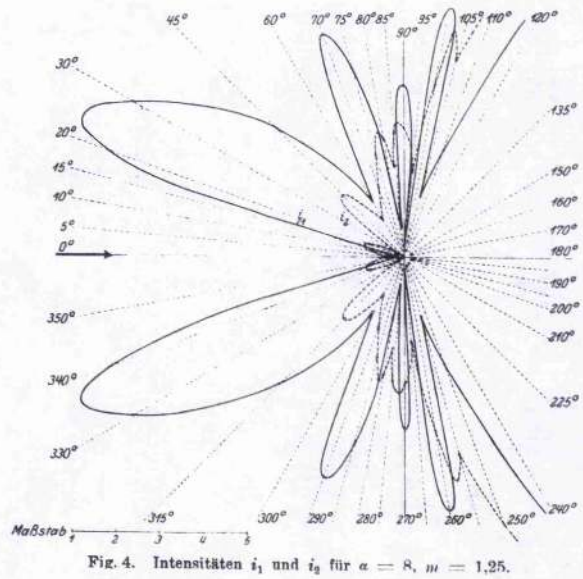

Fig. 4. Intensitäten i_1 und i_2 für $\alpha = 8$, $m = 1{,}25$.

Fig. 6.6: *Intensity distribution for the two orthogonal polarisations i1, i2 of a sphere [20] with diameter $2\rho=1.33\mu m$ ($q=8$, $\lambda=0.523\mu m$) and refractive index $n=1.25$. The polarisation of the component i1 is normal to the plane of the paper and finds its corresponding figure in 6.5a), with the green polarisation also being normal to the observation plane.*

H. Blumer [20] calculated scattering patterns caused by dielectrical spheres with varying radius and refractive index in 1925 according to the theory of Mie. The different polarisation depending patterns, as recorded above with the arrow-head (6.5a --> i1) and anchor-form (6.5b --> i2) of the scattered light, can be seen in one of his diagrams displayed in figure 6.6.
The similarity of these structures is, however, most likely to be accidental as with a beam diameter of 300μm whole clusters of scatter centres amount to a superimposed scattering figure, as opposed to one single sphere as in the case of Blumer's calculations.

The structure of the back-scattered green radiation is dependent on the scattering particle size at the exit surface. By selecting slightly damaged parts on the exit surface the appearance of the back-scattered green radiation can change drastically, as the two figures in 6.7 demonstrate.

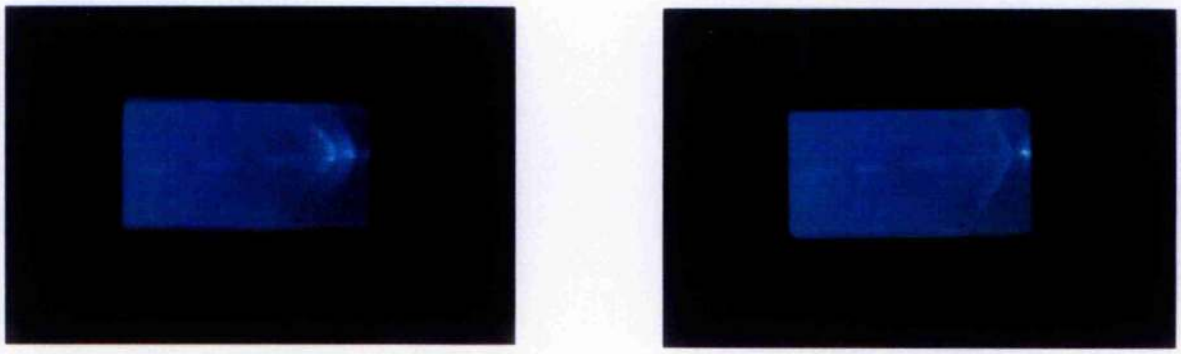

Fig. 6.7: *Two different back-scattered patterns of the frequency doubled component, taken while hitting arbitrary damaged areas of the exit surface.*

At no stage could scattered infra-red radiation be detected within the bulk of the crystal. This is not unexpected, as according to Rayleigh scattering (for scatter centres with $r<<\lambda$), the specialised case of Mie-scattering, the scattered intensity is inversely proportional to the wavelength raised to the fourth power.

$$I_{scat.}^{Ral.} \propto \lambda^{-4} \qquad I_{Green}^{Ral.} = 16 I_{IR}^{Ral.}$$

The very small IR intensities therefore could not be detected as they would be below the sensitivity of the CCD camera. This made detection of the varying IR

intensity during the conversion/back-conversion cycles within the crystal impossible.
The transition from Rayleigh scattering to Mie scattering can be described with the parameter q, which relates the scattering diameter of the centre to the scattered wavelength.

$$q = \frac{2\rho\pi}{\lambda} \qquad 2\rho := \text{Sphere diameter}$$

For: $q \ll 1$: Rayleigh scattering, as in the bulk of the crystal, with even intensity distribution in forward and backward direction.

$q \geq 1$: Polarisation dependent maxima and minima appear in the back scattered direction (q=1), with increasingly dominant forward scattering (q>1).

$q \gg 1$: Reversal of intensity distribution with a dominant backward scattering component (also for n>>1, reflection)

So far only backward scattering could be observed as there was no frequency doubled component at the entrance surface of the KTP crystal. In order to check the nature of the scattering effect at the beginning of these experiments (with possible causes ranging from being either linear (Caustic) up to third order non-linear (Brioullion scattering) processes) a second KTP crystal was used to observe the scattering of the green component after the IR was removed by a harmonic separator. Under these conditions forward scattering could be observed only if a strong defect on the entrance surface could be hit (simulating q>>1). Unexpectedly, the weak forward scattered pattern had the same structure as the backward scattered figure at the exit surface, thereby resembling a symmetric double-sided arrow. The symmetry in the forward and backward scattered patterns, given that two totally arbitrary scatter centres were chosen, appears remarkable and might be worth further investigation at a later date. Appendix A3 contains more CCD frames, which establish that the observed effect is a linear surface scattering effect.

With the intensity of the green radiation at the exit surface being a minimum in each photograph in figure 6.2c-e, in order to suppress the linear scattering effect, each completed conversion / back-conversion cycle finds its equivalent in a minimum in the sinc-function which describes the total converted green power in the case of angle tuning in the xy-plane.

The acceptance bandwidth, defined in this case as the allowed detuning before the second harmonic output drops to half of its maximum value, is 0.3° for angle tuning away from the optimum phase-matched position in the xy-plane ($\delta\phi$). This experimental result, taken from figure 6.4, agrees reasonable well with the expected value of 3.4mrad (0.2°) for $\delta\phi$, as calculated by equation 6.5, with the crystal length, l=10mm. In general, acceptance bandwidths or angles can be calculated for each detuning axis by solving the sinc-function for $\delta\phi$ or $\delta\Theta$, as appropriate, under the condition shown below for $\delta\phi$, and the assumption that the converted output has dropped to half of its phase-matched output:

$$P_{2\omega}(\delta\phi,l) \propto \frac{\sin^2\{\Delta k(\phi_m+\delta\phi)l/2\}}{\{\Delta k(\phi_m+\delta\phi)l/2\}^2} = \frac{1}{2} \;\; ; \;\; \Delta k(\phi_m) \overset{!}{=} 0 \qquad (6.5)$$

The so calculated acceptance angle, $\delta\phi$, is a function of the fundamental wavelength and crystal length. The acceptance angle with the changing fundamental for a given crystal length is shown below:

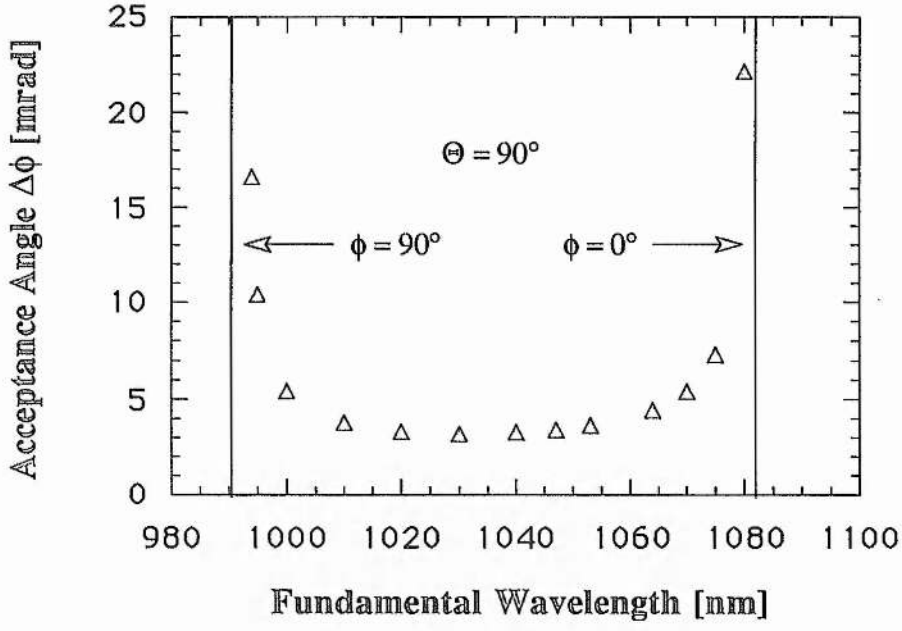

Fig.6.5: *Calculated acceptance angle $\delta\phi$ for a 10mm long KTP-doubling crystal as a function of the fundamental wavelength.*

The asymptotic behaviour of $\delta\phi$ when approaching the NCPM typeII geometries of ϕ=0° and ϕ=90° (Θ=90°), displays less restrictive doubling conditions as compared to the critical phase matched schemes.

The influence of the doubler length on the acceptance angle is very pronounced, scaling faster than l^{-1} (i.e. $\delta\phi$=6.5mrad (@1047nm) for the 6mm long KTP crystal used earlier).

Angle tuning in the yz-plane is less critical, due to the slower variation of the refractive index in this plane. Detuning of ~1° reduces the output power by only 5% in the experiment. The calculations to determine the $\delta\Theta$ acceptance angle are not as straightforward as in the above case, because phase matching is no longer restricted to the principal planes. The procedure of general phase matching in biaxial crystals, which applies here to calculate the phase-mismatch term $\Delta k(\Theta + \delta\Theta)$, has been dealt with in the following short review of frequency mixing in LBO (§ 6.3). The calculated acceptance angle for the 10mm long KTP-doubler is $\delta\Theta$=39.6mrad (2.3°) for a pump wavelength of 1047nm. In a good approximation, the acceptance angle in the yz plane is by a factor of 10 larger than its more critical counterpart in the xy-plane for this doubling scheme in the 1μm region. This magnitude in difference is experimentally of use, as only the ϕ alignment in the xy-plane needs a degree of freedom in rotation, while for the Θ-alignment 'work-shop' precision, aimed at normal incidence of the beam, is sufficient.

So far the focusing conditions have not been considered. To achieve good conversion efficiencies with the low energy pulses of the cw pumped system, tight focusing is required to achieve the necessary peak intensities in the centre of the doubling crystal. Focusing is ultimately limited by the damage threshold conditions of the AR-coated KTP crystal, while less stringent focusing is limited by the effective interaction length within the crystal, if the increase in length has to balance the reduced conversion efficiency under lower pump intensities. The effective conversion length is defined by the confocal parameter of the focusing arrangement as well as the walk-off between fundamental and second harmonic.
If the medium is long compared to the confocal parameter z_o, then the crystal length is replaced by the shorter effective length l_{eff}, which corresponds to the length in which the beam can be considered as focused [7]. Two notations are used for the confocal parameter, z_o and b, being only distinguished by a factor of two.

$$z_o = \frac{\pi \omega_o^2 n}{\lambda} \qquad (6.6)$$

z_o denotes the distance by which the beam waist, with radius ω_o, has been

expanded in one direction by a factor of $\sqrt{2}$ compared to the focused beam waist, while b gives the distance between this condition on both sides of the focus.

The effect of diffraction on the beam divergence also finds its expression in the equation for the conversion efficiency under confocal focusing conditions, as opposed to the solution given in equation 6.3 under a plane wave approximation. The conversion efficiency under the confocal focusing arrangement of $l = 2z_o$ scales only linearly with the crystal length, l, as opposed to an l^2 dependence in the plane wave approximation ($z_o >> l$).

$$\eta_{2\omega}\Big|_{planewave} \propto l^2 \frac{P_\omega}{\pi\omega_o^2} \propto l^2 I \xrightarrow{l=2z_o} \omega_o^2 = \lambda l/2\pi n \qquad \eta_{2\omega}\Big|_{confocal} \propto l P_\omega \tag{6.7}$$

This reduced scaling in length of the conversion efficiency reflects the fact that the use of longer crystals to still satisfy $z_o = l/2$ in the case of confocal focusing calls for bigger beam diameters within the crystal, which reduces the pump intensity and in turn the conversion efficiency.

Detailed theoretical studies of the optimum focusing of Gaussian beams have been performed by Boyd and Kleinman [8]. By introducing the focusing parameter ξ, a relation between the non-linear medium length l, and the confocal parameter b, of the focusing arrangement used, the optimum conversion efficiency is achieved at a value of 2.8 for ξ.

$$\xi_{opt.} = \frac{l}{b} = 2.8 \qquad b = 2z_o \tag{6.8}$$

The improvement in conversion efficiency from the confocal (ξ=1) to the optimum focusing parameter is only in the region of 20%, due to the small variation of the efficiency as a function of ξ in this region.

However desirable confocal focusing conditions are to increase the efficiency of a non-linear process, damage limitations for the non-linear medium often prohibit the optimum focusing condition as stated by Boyd and Kleinman. In the case of KTP values of the focusing parameter ξ has to be kept well below the confocal condition to avoid damage to the crystal, when used with a pulsed pump source.

The above description of optimum focusing holds true only in the absence of walk-off, which is the separation between the wave propagation vector **k** and the Poynting vector **S** of the extra-ordinary wave in a birefringent material,

under certain phase match conditions. The index surface of an ordinary wave is always circular, so that the direction of phase propagation (k) and energy flux (S) are identical. As the index surface of an extra-ordinary wave is elliptical, the direction of the Poynting vector S, being the tangent to the index surface, deviates from the direction of phase propagation and defines the walk-off angle ρ, as shown in the sketch below.

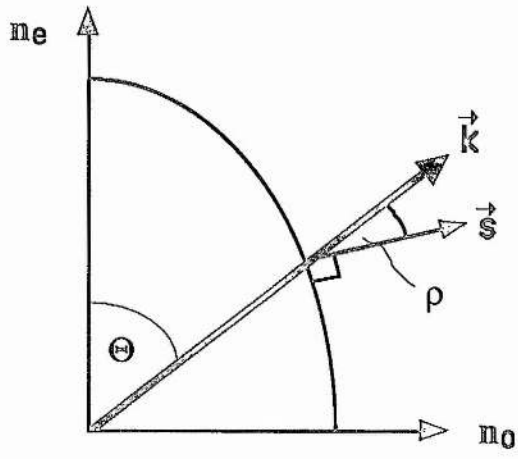

Fig 6.6: Walk-off in a critical phase matched plane, due to the elliptical index surface.

Only non-critical phase matched schemes are walk-off free, with propagation directions along the main axis of the elliptical indicatrix (with pairs of Θ and ϕ being 90° or 0°). This important advantage of these geometries is used to achieve low threshold, high conversion efficiency optical parametric oscillators as described in the following chapter 7.

The upper limit for the effective conversion length is given by the total separation of the fundamental and second harmonic energy propagation paths. This distance is called the aperture length ℓ_a [9] and is a function of the walk-off angle ρ and the beam waist size ω_0 as the expression below shows.

$$\ell_a = \frac{\omega_o \sqrt{\pi}}{\rho} \qquad \text{with} \qquad \tan(\rho) = \frac{1}{n}\frac{\partial n}{\partial \Theta} \qquad (6.9)$$

The aperture length ℓ_a is linear with the waist size. This corresponds to the fact that the change in the phase front curvature is greater the smaller the waist size of the focusing set-up. Tight focusing, as used in high repetition rate conversion schemes, to compensate for the low energy per pulse, is therefore more likely to introduce the aperture length as the limiting conversion length factor.

In the case of a positive uniaxial crystal the walk-off angle is equivalent to:

$$\tan(\rho) = \frac{1}{2}(n_o^{\omega})^2 \left\{ \frac{1}{(n_e^{2\omega})^2} - \frac{1}{(n_o^{2\omega})^2} \right\} \qquad (6.10)$$

This expression also holds true for positive biaxial crystals such as KTP, if phase matching is restricted to the principal planes. In the case of KTP this results in a walk-off angle of ρ=0.2°, with n_o and n_e substituted as given in equation 6.12 .

The phase match conditions for the crystals used during the experiments of this thesis have been calculated by following a standardised approach by A. Roberts [9a]. In performing the calculations along these lines the Ph.D. thesis from G. Robertson, St. Andrews University 1993 [9b], has been a great help.
The material of choice for the doubling of the infrared fundamental radiation at 1047nm was KTP, mostly due to its high effective non-linear coefficient and small walk-off angle under critical typeII phase matched conditions, as well as its stable chemical composition (non-hydroscopic). The table below gives some of the important characteristics mentioned before for KTP.

positive, biaxial crystal	$\Omega = 21.85°$; point group: mm2 ; [12]
transparency	0.35µm - ≤ 2.8µm [13] , ≤ 3.2µm [14]
d_{eff} for typeII doubling	xy-plane: $d_{eeo} = d_{15} \sin^2\phi + d_{24} \cos^2\phi$ [12]
Non-linear coefficients [pm/V]	d_{15}=6.1; d_{24}=7.6; d_{31}=6.5; d_{32}=5; d_{33}=13.7 [4] @ 1064nm, applies for flux- and hydrothermal KTP
acceptance angle @1047nm [mrad (°)]	$\delta\phi$ = 3.4 (0.2), $\delta\Theta$ = 39.6 (2.2) ; (10mm long KTP) $\delta\phi$ = 7.3 (0.45) ; (5mm long KTP)
walk off	0.2° in xy-plane

Table 6.7: Important parameters for KTP as a critically phase matched typeII doubler at 1047nm.

Although KTP is a positive biaxial crystal, the calculations for the refractive indices for the two orthogonal, linear polarised eigenmodes can be substantially simplified, if propagation is limited to the three principal planes, as it is the case for the well known typeII doubling geometry. If the azimuthal angle Θ is confined to 90°, thus limiting the degree of freedom only to changes of the polar angle ϕ in the xy-plane, then the direction cosines [9a] take the simplified form:

$$a_i^1 = \begin{pmatrix} 0 \\ 0 \\ 1 \end{pmatrix} \qquad a_i^2 = \begin{pmatrix} -\sin(\phi) \\ \cos(\phi) \\ 0 \end{pmatrix} \tag{6.11a}$$

With the known direction cosines the refractive indices n^i (i=1,2) for the polarisation eigenmodes e^i can be calculated as follows:

$$\frac{1}{n^{(i)2}} = \left[\left(\frac{a_x^{(i)}}{n_x} \right)^2 + \left(\frac{a_y^{(i)}}{n_y} \right)^2 + \left(\frac{a_z^{(i)}}{n_z} \right)^2 \right] \tag{6.11b}$$

This reduction to the principal planes in a biaxial crystal makes it equivalent to the description of an uniaxial crystal. The doubling process being a typeII process requires the E-vector of the incoming linear polarised wave being under 45 ° to the xy-plane, to achieve maximum conversion by splitting into even orthogonal field components. Therefore one of the orthogonal polarisation orientations within the crystal is always along the z-axis, so that the propagation of this component is described by $n_z(\lambda)$, regardless of the propagation direction within the xy-plane. The propagation of the other component is described by the extraordinary refractive index, being a function of the propagation direction (ϕ counts from the x-axis), fundamental wavelength and the refractive indices $n_{x,y}(\lambda)$.
Finally the phase-matched angle in the xy-plane is determined by the momentum conservation equation, with the energy conservation law already satisfied, as noted below.

$$n_e(\phi, \frac{\lambda_f}{2}) 2\omega_f = n_e(\phi, \lambda_f)\omega_f + n_z(\lambda_f)\omega_f \qquad \text{with}$$

$$n_e(\phi,\lambda) = \Big/ \sqrt{\frac{\sin^2(\phi)}{n_x(\lambda)^2} + \frac{\cos^2(\phi)}{n_y(\lambda)^2}} \tag{6.12a}$$

The indices e, f denote the extraordinary and fundamental wave respectively, while the refractive indices n in the x, y and z plane are described by the appropriate Sellmeier equation (see Appendix I). This non-linear process being a typeII interaction is described in terms of a three wave process as,

$$e \text{ <---> } e + o \qquad 2\omega_f \text{ <---> } \omega_f + \omega_f . \tag{6.12b}$$

The phase-match defining equation 6.12 can always be solved numerically. However, for positive uniaxial crystals a formal solution can be found with Θ_{pm} being the phase matched angle, by matching the refractive indices n(2ω) and n(ω) in the phase matched direction by determining the intersection of the ellipse (n_e) with the circle (n_o) in the index surface interpretation .

$$\sin^2(\Theta_{pm}) = \left(\frac{n_e(\omega)}{n_o(2\omega)}\right)^2 \left(\frac{n_o^2(\omega) - n_o^2(2\omega)}{n_o^2(\omega) + n_e^2(\omega)}\right) \qquad (6.13)$$

For typeII doubling in KTP the change of the phase matched angle with the fundamental wavelength is rapid. The difference in the internal angle is ~12° for a change from 1047nm to 1064nm in the fundamental, thus requiring dedicated KTP crystal cuts for each of the common 1μm laser transitions.

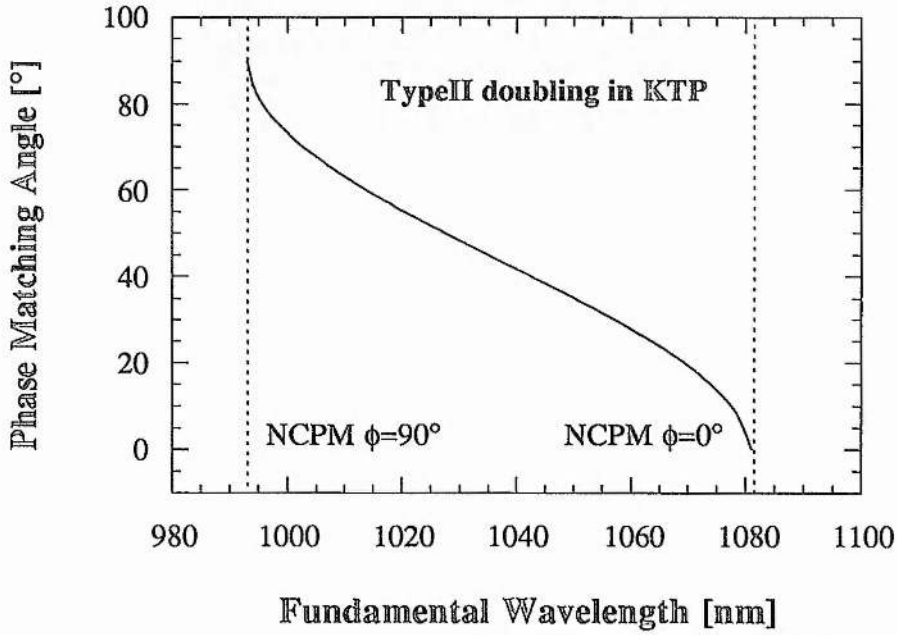

Fig. 6.8: Calculated variation of ϕ for typeII phase matching in KTP with Θ=90°. The rapid tuning of ϕ_{pm} is evident in the small wavelength range covered (~90nm) for a variation of ϕ from 0° to 90°.

The phase-matched propagation directions for the most commonly used 1μm doubling wavelengths are 37.1°, 34.9° and 24.7° for 1.047μm, 1.053μm (both YLF) and 1.064μm (YAG) respectively. Accompanied by an almost constant phase matched fundamental wavelength close to 0° and 90° the phase match condition makes a transition from the critical to a non-critical phase geometry in KTP at around 1081nm (ϕ=0°) and 993nm (ϕ=90°), with considerably relaxed

doubling conditions, in a walk-off free geometry.

The main advantage of typeII (Θ=90°, ϕ=0°) temperature tuned doubling in KTP as used in intracavity cw-doubling of a Nd:$YAlO_3$ at 1080nm by Kimble et al. [25], is that this type of phase matching has no finesse degrading walk-off between the e- and o-beams of the fundamental. Alternative doubling schemes will be briefly discussed towards the end of this chapter, mainly with regard to improvements in the sum-frequency mixing process, with a short excursion into proposing the π-polarised 1072nm line in Nd:YLF to be doubled with a temperature tuned KTP/KTA intracavity typeII doubler.

6.2 Frequency doubling results

Initial experiments were with a 6mm long KTP piece (AR coated, 5x5mm^2 aperture), which was readily available in the laboratory. The typeII critical phase matching at room temperature was achieved by a crystal cut with Θ=90° and ϕ=37°, as determined before.

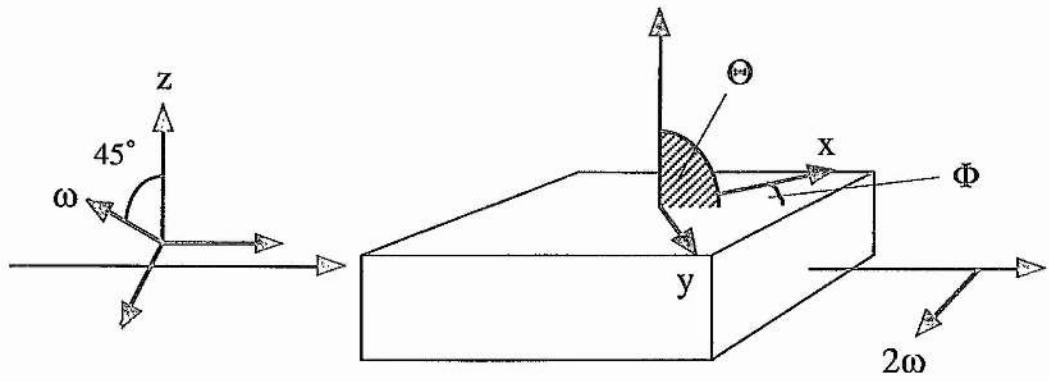

Fig. 6.9: *KTP crystal cut for doubling at 1047nm. The incident fundamental is linearly polarised with 45° towards the o- and e-axis of the KTP typeII doubler.*

The correct polarisation orientation of the fundamental pump radiation was achieved by rotating either the doubling crystal to suit the given pump laser polarisation or by using an AR-coated half-wave plate for 1047nm to rotate the polarisation with respect to the fixed KTP axis. The latter arrangement was preferred for the OPO work, as the additional $\lambda/2$-plate reduces the complexity of the OPO mount.

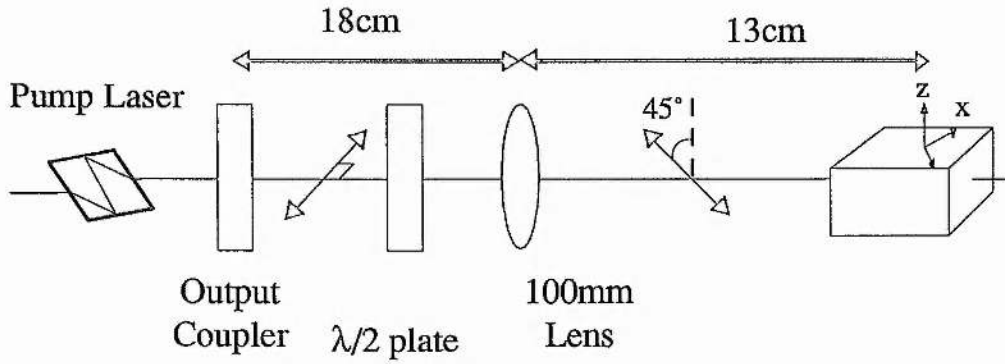

Fig. 6.10: *Sketch of the experimental set-up for external, single pass frequency doubling.*

A spherical lens with a focal length of f=100mm (AR coated) was used to focus into the centre of the external doubler. The distance of the lens was 18cm behind the output coupler and the calculated spot size diameter was about 250µm under these conditions.
This is in acceptable agreement with the measured 300µm spot size, located 130mm behind the focusing lens, due to the divergent input beam. Only a minor change (± 10mm) in the distance between lens and KTP surface was necessary to compensate for the different beam properties with the varying thermal lens for pump powers up to 20W.

The conversion efficiencies reached under these circumstances were in the area of 36% to 44%, depending on the peak power level per pulse (16 to 30kW) and the beam quality. A maximum of just 2.0W average output at 523.5nm and 6kHz repetition rate was achieved (20W diode pump power).

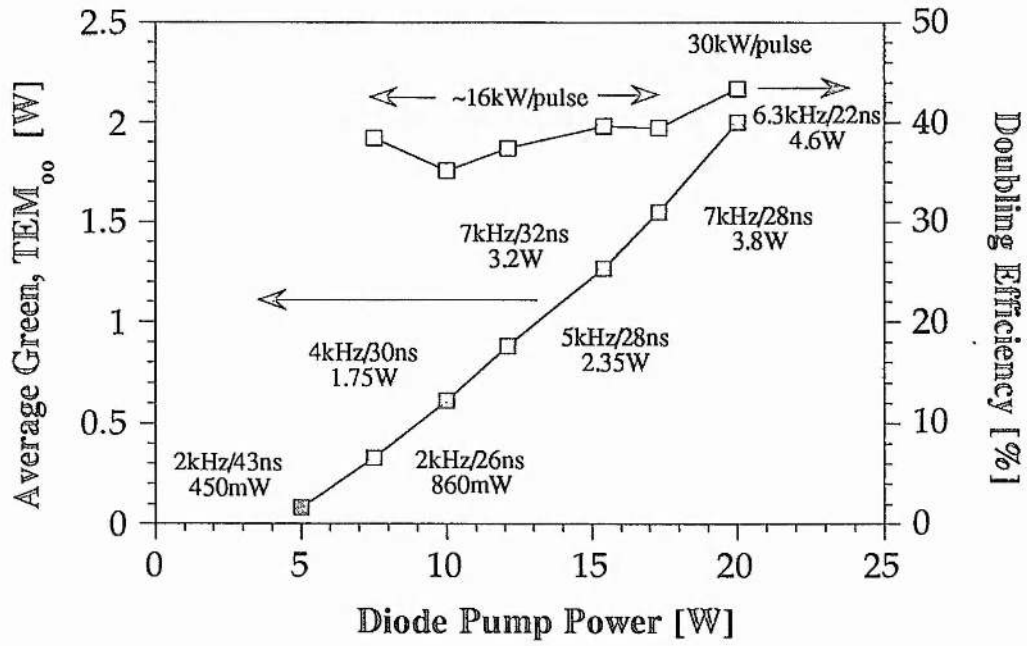

Fig. 6.11a: *Doubling results with an AR-coated 6mm long KTP piece in a set-up as sketched in figure 6.10. The focusing parameter ξ with a value of 0.025 indicates a non-optimised set-up.*

Efforts to optimise the focusing for the length of the crystal, by choosing a lens with f=50mm, corresponding to ~100µm spot size diameter (ξ=0.23), could boost the conversion efficiency to 48% (compared to 23% for the 100mm lens) under peak powers as low as 7kW per pulse.

Unfortunately the KTP suffered catastrophic bulk damage under these conditions after a few minutes operation, corresponding to a single shot repetition value of approximately half a million. The damage seems to originate at the coating on the exit surface, as indicated by the surrounding burn mark on the coating. This absorption area then acts as the seeding point for the following bulk failure. The damage intensity for the KTP under the above focusing condition is 63MW/cm^2, a value considerably below the expected damage values for KTP (bulk: ~500MW/cm^2 ; coating: ~300MW/cm^2).

However, it is worth mentioning that under relaxed focusing with the 100mm lens and similar peak intensities no damage occurred in the same piece of KTP. A possible explanation might be the varying quality of the KTP across the aperture, as identified by increased amounts of scattered green light in inferior parts of the crystal bulk or coating.

In the later utilised 10mm long KTP piece from the same supplier (Shan-Dong University, China), the onset of gray tracking could be observed at intensities just below 100MW/cm^2 and focused spot diameters in the 200μm region (~25ns pulses). Staying above this critical spot size and restricting the peak intensities to values around 80MW/cm^2 did not cause any problems under laboratory conditions. The onset of gray tracking in KTP under pumped conditions changes the green output from a TEM_{oo} mode to a blurred non-symmetrical mode structure, which can be reversed into TEM_{oo} again by translating the crystal.

The grey 'track' within the crystal has the same conical appearance as the scattered green light under pumped conditions (see fig. 6.2a). The grey-brownish discoloration also follows the intensity pattern of the scattered green cone, reaching a maximum of discoloration at the exit surface. This illustrates that the photo-refractive damage is at least partly caused by the frequency doubled component and that the seeding point for catastrophic bulk damage due to absorption caused by gray tracking, will always originate from the exit surface, in agreement with the earlier observations.

Nevertheless, the damage mechanism remains uncertain, and tight focusing (≤200μm diameter), even at low peak intensities, appears to be precarious. Interestingly, scaling in average infra-red pump power never caused problems (up to 8W) if the peak intensity per pulse as well as the focused spot size in the crystal was within the safe operation conditions stated above.

A consequence of this uncertain damage behaviour was a change in the approach used to optimise the green performance. Instead of tightening the focus to suit a given crystal length, the crystal length was changed to suit the unproblematic focusing conditions of the 100mm lens. The exclusion of beam radii below 125μm was equivalent with the fact that confocal focusing conditions (ξ=1) could not be realised in these KTP crystals. The table below states two focusing or crystal parameters, which set limits to the useful crystal length. These are the confocal focusing condition (eqn. 6.6), and the aperture length due to walk-off (eqn. 6.9). Both are set in relation to the acceptance angle (which is dependent on the crystal length) and the far-field divergence of the TEM_{oo} pump source.

Focusing vs. damage	Damage limit: $\omega_o = 150\mu m$; $l_{KTP}^{conf.} = 2z_o = 23cm$ Damage: $\omega_o = 32\mu m$; $l_{KTP}^{conf.} = 2z_o = 10mm$
Walk off vs. beam overlap	Walk-off: $\rho = 3.5mrad$ (xy-plane) and aperture length l_a $\omega_o = 150\mu m$; $l_a = 76mm$ $\omega_o = 32\mu m$; $l_a = 16mm$
Acceptance angle vs. divergence of pump laser	Acceptance angle $\delta\phi$ is more critical than $\delta\Theta$ in KTP $l_{KTP} = 10mm$; $\delta\phi_{1/2} = 3.5mrad$ $l_{KTP} = 20mm$; $\delta\phi_{1/2} = 1.6mrad$ Pump beam parameter: $\omega\Theta = 0.33mm.mrad$ (TEM_{oo}) $\omega_o = 150\mu m$; $\Theta = 2.2mrad$ $\omega_o = 32\mu m$; $\Theta = 10.3mrad$

Fig. 6.11b: *Converter length limiting processes in the case of a high repetition rate, single path external KTP-doubler. A multimode pump laser can set the lower limit of the converter length, depending on the acceptance angle of the non-linear converter.*

The table above clearly demonstrates that optimum focusing according to Boyd and Kleinman [8] is only a viable option if neither damage thresholds nor walk-off are limiting factors. Such a situation is rarely encountered in the phase matching of non-linear crystals. In particular the damage threshold for KTP set a limit to the focusing during these doubling experiments, when using a pulsed laser source in the 20ns region.

In the example of the KTP typeII doubler, walk-off is hardly a limiting factor under confocal focusing conditions. Only under tight focusing, with $\xi > 1$, might restrictions due to beam separation apply. With the change to a different material, such as BBO, this situation would change drastically and would restrict severely the interaction length under tight focusing.

Besides these damage and phase matching considerations, the peak intensity achievable determines the achievable conversion efficiency for a given converter length. Calculations by Y.Tang based on a paper by Eimerl et al. [16], identified a length around 12mm as the best compromise in terms of efficiency for the available peak intensity of 70MW/cm^2. This intensity translates into around 40kW peak power per pulse, focused into a spot size of 250µm diameter. Due to time constraints and economic reasons the standard size of 10mm length (AR coated for the fundamental and second harmonic) was used instead. The results of the improved doubling configuration are shown in figure 6.11.

The optimised KTP length improved the conversion efficiency by up to 60% depending on the peak power per pulse and diode pump power level. Up to 2.9W of green output at 6kHz repetition rate in a near diffraction limited mode at 20W diode pump power could then be achieved, as opposed to 2W in the case of the shorter KTP doubler.

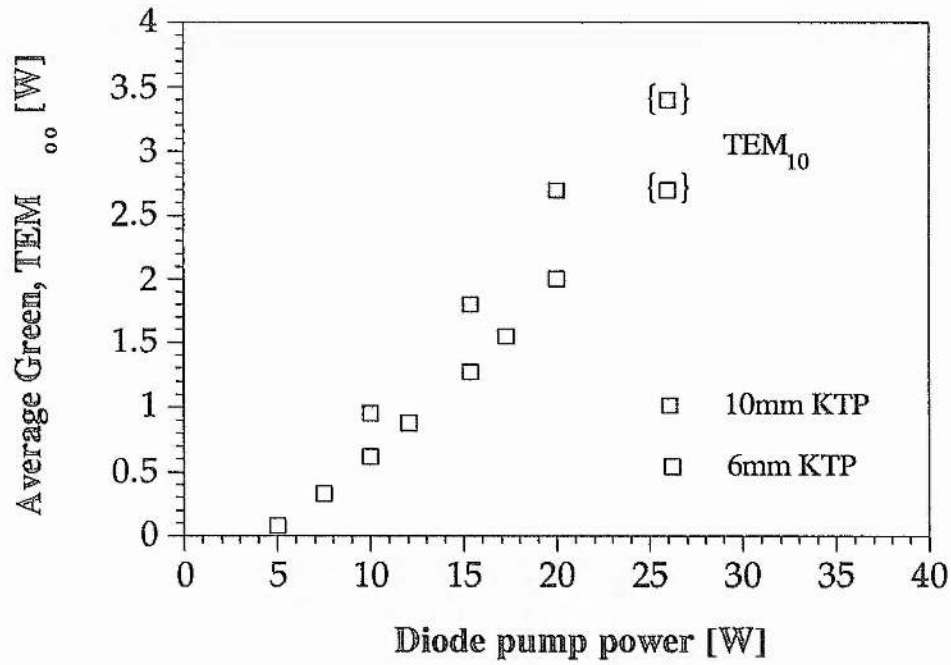

Fig. 6.12a: *A comparison of the maximum achieved average green output power with KTP pieces of different length as a function of the diode pump power. The spot size of the pump beam is ~250µm, using a 100mm lens. The repetition rate varies between 2 and 8kHz.*

At these high pump powers the ability to shape the mode by a parallel movement of both pump modules (i.e. in the plane of the paper in figure 2.4) proved to be valuable in optimising the conversion efficiency. High green output powers could be more easily attained with slightly elliptic modes, although it is possible to maintain symmetric, near diffraction limited, modes with similarly good conversion efficiencies. This tendency to prefer elliptic mode forms starts around 15W pump power and becomes dominant at 26W pump powers where the highest green average power of 3.6W is in the form of a TEM_{10} (as indicated with the brackets in figure 6.11). Efforts to match this result with a circular pump mode did not succeed and the green output was then restricted to 3.2W.

This behaviour is indicative of the fact that elliptical focusing might improve the doubling efficiency. As shown before the phase match conditions in KTP are critical only in the xy-plane. In the orthogonal plane 'non-critical' phase matching conditions exist. Tight focusing with a cylindrical lens in this plane would not cause efficiency limiting walk-off, whereas relaxed focusing in the critical plane will reduce walk-off and keep the peak intensity within the damage limits. The deviation from the circular, near diffraction limited, pump mode appears to simulate these cylindrical focusing conditions in the respective planes and thus compensates for the loss in peak intensity caused by the increased M^2 value of the higher order mode. The degrading of the green beam quality into a mode order close to 2, despite the over 50% conversion efficiency from the fundamental at the 26W diode pump power, was the reason for stopping the doubling experiments at this point.

Nevertheless, the cylindrical focusing might be an interesting alternative to push the maximum green output closer to the 4W border at a later stage. However, the asymmetric propagation after the cylindrical focusing might make additional lenses necessary to reshape the beam, depending on the application.

The varying conversion efficiency under TEM_{oo} operation of the pump as a function of the peak intensities in the centre of the crystal is shown below. The focusing conditions are identical to the prior experiments, with a 250µm beam waist in the crystal. The depletion of the IR pump beam during the doubling process (conversion efficiencies approaching 65%) causes deviation from the square dependence of the conversion efficiency on the pump intensity, given by equation (6.7), which describes the efficiency only for the undepleted case.

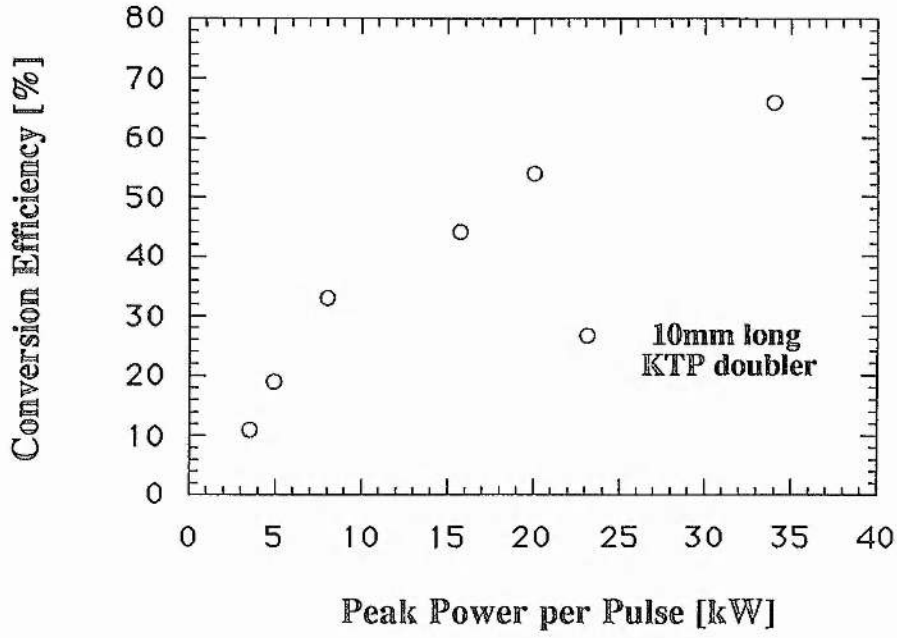

Fig. 6.12b: *Changing conversion efficiency with the peak power of the pump pulse. The beam diameter remains almost constant at 250μm in the 10mm long doubler, due to the relaxed focusing conditions.*

For intensities above 25-30kW the conversion efficiencies increase very slowly. This, together with the decrease in average output power for lower repetition rates, defines the turning point for the average green output power. At this point the higher efficiencies of the doubling process do not balance the decline in average output power. As an example, figure 6.11, which describes the optimised green average output power, shows the pump laser parameter at these turning points for different pump powers. Beyond this repetition rate the green peak power per pulse still increases, till the effective upper state lifetime limit sets a maximum to the extractable infrared pulse energy. This lower limit of the repetition rate was at around 2kHz (see Chapter 5). Beyond this point the green pulse energy stays constant, while the average green output power decreases linearly with the repetition rate.

During these doubling experiments the emphasis was placed on the maximum average power, as this is the real strength of a high repetition rate system as compared to pulsed diode pumped lasers. However, if the frequency doubled laser is used as a pump source, minimum requirements in terms of pulse energies have to be fulfilled. The frequency doubled output was used to pump two other experiments:

- A low threshold, injection seeded Ti:Sapphire ring laser, which was developed by Garry Morrison on a low repetition system [21], and
- frequency tripling experiments, which are described in greater detail in the following two sections.

The output characteristics for the Ti:Sapphire laser are briefly mentioned, in order to underline the beam quality and stability of the pump laser. The ring cavity of the Ti:Sapphire laser consists of a four mirror bow-tie configuration, where the Ti:Sapphire crystal is pumped through one of the folding mirrors close to the crystal. Unidirectional lasing and line narrowing down to single mode operation (≥300 MHz) was achieved by seeding the ring with a single frequency laser diode at 830nm [22]. Seeding has the important advantage of allowing a very low threshold for the Ti:Sapphire ring, of below 200μJ, by inducing unidirectional lasing without causing additional loss within the cavity.

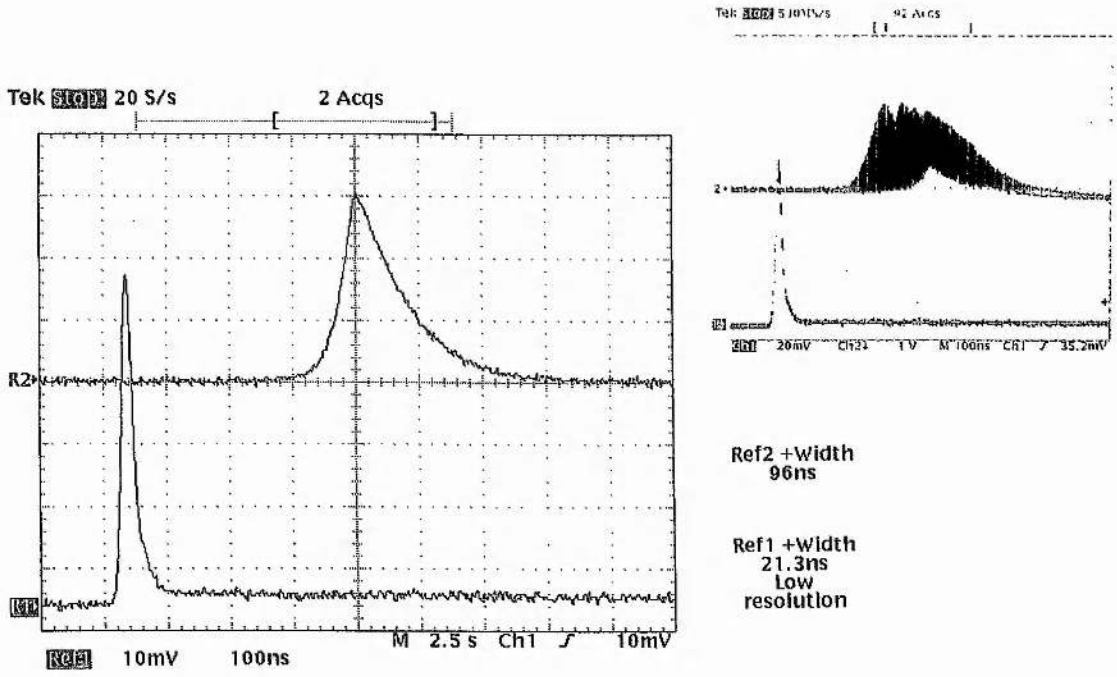

Fig. 6.13: *Ti:Sapphire pulse and Nd:YLF pump laser pulse. The pulse build up time for the Ti:Sapphire pulse shortens by approximately 200ns for well seeded, line narrowed pulses, indicating that the ring cavity is resonant at the seeding wavelength. The repetition rate is 6kHz and the average power 420mW at 630nm. The inset shows oscillations between SLM and multimode operation.*

This does away with the loss prone optical diode and makes short ring cavities easier to achieve. Just as in the Q-switched case the gain-switched cavity should

be as short as possible, in order to minimise the Ti:Sapphire pulse width. The typical pulse shape of the gain switched Ti:Sapphire pulse, delayed by ~300ns from the pump pulse under pumping conditions of 2 to 3 times above threshold, is shown in figure 6.13. By replacing the pulsed diode pumped laser with the cw pumped high repetition system the slope efficiency of the Ti:Sapphire laser improved from 20% to 29%. This increased slope efficiency could be conserved even under high green pump power conditions of 2.5W at 6kHz (25ns pulse width), which extracted 420mW with a pulse width of 100ns (70μJ per pulse). Compared to earlier experiments an average output of 2.7W at this repetition rate would have been expected. Given that optimising a laser for maximum green output and pumping another laser to optimise its output are two slightly different processes (in practical not theoretical terms) the consistence of the high average green or infrared power is one of the positive attributes of the developed laser system.

To finish this short excursion into pumping a Ti:Sapphire laser as an application for the frequency doubled laser, the average output power dependence on the repetition rate of the Ti:Sapphire for different pump power levels are given below.

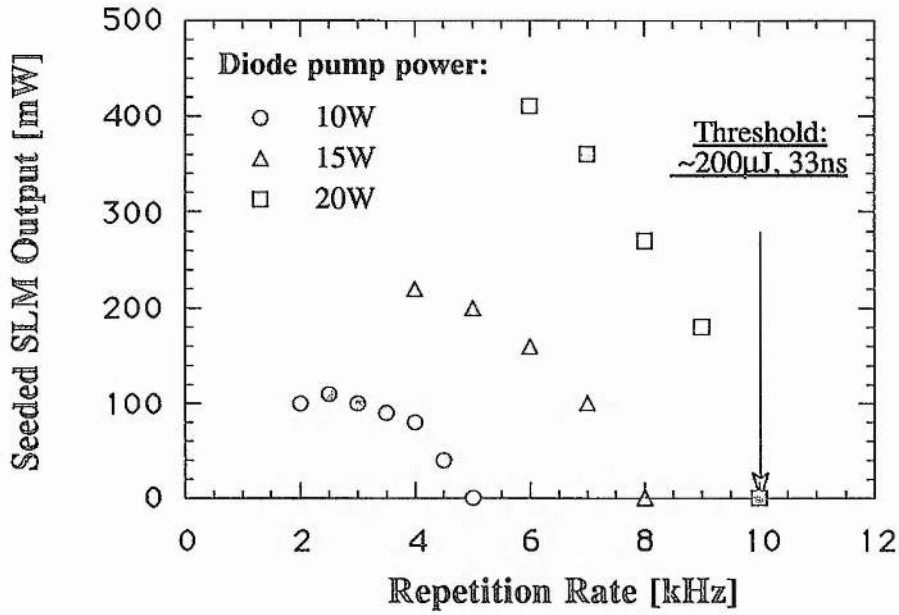

Fig. 6.14: *Average output power (without seeding component) at 830nm of the single longitudinal mode Ti:Sapphire ring laser for a range of diode pump powers up to 20W. The geometrical length of the ring cavity is ~60cm and the seeding power is ≤ 10mW.*

Further development of this Ti:Sapphire laser are under way and are being conducted by Garry Morrison. Improvements are to be expected by replacing the crystal, shortening the cavity and locking the cavity to the seed source [22].

While pumping the KTP doubler at moderate to higher infrared powers (2 to 5W) thermal effects on the phase matching could be observed. These were, however, only of transient nature at the start of the pumping process, until steady state temperature conditions were again established within the KTP. After blocking the pump for a while and then resuming the experiments the doubled output initially dropped by 10-20% depending on the incident average IR pump level. Only to increase once more within about a minute to the steady state value, while the alignment remained unchanged at all times, being optimised for the steady state conditions. The power drop could be immediately compensated by rotating the KTP crystal in ϕ. Given the published temperature dependence of $n_{x,y}$ [23] the total temperature increase within the KTP can be estimated by modifying the earlier acceptance angle calculation of eqn. (6.5). The misalignment term $\delta\phi$ is replaced by the temperature dependent change in the phase mismatch $\Delta k(\phi_m, \Delta T)$.

$$P_{2\omega}(\Delta T, l) \propto \frac{\sin^2\{\Delta k(\phi_m, \Delta T) l / 2\}}{\{\Delta k(\phi_m, \Delta T) l / 2\}^2} = 0.8 \ldots 0.9 \qquad (6.14)$$

In the case of an external, single pass doubling scheme these temperature effects are of no further concern, as long as the temperature gradients across the IR pump beam within the KTP crystal do not cause the de-phasing process. These internal temperature gradients would set a fundamental limit to the IR and green intensities within the doubler, depending on the crystal parameters of absorption at these wavelengths, thermal conductivity and doubler length. However no signs of this final limitation could be observed at incident average powers of up to 5 to 6W. All decreases in the doubling efficiency were always related to transversal mode control problems with the pump beam.

These thermal effects highlight the problems encountered under CW intra-cavity doubling schemes. Assuming circulating powers in the IR were in the 100W range and tight focusing of 30 to 50μm within the KTP (compared to <10W/125μm) the optical path length changes induced by output power fluctuations in the conversion efficiency would cause problems with the stability of the longitudinal mode structure. For this reason most intra cavity

doubled system temperature stabilise not only the doubling crystal, but also the additional intra-cavity elements, such as etalons, within the cavity [24].

To close this chapter a possible use of the 1072nm line of Nd:YLF in combination with a temperature tuned NCPM typeII KTP/A doubler is proposed. The paper mentioned earlier by H. Kimble made use of a temperature tuned KTP typeII doubler, within an external resonant cavity to double 1080nm (from a Nd:$YAlO_3$-laser) with an efficiency of up to 85% [25] under cw operation. The main problem in using the usual typeII CPM configuration is the walk-off between the e- and o-waves of the fundamental, causing losses in a high finesse resonant cavity. The use of a typeII NCPM geometry, which is walk-off free, avoids this problem. However, extreme temperature stabilisation (down to some 20 milli-Kelvin [25]) is necessary to keep the o- and e-wave on resonance within the cavity.
Figure 6.15 shows the temperature tuning of a KTP doubler, assuming the bigger dn/dT temperature tuning coefficients given in [23a], if compared with the later data given by Bierlein & Vanheerzeele [23b].

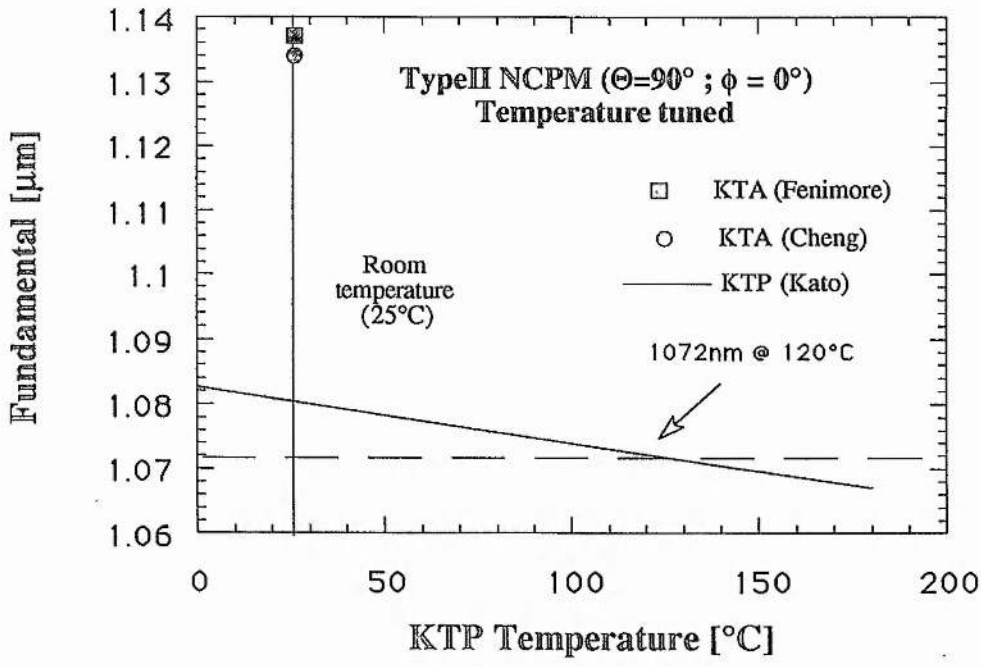

Fig. 6.15: *Temperature tuning of a NCPM (Θ=90°, ϕ=0°) typeII KTP doubler. The temperature tuning coefficients were taken from [23a] and used to obtain temperature dependent Sellmeier equations for calculation of the phase matched fundamental wavelength dependence on temperature.*

This temperature stabilisation requirement by using a typeII geometry is not too much of a disadvantage, if compared to other high power doubling schemes, as they all are most likely to need temperature stabilising of the non-linear crystal to avoid longitudinal mode instabilities, due to heating effects caused by the fundamental and generated green radiation within the crystal. These effects are obvious even under external, single pass doubling and moderate infra-red powers, as described before in this chapter.
Comparing the calculated tuning rate of the flux grown KTP with the actually quoted phase matched temperatures in [25] (56°C and 150°C) to achieve doubling at 1080nm in KTP, makes the idea of achieving temperature tuned phase matching 8nm away from 1080nm, at reasonable temperatures (≤200°C), somewhat doubtful. More interesting is a temperature tuned NCPM approach in KTA (Θ=90°, ϕ=90°). The problem here are the varying Sellmeier equations, each of them being specific to certain dopant levels in flux grown KTA and at times even then only applicable over a fixed wavelength range.

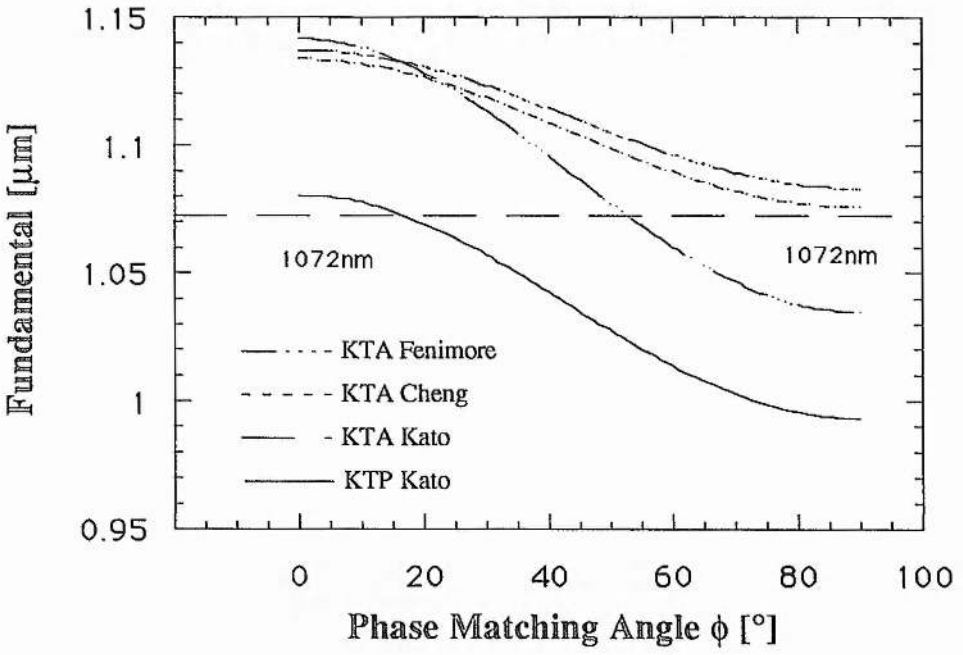

Fig. 6.16: *The fundamental as a function of the phase match angle ϕ (xy-plane) for typeII doubling in KTP and KTA. The various Sellmeier sets for KTA are material and wavelength dependent. Table 7.10 gives an overview of the growth method and optional dopants for each data set.*

The problems connected to finding the relevant set of Sellmeier data is described in detail in chapter 7, where these inconsistencies of the available data

caused problems in predicting the output wavelength of a NCPM typeII KTA-OPO (x-cut).
The cut-off wavelength of the Cheng set at 1073nm coincidences very well with the more exotic lasing wavelength of Nd:YLF at around 1072nm. Even with the evidently very slow temperature tuning behaviour of KTA ($dn_y/dT \sim dn_z/dT$) as derived from the KTA-OPO experiments later, the small difference in wavelength could be bridgeable by heating the crystal, if the Cheng set gives the correct dispersion relation in this wavelength region.
According to our experience the set of Fenimore describes KTA from Crystal Associates very accurately when pumping a NCPM KTA-OPO in the 1μm region, while the results from the set of Kato are not applicable. This and the fact that the Cheng-set describes the Crystal Associates x-cut KTA-OPO very well for shorter pump wavelengths (~800nm) [26] gives rise to the hope that it would be the right set to use in describing doubling in KTA.

Clearly, doubling of 1072nm in a NCPM typeII geometry in KTA is a long shot. Firstly, it would have to be established that Nd:YLF has a high crossection at 1072nm, as expected from the earlier fluorescence measurements, which contradicts measurements by Ryan and Beach, predicting crossection values only comparable to those of 1.3μm operation. However, failing this it would still be desirable to conduct doubling experiments at 1072nm, just to establish which set of Sellmeier equations correctly describes this experiment in KTA sourced from Crystal Associates. To reduce the danger of ending up with an unusable crystal, an uncoated y-cut KTA crystal would be suited best, as it could be used for NCPM-OPO experiments. Otherwise a short (≤5mm) uncoated crystal at $\phi \sim 73°$ (5mm aperture) would give the best chance of resolving this doubling question, by allowing angle tuning.
Alternatively the faint green emission observed, when pumping the NCPM KTA OPO ($\Theta=90°$, $\phi=0°$) with the fundamental polarisation along the z-axis (opposed to pumping along the y-axis, as required for the typeII KTA-OPO) may be used to compare the predictions of different Sellmeier sets.

The very broad angle, temperature and wavelength tolerances of non-critical phase matching are very attractive, especially for low threshold, high repetition rate conversion schemes, as discussed in this thesis. Until recently no room temperature doubling of a main stream Nd-line was possible, till Crystal Associates reported NCPM typeII doubling at 1064nm, using x-cut Sodium doped KTP ($K_{1-x}Na_xKTiOPO_4$) [27].

6.3 Third harmonic generation - a short review

To reach the third harmonic of the fundamental with a χ^2 interaction a two-step conversion process is necessary. This involves as a first step frequency doubling, followed by a mixing process in the second stage between the non-converted fundamental and the second harmonic. With the third harmonic of 1047nm being in the near UV (349nm), absorption at this wavelength becomes an important issue in the material choice for the mixer. BBO and LBO are now well established inorganic, non-linear materials with a transparency range below 200nm (~190nm) and up to 2600nm [17], and therefore often used for short wavelength generation.

LBO was chosen because of its much lower Poynting vector walk-off, as compared to BBO. The short interaction length in BBO under the necessarily tight focusing of a high repetition rate system with pulse energies of up to 1mJ is a severe drawback. This also limits the scope of high repetition rate fourth harmonic generation, which leaves only BBO as the effective, phase matchable inorganic material. For this reason also was the third harmonic generation instead of the quadrupled fundamental preferred as a conversion scheme into the UV.

LBO has the additional material advantage, of being mechanically very hard and non-hydroscopic. On the down side is a reduced effective non-linear coefficient, as compared to BBO, and technical coating difficulties, due to thermal expansion coefficients along the crystal axes with opposite signs. The table below summarises some relevant properties of LBO .

negative, biaxial crystal	$\Omega = 54.6°$; point group: mm2 ; [12]
transparency	0.35μm - ≤ 2.6μm [12]
d_{eff} for typeII mixing	yz-plane: $d_{oeo} = d_{31} \cos\Theta$ [12]
Non-linear coefficients [pm/V]	d_{31}=1.09 ; d_{32}=1.17 @ 1064nm ; [17]
acceptance angle [mrad (°)]	$\delta\Theta = 2.1$ (0.13), $\delta\phi = 38$ (2.3) (16mm long LBO) @1047nm
walk off angle	$\rho = 1°$ in the yz-plane

Table 6.11: Parameters of LBO relevant to high repetition rate, low energy per pulse conversion schemes.

The three wave interaction process which describes sum frequency mixing in non-linear crystals has been dealt with in detail by Armstrong, Bloembergen et al. [18]. This overview will just mention the straightforward phase matching calculation and a brief introduction to the problems of optimising the length of the mixing crystal, depending on photon ratio M and intensity [19]. This known problem is intensified by the presence of walk-off between the fundamental and second harmonic, which has been found to be compensated for by walk-on in the LBO mixer, as shown later in the experimental section.

TypeII (oeo) phase matching for sum-frequency mixing in LBO can be achieved by confining the propagation to the principal planes, by setting ϕ=90°. This simplifies the direction cosines considerably, as mentioned before, with the difference being that the critical tuning plane is in the yz-plane instead of in the xy-plane, as during the frequency doubling experiments.

$$a_i^1 = \begin{pmatrix} 0 \\ -\cos(\theta) \\ \sin(\theta) \end{pmatrix} \qquad a_i^2 = \begin{pmatrix} -1 \\ 0 \\ 0 \end{pmatrix} \tag{6.15}$$

This typeII critical phase matched mixing process is described in terms of a three wave interaction by the following relation:

$$o \;<\!\!---\!\!>\; e + o \qquad\qquad 3\omega_f \;<\!\!---\!\!>\; 2\omega_f + \omega_f \tag{6.16}$$

The frequency doubled component $2\omega_f$ is the extraordinary wave with its propagation described by the extra-ordinary refractive index $n_e[\Theta, n_y(\lambda), n_z(\lambda)]$, and being confined within the yz-plane. The fundamental and UV component are linearly polarised, ordinary waves with refractive indices of n_x. The energy conservation principle is intrinsically satisfied by the three known photon energies, which interact in the sum-frequency mixing process to generate the third harmonic. The phase matching calculation is thus reduced to solving only the momentum conservation equation for θ:

$$n_o(\frac{\lambda_f}{3})3\omega_f = n_e(\theta, \frac{\lambda_f}{2})2\omega_f + n_o(\lambda_f)\omega_f \quad , \quad \text{with} \tag{6.17}$$

$$n_e(\theta,\lambda) = \Big/ \sqrt{\frac{\cos^2(\theta)}{n_y(\lambda)^2} + \frac{\sin^2(\theta)}{n_z(\lambda)^2}} \quad ; \qquad n_o(\lambda) = n_x(\lambda)$$

The refractive indices n_x, n_y and n_z are described by the Sellmeier equations for LBO, where a set refined several times by Cheng [20] has been used (Appendix A). For a fundamental wavelength of 1047nm, the phase matched angle is $\theta_{pm}=46°$ ($\phi=90°$) for generation of the third harmonic in LBO. Compared to the KTP doubler, the tuning for this conversion process is slow and a change from 1047nm to 1064nm in the fundamental needs only a change of 3.8° ($\Theta_{pm}=42.2°$ @ 1064nm) in the phase match angle. This corresponds to a change in the external angle of 6°, and indicates that the same cut of LBO could be used for the most common 1μm pump lasers, if the need arises. The whole tuning curve for frequency tripling in LBO propagating in the yz-plane is shown below.

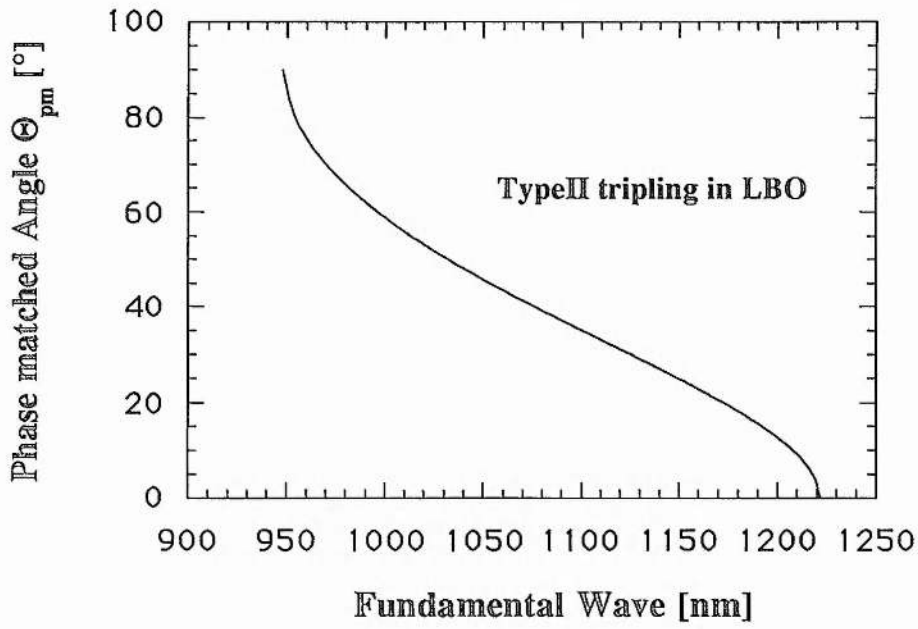

Fig. 6.17: *Possible phase match angle for typeII interaction ($\phi=90°$) to generate the third harmonic in LBO as a function of the fundamental pump wavelength when mixed with the second harmonic.*

The wide range of phase matchable fundamental wavelengths does not imply that a typeII interaction as above will be the optimum tripling configuration for wavelengths away from the 1μm range. In every case the effective non-linear coefficient has to be calculated and attention paid to the walk-off angle, which depends on the focusing requirements. The optimum conversion scheme for high repetition rate lasers is characterised by a high d_{eff}, small walk-off angle ρ and a wide acceptance angle $\Delta\phi$ or $\Delta\Theta$. The first demonstration of sum-frequency mixing into the UV in LBO together with an analysis of the possible typeI and II interactions can be found in a paper by Wu & Chen [14] which

addresses these problems.

So far only phase matching calculations restricted to the principal planes of the biaxial crystals LBO and KTP have been described, which are coincidentally the optimum configurations for doubling and tripling at room temperature in these crystals. In leaving the principal planes no simplification for the direction cosines applies, and the polarisation angle $\delta(\Theta, \phi, \Omega)$ turns into a non-zero value, with Ω being the angle between one of the optical axes with the x-axis in the xz-plane (LBO is a negative biaxial crystal, with $\Omega \geq 45°$, for positive biaxial crystals such as KTP, Ω is measured from the z-axis and $\Omega \leq 45°$). The values for the optical axes orientation have been taken from [12], and are $\Omega_{LBO} = 54.6°$ and $\Omega_{KTP} = 21.7°$. The equation for the polarisation angle δ (negative biaxial case) and the direction cosines are shown in the table below after [10]:

General	CPM with ϕ=90° (in yz-plane)
$a_{(i),1} = \begin{pmatrix} -\cos\Theta\cos\phi\cos\delta + \sin\phi\sin\delta \\ -\cos\Theta\sin\phi\cos\delta - \cos\phi\sin\delta \\ \sin\Theta\cos\delta \end{pmatrix}$	$a_{(i),1} = \begin{pmatrix} 0 \\ -\cos\Theta \\ \sin\Theta \end{pmatrix}$
$a_{(i),2} = \begin{pmatrix} -\cos\Theta\cos\phi\sin\delta - \sin\phi\cos\delta \\ -\cos\Theta\sin\phi\sin\delta + \cos\phi\cos\delta \\ \sin\Theta\sin\delta \end{pmatrix}$	$a_{(i),2} = \begin{pmatrix} -1 \\ 0 \\ 0 \end{pmatrix}$
$\tan(2\delta^-) = \dfrac{\sin(2\phi)\cos\theta}{\sin^2\phi - \cos^2\Theta\cos^2\phi + \cot^2\Omega\sin^2\Theta}$; $\Omega_{LBO} = 57.6°$	

Using the components of the direction cosines, the refractive indices can be determined according to equation 6.11b and the typeII phase matching condition for the mixing process (eqn. 6.16) is solved for pairs of azimuthal and polar angles Θ, ϕ out with the principal planes. The identification of quasi-ordinary and extra-ordinary refractive indices for phase matching not in the principal planes has been done by transferring the labelling in the special case of ϕ=90° to the general case of ϕ, $\Theta \neq 0, 90°$. This results in n_2 being the extra-ordinary refractive index in equation 6.16. Commercial mathematical packages

as MathCad or Mathematica make phase match calculations, even in this general case straightforward, and the calculated phase match loci for a typeII mixer in LBO for both of the common 1μm fundamental wavelengths are shown below.

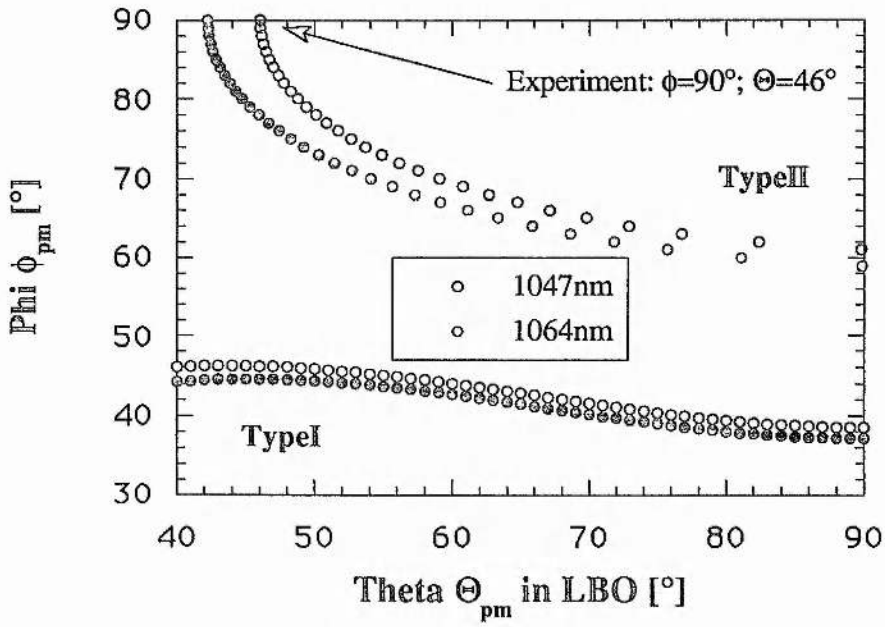

Fig. 6.18: *Critical phase matching out with the principal planes for a typeII (oeo) sum-frequency mixer in LBO with fundamental wavelengths of 1047nm and 1064nm. The typeI (oee) phase match loci have also been calculated so as to discuss the different d_{eff}'s for both schemes.*

The phase matchable direction of Θ=90° and ϕ=62° (@1047nm, typeII) is a good example of the importance of the consideration of the effective non-linear coefficient d_{eff} . According to [12] the d_{eff} becomes zero in this propagation orientation for a typeII (oeo) and typeI (eoo, not phase matchable for tripling purposes) phase matching scheme.

$$d_{oeo} = d_{eoo} = d_{31}\cos\Theta \qquad \text{(in yz-plane)}$$

However, the other typeI (oee) scheme with Θ=90° is distinguished by a non-zero non-linearity as well as a phase matchable orientation (ϕ=39° @ 1047nm), as calculated above (fig. 6.12). With both possible typeI (oee) and typeII (oeo) schemes having similar effective non-linearties, the lower walk-off for the typeII scheme has given it priority over the typeI configuration in a high repetition rate, low energy per pulse conversion regime.

In a two stage non-linear process the above considerations of non-linear coefficient, phase matching and walk-off are only part of the search for an optimum tripling configuration. By using a typeII doubling scheme 50% of the fundamental is not in the required orientation for the subsequent mixing process, which needs one 'IR' and one 'green' photon in the ordinary and extra-ordinary polarisation orientations respectively, in order to satisfy the energy balance. A conversion efficiency of >50% from the fundamental into the green would thus be over-conversion and counter productive for optimised UV generation. The limit for over-conversion in a typeI scheme into the green would be higher, at 66%. A detailed discussion of polarisation mismatch schemes for sum-frequency mixing in LBO can be found in [19].
Technical problems with AR-coatings on LBO, which are even more pronounced in the temperature tuning (T_{match}=~165°C) typeI (eoo) NCPM doubling scheme (Θ=90°, ϕ=0°, propagation along the x-axis) and the generally lower non-linear coefficient (d_{eff}=1pm/V), made conversion efficiencies over the 50% mark with no coatings and moderate crystal length (≤20mm, cost factor) unrealistic. For this reason a KTP/LBO doubling and mixing stage were chosen to achieve conversion into the near UV (349nm) from the pump laser (1047nm).

6.4 Sum frequency mixing results in the near UV

Another immediate application for the green generated, is sum frequency mixing the doubled output with the remaining undepleted fundamental radiation. Again, a suitably cut LBO piece was available in the laboratory. The 16mm long crystal, with a $5x5mm^2$ aperture is, uncoated, which reduces the efficiency of the frequency tripling and also causes problems for the KTP and its coatings, due to absorption of the reflected UV radiation, if the KTP is not protected from the back scattered UV component. Nevertheless, encouraging results were achieved with this non-optimised crystal. The incident polarisations and crystal axes orientations needed to achieve typeII critical phase matching in LBO at room temperature are displayed in the sketch below.

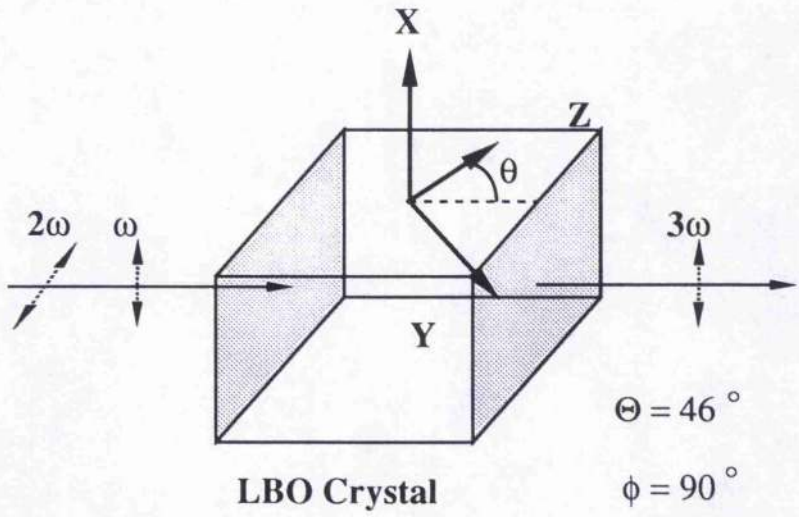

Fig. 6.19: *Illustration of the crystal axes and polarisation orientation for type II critical phase matching at room temperature in LBO.*

One of the problems in combining these two critically phase matched processes is the walk-off introduced in the KTP. With further propagation the separation of the fundamental and doubled radiation will increase. This reduces the most basic requirement for frequency mixing, the overlap of both beams. Re-focusing after the doubling is therefore impractical as the conversion efficiency gained by higher intensities is totally reversed by the reduced interacting area of the input beams. Utilising an uncoated 100mm lens for re-focusing reduced the UV output at 349nm down to below 50mW, as opposed to 150mW in a close coupled set-up of both non-linear converters (10W pump power).

An additional advantage of this close coupled set-up is the need for only one infra-red antireflection coated lens. An ideal re-focusing lens would require a dual band AR-coating or would otherwise introduce considerable loss, so that an uncoated lens might be the better compromise. In addition to close coupling the walk-off in the KTP can be compensated for by walk-on in the LBO. The considerable improvement in conversion efficiency is shown in figure 6.15.

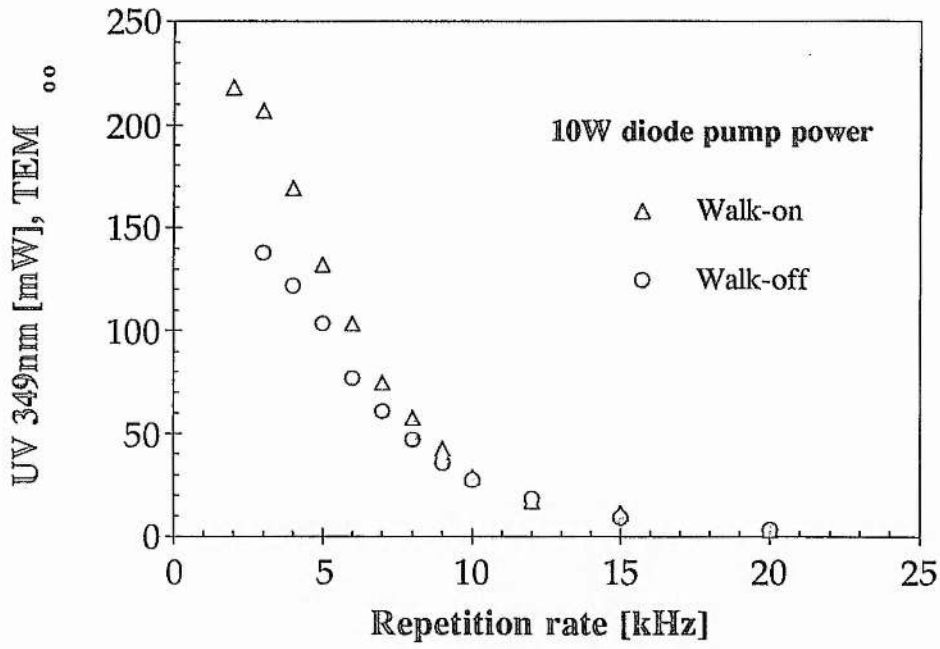

Fig. 6.20: *Higher conversion efficiencies can be achieved by facilitating walk-on instead of walk-off for the doubled and fundamental beams. The crystal positions for further walk-off or compensating walk-on are separated by a rotation of 180° around the axis of beam propagation. The results displayed are at 10W diode pump power.*

The close coupled KTP and LBO pieces made a change in the focusing lens necessary. The longer Raleigh-length of a 125mm lens, as compared to the previously 100mm lens, optimised the overall performance into the UV, by sacrificing conversion efficiency into the green for a tighter beam diameter in the LBO. At the same time the relaxed focusing reduces the problem of possible over-conversion into the green. The distance of the AR-coated 125mm lens from the output coupler of the laser was again 18cm, the centre of the KTP piece was 11cm behind the lens and the centre to centre distance of the KTP and LBO was approximately 60mm. This minimum separation of 60mm was caused by a non-optimised set-up (both crystals were each mounted on a prism table and rotation stage). Also, the uncoated LBO required a spatial filter in the

form of a pin hole between the KTP and LBO, to prevent reflected UV from deteriorating the KTP doubler by absorption.
A picture of the pin hole arrangement can be seen on the next page (figure 6.16) as well as the fluorescence of the 349nm on a piece of paper, and the undepleted green beam. The separation between the frequency tripled and doubled output is achieved by a combination of beam splitter (HR 349nm, 45° and HT 523.5nm, 0°) and prism. The prism is added to ensure that no leakage of green or infra-red changes the UV output measurements. This caution is exercised as the UV beam splitter used exhibits a fairly strong polarisation dependent infra-red leakage (5 - 15%).
After these first optimisations and precautions at the 10W pump level were concluded, higher diode pump powers of up to 20W did not cause problems. The results shown in figure 6.17 are corrected for the Fresnel losses on the surfaces of the Quartz prism (6% per surface). No correction, however, has been applied for the losses on the uncoated LBO piece.
Higher pump powers than 20W show only a marginal improvement in the converted UV output (i.e.: 750mW for 23Wof diode pump power). This is due to the deteriorating beam quality, amplified by the dependence of the mixing process on beam overlap.
A later analysis will show if there is any scope in cylindrical focusing, to improve the tripling efficiency at pump powers below the 20W mark. A certain improvement would be gained by AR coating the LBO piece. The minimum requirement would be an UV anti-reflection coating, to protect the KTP and improve UV output. If the damage threshold allows for a two band coating, then a combined IR/green AR coating could be added. The two-band coating would be deposited onto the entrance aperture of the LBO crystal, while the single layer anti-reflection UV coating is only necessary at the exit aperture, to reduce reflection losses and protect the KTP from UV damage. The split of the coatings minimises the necessary layers on the difficult to coat material LBO [22]. The length of the LBO piece is an added important parameter, which has not been reviewed yet.

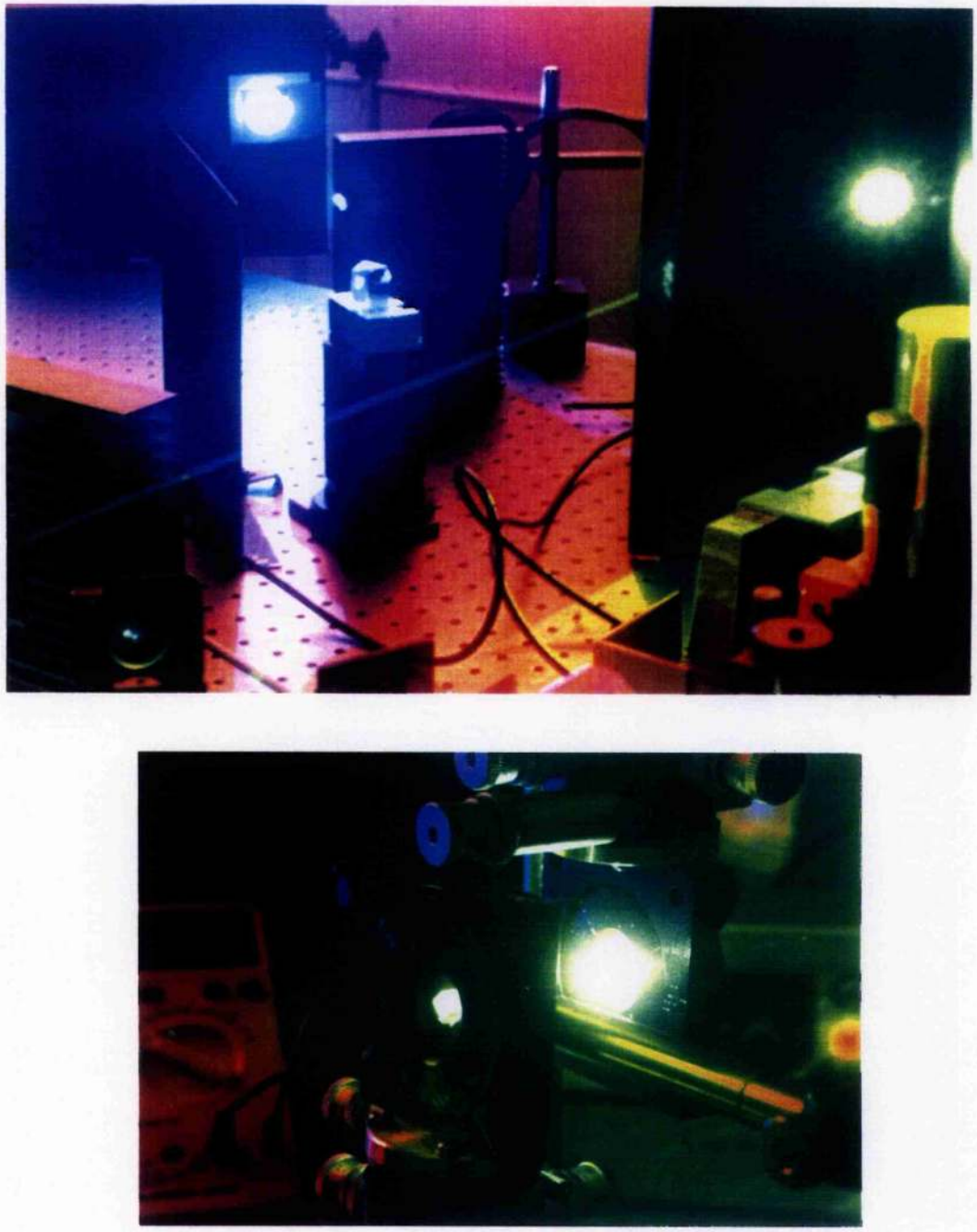

Fig. 6.21: *The blue fluorescence on a piece of paper caused by the incident UV is clearly visible, as is the undepleted green beam. The picture below shows in close-up the narrow gap between the KTP and LBO pieces. The pin hole in between is necessary to protect the KTP from the UV reflection of the uncoated LBO piece.*

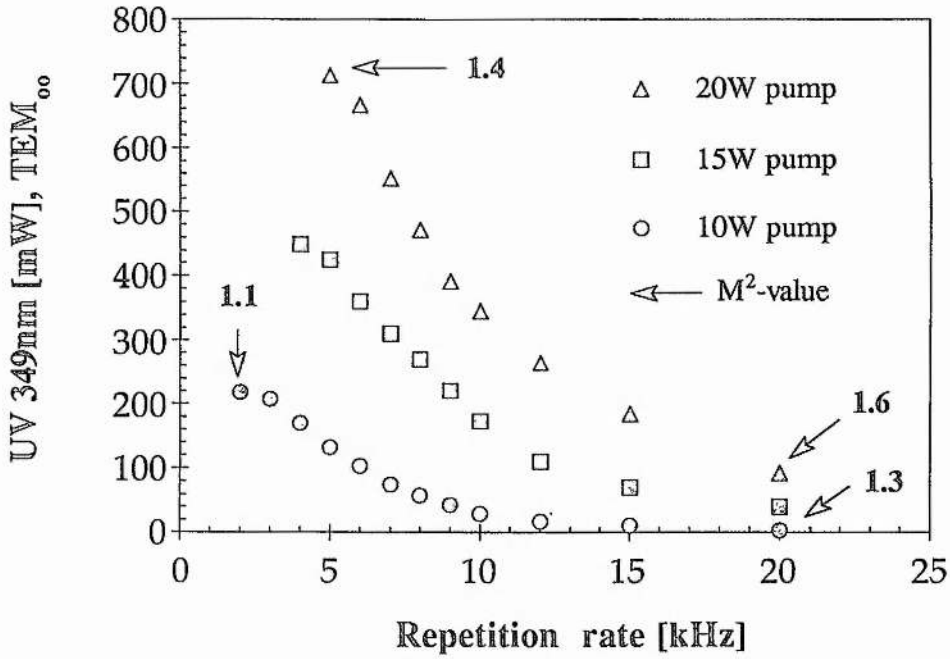

Fig. 3.16: *Depending on the repetition rate average output powers of up to 720mW in the near UV at 349nm are feasible for a diode pump power of 20W.*

The UV output power in the above experiment has been optimised for maximum output at low repetition rates. For some applications, such as hardening resins out of the fluid phase to model three dimensional objects, a very high repetition rate UV output (≥15 to 20kHz) could replace more traditional cw near UV sources such as a He-Cd gas laser (354nm, P_{out}≤30mW). Under these circumstances intracavity doubling might provide a higher average green output, by taking advantage of the higher intra cavity intensities, than in the case of external single pass doubling. Contrary to the usual intra-cavity doubling scheme [23], the frequency doubled radiation would not be the only output loss, as output coupling at the fundamental wavelength is essential for the mixing process, reducing the advantage of intra-cavity doubling.

A typeI NCPM scheme in temperature tuned LBO for generating green radiation without the walk-off problems generated by the KTP doubler would be the preferable alternative for intra-cavity doubling. This would not only allow re-focusing into the LBO but, more importantly, all of the coupled out infra-red polarisation would have the suitable orientation for the following mixing process, keeping the additional IR output coupling losses to a minimum, thus maximising the intra-cavity intensity.

Even if no improvements are possible, the frequency tripling scheme demonstrated here, already reaches 120 to 150μJ in 25ns (peak power: 6kW at 349nm, 5kHz), which should allow its use as a pump source for a tuneable LBO-OPO, with a possible tuning range covering the visible into the infra-red [24]. However, this goal has been postponed, due to the limited remaining time. As an intermediate step, and to gain the necessary experience with high average power and high repetition rate pumped OPO's, it has given precedence to the experimentally easier option of an infra-red pumped KTP/KTA-OPO. These results will be discussed in the next section.

6.5 Conclusions

These first applications of the Nd:YLF laser confirmed the importance of an excellent beam quality for non-linear optical applications. The combination of optimised KTP doubler length for the peak powers available and near diffraction limited output at high average powers demonstrated the possibility of a multiwatt (~3W) green source with repetition rates in the kHz region (5-6kHz).

The subsequent frequency mixing experiments again benefited from the high quality of the pump laser. At an early stage of the optimising process promising results were achieved (~700mW of 349nm). An overview about the experimental results is given in table 6.18.

Green (523.5nm)	TEM_{10} 26W pump power	3.6W @ 7kHz, 25ns ~50% IR conversion
	TEM_{oo} 20W pump power	2.9W @ 6kHz, 27ns ~58% IR conversion
	TEM_{oo} 10W pump power	1W@ 4kHz, 30ns ~60% IR conversion
UV (349nm)	TEM_{oo} 20W pump power	720mW @ 5kHz, 24ns ~15% IR conversion
Single pass frequency converters	Doubler 10mm long KTP critical type II AR/AR 1047 & 523nm	Sum-frequency mixer 16mm long LBO critical type II uncoated

Table 6.18: *Summary of the frequency conversion experiments with emphasis on the results and experimental configurations.*

The limitations during these experiments were mainly pump laser induced. Damage in the converter crystals could be circumvented by choosing an appropriate focal spot size, with matching converter length. Critical in the damage behaviour appeared to be not only the single pulse peak intensity in the crystal, but also the focal spot size. No adverse damage effects could be experienced for scaling in repetition rate.

The medium term stability of the KTP doubler crystal was unproblematic during the experiments (~20 hours high average power green), if the limitations for peak power intensities and focal spot size were followed.

How far gray tracking in KTP will be a problem for this application in the long term remains to be seen. Slight traces of gray tracking were observed after the UV experiments, possibly due to back scattered UV light, with no changes in the typical performance.

Future work should concentrate on the UV generation, as it is hoped that an optimised set-up will push towards the 1W average power border. This conversion scheme is especially interesting because of its application as a pump source for a broadly tuneable LBO-OPO covering the visible and near infra-red. In connection with the frequency tripling experiments, a typeI NCPM scheme in temperature tuned LBO for green generation might improve efficiency and has no potential long term gray tracking problems. This doubling geometry might also have the best chance to improve the higher repetition rate (15 to 25kHz) UV output, with an intra-cavity doubling configuration.

References

[1] C.Rahlff , B.D.Sinclair , W.Sibbett & M.H.Dunn - **"High power end-pumped effects and applications in Nd:YLF at 1047 and 1321nm"** Paper CThG4, Conference on Lasers and Electrooptics, Anaheim, May 1994

[2] P.A.Franken, A.E.Hill, C.W.Peters & G.Weinreich - **"Generation of optical harmonics"** Phys. Rev. Lett. 7,118, 1961

[3] F.A.Hopf & G.I.Stegeman - **"Applied Classical Electrodynamics" ; Vol.II: Nonlinear Optics** ; John Wiley and Sons 1988
J.Yao & W.Sheng - **"Accurate calculation of the optimum phase matching parameters in three wave interactions with biaxial non-linear optical crystals"** J. Opt. Soc. Am. B **19**, No.6, 891, 1992

[4] H.Vanherzeele & J.D.Bierlein - **"Magnitude of the nonlinear-optical coefficients of $KTiOPO_4$"** Opt. Lett. **17**, No.14, 982, 1992

[5] J.D.Bierlein & H.Vanherzeele - **"Potassium titanyl phosphate: properties and new applications"** J. Opt. Soc. Am. B **6**, No.4, 622, 1989

[6] A.Yariv **"Optical Electronics"**
Saunders College Publishing, Fourth edition (1991)

[7] G.D. Boyd & D.A. Kleinman - **Parametric interaction of focused gaussian light beams** - J. Appl. Phys. **39**, No.8, 3597 (1968)

[8] D.A. Kleinman **"Laser Handbook, Vol.2"** p.1229
North-Holland (1972)

[9] D.A.Roberts - **Simplified characterisation of uniaxial and biaxial nonlinear optical crystals: A plea for standardisation of nomenclature and conventions-** IEEE J. Quantum Electron. **QE-28**, No.10, 2057,1992
G.Robertson - **"Optical parametric oscillators: A comparison of new materials"** Ph.D. Thesis, University of St. Andrews, May1993

[10] C.Chen & Y.Wu - **New nonlinear-optical crystal: LiB_3O_5 -** J.Opt.Soc.Am.B **6** ,No.4, 616,1989
D.Eimerl, L.Davis, S.Velsko et al. - **Optical, mechanical and thermal properties of barium borate -** J. Appl. Phys. **62**, No.5, 1987

[11] J.A Armstrong, N. Bloembergen & al. ; Phys. Rev. **127**, 1918 (1962)

[12] R.S. Craxton; IEEE J-QE **QE-17**, 1771 (1981)

[13] S. Lin, B. Wu, F. Xie & C. Chen; Appl. Phys. Lett. **59**, 1541 (1991)

[14] B.Wu, N.Chen, C. Chen, D. Deng & Z.Xu - **Highly efficient ultraviolet generation at 355nm in LiB_3O_5 -** Opt. Lett., **14**, No.19, 1080, 1989

[15] V.G.Dmitriev, G.G.Gurzadyan, D.N.Nikogosyan - **"Handbook of nonlinear optical crystals"** Series in optical sciences 64 ; Springer-Verlag 1991

[16] Priv. Com.: Cameron Rae from 'Caladox', with the coating suggestion on LBO as a mixing crystal.

[17] D.W. Anthon, D.L. Snipes, T.J. Pier & M.R. Ressl - **Intracavity doubling of cw diode-pumped Nd:YAG lasers with KTP** - IEEE J-QE QE-28, No.4, 1148 (1992)

[18] G.Robertson, A.J.Henderson, Y.Tang, M.H.Dunn et al. - **Comparison of lithium triborate and b-barium borate as nonlinear media for optical parametric oscillators** - J. Opt. Soc. Am. B 10, No.9,1737, 1993

[19] Born & Wolf " Principles of Optics" 6th. edition
G. Mie; Annalen der Physik 25, 377 (1908)

[20] Hans Blumer - **Strahlungsdiagramme kleiner dielektrischer Kugeln** - Zeitschrift für Physik 32, 119 (1925)

[21] G. Morrison, C. Rae, M. Ebrahimzadeh & M.H. Dunn - **Comparison of all-solid-state gain switched Cr:LiSAF and Ti:Sapphire lasers** - Paper P3-1, QE-12, Southampton, September 1995

[22a] N.P. Barnes & J.C Barnes - **Injection seeding I: Theory** - IEEE J-QE QE-29, No.10, 2670 (1993)

[22b] G. Morrison, C. Rahlff, M. Ebrahimzadeh & M.H. Dunn - **A high-average-power, all-slid-state, single frequency Ti:Sapphire laser** - Paper CTuJ4, accepted for CLEO, Anaheim 1996

[23a] V.G.Dmitriev, G.G.Gurzadyan, D.N.Nikogosyan - **"Handbook of nonlinear optical crystals"** - Series in optical sciences 64 ; Springer-Verlag (1991)

[23b] J.D.Bierlein & H.Vanherzeele - **"Potassium titanyl phosphate: properties and new applications"** J. Opt. Soc. Am. B, 6, No.4, 622, 1989

[24] L.Y. Liu, M. Oka, W. Wiechman & S. Kubota - **Longitudinally diode-pumped continuous-wave 3.5W green laser** - Opt. Lett. 19, No.3, 189 (1994)
Priv. Com.: **Edinburgh Instruments**, Edinburgh, UK

[25] Z.Y.Ou, S.F.Pereira, E.S.Polzik & H.J.Kimble - **85% efficiency for cw frequency doubling from 1.08 to 0.54μm** - Opt. Lett., 17, No.9, 640, 1992

[26] S. French, M. Ebrahimzadeh, A. Miller - **High-power, high-repetition-rate picosecond optical parametric oscillator for the near- to mid-infrared** - Opt. Lett. 21, No.2, 131 (1996)

[27] R.A. Stolzenberger, J. Rottenberg & D.N. Loiacono - **Noncritically phase matched $K_{1-x}Na_xTiOPO_4$ for second harmonic generation of 1064nm** - Paper CPD50-1, CLEO, Baltimore 1995

Chapter VII.

Infra-red pumped KTP / KTA - OPO's

As the first OPO device to be pumped, an infra-red pumped KTP-OPO, was chosen, as this laboratory already has had some practical experience with this particular device [1]. Furthermore, this OPO is especially suitable for the cw pumped, repetitively Q-switched laser developed because of its previously demonstrated low threshold ability in a walk-off free geometry [2].

The rapid progress in being able to pump this KTP-OPO with thresholds as low as 6kW per pulse (~200μJ in 38ns) while achieving conversion efficiencies of around 30% into the signal for the 40kW per pulse regime is mainly due to experience previously gained by J. Terry, Y. Cui and Y. Tang. The following section deals only with the issues needed to adapt the OPO to the characteristics of the Nd:YLF pump laser. For a more detailed review of KTP-OPO's please see [3].

In extending these experiments to suit the needs of the new pump laser two possible damage mechanisms had to be paid attention to:

- Peak power damage, due to the resonating signal wave, set a limit on the curvature of the OPO mirrors. Stronger curvature, corresponding to a tighter signal beam waist, would reduce the threshold of the device, but had to be limited to safe signal intracavity intensities to avoid coating damage.
- Average power damage, due to absorption of the idler wave in the KTP around 3.2μm, set a limit to the average pump power or repetition rate at a given conversion efficiency.

To reduce the damage risks associated with high average powers and

repetition rates, the laser source was deliberately made inefficient in terms of average output power. This was achieved by over coupling the cavity with a 50% output coupler (instead of the usual 30% transmission) and reducing the repetition rate down to 125Hz, while maintaining the peak power per pulse in the 40 to 70kW region. With only 90mW average output power at 10W diode pump power a safe mode of operation for the initial experiments could be established.

The high absorption losses of KTP in the region above 2.8μm restrict the KTP-OPO output to the signal wave in the 1.5μm region. With KTA, an isomorph of KTP, now being commercially available, in sizes suitable for high repetition rate applications, an OPO in the mid-infrared at 3.44μm was realised. So far only moderate conversion efficiencies in the region of 6 to 8% from the infra-red into the idler have been achieved for the KTA-OPO. The use of a three mirror cavity, incorporating a CaF_2-polariser to spatially separate the idler and signal, allowed the use of any 1.5μm mirror, regardless of its substrate.
The comparison of these two NCPM phase matched OPO's in terms of beam quality and linewidth is currently being worked on and the preliminary results are presented here.

7.1 Phase-matching of the infrared pumped KTP/KTA - OPO

The crystal cut used for these experiments is for a typeII non-critically phase matched scheme. The pump radiation propagates along the x-axis (x-cut) of the crystal and is linearly polarised along the y-axis. The generated signal has the same polarisation orientation as the pump, while the idler wave is polarised orthogonally, and is thus parallel to the z-axis. An overview of the whole experimental set-up and the polarisation orientations involved is given on the next page in figure 7.1.

In the case of non-critical type II phase matching in KTP with Θ=90° and Φ=0° the refractive indices $n^{(1,2)}$, which describe the phase propagation of the polarisation eigenmodes e^1 and e^2 in KTP can be simplified to:

$$n^{(1)} = n_y \qquad \text{and} \qquad n^{(2)} = n_z \tag{7.1}$$

The wavelength dependence of $n_{y,z}$ is described by the Sellmeier equations for KTP. The Sellmeier coefficients used to calculate the signal and idler wavelengths according to momentum (eqn.7.2) and energy conservation (eqn.7.3) have been taken from a publication by Kato [4] (see also Appendix A). A numerical solution of the two defining equations of momentum and energy conservation describes the signal and idler components of this three wave interaction process for a given pump wavelength:

$$n_y(\lambda_p)\,\omega_p = n_y(\lambda_s)\,\omega_s + n_z(\lambda_i)\,\omega_i \qquad \text{and} \tag{7.2}$$

$$\omega_p = \omega_s + \omega_i \ , \tag{7.3}$$

The indices p, s and i denote pump, signal and idler wavelength λ or corresponding angular frequency ω. For a pump wavelength of 1047nm this yielded a predicted wavelength set for signal and idler of

$$\lambda_{signal} = 1547\text{nm} \qquad \text{and} \qquad \lambda_{idler} = 3240\text{nm},$$

if the Sellmeier set by Kato was used. The experiment itself resulted in a measured signal wavelength λ_{signal}=1540nm. The Sellmeier set proposed by Vanherzeele for hydrothermally grown material [5] is a slightly better description of the flux grown material sourced from Shan-Dong University, China, in predicting λ_{signal}=1539nm, if only for this specific application.

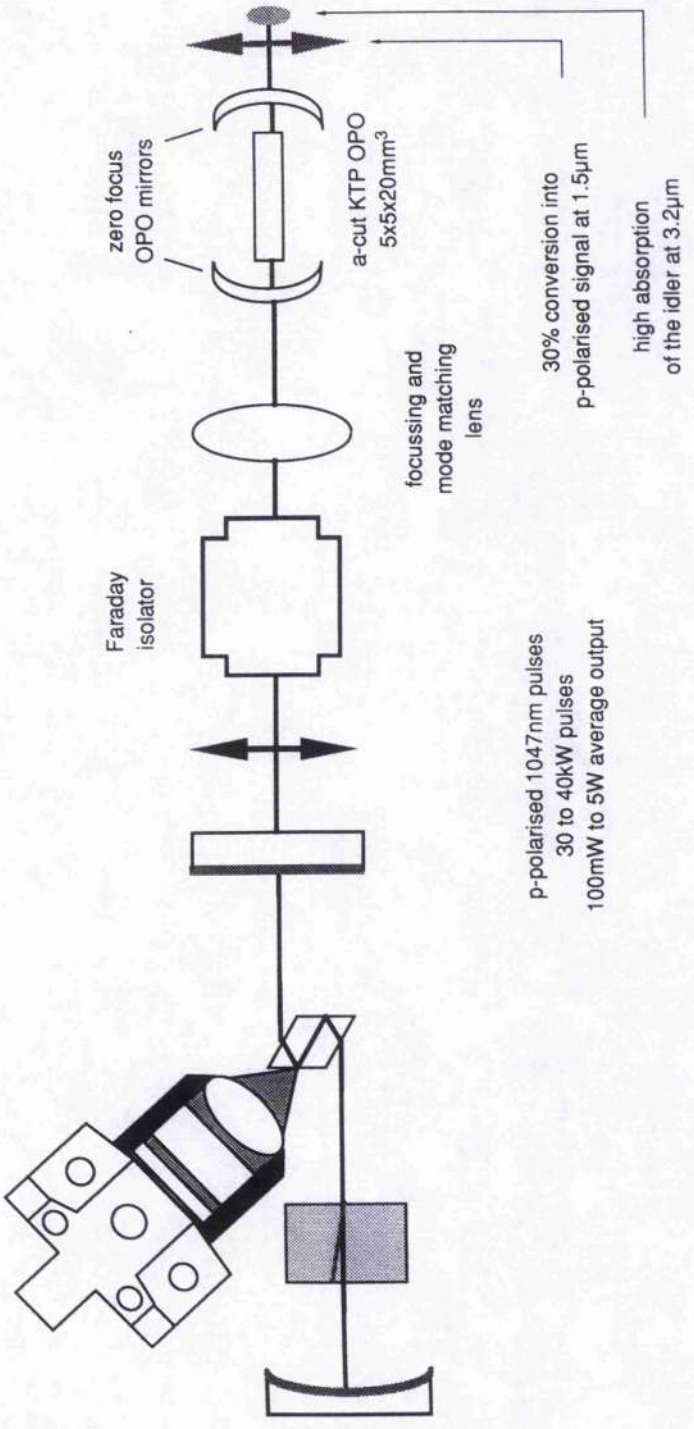

Fig. 7.1: *Sketch of the KTP-OPO set-up. Key components are the zero-focus OPO cavity mirrors, which simplify the set-up especially for the case of small radii of curvature (typical 100mm, cc), and the Faraday isolator. Isolation is necessary as otherwise the pulse-to-pulse stability is greatly reduced by 1µm feed-back into the laser cavity.*

By computing the signal and idler wavelength for a broad region of pump wavelengths, as shown in figure 7.2, it can be seen that this NCPM typeII OPO has two degeneracy points at 541nm and 1.63μm.

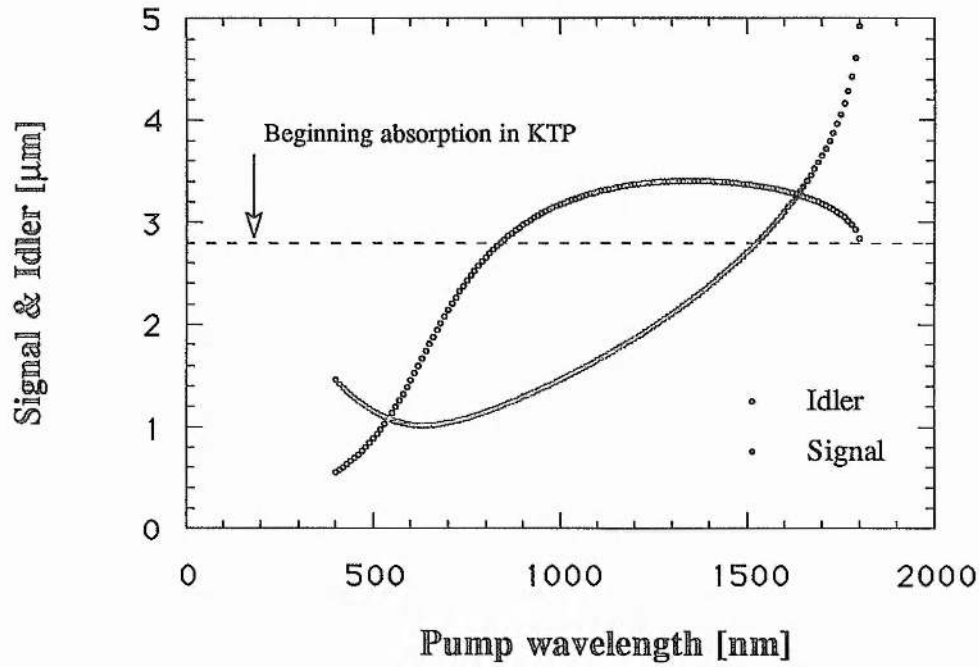

Fig. 7.2: Signal and idler wavelength pairs for a varying pump wavelength range of a NCPM typeII OPO in KTP (x-cut, Θ=90°, ϕ=0°).

The graph also illustrates the problem of defining the name of the high frequency wave of the OPO as the signal, and the low frequency wave as the idler, as this situation reverses past the degeneracy points. A better definition, at least for singly resonant OPO's, is to define the resonating wave as the signal wave, while the idler wave is then the non-resonant, unconstraint wave, of the OPO. In this chapter the signal is always the lower wavelength component of the OPO output at 1.54μm, due to the fixed pump wavelength at 1047nm, as well as the resonating wave, except for in some preliminary KTA-OPO experiments.

The main advantages of the non-critically phase matched OPO-geometry are:
- No walk off and
- High acceptance angle,

making the use of long crystals and tight focusing (damage limitations permissible) possible to compensate for the low energy per pulse of a high repetition rate system. Another advantage is the inherent low linewidth of

these KTP/A-OPO's, if pumped in the 1μm region, as they are then far away from the two degeneracy points. The narrow OPO-linewidth is also caused by the small refractive index change in the pump, signal and idler region. This flat $dn/d\lambda$ variation in the infrared region is indicative of one of the main disadvantages of this infrared pumped NCPM KTP-OPO; the slow tuning rate.

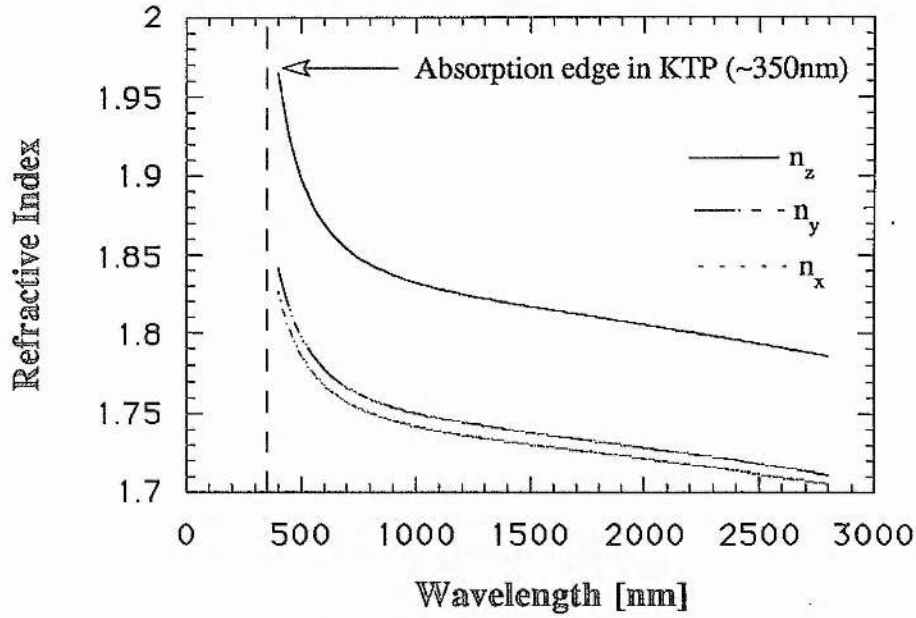

Fig. 7.3: Dispersion curves for the biaxial KTP. Widely tunable OPO's require short pump wavelengths, in order to take advantage of the maximised refractive index variation in this region.

The widely tunable, UV-pumped, critically phase matched LBO-OPO's [6] are for this reason primary candidates for line-narrowing techniques, especially near degeneracy [7]. In general the total linewidth of the OPO is given by three independent contributions, which are:

- the pump laser linewidth
- the pump divergence as defined by the focusing set-up and pump laser mode quality
- the phase matching bandwidth of the OPO material

These three different contributions can be shown to be described by the following equations [7]. They are based on the assumption for the value of the allowable momentum mismatch Δk of π/L, which corresponds roughly to a halving of the single pass parametric gain [8].

Contribution of:	*Variation of the signal frequency (resonant)*
Pump laser linewidth	$d\nu_s = \Delta\nu_p \dfrac{\left[(n_p - n_i) + \lambda_i \dfrac{dn_i}{d\lambda_i} - \lambda_p \dfrac{dn_p}{d\lambda_p}\right]}{\left[(n_i - n_s) + \lambda_s \dfrac{dn_s}{d\lambda_s} - \lambda_i \dfrac{dn_i}{d\lambda_i}\right]}$
Pump beam divergence	$d\nu_s = \dfrac{c}{2L} \dfrac{\partial n_p}{\partial \Theta} \Delta\Theta_p \left[(n_i - n_s) + \lambda_s \dfrac{dn_s}{d\lambda_s} - \lambda_i \dfrac{dn_i}{d\lambda_i}\right]^{-1}$
Phase matching	$d\nu_S = \dfrac{c}{L} \left[(n_i - n_s) + \lambda_s \dfrac{dn_s}{d\lambda_s} - \lambda_i \dfrac{dn_i}{d\lambda_i}\right]^{-1}$

The indices p, s, i denote pump, signal and idler as before, and with:

$\Delta\nu_p$:= pump laser linewidth,

$\Delta\Theta_p$:= pump laser divergence and L := non-linear crystal length.

The phase matching bandwidth is in general the dominating contribution to the total OPO linewidth (i.e. exceeding 10nm near degeneracy in LBO if pumped in the UV [7]), while the influence of the pump divergence, especially in the NCPM geometry investigated, is very small (the variation $\partial n_p/\partial\Theta$ is very small, due to the wide acceptance angle). The influence of the pump linewidth is also minimal, assuming a spectrally narrow pump of less than 1nm, which is not unreasonable.

The strong increase in linewidth near degeneracy ($n_s = n_i$) finds its expression in the inverse dependency of all three linewidth components on the (n_i-n_s) factor, while a strong $dn/d\lambda$ dependency would also broaden the signal spectrum of the OPO, as mentioned before.

The main obstacle in high repetition OPO work is to reach sufficiently low thresholds, with typical pulse energies being less than 1mJ (25nš). For this reason a NCPM x-cut OPO was used, as this propagation direction (Θ=90°, ϕ=0°) has a higher effective non-linear coefficient than the y-cut, NCPM OPO (ϕ=90°), which is also possible . Angle tuning of these devices is also possible, but in the end not practical in a high repetition set-up, as the long crystals used (≤25mm) restrict the internal tuning angle severely (≤ ± 10°), if standard crystal apertures are used (5mm). Other important drawbacks to angle tuning are

increased thresholds, caused by leaving the NCPM geometry, and likely reflection losses with the AR-coated (for 0°) KTP crystal. The tunability achieved is still very restricted, with a change of ~50nm for a change of propagation direction of 90° (ϕ=0° --> ϕ=90°) in the xy-plane. Also temperature tuning of KTP is extremely restricted, as shown in chapter 6, and only worthwhile considering if a few nm change in the emission wavelength is required. The most practical approach to tuning these KTP OPO's is a tuning of the pump laser itself, as it can be provided by a Ti:Sapphire laser.
Figure 7.4 gives an overview of the signal output of non-critical phase matched KTP/A OPO's in the 1μm pump laser region.

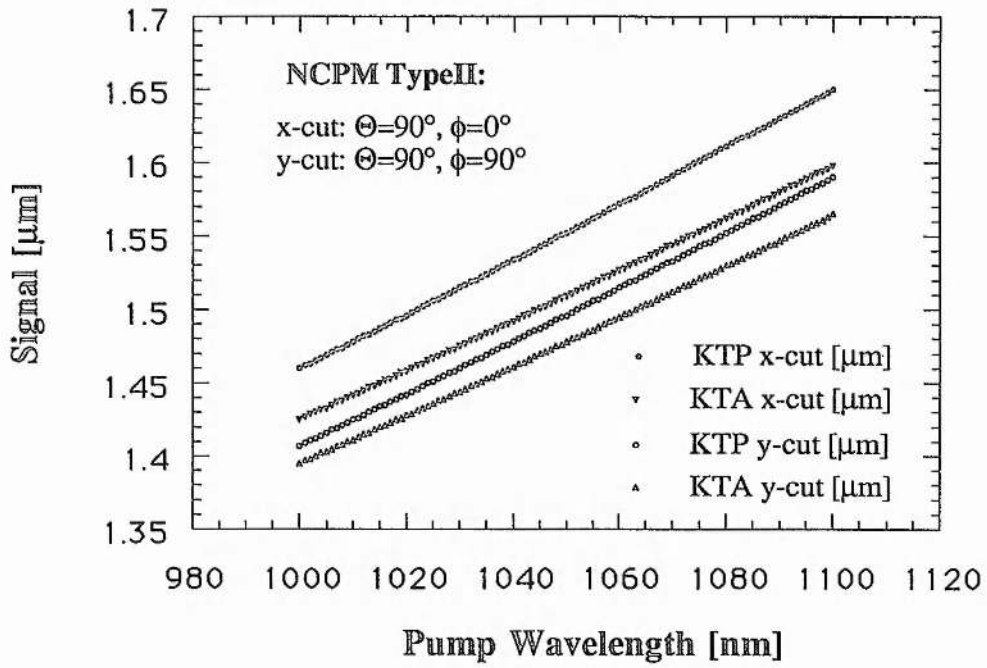

Fig. 7.4: Signal wavelength of NCPM KTP/A OPO's in the 1μm pump laser region.

The y-cut KTP/A signal data is only given out of interest, as this thesis deals only with the NCPM OPO with the propagation direction along the x-axis. A comparison of these two types of NCPM OPO's in KTP has been done by L. Marshall [2], who also recently published the results for an intracavity KTA-OPO [9] (10mm long crystal) with a very impressive conversion efficiency of upto 19% from the IR (8W) into the 3.5μm region (1.5W, at 10kHz). The signal output at the 8W pump power level was 3.8W, corresponding to 48% conversion efficiency.

7.2 High repetition rate KTP-OPO at 1.540μm

With the idler wavelength of the NCPM typeII KTP-OPO being above 2.8μm for the case of an infrared pump laser around 1μm, absorption in the KTP becomes a critical issue [4]. Figure 7.5 shows a transmission spectrum for flux grown KTP and KTA as supplied by Crystal Associates [10].

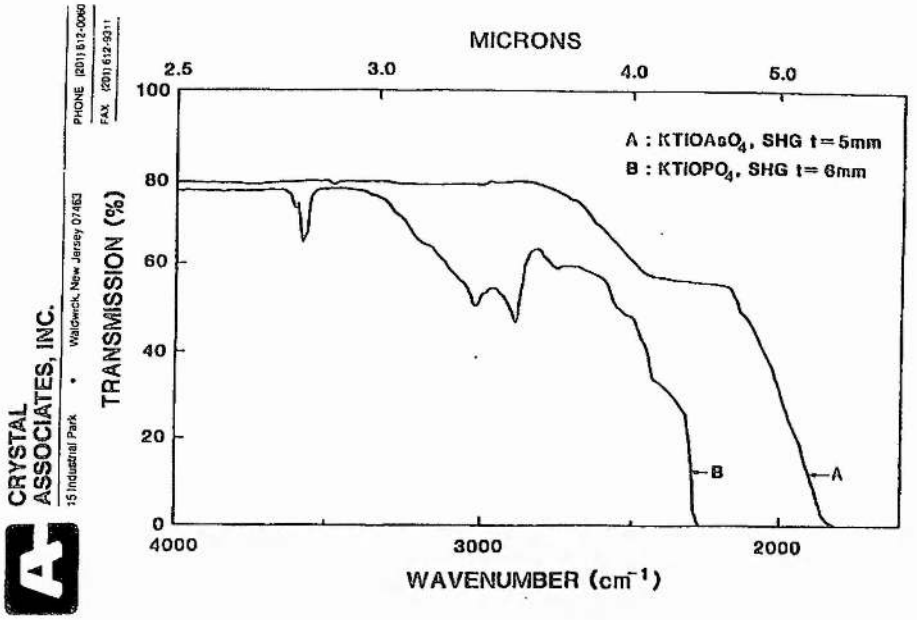

Fig. 7.5: A transmission spectrum of flux-grown KTP and KTA in the far infrared region above 2.5μm [10]. The off-set from 100% transmission is caused by the Fresnel reflection off the uncoated sample surfaces.

The advantage of KTA is obvious if operation in the idler region is required. It has not been possible so far to detect any 3.2μm radiation from the KTP-OPO. Therefore KTA, with the same non-critical typeII geometry, has been the material of choice, in order to realise an OPO in the mid-infrared with the idler wavelength around 3.5μm, as described in the next section. Due to the strong idler absorption in the KTP an anti-reflection (AR) coating for this wavelength was not necessary, thus reducing the coating requirements to be AR for the pump and signal radiation at 1.047μm and 1.55μm respectively.

The main objective of the OPO cavity design and mode matching lens is to minimise the threshold of the system, so that 40kW per pulse are sufficient to pump the OPO several times above threshold. The parameters shown below are important in lowering the threshold significantly below the 40kW peak power region:

- Cavity length: As parametric gain is only present during the time duration of the pump pulse the round trip time of the resonating signal wave should be as short as possible to attain low thresholds and high efficiencies. The OPO cavity used had a length of ~30mm, mainly due to the KTP crystal length.
- OPO crystal length: In the absence of walk-off effects, due to the non-critically phase matched geometry, the threshold decreases with increasing crystal length. According to calculations by Y. Tang, a 25mm long KTP piece should be sufficient to lower the threshold into the 10kW region, if the signal and pump mode sizes are kept to approximately 200 and 300μm respectively in diameter.
- Mode matching and curvatures of OPO cavity mirrors: For a given length of the cavity the radius of the mirror curvature defines the mode waist of the singly resonant signal radiation. By choosing small radii of curvature the spot size of the resonant mode can be reduced, thus lowering the threshold of the OPO. Assuming a constant beam diameter of the pump radiation, the slope efficiency will decrease as a result of the tight signal waist, which is essential for the lower thresholds. This effect can be partly compensated for by tightening the pump focus accordingly.

The experiments were performed with the existing pairs of mirrors from the previous KTP-OPO work mentioned earlier. Concave radii of curvature of 500, 100 and 20mm were available, each with 20% output coupling for the signal wave, thus permitting only symmetric cavities in terms of output coupling. The standard cavity length is around 30mm, mainly dictated by the 25mm long KTP piece. In a first attempt a concave curvature of +500mm was not sufficient to reach threshold (~190μm radius of the signal wave) with up to 40kW peak power per pulse.

Tighter focusing with +100mm curvature mirrors, corresponding to ~125μm signal spot size in the centre of the KTP crystal, was successful. Under these OPO cavity conditions the pump beam is focused down to ~300μm in diameter, using a 100mm AR-coated spherical lens and a threshold as low as 6kW could be accomplished. The resulting OPO-pulse, pump pulse and depleted pump pulse is shown in figure 7.6.

Due to the symmetric output coupling of 20% at each side of the OPO cavity, half of the converted pump radiation is not accessible, as it is coupled back into the path of the pump laser. However, to calculate the conversion efficiency we doubled the measured output of the OPO, in order to compensate for the high reflector at the signal wavelength, which in a later stage replaced the output

coupler at the input end of the OPO. With this assumption conversion efficiencies into the signal wave of more then 30% could be measured for pulse peak powers of 30 to 40kW. Later high average pump power experiments with the optimised OPO cavity confirmed the expected conversion efficiencies to be in the 30% region.

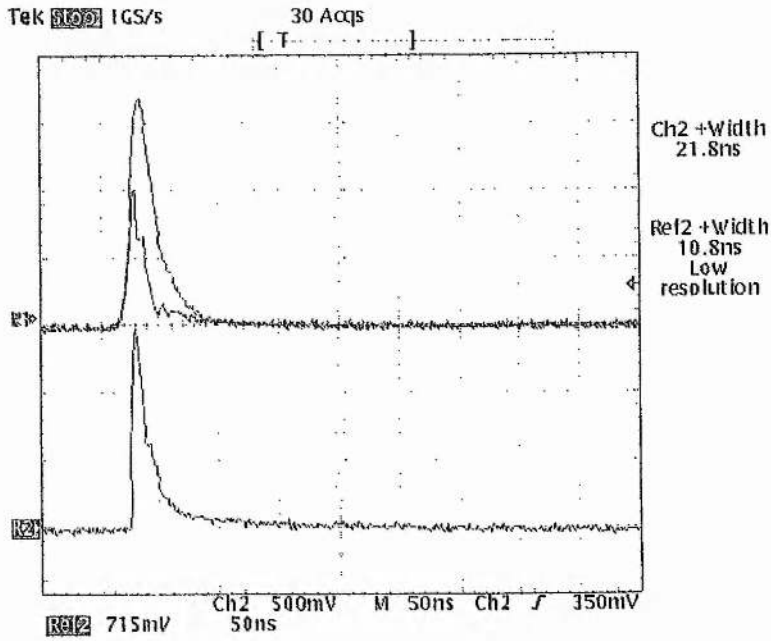

Fig. 7.6: *The lower trace shows the OPO signal pulse. The sharp rising edge of this pulse is delayed about 6ns towards the start of the pump pulse. The pump pulse as well as the depleted pump are shown in the upper trace. The repetition rate is 125Hz and the average input power into the OPO is approximately 90mW at 1047nm.*

To differentiate between pump, signal and idler radiation either a fused silica prism, correcting for the Fresnel losses on the prism surfaces, or a calibrated silicon filter (5% transmission cut on at 1200nm, T=95% @ 1540nm)was used. The fused silica prism was mainly used to separate the signal and idler radiation, after the undepleted pump light was blocked by the silicon filter.
We have not been able to detect any idler output so far. This part of the converted pump light must be at least to 80 - 90% absorbed in the 25mm long KTP piece. The OPO mirrors (substrate: Infrasil) as well as the coatings (high transmission at 3.2μm) cannot account for these losses. Attention also has to be paid to the transmission behaviour of the fused silica prism (T~80% @ 3.2μm expected) after 3.2μm radiation is clearly detected. A germanium filter, which is able to block any signal radiation would have been a better choice for detecting

traces of 3.2μm radiation (an option, later used with the KTA-OPO).
The variation of the signal conversion efficiency with the peak power per pulse is displayed in figure 7.7 :

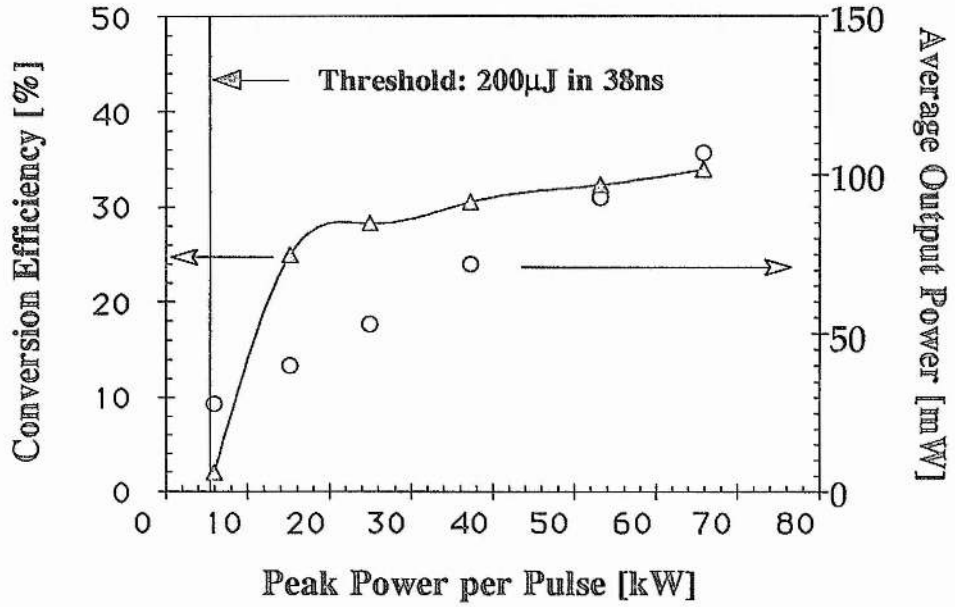

Fig. 7.7: Conversion efficiency into 1.547μm and averaged pump power at 1.047μm as a function of the peak per pulse. The repetition rate is 125Hz.

A levelling out of the conversion efficiency is reached at peak powers around 20kW per pulse. This, in combination with the low threshold of 6kW per pulse, gives rise to two conclusions:

- A further lowering of the threshold does not seem to be appropriate, as the present crystal length and signal beam waist guarantee operating conditions of several times above threshold for conversion efficiencies close to the saturation level, without damage problems.
- The small variation in the conversion efficiency for conditions between 4 to 10 times above threshold indicates a possible higher tolerance of the conversion efficiency against beam quality decline, associated with high average power operation of the pump laser.

The measured signal output wavelength is 1541nm ± 3nm, using a 0.25m monochromator. A spectrum taken by a fibre coupled optical spectrum analyser could narrow the emission wavelength down to 1539nm ± 0.3nm. A comparison of the spectral width of the KTP and KTA-OPO's is given at the end of this chapter. The agreement of the measured 1539nm with the predicted

signal at 1547nm, based on the Sellmeier set by Kato is acceptable. This small variation is no problem, and is probably due to minor material differences. The slightly different signal wavelength is in so far relevant if a further use of the signal in a mixing process is planned. This is the case in an experiment currently underway by Y. Tang and C. Rae in our department [11]. A non-critically typeI temperature tuned LBO crystal is being used as a sum-frequency mixer to provide an alternative pump source in the red for a Cr:LiSAF laser. The difference in the signal wavelength has to be accounted for by cooling the LBO slightly below room temperature.

The beam quality of the KTP-OPO has not been investigated so far. One unexpected property concerning the propagation of the OPO output is the appearance of a ring structure, becoming visible some 15 to 20cm behind the signal beam waist. This effect is not understood yet and the observed mode forms vary from a half-moon-like shape to the mentioned ring structure, despite the OPO being pumped with a TEM_{oo} mode. On very rare occasions OPO TEM_{oo} mode properties could be observed, however the only reproducible experimental result was that of non-symmetric, parts of a TEM_{oo} mode resembling, mode structure.
This dissatisfying and confusing experimental evidence has also been noted by J. Terry [3] and Y. Tang, each using different KTP materials (hydrothermally and flux grown material) as well as different pump lasers. With the recent interest in OPO sources extending into the 5 to 10μm area [9,12,13], KTP/A-OPO's are becoming important pump sources for these $ZnGeP_2$ or CdSe-OPO's and beam quality characteristics of the KTP/A-OPO pump sources will be important. Contrary to the KTP-OPO the KTA-OPO exhibits TEM_{oo} operation without problems, as will be shown in the KTA section later. However, the confusing KTP-OPO mode behaviour needs further attention.

A second, minor problem is a feedback effect between the OPO and laser cavity. This coupled cavity effect influences the pulse-to-pulse stability negatively, giving rise to fluctuations in the converted OPO output. This problem was easily solved through decoupling the cavities by means of an optical isolator. A reduction of the order of 15% of the pump power is the drawback of this obvious solution.

The transition to the high average output power KTP-OPO made changes to the OPO cavity necessary. A single sided output was needed to protect the

pump laser against the signal output. On the input side of the OPO the 20% output coupler (@ 1540nm) was replaced by a high reflector for the signal (R = 98%) with a transmission of T = 90% (@1047nm). The highest available output coupler of T=30% (@1540nm) replaced the second 20% output coupler of the first OPO cavity described above. The radius of curvature of the concave OPO mirrors remained the same at r=100mm, as did the length of the OPO cavity at 30mm.

The modified experiment reached a conversion efficiency of 28% into the signal for a peak power of ~30kW per pulse as in the low repetition rate results shown before, with the important difference of a change to a single sided output. The figure 7.8 shows the results of extending these experiments into the high average power region. The conversion efficiency into the signal stayed between 25%-28%, decreasing slightly with an increasing pump power level. There was no indication of bulk damage due to thermal problems caused by the absorption of the idler within the small volume of the OPO cavity mode.

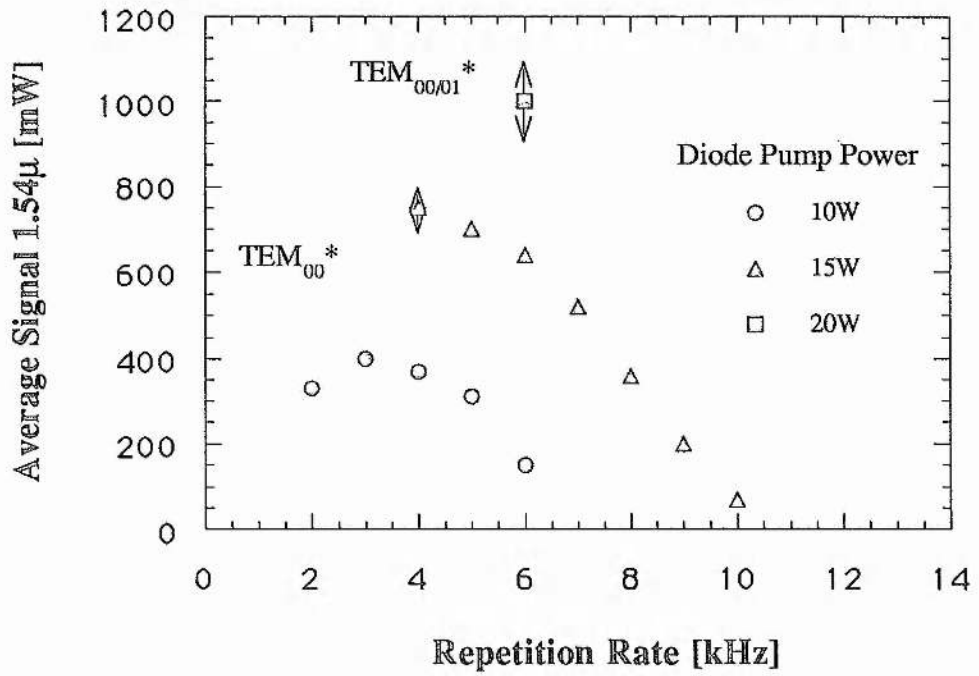

Fig. 7.8: The average signal output at 1540nm for diode pump power levels between 10 and 20W for the x-cut KTP-OPO. The arrows indicate output power fluctuations over the time duration of a minute.

The observed increase in the average signal output power fluctuations with higher fundamental power levels may be connected to thermal effects caused by the absorption of the idler in the KTP. The pump laser peak power stability

was not correlated to these observed variations in the conversion efficiency. However, it has to be noted that these fluctuations were also observed when the average fundamental pump power level was around 100mW, with isolation of the laser source in place, and are a characteristic of the KTP-OPO resonant operation, if compared to the single pass conversion processes. At this low average pump powers the occasional reduction in the conversion efficiency could be only detected with the germanium photo diode, and had no effect on the thermal power meter, with its very slow response time (~1s region). In order to analyse these characteristic output power fluctuations attention should be paid to the transversal mode structure of the pump laser on a pulse to pulse basis and its influence on the pulse built-up-time behaviour of the OPO. The pulse build-up-time of a ns-OPO close to threshold is one of the most critical loss sources, considering that OPO's are relying on the built-up from the zero-point energy fluctuations (E_o=1/2 hν). This is in a marked contrast to the noise level in a laser cavity, which is provided by the spontaneous fluorescence from the upper laser level.

The designation TEM^*_{oo} in figure 7.8 indicates the restrictions of the mode quality apply, as has been noted before. At the 20W pump power level the increased average output at higher order modes made it easier to maintain high average output powers by tuning the pump source to an TEM_{10}. If a TEM_{oo} mode had to be maintained, 1000mW instead of 1100mW was the upper limit which could be sustained.
During these experiments it became obvious that pump mode and resonant OPO signal mode did not always have the same transverse mode form. These different transverse mode forms of pump laser and OPO modes are in contrast to the straightforward situation encountered in single pass non-linear conversion schemes.
Much more effort is necessary to achieve a better understanding of the relation between transverse pump mode and resulting KTP-OPO mode. Some of the confusion surrounding these question is also connected to the extreme experimental difficulty of detecting these mode structures reliably and quickly. The use of a fluorescent card as an easy alternative which is also mainly used in this work, but is easily open to misinterpretation. Silicon detectors used in CCD cameras are transparent to the signal wavelength, making expensive and damage sensitive vidicons necessary, to monitor the mode structure continuously for quick capturing onto a frame grabber system. Such a system has been used to capture the TEM_{oo} KTA-OPO mode structure.

Despite the two problems of pulse to pulse stability and mode quality of the signal output, both appearing to be intrinsic to the externally pumped KTP-OPO operation, the results achieved were respectable in providing a 1W source at 1.54μm with pulse durations in the 16ns region (pump pulse: 25ns) at pump conditions of 6 times above threshold. The shortening of the OPO signal pulse is due to the pulse built-up effects within the cavity (fig. 7.6).

7.3 KTA Sellmeier equations and OPO performance at 3.44μm

Potassium Titanyl Arsenate (KTA) has the advantage of enhanced transparency in the mid-infrared region (~3μm) over KTP, which is the well established material for up-converting 1μm laser radiation into the 1.5μm region [1,2]. Although parametric oscillation in KTP at 3.26μm has been demonstrated [4], the absorption of the idler wavelength is critical in high repetition rate KTP/KTA-OPO's, as longer crystals are used to compensate for the lower pulse energies of the cw pumped laser.
The KTA-OPO experiments, like the KTP ones, were conducted in two stages. This time, however, material quality difficulties with the first KTA sample made a second effort necessary to achieve a mid-infra-red OPO at 3.44μm with a reasonable pump depletion.
First results were achieved when pumping a 7mm long KTA-crystal cut for non-critical typeII phase matching (x-cut) at 1047nm. This initial experiment highlighted the critical dependence of the signal and idler wavelengths on the growth technique used for the KTA. The absence or presence of the dopant Indium or Iron oxide, added at times to promote single domain structure of the KTA, changes the phase matching conditions, resulting in a shift of ~70nm in the signal, corresponding to ~280nm in the idler. This first experiment mainly provided the knowledge to choose the appropriate Sellmeier equation, which is important in view of the OPO mirror specification. The following two sections give a summary of the important results in each area, which were achieved with a KTA crystals sourced from Shan Dong University, China and Crystal Associates, USA.

The increased transparency range, together with a similar effective non-linear coefficient [14: higher d_{eff}, 14a: lower d_{eff}], as compared to KTP, makes KTA an ideal material for OPO applications in the medium infrared region. However initial growth problems, namely guaranteeing single domain structure, made the availability of KTA in crystals long enough to be suitable for low threshold operation difficult. The growth technique has since been improved and x-cut crystals up to a maximum length of 30mm are available now (Crystal Associates).

The x-cut KTA crystal (Θ=90°, Φ=0°) of 7mm length with an aperture of 3x3mm^2 (y-z plane) was originally intended for a doubly resonant cw OPO [15]. The crystal has a triple AR coating on both apertures for the fundamental

(1047nm), signal (1570nm) and idler (3160nm), using Cheng's Sellmeier coefficients [16] to predict the OPO wavelength set. Unfortunately, giving the highest priority to signal and idler anti-reflection properties resulted in a total of 40% reflection of the pump wavelength.
Despite the very short crystal, of 7mm as compared to the 25mm long KTP piece, and the high losses on the KTA surfaces, threshold could be reached at 240μJ (after losses) in 16ns when focusing down to a pump spot radius of 100μm at the centre of the KTA. A trace of the pump pulse (125Hz repetition rate) and OPO output is shown in figure 7.9.

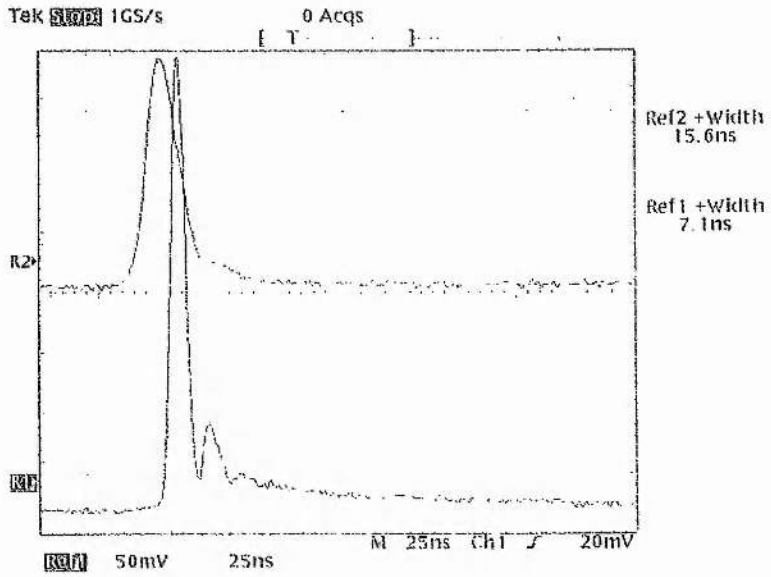

Fig. 7.9: *Signal pulse at threshold of a probably doubly resonant KTA-OPO. The peak OPO signal pulse appears past the maximum of the pump pulse. The rising edge of the signal pulse coincidences with the peak of the pump pulse. The wavelength of the signal was measured to 1505.5nm ± 0.5nm.*

The OPO cavity configuration was formed by two identical zero-focus mirrors with a radius of curvature of 20mm on the coated concave side. Coatings were specified to be R= 90% @ 1.6μm and R= 98% @ 3.2μm. The geometrical length of the OPO cavity was 20mm. Due to the high grade of reflection for signal and idler, combined with the difficulty of reproduction of the threshold results, it seems likely that the OPO needed to be doubly resonant to reach threshold conditions. The threshold behaviour under temperature tuning, as plotted in figure 7.12, confirms this assumption. In addition only parts of the KTA aperture were able to reach threshold.

Measuring the signal with a 0.5m monochromator resulted in the unexpected wavelength of 1503nm (±3nm) at room temperature, as opposed to the predicted 1570nm using Cheng's Sellmeier set. This result was cross-checked with a second monochromator. The gap of ~70nm to the predicted signal widened to ~285nm in the idler.

Unfortunately the KTA-crystal deteriorated very quickly and even at pump conditions of 4 times above threshold no depletion or reduction of the signal output fluctuations could be observed. No visible damage on the coatings or bulk damage explained this 'threshold-like' response. To investigate that unusual behaviour the KTA-OPO was pumped with a pulsed diode pumped Nd:YLF laser [17], developed by Cameron Rae at St. Andrews, permitting higher energies per pulse (up to 10mJ in 10ns). However, no improvement in terms of a reaching pump depletion could be detected and the threshold of the OPO steadily increased.
This behaviour is attributed to a multi domain problem in the 7mm long KTA. Under pumping a further depoling of the structure could lead to the experimentally observed increasing threshold over the whole aperture. These multi domain problems in as grown undoped KTA are well known [16]. The crystal growers at Shan Dong University used an undoped Arsenate flux, which offers a better chance of achieving a single domain structure. KTA grown from undoped Tungstate fluxes are highly multi domain (typical size of 50μm) and dopants are essential to promote single domain structure.
Due to the problematic threshold behaviour only very little energy was available and a wavelength measurement at around 3.5μm proved impossible, as only thermal detectors were available, which would require a few mW average output power behind the monochromator. A suitable detector would be a photo conductive Lead Selenid (PbSe) cell, possibly cooled down to -20 or -30°C by a Peltier unit to improve sensitivity.
Interestingly, a non-phase-matched off-axis sum frequency mixing process generated red light and provided an opportunity to cross-check the signal wavelength. As the symmetric red spots always coincided with the signal pulse, a mixing process between the pump and signal seemed likely. A measurement of the red emission determined the wavelength as λ_{red}=616.4nm, thus making it possible to verify the signal wavelength again, using the energy conservation relation:

$$1/\lambda_{red} - 1/\lambda_{pump} = 1/\lambda_{signal}^{*} \quad \text{which yielded} \quad \lambda_{signal}^{*} = 1501\text{nm},$$

which is in reasonable agreement with the earlier measured value.
In addition, a non-phase matched faint blue/UV generation was detectable, also coinciding with the red pulse. This mixing process was only observable under strong pumping, which deteriorated the KTA-crystal rapidly, and no wavelength measurement could be taken for that reason. However SFM between the red pulse and the pump or signal again seems likely, resulting in $\lambda_{blue} \sim$ 388nm or 437nm. The lower wavelength is also closer to the absorption shoulder at around 350nm in KTA.

The confusing behaviour of the KTA crystal grown by Shan Dong University, China became a bit clearer with the help of Crystal Associates, which are the supplier of the 15mm long (aperture: $3x3mm^2$) x-cut KTA piece used to proceed with an OPO in the 3.5μm region.
Fenimore et al. [18] derived Sellmeier coefficients from refractive index measurements of KTA grown by Crystal Associates. This KTA is grown out of an arsenate flux, with no dopants like Indium or Iron Oxide added, in order to help single domain growth. The Sellmeier equation used has the form:

$$n^2 = A + B / \{1 - (C/\lambda)^2\} - D\lambda^2 \qquad (3.4)$$

The Sellmeier coefficients are as follows:

Ax := 1.90621	Bx := 1.23612	Cx := 0.19687	Dx := 0.01024
Ay := 2.16156	By := 0.99863	Cy := 0.21862	Dy := 0.01098
Az := 2.14786	Bz := 1.29559	Cz := 0.22719	Dz := 0.01436

These Sellmeier coefficients predict the 1μm pumped OPO output wavelength of flux grown undoped KTA accurately, as can be seen in the table of 1μm pumped OPO's in the ns-region:

Author	pumped @ [nm]	Exp.: Signal [nm]	Theo: Signal [nm]	Growth Method	Sellmeier Eqn. used
Stolzenberger [19]	1064	1539±3	1534	Arsenate Flux no dopants	Fenimore [18]
This work	1047	1503±3 1504±0.5	1504 1504	Shan Dong Crystal Assoc. Both sources: Arsenate Flux no dopants	Fenimore [18]
Bosenberg [20]	1064	1520 (Arsen.) 1524 (Tungs.)	1521	Arsen./pure Tung./doped	adjusted Cheng in D
Kato [21]	1064	1601	1601	Tungstate flux / doped	own set, being similar to Cheng's

Table 7.10: *Overview of some infrared pumped ns OPO's using KTA.*

As can be seen, however, the situation is far from being consistent and each derived Sellmeier equation describes only a few specific experiments satisfactorily. Even the influence of the same dopings (very similar concentrations of Fe_2O_3 of between 0.47 and 0.32wt%) in Tungstate flux grown single domain KTA leads to different results, as becomes obvious from the experiments by Kato and Bosenberg.

Furthermore, none of the mentioned Sellmeier equations describes the typeII non-critical phase matching accurately over an extended pump wavelength range. Even the Sellmeier equations by Fenimore derived using KTA from Crystal Associates are only accurate for pump radiation in the 1μm region. Experiments here at St. Andrews by S. French and M. Ebrahimzadeh [22] with a femto second KTA-OPO pumped around 800nm show a different signal and idler wavelength than predicted by the Fenimore set. Although the KTA was again sourced at Crystal Associates in the above mentioned experiment. The predicted signal wavelength is, at 1145nm, 30nm short of the measured 1175nm, assuming a pump at 800nm. However in this pump region the Sellmeier equations of Cheng and Kato are very accurate with predictions of 1175 and1176nm respectively.

The spread in the signal wavelength is magnified in the matching idler wavelength due to the reciprocal dependence between energy and

wavelength. The magnitude of the variation in prediction of the idler is given in the graph below:

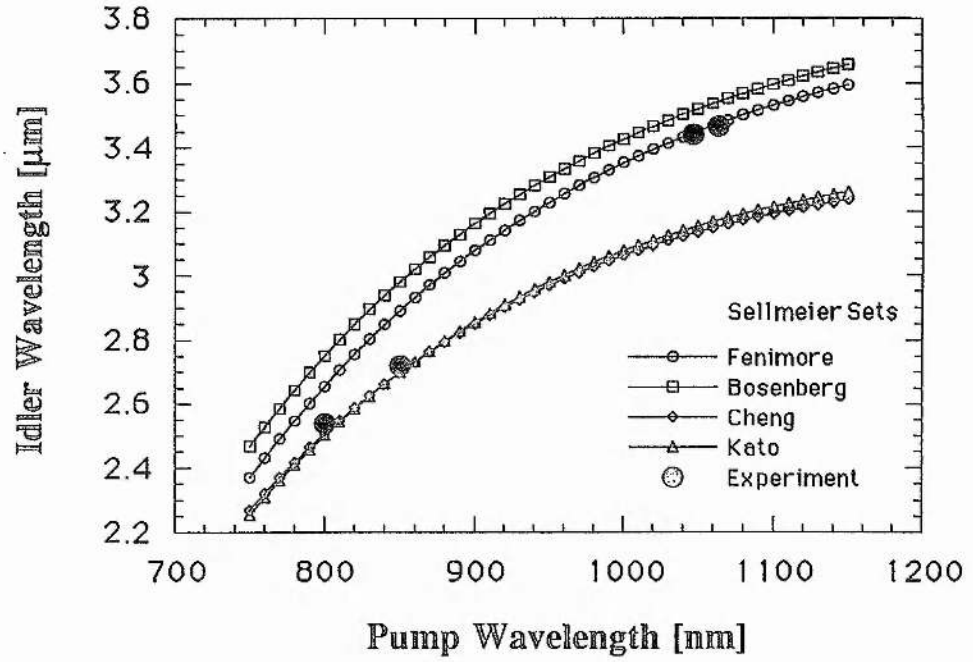

Fig. 7.11: *Comparison of the predicted idler wavelength of a x-cut KTA-OPO with experimental results in the pump region between 800 and 1064nm. Using several Sellmeier sets predicts the idler only in parts of the pump region. Experiments in both pump regions use KTA sourced from the same grower; Crystal Associates. Results taken by French[22], Stolzenberger [18] and the author.*

In general the Sellmeier equations of Cheng and Kato predict the KTA-OPO wavelength accurately in the 800nm region. Both sets describe the same variation of the refractive index with wavelength, despite the fact that they have been derived for undoped arsenate flux grown KTA (Cheng) and doped (Fe_2O_3) tungsten flux grown KTA (Kato). Bosenberg showed that with small changes to the D coefficients of the original Cheng set a match could be achieved with his OPO wavelengths results, pumped at 1.064µm. This further indicates that the only problem with Cheng's set are inaccuracies in the D coefficients, which are the infrared correction terms. The independently measured set by Fenimore described the 1.047µm pumped OPO results best and it is used for the work with the mid infrared OPO during this thesis. Interestingly, the Kato and Cheng sets give rise to considerably different predictions if KTA is used as a typeII doubler, as shown at the end of the last

chapter. This is despite both sets give an almost identical description of the non-critically phase-matched KTA-OPO.
Until the evident contradictions within even the existing KTA Sellmeier sets, as well as the influence of dopants on the refractive index of KTA, is resolved, it is best to rely on supplier and pump wavelength specific Sellmeier equations.

Temperature tuning of this KTA-OPO was also attempted. However no change in signal wavelength could be recorded within the measurable accuracy of a 0.5nm (0.5m monochromator) if the OPO crystal was heated in 2°C steps from 20°C to 60°C. The peak of the signal was in both cases at 1503nm. If there was any tendency to change wavelength with the rising temperature, then the emission peak shifted towards lower wavelengths. Due to the intensity fluctuations in the OPO output near threshold and the width of the emission, this small drift was not significant. Assuming a similar temperature tuning behaviour (dn(y,z)/dT) for KTA as established with KTP, a decrease in the signal of 3 to 4nm would have been expected with a 40°C temperature rise.
The threshold of the KTA-OPO however showed a pronounced periodic change with the rising temperature. This behaviour is sketched in the figure below:

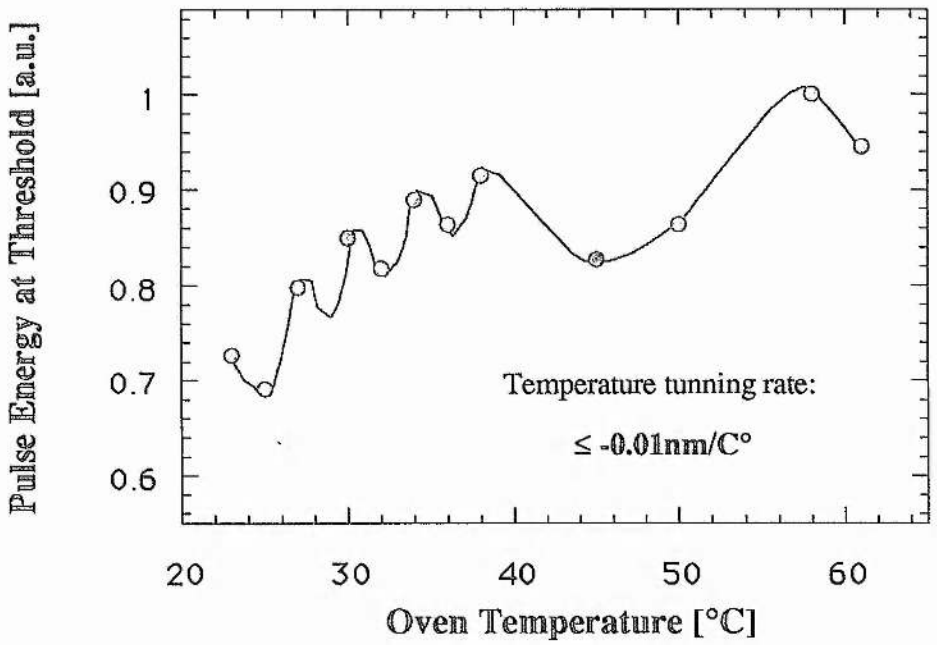

Fig. 7.12: *Periodic fluctuations of the threshold with the rising temperature. Only a few points have been taken and the connecting line gives only qualitative information about the threshold behaviour between measurement points. The periodic threshold change suggests that this is a doubly resonant OPO.*

The optical path change in the OPO cavity due to the thermal expansion of the KTA along the x-axis induces a change in the resonance condition.
In the case of a singly resonant OPO the signal can adjust itself continuously to these changes, with the idler following constraint free, only satisfying the energy conservation condition. The change in threshold would therefore be negligible for a singly resonant OPO.
The periodic threshold dependence on the crystal temperature as shown above therefore strongly suggests, that the KTA-OPO was doubly resonant. Changes in the resonance condition have to be simultaneously satisfied by signal and idler to maintain the lower threshold of the doubly resonant configuration. This condition might not be possible, with the result that the threshold rises towards the maximum value, which is represented by the singly resonant configuration. The periodic behaviour is given by optical path changes which are multiples of the idler and signal wavelength. However, this is only a very schematic interpretation and fluctuations of the geometrical cavity length due to vibrations in the mounts are also likely to complicate the whole changing threshold behaviour.

The problematic material quality and short length of the KTA crystal combined with the low energy per pump pulse of the high repetition rate laser source, made these experiments with a doubly resonant pulsed OPO difficult and time consuming. On the positive side the difficulties with the existing Sellmeier equations were highlighted during these experiments. With the help of Crystal Associates [19] the correct Sellmeier set could be identified for pumping KTA which is flux grown from an undoped Arsenate solution (table 7.10), in the 1μm region.

Subsequently a 15mm long x-cut KTA crystal was ordered (Θ=90°, Φ=0°) from Crystal Associates and triple anti-reflection (AR) coated by Lightning Optical Corporation. This time the AR-coating in the idler region of 3.44μm was vital, as the main motivation for this KTA-OPO was an optimised output in the mid-infrared, which is not a possible option with KTP in combination with a high repetition source. Another hold-up happened when the new KTA crystal was broken during the coating process and a new crystal had to be ordered. This mishap presented us with a 15mm and two refurbished 8 and 5mm long pieces at the price of the original order, which proved to be an advantage during the later experiments.

One of the main experimental problems in passing the 3μm emission mark is that the Quartz (Bk7) mirror substrates start to absorb significantly, which renders them unusable as output coupling mirrors for an OPO at 3.44μm. Infrasil or CaF_2 substrates have to be used instead, which is often connected to longer delivery times and complicates the coating process.
To lessen these constraints on the output coupler in terms of reflectivity and substrate choice, as encountered in the usual two mirror cavity, a CaF_2-Brewster plate was used, being a remainder from the earlier mentioned KTA cw-OPO project, in order to configure the three mirror cavity shown in figure 7.13, so as to optimise the idler output of the KTA-OPO with existing mirror sets.

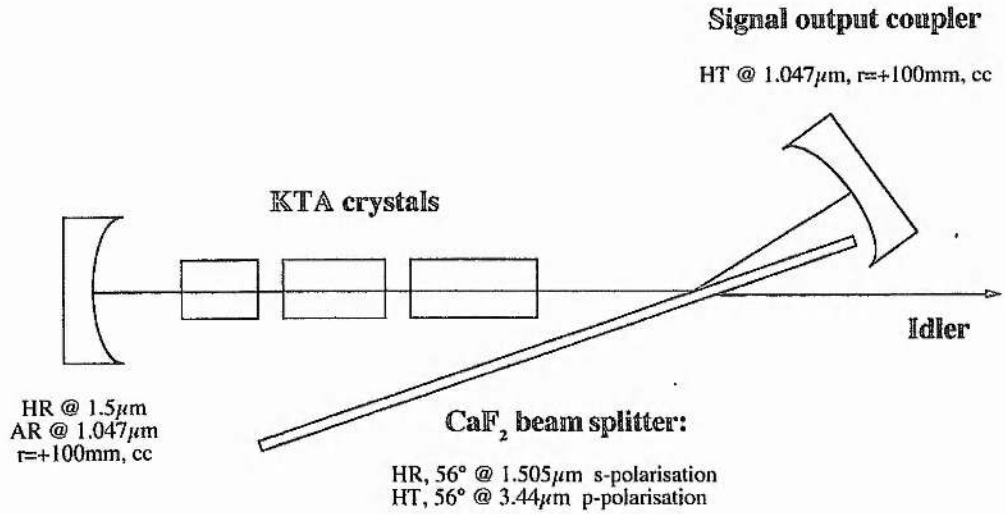

Fig. 7.13: *The three mirror cavity, originally used in doubly resonant OPO's [23], reduces substrate and coating constraints on the output coupler. The CaF_2-polariser separates the signal and idler spatially, with the signal being resonated and the idler being extracted after each single pass through the KTA.*

This arrangement made it possible to use Bk7 mirror substrates, which are used in the Cr:YAG work at St. Andrews [24], to find an optimum signal reflectivity, in order to maximise the idler output. In a later stage it is also planned to resonate the idler, while extracting the signal single pass, an option which can not be pursued in KTP. This set-up will also be useful to investigate the OPO linewidth changes at 1.5μm, which depend on the resonance condition of the OPO. The CaF_2 Brewster plate is therefore a very useful tool to optimise and investigate this OPO, although the usual two mirror cavity is performance-wise preferable once the optimised set-up is found.

Although the KTA crystal has a nominal length of ~28mm, it consists of three KTA pieces from the same supplier, due to the breakage mentioned earlier. All crystals are triple AR-coated (R=0.3% and R=3.5% for the signal and idler respectively). The three crystals are a sliding fit in a Perspex mount (mechanical tolerance ~0.1mm), which results in a maximum axis misalignment in the order of 10mrad between the longest and smallest KTA crystal, which is well within the acceptance angle of this non-critically phase-matched geometry. The main problem in lining the three KTA pieces up is the unknown axis misalignment between the two different crystal batches. To check any problems related to axis misalignment of the three samples, the threshold of the KTA-OPO was measured for different combined crystal lengths.

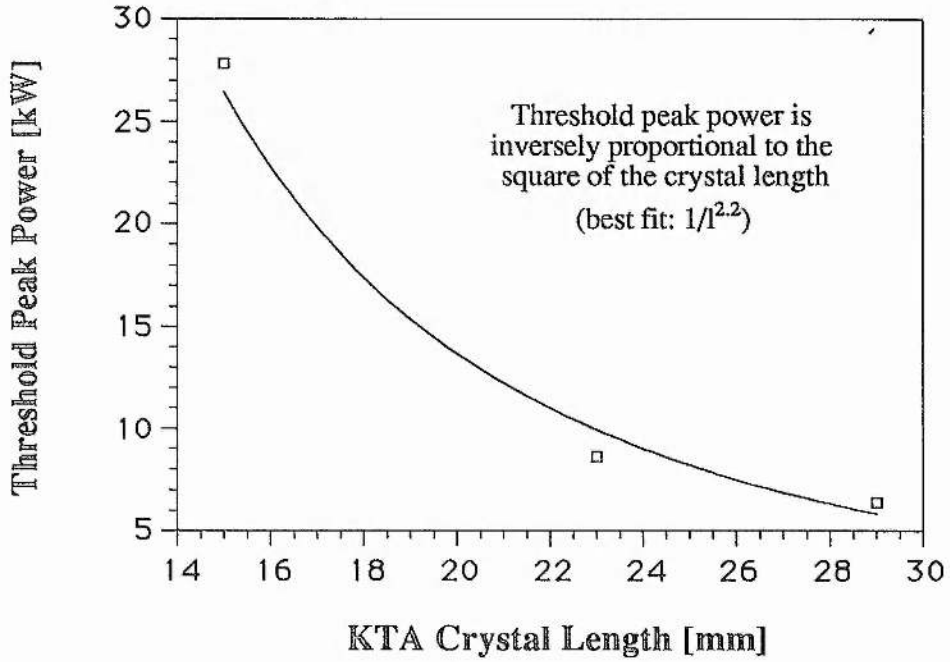

Fig. 7.14: *The threshold peak power as a function of the total crystal length under the condition of identical focusing and cavity conditions.*

The scaling behaviour of the threshold peak power, which is inversely proportional to the square of the total crystal length [25], indicates that the use of three separate AR-coated KTA pieces to simulate a longer crystal is possible in a NCPM typeII OPO.

$$I_{Thresh.} \propto \frac{1}{l_{eff}^2 \kappa(d_{eff}, \lambda_S, \lambda_I) g_S(\omega_s, \omega_p)} \tag{7.4}$$

The threshold pump flux is also inversely proportional to the coupling constant κ, scaling with the square of effective non-linear coefficient, d_{eff}, and the inverse of the signal and idler wavelengths λ_s, λ_i. The threshold of the OPO device can be further lowered by decreasing the ratio of signal beam radius, ω_s, to the pump beam radius, ω_p, which is described by the signal spatial mode coupling coefficient g_s.

The use of three KTA pieces permits to alter the conversion length and output coupling of the signal independently, so as to optimise the idler output in the presence of absorption in the 3μm region. Furthermore, absorption measurements at the idler wavelength in KTA are possible, with the KTA-OPO generating the test beam for one of the externally placed KTA crystals. A slightly tilted input beam about 1° away from normal incidence, makes separation of coating and bulk losses possible. The idler bulk absorption in the 6mm long KTA piece so measured is 14%, corresponding to an absorption coefficient of α=0.025/mm (for KTP: α=0.054/mm @ 3.44μm), indicating that idler absorption is still a problem in KTA, although its performance in the 3.5μm region is a clear improvement on the KTP-OPO. The absorption coefficient of KTP at 3.44μm is only given as a comparison, as the relevant idler wavelength for KTP would be 3.27μm. Relating this to figure 7.5 would result in an estimated absorption coefficient of similar magnitude as measured at 3.44μm.
However, only direct absorption measurements on the OPO crystal used are convincing, as absorption phenomena can be highly localised and might also vary with the growth method, or even worse with the batch number. The huge variation for the transmission spectra in the literature [4, 10, 26] for the 3 to 5μm region is an affirmation to this varying crystal quality obviously encountered.

Initially it was planned to reduce the output coupling on the singly resonant signal of the KTA-OPO, to generate a very high intra-cavity signal field and thus maximising the at the same time generated idler wave, keeping in mind that the parametric conversion process has to generate one idler photon for each intra cavity signal photon. The experiment, however, showed a strong correlation between the coupled out signal intensity and the single pass, extracted idler intensity, with a close to 100% output coupling. The best result in optimising the idler was reached at 8% conversion efficiency into 3.44μm for a signal output coupling of 4%.

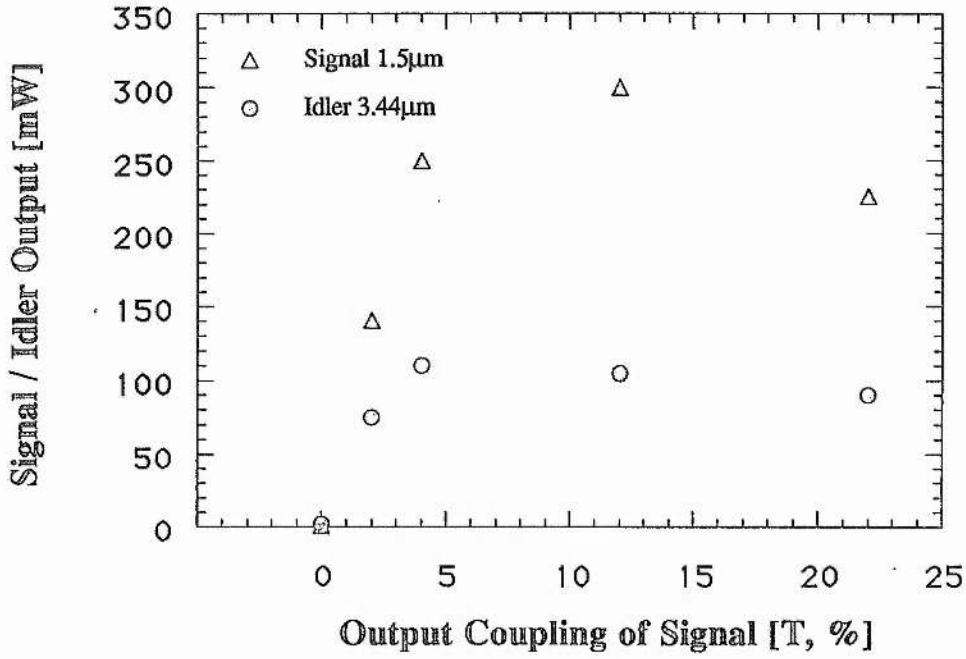

Fig. 7.15: *Signal and idler output of the KTA-OPO as a function of the signal output coupling, which is the singly resonant wave within the OPO (10W diode pump power). The idler is extracted after a single pass, with the CaF_2-beamsplitter being HT (T≥95%) for the p-polarised idler wave.*

The reason for the almost constant idler output for signal output coupling transmissions between 4 and 22% is not yet understood, as is the unexpected and very low idler output for an almost zero output coupling of the signal. A possible explanation is back conversion of the signal and idler into the pump for very high intracavity fields in the case of the high reflecting signal mirror.
A similarly almost constant idler output can be observed in the repetition rate region of several kHz for cavities with a given output coupling (fig. 7.16), when the signal output is still increasing. In this case a non-linear, accidentally phase-matched, conversion process, involving the idler is a possible explanation, which will be investigated at a later point. The varying signal and idler output powers with repetition rate is shown in figure 7.16
With the use of a two mirror OPO cavity for the KTA, 750mW at 6kHz could be achieved at the signal, representing a maximum 21% conversion efficiency from the infra-red pump at 6kHz. Under these conditions the conversion efficiency into the non-resonant idler was 6%. With the assumption of no losses and no other conversion processes being present, the ratio of signal and idler output has to follow the ratio of the energies of signal and idler photons, as the

parametric effect is an energy conversion process. This results in an expected ratio of 2.3 of signal to idler conversion efficiency, and would lead to an expected 9.2% conversion efficiency rather then the measured 6% into the idler. The main source of the difference in conversion efficiency is given by the absorption of 3.44μm in KTA, as measured before. However, this absorption, being a linear effect for a fixed crystal length, does not explain the different tendencies of the signal and idler output with the repetition rate as noted before.

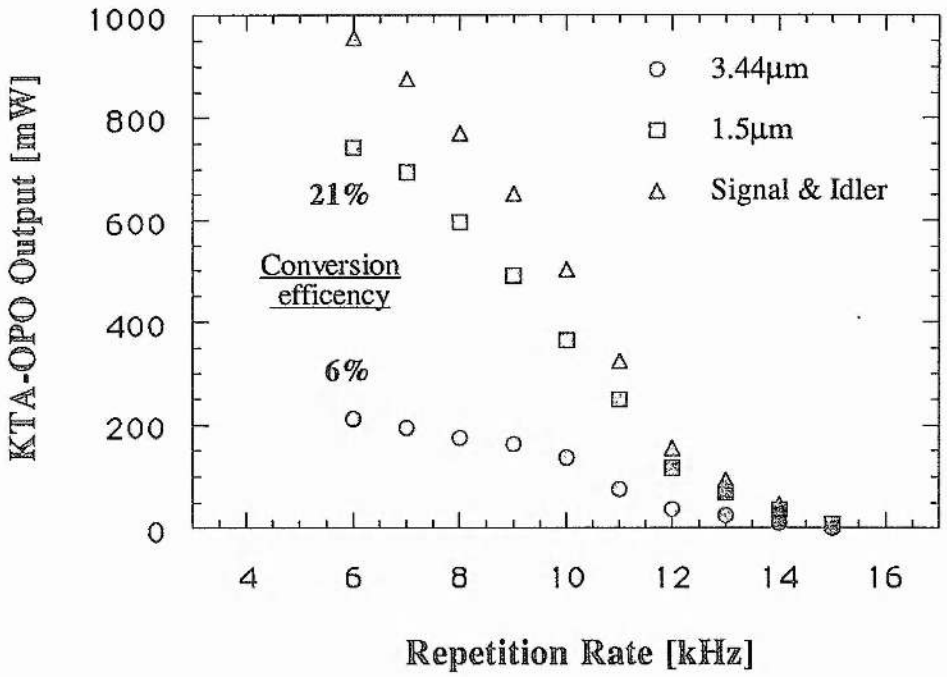

Fig. 7.16: *The KTA-OPO outputs as a function of the repetition rate at a diode pump power of 20W. In this case a conventional two mirror cavity with a signal output coupling of 10% was used. Notable is the almost constant idler output between 6 and 9kHz, when the average signal output is still increasing.*

The fact that absorption is an important loss source was confirmed by reducing the total length of the KTA by removing the 6mm long piece but keeping the optical length of the OPO-cavity constant. At the 10W pump power level similar output powers for the idler were registered as previously with the full KTA length of 28mm, while the signal output was reduced.

A spectral analysis of the KTA output confirms the Sellmeier equations by Fenimore [18] in the 1μm pump region [19, 27]. The transversal mode structure of the signal output at 1.505μm is close to single mode (TEM_{oo}). It is much superior to that from a KTP-OPO, operating at 1.539μm, but otherwise under identical TEM_{00} pump conditions. To document the improved transverse mode structure a Vidicon camera, with a sensitivity extending to 1.8μm, and connected to a frame grabber, was used.

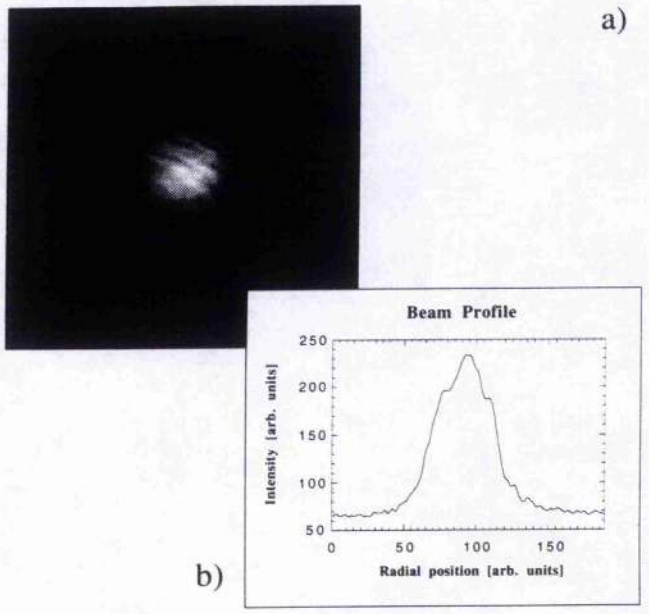

Fig. 7.17: *The transverse mode structure of the signal radiation from a KTA-OPO. The mode was imaged by a lens onto the Vidicon chip. Heavy filtering, necessary to protect the very sensitive camera, introduced the interference pattern. The intensity plot demonstrates the Gaussian intensity distribution, without 'holes' in the centre, as it is characteristic for the KTP-OPO.*

The much improved mode quality is one of the advantages of the KTA-OPO over the KTP device. This might balance the reduced conversion efficiency into the signal, for similar length crystals of KTA and KTP being used, if the OPO is used as a pump source for mid infra-red OPO materials as CdSe.

The ability which was earlier mentioned of being able to reduce the linewidth of the pump laser by incomplete Q-switching on a cw background is useful in order to demonstrate the linewidth dependence of the NCPM OPO on the pump laser linewidth. In general the total linewidth of the OPO is given by three independent contributions, which are:

- the pump laser linewidth

- the pump divergence defined by the focusing set-up and pump laser mode quality
- the phase matching bandwidth of the OPO material

By changing the pump laser linewidth from 25GHz down to 3-5GHz the KTP-OPO signal output narrows considerably from 0.6nm down to a resolution limited 0.2nm, when the spectrum is measured with an optical spectrum analyser. Figure 7.18 compares the signal spectrum under free running and improvised self-seeded (with a loss of pump laser pulse-to-pulse stability) conditions.

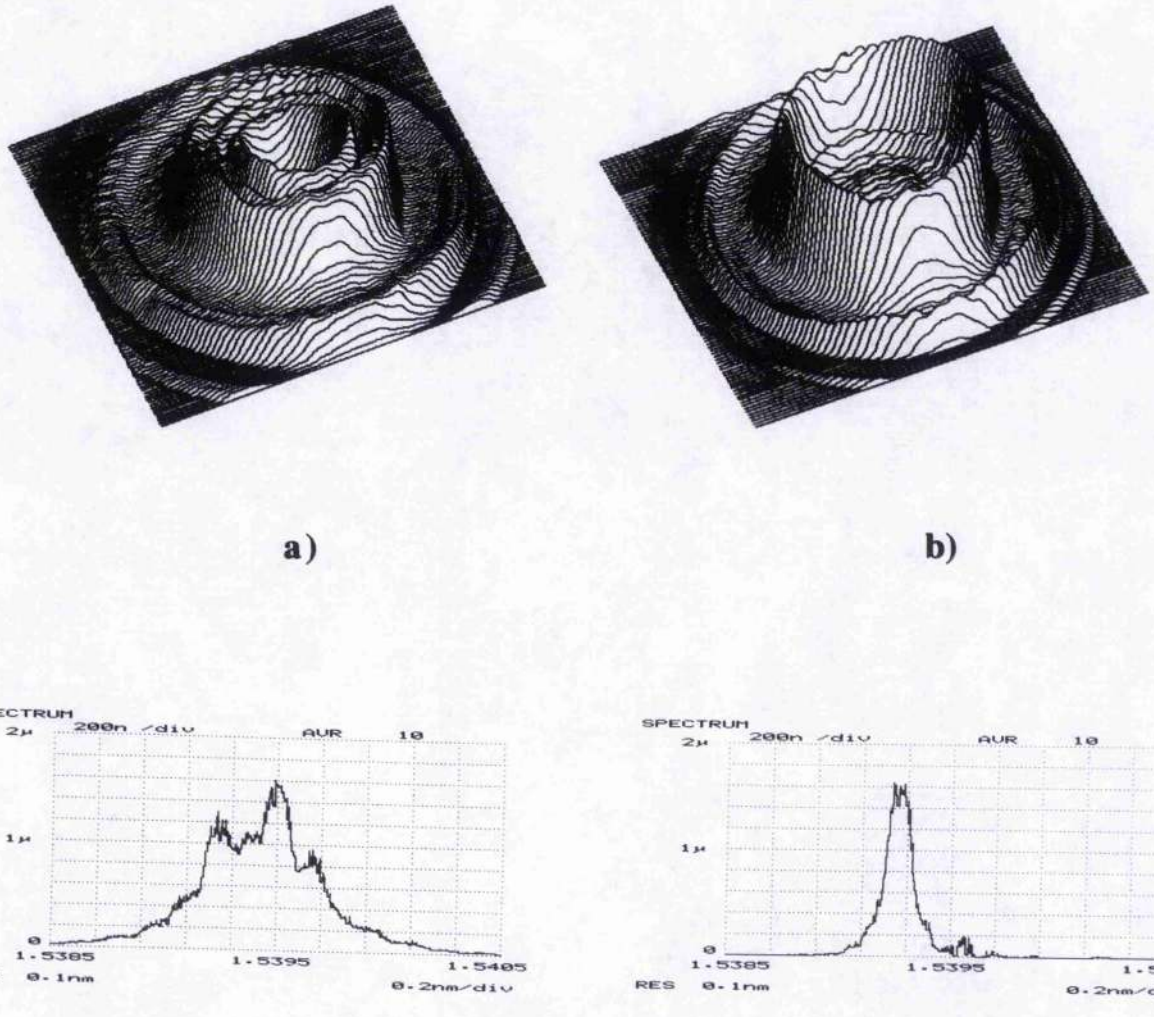

Fig. 7.18: *Comparison of the pump laser linewidth contribution to the KTP-OPO output. The structure of the Fabry-Perot fringe pattern taken from the doubled pump laser under free running (**a**)) and self seeded (**b**)) conditions finds its expression in each of the recorded signal spectra.*

With the same three peak structure evident in the signal spectrum, as well as in the spectrum of the pump laser, it becomes obvious that the laser linewidth is the dominating influence in the total OPO linewidth. In narrowing the pump laser emission down to approximately 5GHz, only one dominant signal peak is detectable in the signal spectrum and the linewidth of this peak is likely to be resolution limited. During this transition from free running to self seeded operation neither the phase match bandwidth (same crystal) nor the focusing set-up or transverse mode structure were changed. The influence of imperfect phase matching ($\Delta k \neq 0$) (without a variation in k_s and fixed $\omega_{p,s,i}$) on the signal, due to the phase matching bandwidth, can be calculated by taking the derivative of the phase mismatch term Δk with respect to ω_s. Changing variable to λ, the following expression of the signal frequency variation can be shown to be [7]:

$$d\nu_S = \frac{c}{L}\left[(n_i - n_s) + \lambda_s \frac{dn_s}{d\lambda_s} - \lambda_i \frac{dn_i}{d\lambda_i}\right]^{-1} \tag{7.5}$$

This expression is based on the assumption earlier introduced that the available parametric gain has halved with a phase mismatch of $\Delta k = \pi/L$, and this value was used for all the of the following linewidth calculations. Equation 7.5 expresses the earlier mentioned fact that the contribution of the phase matching bandwidth is at its maximum for phase matching schemes close to degeneracy ($n_s \sim n_i$) and for fast tuning geometries with a maximum in $dn/d\lambda$. Furthermore, the phase matching bandwidth is inversely proportional to the crystal length, L, making the use of longer crystals in NCPM schemes not only advantageous in terms of low thresholds, but also in reducing the linewidth component, due to the phase match geometry.

A similar expression to the above can be found for the signal frequency variation, caused by the bandwidth of the pump laser, calculated in this case by taking the derivative of Δk with respect to ω_p.

$$d\nu_s^{pump} = \Delta\nu_p\left[(n_p - n_i) + \lambda_i \frac{dn_i}{d\lambda_i} - \lambda_p \frac{dn_p}{d\lambda_p}\right]\left[(n_i - n_s) + \lambda_s \frac{dn_s}{d\lambda_s} - \lambda_i \frac{dn_i}{d\lambda_i}\right]^{-1} \tag{7.6}$$

Calculating both individual bandwidth contributions to the signal linewidth shows that the phase matching bandwidth is still the dominant effect. The calculated phase matching contribution is 110GHz (0.87nm @ 1540nm), while the total pump frequency spread contribution is in the order of 25GHz (0.2nm).

This calculated ratio of contributions predicts a reversed situation to the experimental linewidth measurements, where the signal linewidth clearly follows the pump, reducing the signal linewidth down to 0.2nm. Despite this, the measured linewidth in the case of the free running pump of 0.6nm agrees reasonably well with the predicted total linewidth of ~1nm. The remarkable behaviour is the pronounced narrowing of the signal, with a narrowing of the pump. At this stage the smaller than firstly expected linewidth is attributed to the homogeneously broadend nature of the parametric fluorescence. This is in analogy to the laser linewidth reduction in homogeneously broadend systems, due to gain-competition, if compared to inhomogeneously broadend transitions as present in Nd:Glass. The phase matching bandwidth is therefore likely to define only an upper limit for the OPO linewidth.
By comparing the spectral width of the KTA-OPO output (15mm long x-cut crystal) with the KTP-OPO output (incorporating the longer, 25mm, crystal), an increase in the total linewidth can be observed, with the experimental pump and OPO-cavity conditions are kept identical.

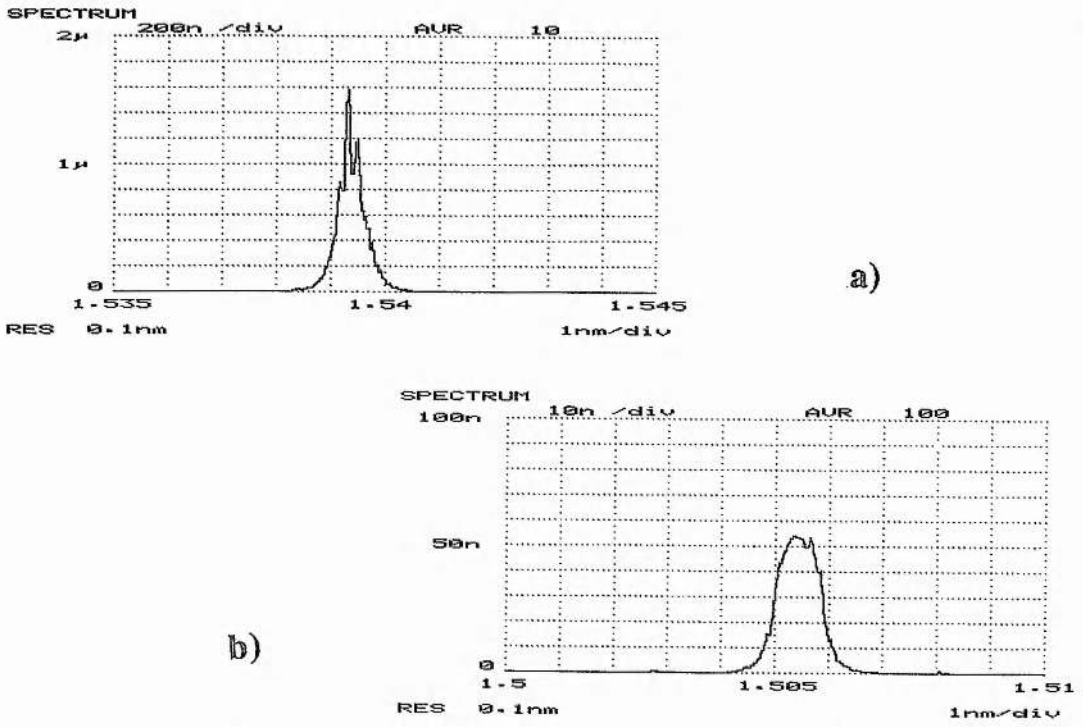

Fig. 7.19: *Spectra of the KTP (a)) and KTA-OPO (b)). The linewidth of the KTA-OPO increases to 1nm as compared to 0.6nm in the KTP case. Besides the shorter crystal length of the KTA-OPO (15mm instead of 25mm), the other experimental pump parameters such as pump beam divergence, spectral width and cavity geometry remained unchanged. Pump conditions are twice above threshold.*

The KTA-OPO linewidth taken on its own is again in acceptable agreement with the phase matching bandwidth component of the total OPO linewidth. The wider KTA-OPO signal emission is therefore related to the shorter crystal length used, demonstrating that the phase matching bandwidth is inversely proportional to the crystal length, L (eqn. 7.5). The line narrowing effect of the pump laser self-seeding could at the time not be demonstrated, as threshold for the 15mm long crystal could not be reached under these conditions.

The linewidth characterisation of these KTP/A OPO's will be the aim of further investigation. Besides varying the finesse of the resonating OPO cavity at 1.5μm, while recording the signal linewidth, it will also be interesting to resonate the 3.5μm component of the OPO output, while monitoring the constraint free idler at 1.5μm. These experiments, however, will be conducted again at low average pump powers, as at the very beginning of the KTP-OPO experiments, because the remaining absorption of the now resonant 3.44μm radiation in KTA might cause damage problems.

7.4 Conclusions

The main success during these experiments is in the tailoring of the KTP-OPO to the needs of the high average power laser system developed in this thesis, mainly by choosing the appropriate KTP crystal length. The 6kW threshold level permits operation several times above threshold as anticipated. Bearing in mind that only existing mirrors were used, a respectable 25 to 30% conversion efficiency has been achieved. The high average power KTP-OPO experiments reached average output powers of 1.1W at 1539nm (6kHz repetition rate) with a diode pump power level of 20W. The main KTP-OPO results are shown in table 7.20:

Pump laser	Aim: Optimising at low average power, but high peak powers	--> Over coupled T=50% 90...180mW; 125...250Hz ~40kW, 18ns pulses
OPO cavity and threshold	l_{geo}: 30mm, roc: +100mm (cc) output: T = 30% @ 1.54µm	Threshold ≤ 6kW 200µJ in 38ns
Conversion effic n. (@125Hz)	signal @ 1.54µm idler @ 3.24µm	≥30%, ~12 - 16ns pulses ≤2%, absorption in KTP
High average signal output	typical 1W at 6KHz in 20ns pulses;	~25%, after isolator (15% loss)
Signal linewidth mode quality	0.6nm (@ $2 \cdot P_{thresh}$), linewidth follows pump: ≤ 0.2nm for pump narrowed to ~5GHz	Transv. mode resembles parts of a TEM_{oo} or Donut mode (align. dependent)
KTA-OPO output	signal @ 1.505µm idler @ 3.438µm	~20% into signal ≥ 6% into idler

Table 7.20: *Summary of the experimental data for the KTP/A-OPO experiments.*

The unproblematic transition from the low to the high average power KTP-OPO indicates that there are no problematic thermal effects caused by the idler absorption in KTP. No bulk damage problems under average fundamental powers of 4 to 5W focused into a 300µm diameter spot, with an OPO mode diameter of ~250µm have been noted. The conversion efficiency also remains stable under repetition rate scaling.

To improve the 25-28% conversion efficiency into the signal as demonstrated, corresponding to 1.1W of 1539nm at 20W diode pump power, new OPO mirrors would be necessary.
Optimising the output coupler would include:
a) Changing the output coupling to 40%
b) Experimenting with double passing the pump, thus enhancing the round trip gain. This might cause further problems with the pulse to pulse stability of the OPO, depending on the de-phasing of the signal components, generated now in both directions, relative to each other.

Optimising the input mirror would include:
a) Higher transmission for the fundamental (now: T = 90% @ 1047nm)
b) Higher reflection for the signal (now R = 98% @ 1540nm)

The first set of KTA experiments underlined the importance of a careful choice of the Sellmeier equation in order to predict the signal and idler wavelengths accurately. Currently the existing Sellmeier equations are only correct for restricted wavelength ranges, in combination with specific KTA-material from one particular grower. In the case of the NCPM, typeII KTA-OPO and KTA sourced from Crystal Associates (dopant free, Arsenate flux grown material) the Sellmeier set from Fenimore [18] is a very good description.
The main advantage of KTA is the transparency in the 3.5μm region, which results in a maximum of 260mW (extracted at 6kHz) of the non-resonant idler at 3.44μm. There is, however, still a notable remaining absorption in KTA at 3.44μm, with an absorption coefficient of $\alpha = 0.025/mm$. The first preliminary experiments also indicate that the effective non-linear coefficient of KTA is comparable, if not slightly smaller than that of KTP.
A second area of improvement over the KTP-OPO is the transversal mode structure of the KTA-OPO, in being TEM_{oo}, instead of resembling only parts of the TEM_{oo} or a donut mode. This might turn out to be an important advantage with this class of OPO's being the potential pump sources of the newer mid-infrared materials such as CdSe.

Future work will concentrate on improving the idler output at 3.44μm further, and on a better characterisation of the mechanism which defines the balance of the contribution by the pump laser linewidth and phase matching bandwidth of the KTP/A-OPO towards the total OPO linewidth. Attention will also be paid to the surprisingly constant idler output in figure 7.16, when the signal output is still increasing.

References

[1]: J.A.C. Terry, Y. Cui, Y. Tang, W. Sibbett & M.H. Dunn - **Low-threshold operation of an all solid-state KTP optical parametric oscillator** - J. Opt. Soc. Am. B **11**, No.5, 758 (1994)

[2]: L.R. Marshall & A. Kaz - **Eye-safe output from noncritically phase-matched parametric oscillators** - J. Opt. Soc. Am. B **10**, No. 9, 1730, (1993)

[3]: Jonathan Terry **"All-solid-state, infra-red pumped KTP OPO"** Ph.D. Thesis, University of St. Andrews, (1994)
L.R. Marshall, J. Kasinski, A.D. Hays & R.L. Burnham - **Efficient optical parametric oscillator at 1.6μm** - Opt. Lett. **16**, 681 (1991)
J.D. Bierlein & H. Vanherzeele - **Potassium titanyl phosphate: properties and new applications** - J. Opt. Soc. Am. B **6**, No.4, 622 (1989)

[4]: K. Kato - **Parametric oscillation at 3.2μm in KTP pumped at 1.064μm** - IEEE J. QE. **QE-27**, No.5, 1137 (1991)

[5]: H. Vanherzeele, J.D. Bierlein & F.C. Zumsteg - **Index of refraction measurements and parametric generation in hydrothermally grown $KTiOPO_4$** - Appl. Opt. 27, 3314 (1988)

[6]: Y.Tang, Y. Cui & M.H. Dunn - **Lithium triborate optical parametric oscillator pumped at 266nm** - Opt. Lett. **17**, No.3, 192 (1992)

[7]: G.Robertson - **"Optical parametric oscillators: A comparison of new materials"** Ph.D. Thesis, University of St. Andrews, May1993

[8]: R.G. Smith - **"Lasers: A series of advances; Vol.4 "** - p.197 Dekker, New York (1976)

[9]: L. Marshall, A. Johnson & al. - **Efficient 2-5μm KTP, KTA and $ZnGeP_2$ optical parametric oscillators** - Paper **PDP14** , Advances in Solid-State Lasers, San Francisco, January 1996

[10]: Priv. Com.: with R.Stolzenberger (through Dereck Reid, Univ. of St. Andrews) at **Crystal Associates**, Inc. , Waldwick, New Yersey 07463, USA

[11]: Priv. Com.: With Y.Tang, C. Rae at St. Andrews University

[12]: P. Moulton & al. - **Tandem OPO source generating 1.5 to 10μm** - Paper **PDP6** , Advances in Solid-State Lasers, San Francisco, January 1996

[13]: P. Katteridge & al. - **8μm $ZnGeP_2$ OPO pumped at 2μm** - Paper **PDP13** , Advances in Solid-State Lasers, San Francisco, January 1996

[14]: J.D. Bierlein & H. Vanherzeele - **Linear and nonlinear optical properties of flux-grown $KTiOAsO_4$** - Appl. Phys. Lett. **54**, No.9, 783 (1988)

[14a]: K. Kato - **Second-Harmonic and sum-frequency generation in $KTiOAsO_4$** - IEEE J. Quantum Electron. **QE-30**, No.4, 881 (1994)

[15]: Priv. Com.: with Finlay Colville at the University of St. Andrews

[16]: L.K. Cheng, L.T. Cheng, J.D. Bierlein, A. A. Ballman & F.C. Zumsteg - **Properties of doped and undoped crystals of single domain $KTiOAsO_4$** - Appl. Phys. Lett. **62**, No.4, 346 (1992)

[17]: Cameron Rae, D. Withers & M.H. Dunn - **Royal Society laser system** - Demonstrated at the Exhibition of the Royal Society, 1993

[18]: D.L. Fenimore, K.L. Schepler, U.B. Ramabadran et al. - **Infrared corrected Sellmeier coefficients for potassium titanyl arsenate** - J. Opt. Soc. Am. B **12**, No.5, 794 (1995)

[19]: Priv. Com. with R.Stolzenberger about his 1064nm pumped KTA-OPO results **Crystal Associates**, Inc. , Waldwick, New Yersey 07463, USA

[20]: W.R. Bosenberg, L.K. Cheng & J.D. Bierlein - **Optical parametric frequency conversion properties of $KTiOAsO_4$** - Appl. Phys. Lett. **65**, No.22, 2765 (1994)

[21]: K. Kato - **Second-Harmonic and sum-frequency generation in $KTiOAsO_4$** - IEEE J. Quantum Electron. **QE-30**, No.4, 881 (1994)

[22]: S. French, M. Ebrahimzadeh, A. Miller - **High-power, high-repetition-rate picosecond optical parametric oscillator for the near- to mid-infrared** - Opt. Lett. 21, No.2, 131 (1996)

[23]: F.G. Colville, A.J. Henderson, M.H. Dunn & al. - **Continuous-wave parametric oscillation in lithium triborate** - Opt. Lett. **18**, No.3, 205 (1993)

[24]: G. Valentine, G. Kennedy & W. Sibbett - **All-solid-state, compact, mode-locked Cr:YAG laser** - accepted for Euro-CLEO 1996, Hamburg

[25]: S.J. Brosnan & R.L. Byer - **Optical parametric oscillation threshold and linewidth studies** - IEEE J. Quantum Electron. **QE-15**, 415 (1979)

[26]: W. Koechner **"Solid-State Laser Engineering"** , p. 583 4th. Edition (1995), Springer-Verlag

[27]: C. Rahlff, Y. Tang, W. Sibbett & M.H. Dunn - **High repetition rate, mid-infrared KTA-OPO at 3.44μm** - accepted for CLEO'96, Paper CWF **16**

Chapter VIII.

Conclusions & Future Work

This section will take a more general view of the results of this thesis. Summaries of the exact performance can be found at the end of each experimental section. At this point it seems to be appropriate to discuss both the obvious progress and the shortcomings of this work, as well as the limits of the approach taken at the beginning of the thesis.
The outlook on future work can be separated into a part concerned with improving the laser, and another section concentrating on non-linear conversion schemes which would be suited to the characteristics of the high repetition rate Nd:YLF laser developed.

The success of this work lies in the fact that the risks of the unusual combination of the laser material Nd:YLF and high power cw diode end-pumping were balanced by the pump geometry and dimensions of the rhombic slab at a very early stage of the high power diode-pumped solid state laser development. This allowed optimum conditions for cw-pumped, repetitively Q-switched operation in a TEM_{00} mode, without being limited by the adverse thermo-mechanical properties of the laser host. An additional advantage is the compactness of this laser and the low complexity of the cavity design.
The result is a reliable, efficient, near diffraction limited and high average power laser, which is an excellent pump source for non-linear frequency conversion schemes due to its short pulses and linearly polarised output. The adaptation of the frequency converters or OPO's for the lower peak powers, characteristic for a cw pumped system, resulted in high conversion efficiencies. Therefore the benefits of a cw pumped repetitively Q-switched system with high average powers and high repetition rates could be preserved in the up or down converted radiation, covering a region from the near UV (349nm) to the mid-infrared at 3.445μm.

This end-pumped laser configuration drew attention in the form of an invited talk at CLEO '94 and subsequent commercialisation by I.E. Optomech at CLEO '95. The system developed during this thesis was state-of-the-art in '94 and pioneered:

- High average power (≤20W per surface) diode bar, end-pumping in Nd:YLF.
- Characterisation of positive, end-effect governed lensing in Nd:YLF.
- Multiwatt (up to 2.9W) TEM_{oo}, Q-switched (25ns), high repetition rate green source.

Other areas of this thesis, worth highlighting, include:

- Spatially resolved characterisation of excited state absorption processes in Nd:YLF under high density end-pumping at 1.047 and 1.321μm.
- Comparison of laser parameters at 1047 and 1321nm, with special attention to the different thermal lensing coefficients of these transitions, in identical experimental set-ups.
- High average power up- and down-conversion schemes for the 1μm laser with high efficiencies at the kW-level (pump: 4.8W @ 1047nm):
  - UV (349nm): 0.75W (15%)
  - IR (1505 nm): 0.75 (18%)
  - Green (523.5nm): 2.9W (60%)
  - IR (1540nm): 1.1W* (27%)
  - IR (3445nm): 0.26W (6%)

  All results TEM_{oo} (except *) and 5kHz repetition rate (20W pump power).
- Comparison and highlighting of inconsistencies in the currently available KTA-Sellmeier equations sets.

The problem of the distortions of the pumped surfaces, which cause the end-effect dominated lensing, also defines the scaling limit of this end-pumped laser in the current form. As the pump power increased, degrading of the cavity quality set the scaling limit, as only the non-aberrated spherical lensing could be corrected for with the spherical mirrors used. These additional pump power induced losses, despite stable round trip conditions make TEM_{oo}, or even just increased multi-mode, operation finally impossible. The final, sensible, pump power limit was reached at total pump powers of 34W, corresponding to 17W per surface. The proven and safe 20W pump power level per surface in Nd:YLF is only meaningful for providing a safety margin for the development work at the 10 to 15W pump power level per surface .

This work could achieve 5W in a near diffraction limited mode (M^2~1.3) at 1047nm under Q-switched conditions. When compared with the characteristics

of the cw operation at this output power or pump power level it has again to be emphasised that the whole system developed is primarily a Q-switched laser system. The reliability, good efficiency and short pulses given by the pump geometry and material choice still make this first generation repetitively Q-switched Nd:YLF laser a respectable pump source, four years after its initial design.

As a general concept for cw high power lasers with ≥5W TEM_{oo} output in the fundamental, the end-pumped approach in the form presented in this thesis, using linear laser diode arrays and simple focusing optics in combination with a partly monolithic resonator (the pumped windows are also cavity mirrors) is problematic. A better correction of the phase distortions originating from the pumped surfaces has to be the considered to reach scalability beyond the 5 to 6W diffraction limited output barrier.
To correct these distortions a low threshold, high reflecting, phase conjugating mirror would be the perfect solution, as it would allow correction for all pump power levels. However, as this correction technique is not yet applicable to cw diode pumped systems [1], corrective optics would have to be used which have the inherent drawback that they can compensate only for a certain pump power bandwidth. This corrective optic technique has been used in a high power end-pumped Nd:YAG laser to produce 60W TEM_{oo} output at 25% efficiency [1] in a totally symmetric cavity with two identically pumped rods. Although this work shows impressive and very detailed knowledge of the aberrations introduced through the pumped surfaces, it shifts the problem onto the reproducibility of the exact thermal conditions for which the corrective optic has been tailored. From the experience of this work with pumped surfaces (a total of two surfaces) of up to 20W from one diode, as compared to the 60W per surface (from 4 diodes) and a total of four pumped surfaces in [1], this might cause considerable problems in practice.

In order to carry on the development in high power, repetitively Q-switched lasers it would be very useful to expand on two areas of this thesis. The main effort would concentrate on a quantitative description of ESA in Nd:YLF, while the second area would be the characterisation of anisotropic lensing depending on the diode pump profile and its compensation, using a combination of cylindrical and spherical optics [2]. Both subjects are addressed under the following headings:

◦ Comparison of the Q-switch dynamics at 1.0 and 1.3μm

As an intermediate step, modelling of the Q-switched behaviour is necessary to achieve quantitative information on the magnitude of the cycling inversion, which depends on the intra-cavity intensity and pump power density, in order to confirm the qualitative results and conclusions presented in Chapter 5. The important aspect of this model would be to differentiate between constant cavity losses, pump power dependent losses (due to end-effect governed lensing) and intensity dependent losses caused by the Q-switching. The opportunity to compare the 1.0 and 1.3μm transition in a system which allows free access to the pumped area, and thus fluorescence, due to its single sided cooling and polished cooling surface, gives ideal experimental conditions for investigation of any aspect of this effect.

The next step would be a dedicated spectroscopic work, in order to determine the crossections, lifetimes and branching ratios between radiative and non-radiative decay routes. These could then be compared to the results of the rate equation model, which would be based on the assumptions presented in Chapter 5. Calibrated emission and absorption spectra are ultimately necessary to come to a valid conclusion about the importance of excited state absorption of laser radiation in Nd:YLF.

◦ Connection between non-astigmatic lensing and pumped volume

Different methods were employed to describe the end-effect governed thermal lensing under cw and Q-switched conditions, but they have only been done for the output optimised fluorescence profile. The dependence of the astigmatism on the geometry of the pumped volume in connection with the folded resonator path has never been explicitly demonstrated. This characterisation is of importance, if a change to circular pump profiles, as provided by fibre-coupled diode modules or beam shaping devices, is contemplated. Circularly symmetric pump profiles in the anisotropic host YLF should give rise to astigmatic lensing.

This analysis would be best complemented by resonator designs to compensate for astigmatism. An important consideration for this kind of work are suitable pump geometries, which are insensitive in their astigmatism behaviour during resonator path alignment. Such systems are by definition side-pumped systems or end-pumped systems with very restricted degrees of freedom. These are not systems such as the one developed in this work.

Future Work

Given the task to develop a new system, a side-pumped system along the lines of the Schwartz Electro-Optics system would be the preferred solution. Side pumping, with only a collimating lens in the high divergence plane of the diode, has by definition the principal advantage of reduced pump densities in the laser host, thus reducing the adverse thermal effects of a strongly focused pump beam.

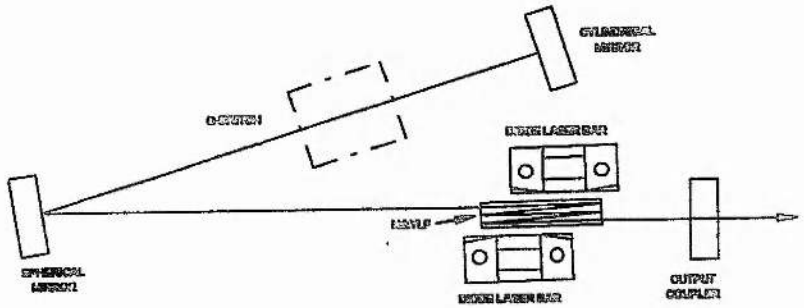

Fig. 1. Schematic of laser (5-pass Nd:YLF).

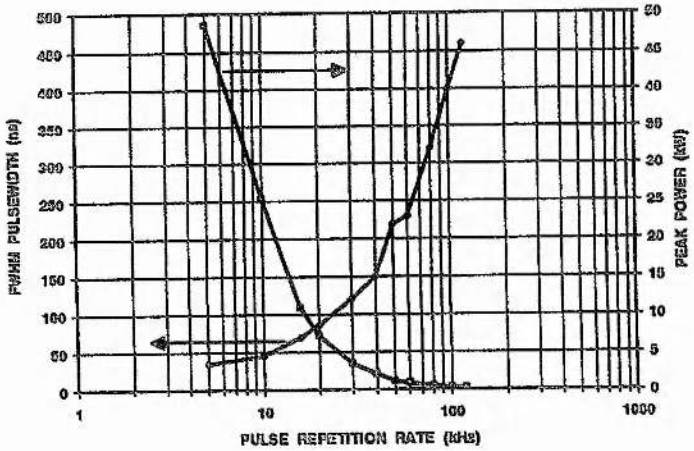

Fig. 2. Peak power, pulse-width vs. PRF.

Fig. 8.1: *A side-pumped repetitively Q-switched Nd:YLF slab laser developed by Harrison of Schwartz-Electro-Optics in 1995 [2]. The **c**-axis orientation maximises the gain for the folded resonator path, while the pump radiation is parallel to the **a**-axis, reducing the absorption as desired in an side-pumped system.*

Pumping through antireflection coated windows (@797nm), while reflecting the tightly folded resonator path on the remaining two unpumped windows, separates the pumped, distorted windows from the cavity defining, now undisturbed surfaces in this partly monolithic design. This reduces any thermal effects due mainly to bulk effects, which will prevent the extremely strong and aberrated lensing associated with the end-effect governed lensing characterised

in this thesis.
The main disadvantages traditionally associated with side-pumping, such as reduced efficiency and difficult transversal mode control appear to have been overcome with this system. High efficiencies of up to 33% (slope) have been realised by the tightly folded resonator path. The quoted TEM_{oo} operation at IR output power levels is remarkable and might be partly attributed to the spatially varying loss caused by the ESA in Nd:YLF under Q-switched conditions.

However, following published concepts in the field of high power lasers can be as time consuming as developing new systems. In the experience gained during this work it appears that attention to details is vital for success with the development of solid state lasers. In particular slab systems, with their tendency to parasitic oscillations, are unforgiving of design mistakes relating to the geometry, surface and coating specifications, which can easily render them useless. Taking this necessary learning curve into account a lot is to be said in staying with the basics of the slab system described in this thesis, or in taking the whole risk of a 'new' development.

Given the chance to modify the current system the partly monolithic design of the zig-zag slabs would be given up and replaced by pumping through external, non-distorted mirrors, with the slab windows only anti-reflection coated. This change would have to go along with the use of fibre coupled diode pump modules or 'beam shaped' linear array diodes, firstly to achieve the necessary working distance for the external mirrors and secondly to gain a circularly symmetric pump volume. This pump module change away from focused diode arrays would optimise the efficiency and transverse mode control at the same time. Before these expensive changes to the existing design, tests with a low power fibre coupled module are important to confirm these expected improvements and optimise the focusing of a now unpolarised pump beam, as the fibre bundle is not polarisation preserving.
All these changes are mainly aimed at an improvement of the beam quality of the laser, as the system in its current form is already comparable in average output power alone with the now leading systems, if pumped with 30W of diode output. In particular the short Q-switched pulse duration (down to 10ns as compared to ~40ns in figure 8.1) are the main advantage of this laser. Only the beam parameter product of $M^2=2$ renders this mode of operation not suitable for most non-linear optics experiments.

If the use of a fibre coupled pump module is not possible, then the use of a micro-lens array to optimise the existing, simple focusing optics is an alternative to improve the Nd:YLF slab laser further.
Besides these changes to the slab and pump modules, it has to be recalled that the acousto-optical Q-switching device used is already close to the limit of its switching time capabilities in the current set-up. If higher energy per pulse is the main requirement (as for non-linear optical applications), then an acousto-optical Q-switch with a faster speed of sound becomes necessary. Higher average power pumping in combination with the existing acousto-optical Q-switching device would only scale the average power of the system at increased repetition rates.

The future direction on the non-linear optics side should concentrate on the transition from the well explored route of designing low threshold OPO's in the walk-off free, non-critically phase matched (NCPM) geometry, to tunable critically phase matched (CPM) OPO's, which still match the characteristics of low energy, high repetition laser systems [3]. The next important step would be the combination of the frequency conversion into the near UV with the experience gained of operating the low threshold KTP-OPO to study an UV pumped, broadly tuneable LBO OPO in the visible. A more detailed overview of possible future activities is given under the respective headers below:

◦ KTP/A-OPO: The main aim, after the high average power capability of these low threshold OPO has been demonstrated is to concentrate on the beam quality and linewidth issues of these OPO's. In particular the reason for the ring structure of the KTP-OPO signal output in the far field has to be investigated, as at the time of writing KTP, as compared to KTA, is the much more matured and preferable non-linear material for applications below 2.8μm. Beam quality issues of the down-converted radiation in the 1.5μm and 3.4μm region are of growing importance, as this class of OPO's can be used as pump sources for mid-infrared OPO's [4].

◦ UV generation: Optimising the focusing into the doubler and LBO tripler, and choosing the appropriate length of the then AR-coated LBO frequency mixer, should improve the conversion efficiency into 349nm further, so that the 1W level could become a realistic target. Additionally, a type I NCPM LBO doubler instead of the KTP Type II CPM crystal so far used could boost the

green and/or UV generation. The UV range is of special interest as it is the pump wavelength for tuneable OPO's in the visible.
The 262nm UV region, accessible by frequency doubling of the green in BBO, would be a very interesting addition. A few experiments during this thesis with this typeI critically phase matched process suggested that it might be too inefficient to be used as a frequency quadrupled pump source, due to the combination of low available peak power and considerable walk-off. Nonetheless the capability of the high repetition rate laser at the edge of its abilities would be interesting in itself.

◦ UV pumped LBO-OPO: At present the converted IR pump source can deliver 120 to 150μJ in 25ns at 349nm (5 to 6 kHz). This should be sufficient to get above the threshold of a CPM type I LBO-OPO and thus open the possibility of a high repetition rate, tuneable all-solid-state source in the visible. The threshold optimisation of this critically phase matched OPO is more complicated, as the walk-off limits tight focusing and useful crystal length; parameters which have been used in the non-critically phase matched geometry to improve the KTP-OPO. It will be interesting to see in how far the main advantage of a cw pumped Q-switched laser - the high average output power - can be preserved in the tuneable, visible radiation.

In retrospect this thesis has established that Nd:YLF is an excellent gain material for cw-pumped, high repetition rate, Q-switched lasers operating at 1047nm. The positive material parameters, such as high energy storage capacity and natural birefringence are not hampered by the low thermal shock parameter of Nd:YLF.
The low threshold, non-linear conversion processes demonstrated that the benefits of a cw pumped, repetitively Q-switched laser - high average power and high repetition rates - can be preserved in the converted radiation, even under the condition of multi step conversion processes.

References:

[1]: S.C. Tidwell, J.F. Seamans & M.S. Bowers Opt. Lett. 18, No. 2, 116, (1993)
[2]: J. Harrison, P.F. Moulton & G.A. Scott, Paper CPD-20 CLEO 1995
[3]: Y. Tang, C. Rae & M.H. Dunn, Paper CWF14 CLEO 1996
[4]: P. Moulton & al. Paper PDP6 , Advances in Solid-State Lasers 1996

Appendix

A1. Sellmeier equations
A2. Sources & Measuring Equipment
A3. Mie-Scattering on a coated KTP surface
A4. Brewster angle in anisotropic materials
A5. Publications
A6. Errata

A1. Sellmeier equations

A2. Sources & Measuring Equipment

a) **CW laser diodes**

20W cw AlGaAs diode laser array
SDL 3460 (48 emitters, 10mm x 1μm aperture), λ_D ~ 800nm (centre)
Note: No longer manufactured in this package, now only 20 emitters and wavelength restrictions. Optopower diodes (agent: Spectra Physics) might be a worthwhile alternative.

AMS-Electronics LTD. (New agent, former Spectra Physics)
Castle Circus House, 136 Union Street
Torquay TQ2 5QG
Tel.: 01803-200655 Fax: 01803-200656

b) **Diode drivers**

Constant current supply unit with full short circuit protection
CZ 115 (maximum 40A, up to 6V)

Kingshill Electronics Products LTD.
Springhead Enterprise Park
Northfleet
Kent, DA11 8HJ
Tel.: 01474-327833 Fax: 01474-564796

c) **Nd:YLF slabs**

Rhombic cut **Nd:YLF slabs** ~ 7 x 7 x 2 mm^3 (see figure 2.4)

Lightning Optical Corporation
431 E. Spruce Street
Tarpon Springs, Florida 34689, USA
Tel.: 001-813-938-0092 Fax: 001-813-938-9493

d) **Focusing optics**

- **Rod lens:** f = 1.2mm, uncoated, fused silica
1.6mm dia., 20mm long

Off the shelf lenses are available from Spindler & Hoyer but they are difficult to mount due to only 12mm length.
Agate Products Limited address on next page

Agate Products Limited
2/4 Quintin Avenue
Merton Park
London, SW 20 8LD
Tel.: 0181-5428266 Fax: 0181-5409876

- **Cylindrical lens** (f = +12mm) and **aspherical condenser** (f = +8.5mm) AR/AR coated, broadband (650 - 1000nm)

Newport Ltd.
4320 First Avenue, London Road
Newbury
Berks., RG13 2PZ
Tel.: 01635-521-757 Fax: 01635-521348

e) **Mirrors, beamsplitters and polarisers**

Laseroptik GmbH.
Gneisenaustr. 14
D- 30826 Garbsen, Germany
Tel.: 0049-5131-45970 Fax: 0049-5131-459720

f) **Temperature control equipment**

- **Temperature controllers**
  Proportional temperature controller **model 70A** (module)

Nexus Custom Electronics, Inc.
Prospect Street, PO Box 250
Brandon, Vermont 05733-0250, USA
Tel.: 001-802-247-6811 Fax: 001-802-247-3946

- **Thermocouple for temperature controllers**
  Miniature **ntc thermistor 10kΩ**, RS-no.: 256-045

RS
PO Box 99
Corby
Northants, NN17 9RS
Tel.: 01536-201201 Fax: 01536-201501

- **Heating resistors in diode cooling blocks**
  ~ 110Ω, nominal 24W (consists of 6 parallel 680Ω, 4W resistors)
  under cooled conditions these resistors can be overloaded well into the 100W region. Supplier: RS (see above)

- **Thermal conductive epoxy to implement heating resistors**
  'Green epoxy' from Marlow Industries, Inc.

Marlow Industries UK
7 Laura House, Jengers Mead
Billingshurst
West Sussex, RH14 9NZ
Tel.: 01403-784849 Fax: 01403-782901

- **Indium foil (for slab & laser diodes)**
  125μm thick Indium foil

Advent Research Materials LTD.
Blyth Road, Industrial Estate
Halesworth
Suffolk, IP19 8DD
Tel.: 01986-874555 Fax: 01986-874557

- **Miniature water connectors and hosepipes:**

The West Group
Aston Road, Waterlooville
Portsmouth, PO7 7XY
Tel.: 01705-266031 Fax: 0.1705-240323

g) **Q-switching equipment**

- **Q-switch**
  Type **QS 080,** anti-reflection coated at 1064nm (off the shelf item)
  80MHz operating frequency, maximum cw RF power 3W
- **Q-switch driver**
  Type **MD 080-4A** with 4W maximum RF output (cw)
  80MHz band centre

Isle Optics
Unit 1, Monks Dairy, Isle Brewers
Taunton
Sommerset, TA3 6QL
Tel.: 01460-281557 Fax: 01460-281235

h) **Non-linear crystals**

- 5 and 10mm long **KTP doubler** for 1047nm (5 x 5mm^2 aperture) coated AR/AR @ 1047 & 523.5nm, flux grown
  Source: Shandong University, Jinan, China (Agent: Caladox)

- 16mm long **LBO tripler** for 1047nm (5 x 5mm^2 aperture), uncoated
  Source: Castech, Fuzhou, China (Agent: Photox)

- 25mm long **KTP-OPO crystal** (5 x 5mm^2 aperture)
  7mm long **KTA-OPO crystal** (3 x 3mm^2 aperture)
  coated AR/AR @ 1.047 & 1.55μm (& 3.5μm, KTA), flux grown
  Source: Shandong University, Jinan, China (Agent: Caladox)

Caladox Ltd.
The Observatory, Buchanan Gardens
St. Andrews
Fife KY16 9LZ
Tel.: 01334-479633 Fax:01334-479632

Photox Optical Systems
PO Box 274, 2 Pullens Lane
Headington
Oxford, OX3 0BJ
Tel.: 01865-64563 Fax: 01865-741778

Measuring Equipment

i) **Power meter**

Ophir power meter head **30A** (up to 30W cw), analogue display AN
Surface absorber, spectrally flat 0.2 - 20µm ± 3%
Supplier: **Optilas** (Fax: 01908-221110)

ii) **Spectrum analyser**

Anritsu Optical Spectrum Analyser **MS 96 0A**, fibre coupled input
Range: 0.6µm - 1.6µm, 0.1-0.2nm resolution
Supplier: **Anritsu Wiltron Ltd.** (Fax: 01582-31303 Tel.: -418853)

iii) **CCD - Camera**

Kappa CCD-camera **CF6/1**
Spectral sensitivity: 300 - 1200nm, exposure time: 1/50 - 1/1800 sec.
sensing area: 8.8mm (H) x 6.6mm (V), elements: 600 (H) x 590 (V)
each pixel: 11 x 11.3µm (H,V)
Supplier: **Henke, Sass & Wolf** (Fax: 01993-822614)

iv) **Detector card**

- 1047 & 1321nm: **Infrared Display Card**, type: 06 DLA 002
low sensitivity, high damage threshold ; 800 - 1400nm
Supplier: Melles Griot (Fax: 01223-425310)
- 1.55µm : **Infrared Display Card**, type: **Quantex Q-32-R**
high sensitivity, extended detecting range, 800 - 1700nm
Supplier: **AG Electro-Optics** (Fax: 01829-733679)

v) **Digital oscilloscope**

Tektronix TDS 350, 1GHz sampling, 200MHz analogue bandwidth
real time sampling rate: 1 sample/ns
Supplier: **Tek Direct** (Fax: 01628-41220)

vi) **Photo diodes**

- 1047nm: **BPW 28B**, silicon photo detector (no longer available)
ac-coupled, 130V reverse bias, rise time < 1ns
- 1321nm: **GM 3**, germanium photo detector
ac-coupled, 9V reverse bias, rise time ~ 2ns
Supplier: **L.G. Products Ltd.** (Fax: 01932-829606)

A3. Mie-Scattering on a coated KTP surface

The following two pages illustrate that the position of the anchor or arrow like scattering figure with regard to the exit surface of the KTP is dependent on the distance between the crystal surface and the frequency doubled beam.

Both sequences were taken for distances of 0.5mm, 1mm and 2mm between the upper edge of the green beam and the respective crystal surface, which was the plane of observation. The scatter pattern moves backwards with increasing separation between crystal surface and green beam.
The first pictures in each sequence are shown in figure 6.5 on page 161. The additional frames are only presented here in order to underline that the unexpected intensities at the exit surface of the KTP crystal are a linear scattering effect.

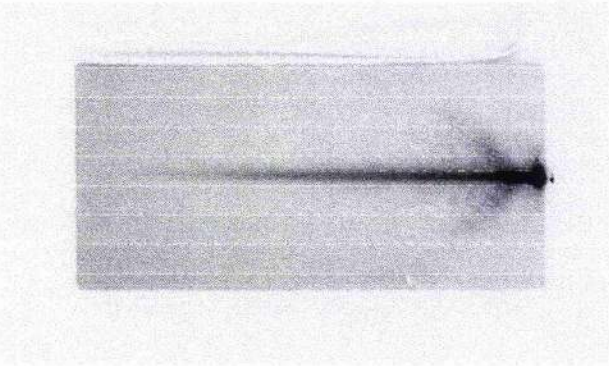

0.5mm

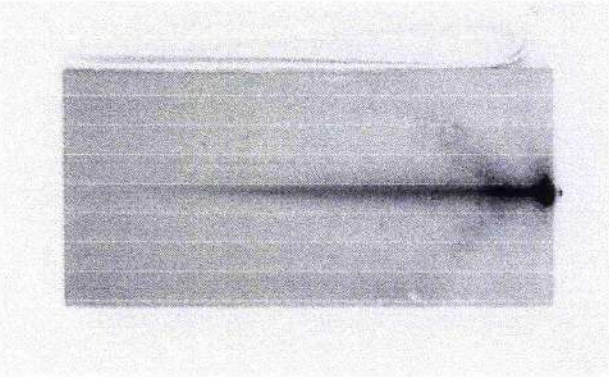

1.0mm

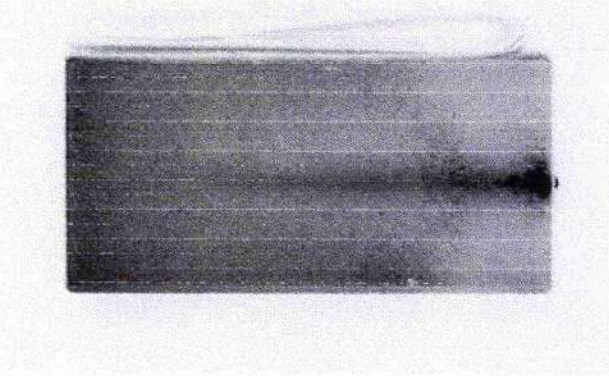

2.0mm

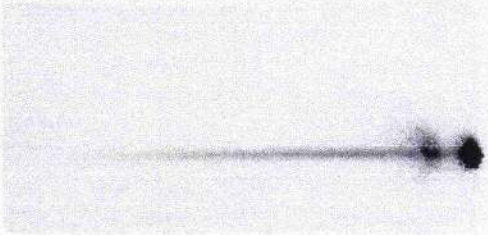

0.5mm

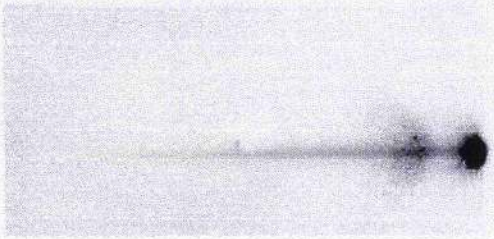

1.0mm

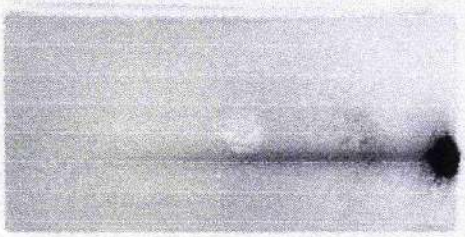

2.0mm

A4. Brewster angle in anisotropic materials

V.1. Brewster angle for the extraordinary beam in uniaxial crystals

Refraction as described by Snell's law applies to the propagation of the wave front, i.e. it relates wave normal directions in the two media. In the normal case of isotropic media the propagation direction of the wave or phase front (vector $\mathbb{n}$) coincides with the direction of the energy flux given by the Poynting vector $\mathbb{s}$ ($\mathbb{s} = \mathbb{S} / |\mathbb{S}|$).
In the case of an extraordinary beam in an uniaxial crystal the beam path is not described by Snell's law, which implies that the usual equation for the Brewster angle does not hold any more. The difference angle δ between the wave normal vector $\mathbb{n}$ and the energy vector $\mathbb{s}$ can be calculated as follows [1]:

$$\cos\delta = \frac{\langle \mathbb{E}\ \mathbb{D}\rangle}{|\mathbb{E}\mathbb{D}|} = \frac{\langle \mathbb{E}\ \varepsilon\mathbb{E}\rangle}{|\mathbb{E}\varepsilon\mathbb{E}|} \quad ; \qquad \varepsilon = \begin{pmatrix} \varepsilon_x & 0 & 0 \\ 0 & \varepsilon_y & 0 \\ 0 & 0 & \varepsilon_z \end{pmatrix} \qquad (1)$$

Bearing in mind this change in the direction of the energy flux and recalculating the fresnel equations, considering energy conservation and continuity of the tangential component of the $\mathbb{E}$-field at the dielectric boundary, yields in the following result for the reflection coefficient of the parallel $\mathbb{E}$-field at this boundary:

$$q_{\parallel r} = -\frac{E_{\parallel r}}{E_{\parallel i}} = -\frac{\tan(\alpha - \beta)}{\tan(\alpha + \beta)} \quad ; \qquad \beta = \beta_n + \delta \qquad (2)$$

Therefore the condition for the Brewster angle (for notation see figure V.1) has to be rewritten to:

$$\Theta_B + \beta_n + \delta = 90° \qquad (3)$$

$\delta > 0$: optical positive (e.g.: YLF)

$\delta < 0$: optical negative (e.g.: Calcite)

Where β_n is the angle of the refracted phase path described by Snell's law [1]:

$$\sin\beta_n = \frac{\sin\alpha}{n_e(\vartheta)} \quad ; \quad \frac{1}{n_e^2} = \frac{\cos^2(\vartheta)}{n_0^2} + \frac{\sin^2(\vartheta)}{n_e^2} \qquad (4)$$

By suitable mathematical manipulations β_n and the correction angle δ can be calculated, for a known angle of incidence α and orientation angle γ of the crystal optic axis to the surface, as follows:

$$\tan \beta_n = \frac{P}{\sin\gamma \cos\gamma \left(\frac{1}{n_o^2} - \frac{1}{n_e^2}\right) + \sqrt{\frac{P}{\sin^2\gamma} - \frac{1}{n_o^2 n_e^2}}} \quad ; \quad P = \frac{\sin^2\gamma}{n_o^2} + \frac{\cos^2\gamma}{n_e^2}$$

$$\tan \delta = \frac{\tan\vartheta \,(n_e^2 - n_o^2)}{n_e^2 + n_o^2 \tan^2\vartheta} \quad ; \quad \vartheta = 90° + \gamma - \beta_n \qquad (5,6)$$

In the case of this slab the calculated correction angle δ equals zero, as the orientation of the incident beam is at 90° to the crystal axis. Applying these equations to the earlier described end pumped slab (previous RARDE report, p. 16 ff) results in a correction angle δ of around 0.8°. Due to the zig-zag path inside the crystal this makes only a change in the form of the rhombic shaped slab by 0.2° necessary. The practical merit of this problem is in the case of YLF therefore limited. Nevertheless with stronger birefringence as for example in Calcite ($\Delta n = 0.172$, opposed to $\Delta n = 0.022$ in YLF) a maximal correction angle δ of 6.3° becomes possible.

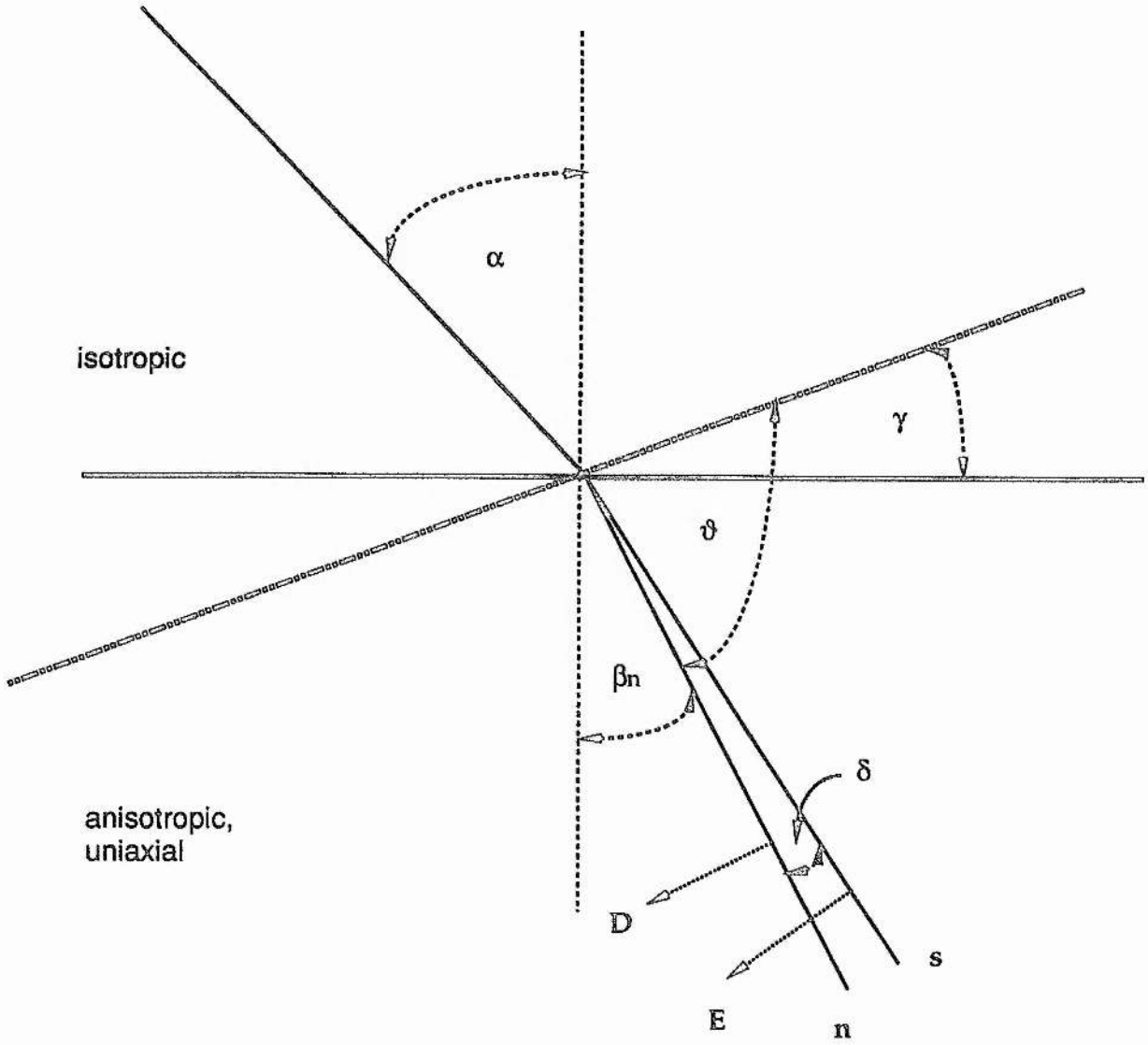

Fig.V.1: Brewster angle in anisotropic materials

A5. Publications

Poster at the UK Quantum Electronics Conference 11, Belfast, August 1993
Rahlff, Sinclair, Sibbett, Dunn
'Scalable cw diode end-pumped Nd:YLF slab system'

Talk at the Institute of Physics Annual Congress, Brighton, April 1994
MacKinnon, Rahlff, Sinclair, Sibbett, Dunn
'Contrasts in diode pumped lasers:
From slab systems to micro-chip lasers'

Paper CThG4, CLEO'94, Anaheim, May 1994
Rahlff, Sinclair, Sibbett, Dunn
High power end-pumped effects
and applications in Nd:YLF at 1047 and 1321nm

Paper CTuJ4, accepted at the CLEO'96, Anaheim, June 1996
Morrison, Rahlff, Ebrahimzadeh & Dunn
A high-average-power all-solid-state laser
single-frequency Ti:Sapphire laser

Paper CWF16, accepted at the CLEO'96, Anaheim, June 1996
Rahlff, Tang, Sibbett & Dunn
High repetition rate, mid-infrared KTA-OPO at 3.44μm

A6. Errata